Master Thesis

Active Direct Sound Control

Application in Hearing Instruments

conducted at the
Signal Processing and Speech Communication Laboratory
Graz University of Technology, Austria

in co-operation with
Phonak AG
Stäfa, Switzerland

by
António Maria Hölzl, 0573048

Supervisors:
Dipl.-Ing. Dr.techn. Martin Hagmüller
Dipl.-Ing. Dr. Markus Hofbauer (Phonak AG)
Dr. sc. techn. Alfred Stirnemann (Phonak AG)
MSc. Thomas Zurbrügg (Phonak AG)

Assessors/Examiners:
Univ.-Prof. Dipl.-Ing. Dr.techn. Gernot Kubin

Graz, January 14, 2013

Abstract

Hearing instruments that do not acoustically seal the ear canal (vented fitting) have become more popular in recent years. The wearing comfort is increased by airing the ear canal through the vent in the earpiece. This fitting method has been made possible due to the development of powerful feedback cancelers that successfully deal with the problem of sound being fed back from the receiver through the vent to the outer microphone. At the same time, the ambient sound intrudes the ear canal through the vent and superimposes the processed sound of the hearing aid at the ear drum.

The superposition of the hearing instrument sound and the unprocessed sound, i.e. the direct sound, causes a deterioration of the sound quality because of the comb filter effect. Moreover, the intelligibility is reduced because the benefits of the hearing instrument algorithms are less perceptible because the processed sound is partially masked by the unprocessed direct sound.

This thesis studies the attenuation of undesired sound at the ear drum using in-the-ear hearing aids. The ambient sound is sensed by the outer microphone and played back phase-inverted by the receiver such that the direct sound is attenuated at the ear drum (destructive interference).

A static and an adaptive system approach are introduced and implemented on a real time system. The acoustic environment as well as its influence on the receiver and the achievable attenuation are outlined. The limits of the system concerning audible distortions and their prevention are discussed and objective measures to evaluate the distortions are introduced.

The developed framework for the static system as well as the algorithms of the adaptive system and their adjustments to the acoustic environment are described. Both approaches are analyzed on a real time system with real world signals and compared to simulations conducted in MATLAB® and Simulink® .

The results show that an attenuation of more than 10 dB between 200 Hz and 2 kHz can be achieved. The maximal ambient sound level at which distortions are not audible is signal dependent and can exceed 90 dB SPL for speech-like noise.

Compared to the static approach, the adaptive method shows no significant improvement on the achievable attenuation. Therefore, the considerably higher complexity and computational cost of the adaptive system would not be justified. Thus, the static approach is preferable for the implementation in hearing instruments.

Kurzfassung

Hörgeräten, die den Ohrkanal nicht mehr akustisch verschließen (offene Anpassung), haben in den letzten Jahren zunehmend an Bedeutung gewonnen. Dies liegt an dem gesteigerten Tragekomfort, der durch die Belüftung des Ohrkanals mittels einer Öffnung im Ohrpassstück erreicht wird. Möglich wurde diese Art der Anpassung mit der Entwicklung von leistungsstarken Rückkopplungsunterdrückern, da der Hörgeräteschall über die Öffnung an das Außenmikrofon zurückgeführt wird und Rückkopplung verursachen kann. Umgekehrt gelangt der Umgebungsschall über die selbe Öffnung an das Trommelfell und überlagert den vom Hörgerät verarbeiteten Schall.

Die Überlagerung des Hörgeräteschalls durch den unverarbeiteten Schall, dem sogenannten Direktschall, führt zum Einen zu einer deutlichen Qualitätsreduktion aufgrund des sich ergebenden Kammfiltereffekt und zum Anderen zur Verschlechterung der Sprachverständlichkeit.Die Wirkung der Hörgerätealgorithmen kommt durch die Maskierung des Direktschalls nicht mehr voll zum Tragen.

Diese Arbeit befasst sich mit der Unterdrückung des Direktschalls am Trommelfell mittels Im-Ohr Hörgeräte. Der Umgebungsschall wird mit dem Außenmikrofon aufgezeichnet und über den Ohrhörer gegenphasig ausgespielt, sodass der Direktschall am Trommelfell gedämpft wird (destruktive Interferenz).

Ein statisches und ein adaptives Verfahren werden vorgestellt, die auf einem Echtzeitsystem implementiert sind. Die akustischen Gegebenheiten sowie deren Einfluss auf den Ohrhörer und auf die erreichbare Unterdrückung werden beschrieben. Die Grenzen des Systems hinsichtlich hörbarer Verzerrungen und deren Vermeidung werden diskutiert und Maße zur Beurteilung der Verzerrungen aufgeführt.

Das entwickelte statische Verfahren mit der zugrundeliegenden Signalverarbeitung sowie die für das adaptive Verfahren eingesetzten Algorithmen werden vorgestellt. Die Anpassung beider Methoden an die akustischen Gegebenheiten wird im Rahmen der Arbeit aufgezeigt. In einer Echtzeitumgebung wird die Leistungsfähigkeit der Verfahren mit realen Signalen untersucht und mit Simulationen in MATLAB® und Simulink® verglichen.

Die Ergebnissen zeigen, dass mit dem entwickelten Verfahren eine Unterdrückung von mehr als 10 dB zwischen 200 Hz und 2 kHz erreichbar ist. Der hierbei maximale Umgebungsschallpegel, bei dem das System verzerrungsfrei arbeitet, ist von der Signalklasse abhängig und erreicht über 90 dB SPL für Sprachgeräusche.

Mit dem adaptiven Verfahren sind gegenüber dem statischen Verfahren in der gegebenen akustischen Umgebung keine signifikanten Vorteile zu erzielen, welche die deutlich höhere Komplexität und den höheren Rechenaufwand rechtfertigen würden. Das statische Verfahren ist daher für die Implementierung in Hörgeräten vorzuziehen.

Statutory Declaration

I declare that I have authored this thesis independently, that I have not used other than the declared sources/resources, and that I have explicitly marked all material which has been quoted either literally or by content from the used sources.

date

(signature)

Abbreviations

ADSC	Active Direct Sound Control
ANC	Active Noise Control
AOC	Active Occlusion Control
BTE	Behind The Ear hearing instrument
CIC	Complete In the Canal hearing instrument
DC	Direct Current
DSP	Digital Signal Processor
FB-ANC	Feedback Active Noise Control
FF-ANC	Feed-Forward Active Noise Control
FIR	Finit Impulse Response
FxFLMS	Filtered-x Frequency-domain Least Mean Squares algorithm
FxNLMS	Filtered-x time-domain Least Mean Squares algorithm
HI	Hearing Instrument
IIR	Infinite Impulse Response
IR	Impulse Response
ITC	In The Canal hearing instrument
ITE	In The Ear hearing instrument
ITE-HM	In the Ear Hardware Model
LMS	Least Mean Square
LTI	Linear time-invariant
M_c	Canal microphone
M_0	Outer microphone
MPO	Maximal Power Output
NCD	Noncoherent Distortion
OEG	Open Ear Gain
PEAQ	Perceived Audio Quality
PSD	Power Spectral Density
R	Receiver
REAG	Real Ear Aided Gain
REOG	Real Ear Occluded Gain
RIC	Receiver In the Canal hearing instrument
RLC	Resistance-Inductance-Capacitance circuit
RMS	Root Mean Square
RTS	Real Time System
SNR	Signal to Noise Ratio
SPL	Sound Pressure Level
THD	Total Harmonic Distortion
TNCD	Total Noncoherent Distortion

Contents

Abstract i

Kurzfassung iii

Abbreviations vii

1 Introduction 1
- 1.1 Objective . . . 1
- 1.2 Active noise control variants . . . 2
- 1.3 Overview . . . 4

2 Acoustic system environment 7
- 2.1 The vent effect . . . 7
  - 2.1.1 Impact on REOG . . . 10
  - 2.1.2 Impact on the receiver - the ventloss . . . 14
  - 2.1.3 Impact on ADSC compensation filter . . . 18
- 2.2 Measurement of the transfer functions . . . 21
  - 2.2.1 Canal microphone position . . . 22
  - 2.2.2 Measurement of the REOG . . . 23
  - 2.2.3 Measurement of the PLANT . . . 24
- 2.3 Variability of the transfer functions . . . 27
- 2.4 Receiver Distortion Limits . . . 30
  - 2.4.1 Subjective bound . . . 31
  - 2.4.2 Algorithmic bound . . . 39
- 2.5 Conclusion . . . 44

3 Static ADSC Filter Design 45
- 3.1 Design Requirements . . . 46
- 3.2 Manual Biquad Filter Design . . . 47
  - 3.2.1 Design of REOG Filter . . . 47
  - 3.2.2 Design of the inverse PLANT Filter . . . 48
  - 3.2.3 Design of the Compensation Filter H_{COMP} . . . 50
- 3.3 Filter Design with Approximation Methods . . . 51
  - 3.3.1 Requirements on the Approximation Methods . . . 51
  - 3.3.2 Methods overview . . . 52
  - 3.3.3 Procedure of the Gauss Newton Method . . . 55
- 3.4 Static Filter Approximation Framework . . . 57
  - 3.4.1 Overview . . . 57
  - 3.4.2 Low Frequency Limitation . . . 58
  - 3.4.3 Pre-equalization of H_{COMP} . . . 61
  - 3.4.4 Filter Validation . . . 62

4 Adaptive ADSC Filter Design **65**
4.1 LMS algorithm for ADSC . . . 66
4.1.1 Inclusion of the PLANT - the FxLMS algorithm . . . 66
4.1.2 PLANT estimation . . . 68
4.1.3 Step size and Stability of the FxLMS . . . 69
4.1.4 Convergence time of the FxLMS . . . 70
4.1.5 Performance of the FxLMS . . . 71
4.2 Time and Frequency Implementation of FxLMS . . . 71
4.2.1 Time-Domain FxLMS . . . 72
4.2.2 Frequency-Domain FxLMS . . . 73
4.3 Algorithm Modification for ADSC in HI framework . . . 75
4.3.1 Low frequency limitation . . . 75
4.3.2 Pre-equalization of the adaptive Filter . . . 77

5 Results **81**
5.1 Static Design . . . 81
5.1.1 Difference between Calculations and Measurements . . . 82
5.1.2 Variability of the attenuation . . . 83
5.1.3 Maximal SPL . . . 85
5.1.4 Low frequency Limitation . . . 86
5.2 Adaptive Design . . . 88
5.2.1 Simulation with ideal transfer functions . . . 88
5.2.2 Measurements with real transfer functions . . . 89

6 Conclusion and Further Work **93**
6.1 Conclusion . . . 93
6.2 Further Work . . . 94

A Calculation of the Algorithmic Bound **97**

B Approximation Algorithm **99**
B.1 Equation error minimization . . . 99
B.2 Gauss-Newton method . . . 100

C Additional Results **103**
C.1 Static results . . . 103
C.1.1 Differences between Calculations and Measurements . . . 103
C.1.2 Variability of the attenuation . . . 103
C.1.3 Maximal SPL . . . 108
C.1.4 Low frequency Limitation . . . 108
C.2 Adaptive results . . . 109
C.2.1 Simulation with ideal transfer functions . . . 109
C.2.2 Measurements with real transfer functions . . . 110

D Measurement Equipement **117**
D.1 Hardware . . . 117
D.3 Measurement Setup . . . 120

Bibliography **121**

1 Introduction

Active direct sound control (ADSC) is a specific application of sound control designed for hearing aids and belongs to the well-known subject area of active noise control (ANC). ANC is widely used for the attenuation of unwanted sound and vibrations, in particular for low frequency disturbances, where passive attenuation is usually not feasible anymore. Its application field extends from the industry to the consumer electronics and covers among others the reduction of engine noise or air flow inside a duct as well as the attenuation of the ambient sound in headsets [1].

ANC uses the principle of superposition of sound waves such that they compensate each other at a desired location. This technique is called destructive interference and was first patented by Lueg in 1936 for acoustic waves [2]. In general, the unwanted sound waves are detected by one or more microphones, whose electric output signals are fed to an analog or digital controller. The controller drives one or more loudspeakers, which produce a sound field with inverted phase at the desired location, such that the unwanted sound is canceled out.

ANC has high requirements on the hardware of the controller. For the developed system the controller has to generate an accurate phase inverted signal within the propagation delay between the microphone and the loudspeaker. These demands are fulfilled by digital controllers with fast input/output paths, which have now entered also the hearing instruments industry.

1.1 Objective

With the entry of digital signal processors in the hearing aid industry and the development of complex algorithms such as feedback canceler the demand for so-called vented hearing instruments, which do not seal anymore the ear canal, increased rapidly. The achieved wearing comfort, however, has the drawback that the ambient sound is not attenuated anymore passively by the earpiece of the hearing instrument but propagates through the ear canal up to the ear drum. This propagation path from the outside of the ear to the ear drum is called *direct sound path* and depends on the acoustic coupling of the earpiece to the ear. The incident unprocessed ambient sound is referred to as the *direct sound* and superimposes the HI-processed sound at the ear drum.

In particular at low frequencies, the superposition of the unprocessed and processed sound has two drawbacks for the hearing impaired user:

- The direct sound masks the HI-processed sound and, hence, annuls the hearing improvements provided by the HI algorithms.
- the direct sound may have a similar amplitude as the HI-processed sound, which is delayed by a few milliseconds due to the signal processing of the hearing aid. The superposition of both signals results in the so called comb filter effect, which has equidistant zeros and peaks and deteriorates the sound quality of the hearing instrument. The comb filter effect is perceived as a "rough" or "hollow" sound like like in a huge duct and considered in general as disturbing.

ADSC has the objective to attenuate the direct sound in front of the ear drum such that the HI algorithms become audible again also at lower frequencies and the sound quality of the hearing instrument is improved. Although both cases need the control of the direct sound, the former calls for a high attenuation in the frequency range, where the direct sound is dominant, while for the latter case the direct sound must only be attenuated at those frequencies, where the amplitudes of both the unprocessed and the processed sound are close to each other.

ANC is often used in acoustic environments where the unwanted signal, i.e. noise, should be attenuated such that a desired signal becomes better perceptible or its quality is enhanced (e.g. headsets with ANC), which signifies an improvement of the signal-to-noise ratio (SNR). In contrast, in ADSC for hearing instruments the unwanted signal, i.e. the direct sound, is highly correlated with the desired signal, which is the HI-processed sound, because both are filtered versions of the ambient sound in front of the ear. Thus, for individuals with normal hearing the direct sound can not be referred to as noise. However, for hearing impaired people, which are dependent on a HI-processed version of the ambient sound, the unprocessed direct sound deteriorates the intelligibility and the sound quality. In this case the direct sound can be treated as noise, which should be attenuated.

Up to the present day, active direct sound control in hearing instruments is not implemented on any hearing instrument, albeit several patents submitted by hearing instrument companies concerning this subject were already granted [3–6]. Most probably this is due to the high requirements on the controller hardware mentioned above as well as the adverse acoustic conditions for ADSC in hearing aids, which limit its applicability.

Despite the submitted patents, only Serizel published an extensive study about ANC in hearing instruments. In his PhD thesis he discusses on a theoretical base only the combination of active noise control and noise reduction schemes in hearing aids [7]. However, the focus of his thesis and his previous publications is explicitly on noise reduction rather than on the attenuation of the direct sound. Nevertheless, he concludes, based on simulations, that the combination of both systems outperforms standard noise reduction performance. This encourages to research how well ADSC performs solely and how beneficial it is for hearing impaired people.

In the thesis the HI-processed sound is not considered since the focus relies on the maximal achievable attenuation in the frequency range, where the direct sound at the ear drum is dominant.

1.2 Active noise control variants

Active noise control can be realized with two different strategies. Both methods detect the sound waves with one or more microphones and use the gathered information to emit a phase-inverted signal via one or more loudspeakers, which attenuate the sound at a desired location. However, the position of the microphones and the loudspeakers relative to the propagation direction of the sound waves is determining.

The system invented by Lueg in [2] describes the so called *feed-forward ANC* (FF-ANC), where the microphone senses the acoustic waves produced by a primary source before they reach the secondary loudspeaker, which emits the phase-inverted sound. The microphone output is used as a reference signal of the sound field and fed to the controller, who drives the secondary loudspeaker. In this structure the microphone may only record the primary source and has to be acoustically separated from the second loudspeaker in order to avoid any feedback loops.

In 1953 a second method was presented by Olson and May in [8] which became known as *feedback ANC* (FB-ANC). Instead of using a reference signal of the acoustic waves which is used to attenuate the sound at specific location, the FB-ANC attenuates the signal in the vicinity of the microphone and produces there a so-called “zone of quiet” [9]. This is achieved by feeding back the sensed microphone signal to the controller. There, the phase-inverted signal is generated and played through the secondary source. In order to get a stable feedback system, the microphone has to be placed close to the secondary source to keep the propagation delay as small as possible and the resulting loop gain must be less than 1 for all frequencies.

The controller of both methods can be realized either as a static time-invariant filter or as an adaptive time-variant filter. The selection of the controller has to be determined for each ANC application individually as it depends on several factors such as the variability of the acoustic environment, the affordable computational cost or the available hardware. The static approach is favorable since it is less complex and computationally intensive. However, it needs a stable acoustic environment to achieve a constant performance. While the FB-ANC needs only one microphone at the place of the desired attenuation for a static or an adaptive filter approach, the FF-ANC needs, besides the reference microphone at the primary sound source, a second microphone at the desired attenuation location for the adaptive filter case. For the static case a second microphone is only required to design the controller but not during operation. Hence, it can be removed once the controller is designed.

ADSC in hearing aids can be implemented either as a feed-forward or a feedback ANC system with a static or an adaptive controller, respectively. Fig. 1.1 shows the structure of an In-The-Ear hearing aid (ITE) extended by (a) the FF-ANC and (b) the FB-ANC system. Both variants include the static (*green*) and the adaptive (*black*) filter approach.

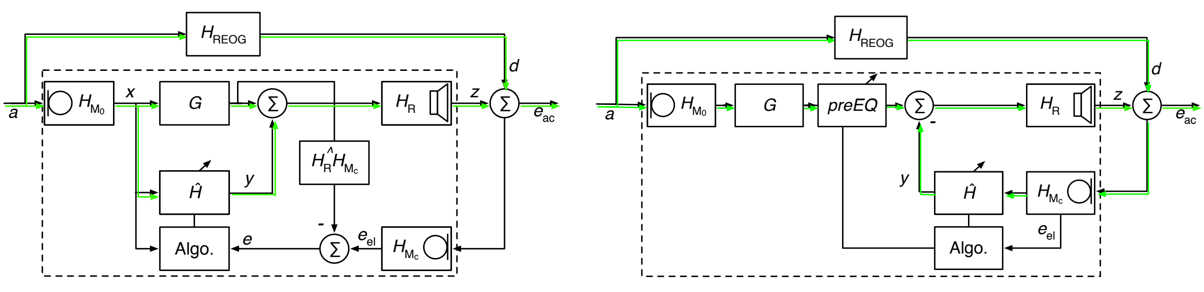

(a) FF-ANC

(b) FB-ANC

Figure 1.1: Block diagrams of ADSC based on (a) feed-forward ANC and (b) feedback ANC

The H_{REOG} (**R**eal **E**ar **O**ccluded **G**ain) block denotes the transfer function from the outside of the ear to the microphone position in the ear canal with the frequency response $H_{\mathrm{M_c}}$, where the sound should be attenuated, and is usually called primary path in the control literature [1].

The acoustic path between the secondary source (R) and the microphone at the attenuation position ($\mathrm{M_c}$) is called secondary path. The static respectively adaptive filter is defined as $\hat{H}$ and the reference microphone of the FF-ANC is denoted by the frequency response $H_{\mathrm{M_0}}$. This microphone is also used for the normal hearing instrument processing, which is pooled by the block G, independently of the implemented ANC system. The HI-processed sound is emitted via the same loudspeaker (R) as the phase-inverted direct sound, which in the hearing instrument industry is called receiver, with the frequency response H_{R}. The additional blocks $\widehat{\mathrm{preEQ}}$ in the feedback and $H_{\mathrm{R}}\hat{H}_{\mathrm{M_c}}$ in the feed-forward case avoid the attenuation of the HI-processed sound by the ANC system.

There are several pros and cons to use the feed-forward respectively the feedback ANC system for ADSC in hearing instruments. FF-ANC is always stable as long as the static or the adaptive filter is stable. Furthermore, the static case needs only a reference microphone, which is already present in ITEs. However, for the adaptive case a second microphone has to be added in the ear canal. A disadvantage of FF-ANC is that only the sound, which is sensed by the reference microphone, can be attenuated in the ear canal.

FB-ANC needs a microphone at the position at which the sound should be attenuated. This implies for ADSC that a microphone has to be placed in the ear canal, which can not be otherwise used by the hearing instrument and may change its characteristics due to the cerumen in the ear canal. A major drawback of FB-ANC is that it can become unstable if the secondary path, the receiver or the canal microphone change and the filter $\hat{H}$ is not adapted. On the other side, FB-ANC attenuates not only the incident direct sound but any sound in the ear canal. In particular for hearing aids, whose earpiece seal the ear canal acoustically, the level of bone conducted sounds like the own voice increases dramatically, which is called the occlusion effect. The reduction of this effect can be achieved by FB-ANC and is known as active occlusion control (AOC) [10].

So far, ADSC based on FF-ANC has only been demonstrated in combination with AOC in an earlier feasibility study [11]. It showed that combining both ANC methods yields a better attenuation than AOC, i.e. FB-ANC, alone. However, the study was conducted with hearing aids which sealed the ear canal acoustically. In this work the performance of the direct sound attenuation for vented hearing aids is examined such that the results of the former study have little meaning.

Due to the advantages of FF-ANC, ADSC is analyzed as feed-forward structure with a static and an adaptive filter approach in this work.

1.3 Overview

This work is divided into three parts, which comprise the acoustic environment, the applied signal processing and the achieved results of the ADSC system.

In the first part of the work (Chapter 2) the acoustic environment, in which the direct sound should be canceled, is investigated. The transfer function from the outside of the ear into the ear canal, i.e. the REOG, the transfer function of the receiver and the resulting ideal compensation filter, which yields a perfect attenuation of the direct sound in front of the ear drum, are presented for different acoustic couplings of prototypes to the ear. The measurement of these transfer functions as well as their variabilities are outlined and discussed for different hearing aid prototypes.

Furthermore, the limits of the receiver in regard of audible distortions and degradation of the potential attenuation of the system are analyzed for narrow and broad band signals and the maximum tolerable sound pressure levels (SPLs) for this application are determined.

The second part introduces the algorithms used for the ADSC system in order to attenuate the direct sound. Chapter 3 covers the static filter approach and presents the used framework. Furthermore, the requirements on the filter design for ADSC in hearing aids are defined and five objective parameters are introduced which allow an evaluation of the attenuation achieved with the designed filters.

Chapter 4 presents two adaptive algorithms commonly used for feed-forward ANC. Special modifications are required and were developed for adaptive ADSC in hearing aids.

The last part of the work presents the performance of the developed static and the adaptive ADSC system in regard of the attenuation of the direct sound (Chapter 5). The results of both systems are discussed and their limits concerning the usability are pointed out.

In Chapter 6 the results of this thesis are summarized and an outlook about the further work is given.

2 Acoustic system environment

The characteristics of the acoustic system environment determine the active direct sound control (ADSC) performance. As mentioned in Chapter 1 active noise control is based on the idea of destructive interference by generating a sound with equal amplitude but opposite phase relative to the unwanted sound at a certain point. Therefore, the acoustic propagation paths from the recording microphone to the canceling point (primary path) and from the receiver to the canceling point (secondary path) as well as the electro-acoustic characteristics of the transducers have to be known.
In the first section of this chapter the acoustic environment of the system is presented and the propagation paths are explained. The second section discusses the measurement methods of the propagation paths as well as the transducer responses and their variabilities are outlined in the third section. The last section discusses the electro-acoustic behavior of the receiver and its limits for ADSC in hearing aids.

2.1 The vent effect

In order to provide the processed HI-sound to the patient, the hearing device must be coupled to the ear canal either by an earmold (Behind-The-Ear (BTE) HIs), a dome (Receiver-In-the-Canal (RIC) HIs) or an earshell (In-The-Ear (ITE), In-The-Canal (ITC) and Completely-In-the-Canal (CIC) HIs). Independently from the device, one distinguishes two forms of fitting these earpieces to the canal: the closed fitting and the vented fitting. A closed fitting implicates the major acoustic changes with regards to an open ear canal because it seals approximately the ear canal. The earpiece acts as a hearing protection and reduces significantly the air exchange between the ear canal and the environment. The lack of air exchange has the disadvantages that it can provoke infections in the ear canal and that it leads to an amplification of the own voice in front of the ear drum. This increase is called occlusion effect and is one of the main reasons of the discomfort reported by closed fitted hearing aid users [12]. The advantage of closed fitting is the passive damping of the direct sound path and the feedback path. Thus, on the one hand, the direct sound interferes less with the processed HI-sound which enhances the perception quality for the user. On the other hand, the output level of the receiver may be increased, particularly, since the enclosed residual volume of the ear canal enables the receiver to produce high sound pressure levels also at low frequencies. This allows the compensation of severe broad band hearing losses.

The discomfort of closed fitting can be diminished by airing the ear canal, which is done by adding a vent to the earpiece. As a result of the vented fitting, the sound pressure inside the ear canal decays which for the occlusion effect is desirable but affects also the processed HI-sound emitted by the receiver. At the same time, the passive attenuation of the direct sound path and the feedback path is reduced which restricts the applicability of vented fitting only to mild and moderate hearing losses. As it will be shown, the attenuation of the propagation paths as well as the pressure drop depends on the dimensions of the vent.

Both fitting methods eliminate a prominent characteristic of the open ear canal which is the $\lambda/4$-resonator with its boost of up to 20 dB around 3 kHz in front of the ear drum. The $\lambda/4$-resonator occurs because the open ear canal resembles a pipe which is terminated by the ear drum. By inserting an earpiece in the ear canal the resonance vanishes and has to be compensated by the gain model of the hearing aid.

In this thesis, ADSC is only investigated for vented earshells as they are used in ITE hearing aids. Since closed fitted hearing aids attenuate the direct sound already passively, there is less need for an additional active cancellation. The choice of ITEs is based on the favorable positions of the microphones, as it will be seen later in this work.

Fig. 2.1(a) shows a model of the closed fitted ITE that seals the ear canal entirely. Hence, the ear canal becomes a closed air volume with a semi-stiff wall, i.e. the ear drum. In Fig. 2.1(b) the vent is added to the ITE so that there is air flux between the canal and the outside. The vent resembles a tube which ends on one side in an infinite volume and on the other side in the same ear canal volume as the closed fitting.

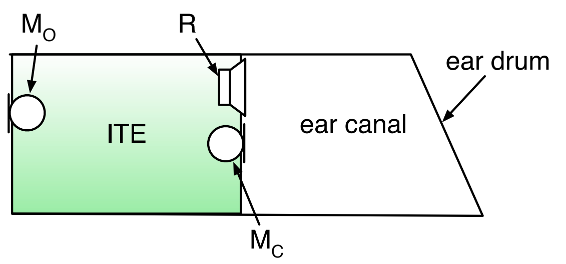

(a) closed fitting

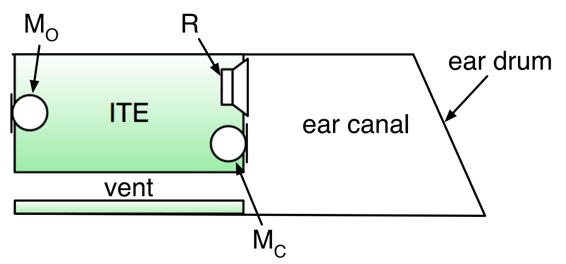

(b) open fitting

Figure 2.1: Hearing Instrument in the ear canal with receiver R, canal microphone M_c and outer microphone M_o

By using the electro-acoustic analogy [13, chp. 3] it is possible to describe the acoustic characteristics with corresponding electric components. Thus, the acoustic network containing the vent and the ear canal can be modeled as an electric circuit, which simplifies the calculation of the impedances and the transfer functions. The sound pressures corresponds to the voltage and the volume velocity corresponds to the current.

The vent is a tube with open ends which is equivalent to the transmission line in the electric domain and has a closed-form solution. The transmission line models not only the air mass inside the tube but also the dissipation of the molecules and the $\lambda/2$-resonances [14]. The electric analogy of the ear canal volume, however, is not exactly defined, since the ear canal volume is bounded by the semi-stiff ear drum and thus it is not an ideal acoustic volume. The behavior of the ear drum depends mostly on the middle ear compliance and together they form a complex acoustic network. Several approximations with lumped parameters were developed over the years which model an average ear canal volume with an average ear drum and middle ear [15, pp. 82-85]. The same applies to the transducers, which are described by lumped-parameter models that include the electrical, the mechanical and the acoustic part. Each transducer has its own parameter set that approximates the real transducer response.

For a rough approximation of the acoustic environment with lumped parameters, the dissipation effects of propagating waves in the tube are ignored and the ear canal together with the ear drum is considered as a volume with stiff walls. Thus, a series of an acoustic resistance and an acoustic mass replaces the tube and the ear canal is modeled by a simple acoustic volume. This is analogous with a series of resistance R_{v} and inductance L_{v} and a capacitance C_{ear} in the electrical domain, respectively. Fig. 2.2 shows the electric components, where Z_{R}, $Z_{\mathrm{M_c}}$ and $Z_{\mathrm{M_0}}$ are the complex impedances of each transducer and Z_{drum} the one of the ear drum.

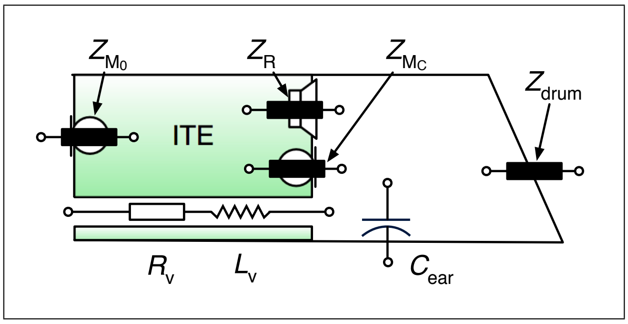

Figure 2.2: Electro-acoustic analogy of an vented ITE, simple model

The approximate impedance of the vent is then described by

$$\begin{aligned} Z_{\mathrm{v}}(j\omega) &= R_{\mathrm{v}} + j\omega \cdot L_{\mathrm{v}} \\ L_v &= \frac{\rho \cdot l}{\pi \cdot r^2} \end{aligned} \tag{2.1}$$

and the approximated impedance of the ear canal volume by

$$\begin{aligned} Z_{\mathrm{ear}}(j\omega) &= \frac{1}{j\omega \cdot C_{\mathrm{ear}}} \\ C_{\mathrm{ear}} &= \frac{V_{\mathrm{ear}}}{\rho \cdot c^2}. \end{aligned} \tag{2.2}$$

where ρ is the mass density and c is the speed of sound. l_{v} and r_{v} are the length and the radius of the vent, respectively, and V_{ear} is the enclosed volume of the ear canal. This approximation resembles the real behavior only at low frequencies where the dissipation effects are small and the ear drum has an impedance similar to an acoustic volume. To get more realistic data, that can be evaluated also for higher frequencies, all simulations are done with cascades of two-ports which incorporate an exact model of the transmission line, a realistic model of an ear canal and the lumped parameter models of the transducer given by the manufacturer. Fig. 2.3 shows the impedances of the vent with the dimensions $l_{\mathrm{v}} = 20$ mm and $r_{\mathrm{v}} = 1$ mm and the ear simulator "earCanal$_{\mathrm{v2}}$" developed at Phonak AG by Stirnemann [16]. For the rough approximation the acoustic resistance is set to $R_{\mathrm{v}} = 10^6\ \frac{\mathrm{Ns}}{\mathrm{m}^5}$ and the ear canal volume $V = 1.4\ \mathrm{cm}^3$. For the sake of completeness, also the input impedance of the canal microphone "Sonion 50GC31" and the Thevenin impedance of the receiver "Sonion E50DA012" (parallel circuit) are plotted. The rough approximation results in a valid simulation for frequencies below 1 kHz (*dot-dashed*) whereas the two-port model (*solid*) simulates also higher dynamics of the vent and the ear drum, which coincides better with real measurements.

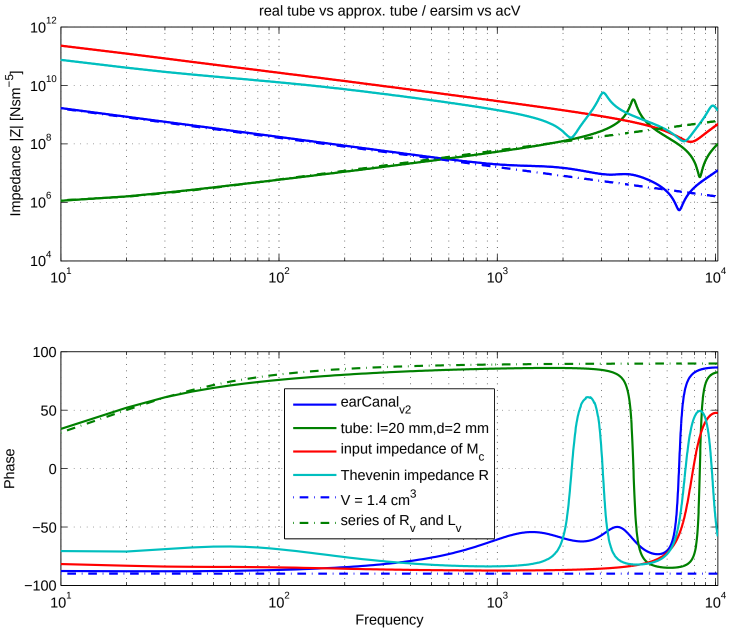

Figure 2.3: Impedances of the vent and ear canal: simulation with the two-port model (solid) *and the rough approximation model* (dot-dashed)

In the following sections the effect of the vent is first pointed out for the direct sound path and for the receiver. Section 2.1.3 introduces the compensation filter $H_{\mathrm{COMP}}(j\omega)$ of the ADSC system and discusses the influence of the vent on it.

2.1.1 Impact on REOG

The real ear occluded gain (REOG) is defined as the transfer function of the direct sound. In other words, the REOG describes the propagation of the sound waves through the vent and the ear canal to the ear drum. This transfer function is of major interest as it corresponds to the primary path of the FF-ANC system used in this work. The ideal environment assumes that the primary sensor - in this application the outer microphone M_0 - records precisely the signal at the entry of the vent, which is physically impracticable. Nevertheless, the sound pressure at the vent entry is always assumed to be the same as at the position of the outer microphone M_0. Furthermore, it is difficult to measure the pressure directly at the ear drum of an individual. Thus, the pressure in the ear canal is measured with the canal microphone M_c. The impact of the microphone position in regard to the ADSC performance is discussed in Section 2.3. Fig. 2.4 shows the measurements taken with the ITE hardware model (ITE-HM) connected to the ear simulator "IEC711" from the company G.R.A.S.

An incident sound wave sees an acoustic network which consists of the vent that ends in the ear canal volume which is terminated by the ear drum. At the transition from the vent to the ear canal volume the input impedance of the microphone M_c and the Thevenin impedance are parallel-connected. Fig. 2.5(a) shows the electric circuit of the REOG with the complex impedances which are plotted in Fig. 2.3. From there it is clear that the impedances of the transducer have little influence in the parallel network and thus can be assumed as infinitely

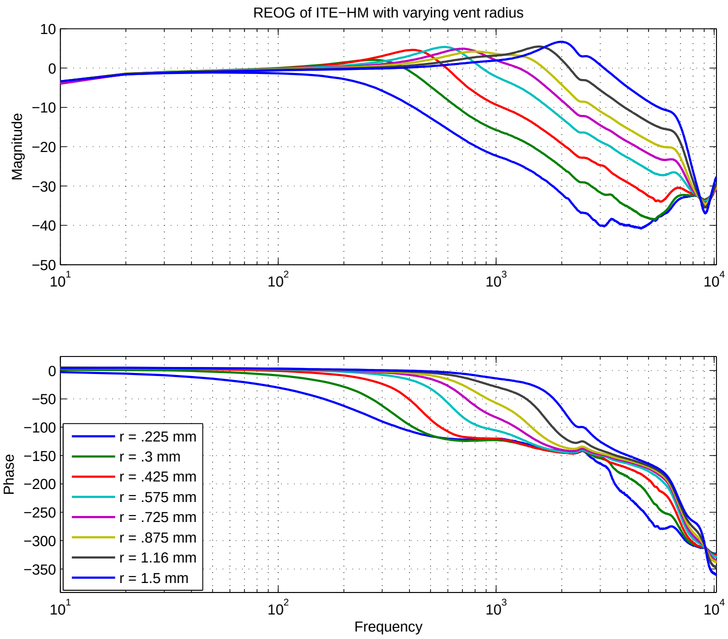

Figure 2.4: REOG *of ITE-HM with varying vent radius: vent length $l_v = 5$ mm, ear simulator "IEC711 G.R.A.S.", outer and canal microphone "Sonion 50GC31", receiver "Sonion E50DA012" (parallel circuit). The plot shows the* REOG *measured with the microphones of the model. The excitation signal is pink noise and the measurement is done in an acoustically sealed box*

high, i.e $Z_R = Z_{M_c} = \infty$. Thus, in a first approximation the network is simplified to Fig. 2.5(b) by using the lumped parameters defined in Section 2.1.

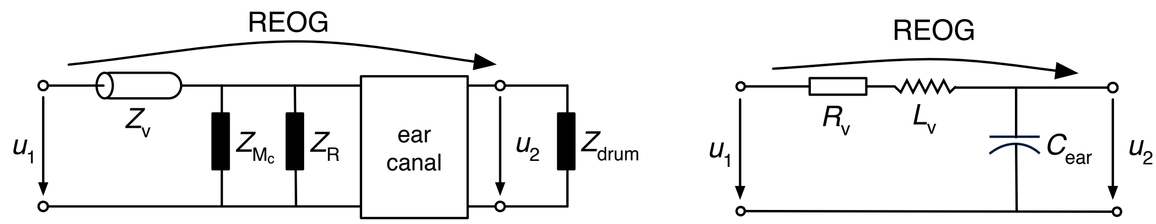

(a) complex electric circuit of the REOG

(b) simplified electric circuit of the REOG

Figure 2.5: Electric circuit of the REOG

The transfer function of the input voltage to the output voltage can then be formulated as

$$H_{\mathrm{REOG}}(j\omega) = \frac{u_2(j\omega)}{u_1(j\omega)} = \frac{Z_{\mathrm{ear}}(j\omega)}{Z_{\mathrm{v}}(j\omega) + Z_{\mathrm{ear}}(j\omega)} = \frac{1}{-\omega^2 L_{\mathrm{v}} C_{\mathrm{ear}} + j\omega R_{\mathrm{v}} C_{\mathrm{ear}} + 1} \tag{2.3}$$

which is the standard equation of a 2^{nd} order series RLC low-pass. Using the acoustic entities of Eqs. (2.1) and (2.2) the cutoff frequency is calculated by

$$f_{\mathrm{c}} = \frac{1}{2\pi\sqrt{L_{\mathrm{v}} C_{\mathrm{ear}}}} = \frac{1}{2\pi}\sqrt{\frac{c^2 r_{\mathrm{v}}^2 \pi}{V_{\mathrm{ear}} \cdot l_{\mathrm{v}}}} \tag{2.4}$$

and the quality factor by

$$q = \frac{\sqrt{L_\mathrm{v}}}{R_\mathrm{v}\sqrt{C_\mathrm{ear}}} = \frac{1}{R_\mathrm{v}}\sqrt{\frac{\rho^2 c^2 l_\mathrm{v}}{\pi r_\mathrm{v}^2 V_\mathrm{ear}}} \tag{2.5}$$

From this approximation follows that a vented earpiece has negligible influence on the frequencies below the resonance of the low-pass filter and corresponds to the open ear canal. For frequencies above the cutoff frequency the damping of the incident sound is 40dB/decade. Assuming a constant environment, the cutoff frequency and the quality factor depend only on the dimensions of the vent and the ear canal volume. From Eq. (2.4) one can see that the cutoff frequency changes linearly with the vent radius r_v, whereas it changes inversely with the square root of the vent length and the ear canal volume. The quality factor, however, increases with the vent length but decreases with the vent radius and ear volume and depends also on R_v. Fig. 2.6 shows the REOG for varying vent radii of the simple model, whereby the length l_v and the resistance R_v as well as the ear canal volume V_ear are kept constant. It should be mentioned that R_v depends on the vent radius and attenuates the resonance with decreasing r_v, which is not included in the simple model.

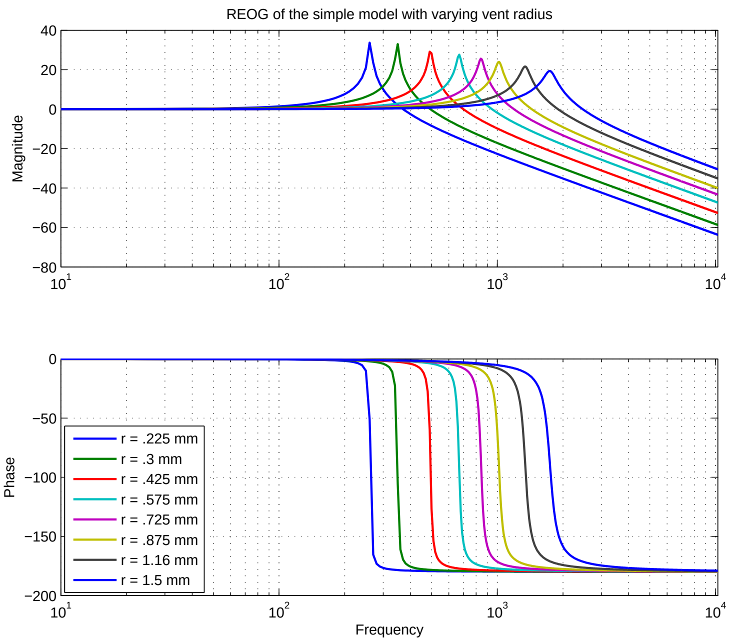

Figure 2.6: REOG *of the simple model with varying vent radius: vent length* $l_\mathrm{v} = 5$ *mm, acoustic Resistance* $R_\mathrm{v} = 10^6\ \frac{\mathrm{Ns}}{\mathrm{m}^5}$*, ear canal volume* $V = 1.4\ \mathrm{cm}^3$*. The vent dimensions correspond to the ITE-HM of Fig. 2.4*

The comparison of this simulation with the real world measurements of Fig. 2.4 reveals evident discrepancies, which makes this model to be significant only to a limited extent. While the resonance frequency and the decay of 40dB/decade coincide at least for vent radii between $r_\mathrm{v} = 0.3$ mm and $r_\mathrm{v} = 0.853$ mm, the resonance peaks and the phase response differ significantly. If the vent radius converges to zero the hearing aid is closed fitted and the direct sound is significantly damped over the entire frequency range. Thus, the quality factor decreases with smaller vents which is not the case in the simulations. It is also known that, if the radius of the vent is equal to the radius of the ear canal r_ear, then the REOG corresponds to the open ear gain (OEG) and the ear canal resembles a stopped pipe with $\lambda/4$-resonances. With the simple 2^{nd} order low-pass equation with constant R_{v} and C_{ear} neither the damping of the resonances nor the $\lambda/4$-resonator can be modeled. Furthermore, the equation does also not consider any time delay caused by the propagation of the sound wave, which changes the phase of the REOG and can be described by

$$\Theta(f,d) = \mathrm{e}^{-j2\pi f \frac{\Delta d}{c}} \tag{2.6}$$

where Δd is the length of the propagation path and c is the speed of sound.

Replacing the series of acoustic resistance and inductance with a real tube alleviates the overshoot problem at the resonance frequency of the simple model and simulates even the damping of a nearly closed fitted shell. To get also the effect of the $\lambda/4$-resonator of the open ear canal it is reasonable to design the ear canal volume as a real tube with an average ear canal radius. The more the radius of the vent r_{v} approaches the radius of the ear canal r_{ear}, the more the REOG merges to the OEG with its characteristic boost near 3 kHz. Using the ear simulator "earCanal$_{\mathrm{v2}}$", which assumes an average ear canal radius $r_{\mathrm{ear}} = 3.75$ mm, allows to simulate the REOG much more precisely compared to the simple model. The resulting model incorporates both the real tube and the ear simulator as two-ports and is thus called two-port model in this thesis. The simulations are run with the same dimensions of the vent as of the ITE-HM.

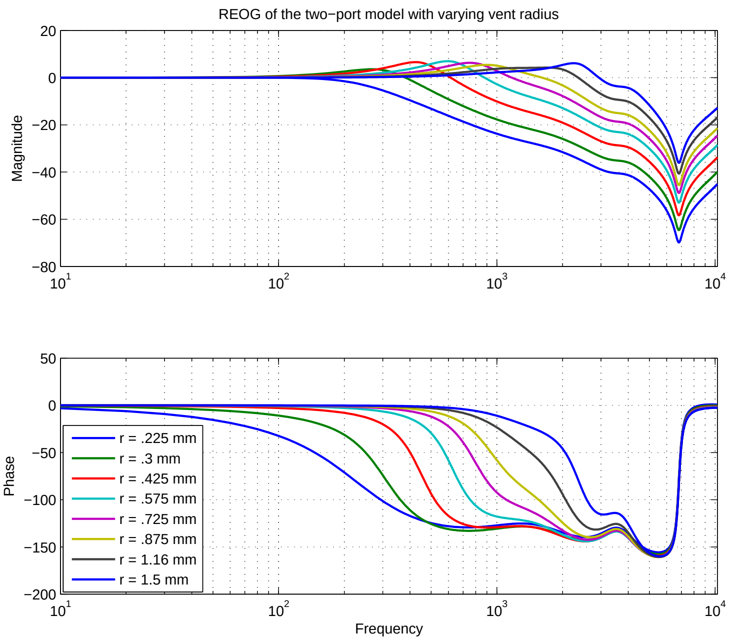

Figure 2.7: REOG *of the two-port model with varying vent radius: vent length* $l_{\mathrm{v}} = 5$ *mm and ear simulator "*earCanal$_{\mathrm{v2}}$*". The vent dimensions correspond to the ITE-HM of Fig. 2.4*

The results of the two-port model coincides well with the measurements of the ITE-HM up to 2 kHz. Above that the model deviates with increasing frequency evermore from the real acoustic behaviors which is mainly caused by the simplified lumped parameter model of the ear simulator. Nevertheless, it can be used to simulate the effects of different ear canal volumes which will be encountered for each individual and to make assumptions about an appropriate filter design. Also complexer vent configurations built up by various tubes with different radii can be adequately analyzed.

2.1.2 Impact on the receiver - the ventloss

The fitting method of earpieces affects not only the direct sound path but changes also the performance of the attached receiver. In general, the receiver of a hearing aid must fulfill several requirements. On the one hand, the output power has to be high enough to compensate the hearing loss of the users without introducing noticeable distortions. On the other hand, the current drain has to be as small as possible so that the operating time of the hearing device lasts for several days. Further, the receiver dimension must be small in order to be mounted in the cases of the hearing devices. In particular, the last two requirements are fulfilled by the balanced-armature electromagnetic transducers which have been almost exclusively used by hearing aid manufactures for years [17, 18]. These receivers are known for their high source impedance which makes them to a volume velocity source and thus nearly independent from the acoustic load of the ear canal. Assuming a voltage driven volume velocity source, depicted in Fig. 2.8, implies that the sound pressure is directly subjected to the acoustic load:

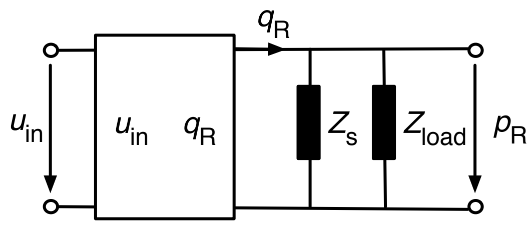

Figure 2.8: Electric circuit of a voltage driven volume velocity source (balanced-armature receiver) with source resistance Z_s and an acoustic load Z_load

$$\frac{p_\mathrm{R}(j\omega)}{q_\mathrm{R}(j\omega)} = \frac{Z_\mathrm{s}(j\omega) \cdot Z_\mathrm{load}(j\omega)}{Z_\mathrm{s}(j\omega) + Z_\mathrm{load}(j\omega)} \approx Z_\mathrm{load}(j\omega), \quad Z_\mathrm{load}(j\omega) \ll Z_\mathrm{s}(j\omega) \tag{2.7}$$

where p is the sound pressure, q is the volume velocity and Z are the respective impedances. Thus, any change of the acoustic configuration, i.e. the acoustic load, alters the sound pressure in front of the ear drum. Fig. 2.9(a) shows the simulation of the "voltage-to-volume velocity" transfer function of the receiver that radiates into a small (*blue*) and a big volume (*green*). In Fig. 2.9(b) the correspondent "voltage-to-sound pressure" transfer functions are depicted.

From there it can be seen that the change of the acoustic load has no significant effect on the volume velocity but on the sound pressure in the ear canal. Since the objective of the ADSC developed in this thesis is the cancellation of the direct sound in front of the ear drum by using the emitted sound pressure of the receiver as interfering source, it is of major interest to know how the sound pressure behaves depending on the vent.

The manufacturers of hearing aid receivers measure their devices for the datasheets in a closed volume, e.g. a '2cc'-coupler, which are used as reference. Connecting the receiver to a vented volume will cause a different receiver response and the ratio between the sound pressure of the vented to the closed volume is called ventloss. Since the behavior of the receiver does not change and $Z_\mathrm{load}(j\omega) \ll Z_\mathrm{s}(j\omega)$ is always valid in this application, the ventloss can be seen as independent from the receiver.

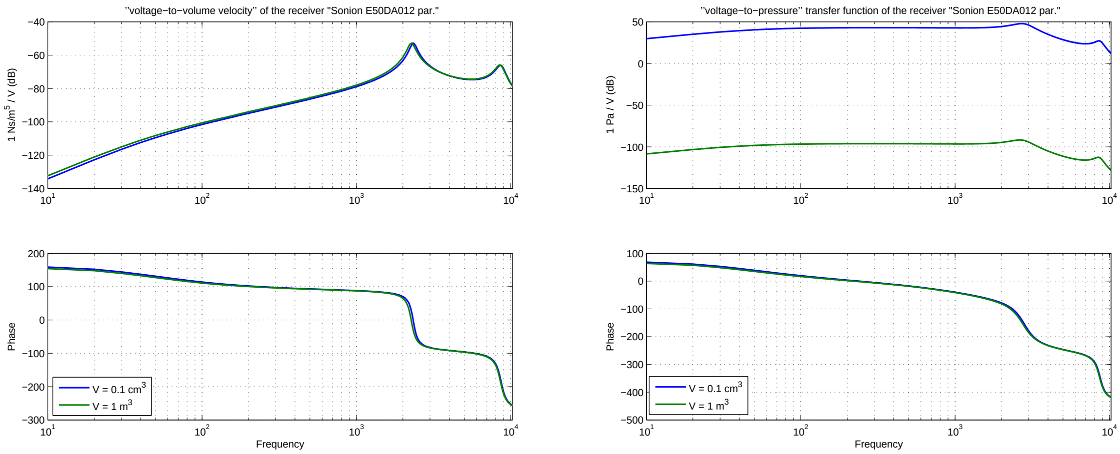

(a) "voltage-to-volume velocity" transfer function (b) "voltage-to-sound pressure" transfer function

Figure 2.9: Simulation of the volume velocity and sound pressure of the balanced-armature electromagnetic receiver "Sonion E50DA012" (parallel circuit) coupled to a small (blue) and a big (green) volume. The receiver has a high output impedance and can be seen as a nearly ideal volume velocity source

The vent effect on the voltage to pressure transfer function of the receiver can be described by an equation similar to the REOG in Section 2.1.1. Therefore, the acoustic network of the receiver load has to be defined both for the closed and the vented case. In the former case the receiver radiates to an ear canal volume which is terminated with the ear drum. In the latter case, the vent is added and builds an acoustic path to the ambient volume in parallel to the ear canal volume as depicted in Fig. 2.2. Applying the electro-acoustic analogy, the acoustic network can be designed as a simple parallel circuit as depicted in Fig. 2.10. For the sake of completeness, the input impedance of the canal microphone M_c is added, too.

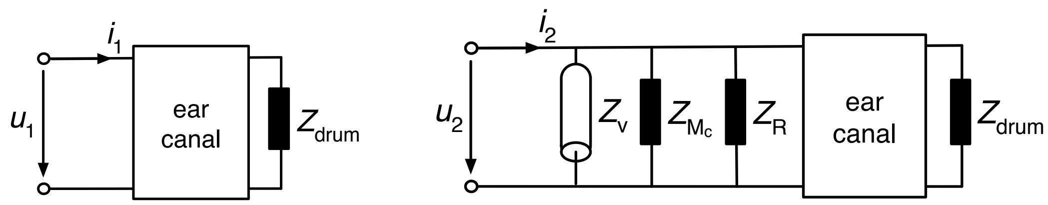

(a) closed fitting (b) open fitting

Figure 2.10: Complex electric circuits of the acoustic load seen by the receiver for closed and vented hearing aids

The networks can be simplified analogous to Section 2.1.1, where a series of acoustic resistance and acoustic mass substitutes the vent and the ear canal volume together with the ear drum and the middle ear is assumed to be an ideal acoustic volume (Fig. 2.11). The canal microphone may be excluded for the same reasons as in Fig. 2.5.

Now, the equation of the closed fitted scenario

$$u_1(j\omega) = Z_{\text{ear}}(j\omega) \cdot i_1(j\omega) \tag{2.8}$$

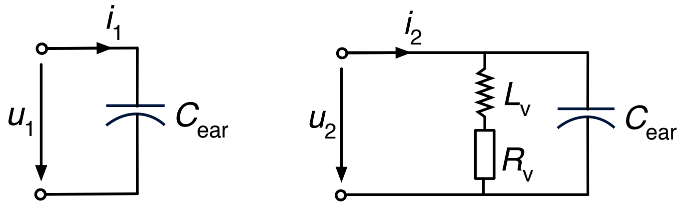

(a) closed fitting (b) open fitting

Figure 2.11: Simplified electric circuits of the acoustic load seen by the receiver for closed and vented hearing aids

and of the vented scenario

$$u_2(j\omega) = \frac{Z_{\mathrm{v}}(j\omega) \cdot Z_{\mathrm{ear}}(j\omega)}{Z_{\mathrm{v}}(j\omega) + Z_{\mathrm{ear}}(j\omega)} \cdot i_2(j\omega) \tag{2.9}$$

can be related to the ventloss by assuming an ideal volume velocity source, i.e. $i_1(j\omega) = i_2(j\omega)$:

$$H_{\mathrm{Vloss}}(j\omega) = \frac{u_2(j\omega)}{u_1(j\omega)} = \frac{Z_{\mathrm{v}}(j\omega) \cdot Z_{\mathrm{ear}}(j\omega)}{Z_{\mathrm{v}}(j\omega) + Z_{\mathrm{ear}}(j\omega)} \cdot \frac{1}{Z_{\mathrm{ear}}(j\omega)} = \frac{-\omega^2 L_{\mathrm{v}} C_{\mathrm{ear}} + j\omega R_{\mathrm{v}} C_{\mathrm{ear}}}{-\omega^2 L_{\mathrm{v}} C_{\mathrm{ear}} + j\omega R_{\mathrm{v}} C_{\mathrm{ear}} + 1} \tag{2.10}$$

Eq. (2.10) can be reformulated such that the relation to the REOG becomes evident [19]

$$\begin{aligned} H_{\mathrm{Vloss}}(j\omega) &= \underbrace{\frac{-\omega^2 L_{\mathrm{v}} C_{\mathrm{ear}}}{-\omega^2 L_{\mathrm{v}} C_{\mathrm{ear}} + j\omega R_{\mathrm{v}} C_{\mathrm{ear}} + 1}}_{2^{nd}\ order\ high-pass} + \underbrace{\frac{j\omega R_{\mathrm{v}} C_{\mathrm{ear}}}{-\omega^2 L_{\mathrm{v}} C_{\mathrm{ear}} + j\omega R_{\mathrm{v}} C_{\mathrm{ear}} + 1}}_{boost} \\ &= 1 - \frac{1}{-\omega^2 L_{\mathrm{v}} C_{\mathrm{ear}} + j\omega R_{\mathrm{v}} C_{\mathrm{ear}} + 1} = 1 - H_{\mathrm{REOG}}(j\omega) \end{aligned} \tag{2.11}$$

The resonance frequency and the quality factor of the high-pass are equal to the low-pass, that describes approximately the REOG (see Eqs. (2.4) and Eq. (2.5)). Fig. 2.12 shows the simulation of the ventloss for the simple model (*solid*), which overestimates the quality factor and has poor coincidence with the real behavior of nearly closed or quasi open fitted earpieces. In particular, the decay towards low frequencies changes in reality with decreasing vent radii from 2^{nd} order to 1^{st} order, i.e. from 40dB/decade to 20dB/decade. This is modeled by the two-port model introduced before, which estimates the vent effect much more accurately (*dashed*). For the comparison with the real measurements, it is necessary to add the receiver as the excitation source to the model. Instead of the ventloss one gets then the receiver response for a certain acoustic load. The produced sound pressure has to be sensed by a microphone, which in this application is the canal microphone, just like for the REOG measurements. This means that the recorded data are a "voltage-to-voltage" transfer function between the receiver and the canal microphone instead of a voltage to pressure function.

The "receiver-to-canal microphone" path is in particular relevant for both the static and the adaptive ADSC case as it will be demonstrated in Chapters 3 and 4 and is called PLANT. For a better comparison with the real measurements depicted in Fig. 2.14 the two-port model includes the canal microphone as well (Fig. 2.13).

As stated before, the vent effect causes a sound pressure drop of the receiver towards low fre-

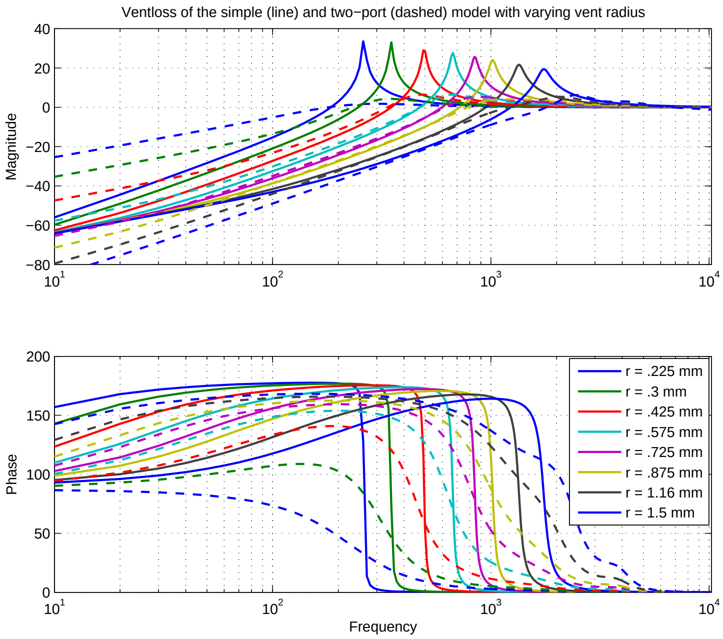

Figure 2.12: Ventloss simulated with the simple model and the two-port model for varying vent radius: vent length $l_{\mathrm{v}} = 5$ mm, acoustic Resistance $R_{\mathrm{v}} = 10^6\ \frac{\mathrm{Ns}}{\mathrm{m}^5}$, ear canal volume $V = 1.4\ \mathrm{cm}^3$ (simple model, solid). Vent length $l_{\mathrm{v}} = 5$ mm and ear simulator "$\mathrm{earCanal}_{\mathrm{v2}}$" (two-port model, dashed). The vent dimensions correspond to the ITE-HM of Fig. 2.14

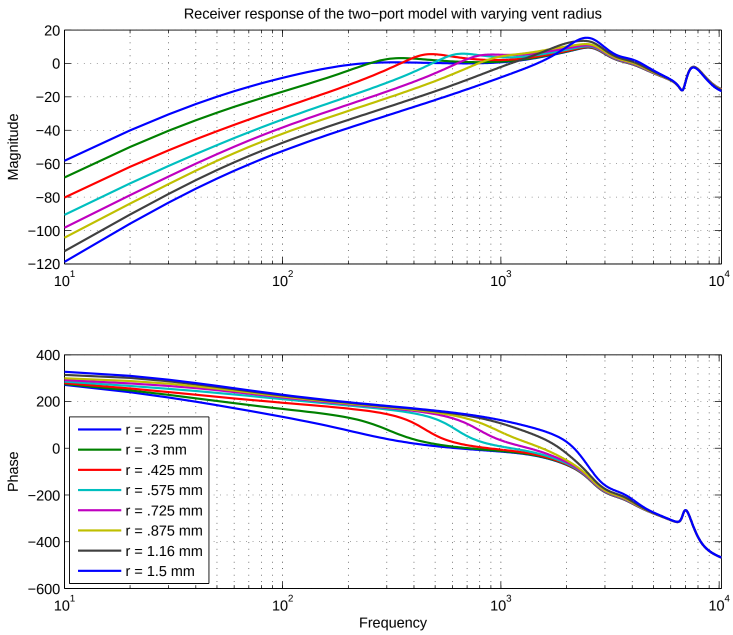

Figure 2.13: PLANT *simulated with the two-port model for varying vent radius: vent length $l_{\mathrm{v}} = 5$ mm, ear simulator "$\mathrm{earCanal}_{\mathrm{v2}}$", canal microphone "Sonion 50GC31" and receiver "Sonion E50DA012" (parallel circuit). The vent dimensions correspond to the ITE-HM of Fig. 2.14*

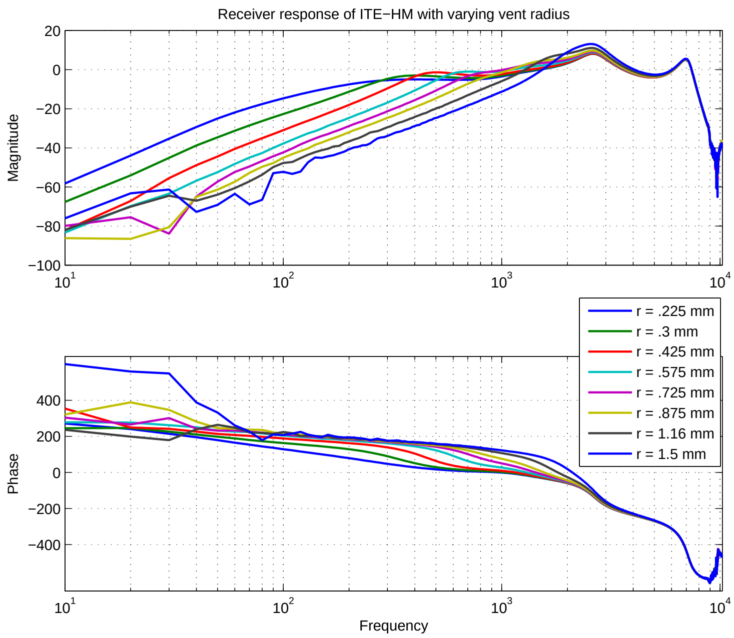

Figure 2.14: PLANT *of ITE-HM with varying vent radius: vent length $l_{\mathrm{v}} = 5$ mm, ear simulator "IEC711 G.R.A.S.", canal microphone "Sonion 50GC31", receiver "Sonion E50DA012" (parallel circuit). The excitation signal is pink noise and the measurement is done in an acoustically sealed box*

quencies. Above the cutoff frequency of the ventloss the receiver response remains unchanged. This implicates that the pressure reduction below the resonance frequency has to be compensated for a receiver of a vented hearing aid in order to attenuate the direct sound, where the direct sound is not damped by the REOG. This can be achieved with a filter that inverts the decay, which induces several disadvantage that are discussed in the course of this thesis.

2.1.3 Impact on ADSC compensation filter

This section discusses the main element of the ADSC system for both the static and the adaptive case: the filter $H_{\mathrm{COMP}}(j\omega)$, also referred to as the compensation Filter. In Fig. 2.15 the simplified block diagram of the static ADSC system is depicted. The $\hat{H}_{\mathrm{COMP}}(j\omega)$ filter block has to process the recorded ambient sound at the outer microphone such that the emitted sound of the receiver eliminates the direct sound at a desired location by destructive interference, i.e. at the ear drum.

Assuming ideal transducers, i.e. a flat frequency response with zero phase over the entire frequency range, the ideal compensation filter $H_{\mathrm{COMP}}(j\omega)$ must be equal to $H_{\mathrm{REOG}}(j\omega)$ with a phase shift of 180° degrees to cancel out the sound at the end of the direct path.

However, the real transducers used in hearing aids do not fulfill the ideal assumption, i.e. $H_{\mathrm{M}_0}(j\omega) \neq 1$ and $H_{\mathrm{R}_{\mathrm{ref}}}(j\omega) \neq 1$ for all frequencies. Fig. 2.16 shows the receiver response coupled to the ear simulator "IEC711" and the microphone response of the ITE-HM measured in an anechoic box. The receiver "Sonion E50DA012" (parallel circuit) has its characteristic resonance frequency around 2.7 kHz and an additional resonance around 7 kHz [20]. The latter arises from the small tube ($l_{\mathrm{v}} = 5$ mm and $r_{\mathrm{v}} = 0.5$ mm) that connects the receiver with the ear simulator. Above the tube peak the response decays with 5^{th} order and at low frequencies

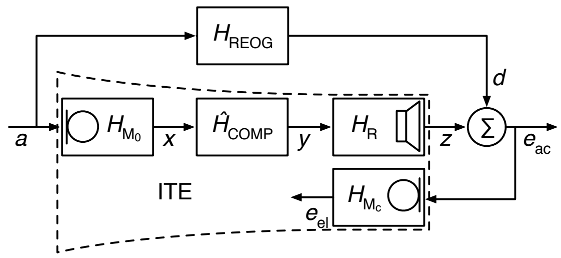

Figure 2.15: Block diagram of the static ADSC system: $H_{\mathrm{REOG}}(j\omega)$ is the direct path, $H_{\mathrm{M_0}}(j\omega)$ is the frequency response of the outer microphone, $\hat{H}_{\mathrm{COMP}}(j\omega)$ is the compensation filter and $H_{\mathrm{R_{ref}}}(j\omega)$ is the receiver response. a is the ambient sound in front of the ear, x is the recorded sound, y is the output of the filter and z is the sound pressure emitted by the receiver. The acoustic error signal e_{ac} vanishes if z is the phase inverted version of the direct sound d. e_{el} is the electric output of the canal microphone.

around 50 Hz with 1$^{\mathrm{st}}$ order caused by the hole in the membrane, which compensates changes of the static pressure. The outer microphone of the ITE-HM ("Sonion 50GC31") has its resonance frequency above the measured frequency range at $f_{\mathrm{res}} = 10.5$ kHz [21]. The depicted peak arises from a tube in front of the microphone membrane whose dimensions are equal to the tube of the receiver. Apart from that, the frequency response is nearly flat over a wide range. One of the characteristics of the built in microphone is its electric 1$^{\mathrm{st}}$ order high-pass with $f_{\mathrm{c}} = 100$ Hz. Furthermore, the microphone has also a hole in the membrane, which induces an additional 1$^{\mathrm{st}}$ order high-pass with a cutoff frequency around 20 Hz.

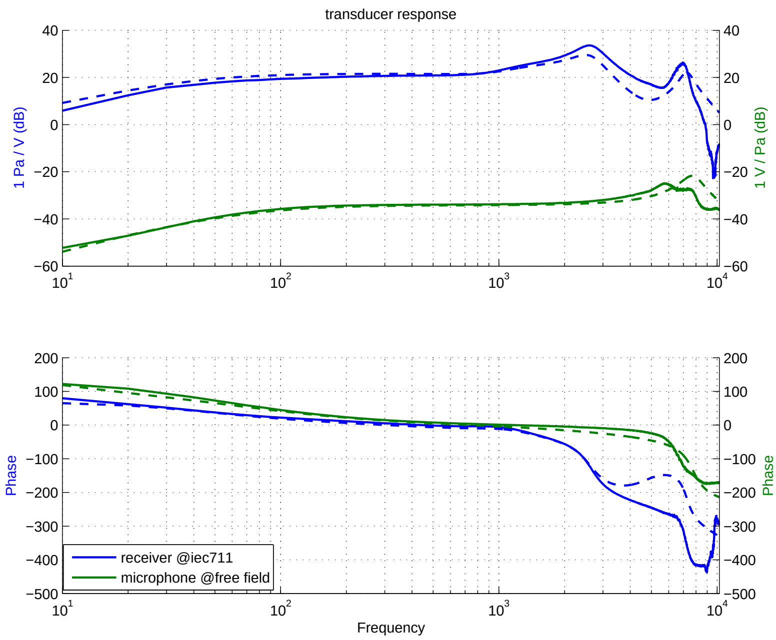

Figure 2.16: Frequency response of the receiver "Sonion E50DA012" (parallel circuit) coupled to the ear simulator "IEC711" (blue) and of the microphone "Sonion 50GC31" in free field (green). The solid graphs are the measurement of the ITE-HM and the dashed graphs are the simulations

In order to cancel the direct sound with real transducers the resulting filter $H_{\mathrm{COMP}}(j\omega)$ must compensate any linear or non-linear distortion. It should be mentioned, that the ventloss can be seen as a linear distortion of the receiver and therefore must be considered, too. The filter $H_{\mathrm{COMP}}(j\omega)$ is not any more just a phase inverted version of the REOG, but

$$H_{\mathrm{COMP}}(j\omega) = -\frac{H_{\mathrm{REOG}}(j\omega)}{H_{\mathrm{M}_0}(j\omega) \cdot H_{\mathrm{R}_{\mathrm{ref}}}(j\omega) \cdot H_{\mathrm{Vloss}}(j\omega)} = -\frac{H_{\mathrm{REOG}}(j\omega)}{H_{\mathrm{M}_0}(j\omega) \cdot H_{\mathrm{R}}(j\omega)} \tag{2.12}$$

where $H_{\mathrm{M}_0}(j\omega)$ is the frequency response of the outer microphone, $H_{\mathrm{R}_{\mathrm{ref}}}(j\omega)$ is the receiver response of a closed fitted hearing aid and $H_{\mathrm{Vloss}}(j\omega)$ is the ventloss caused by the vent. Unless otherwise specified, the transfer function of the receiver includes always the ventloss in this work and is denoted by $H_{\mathrm{R}}(j\omega)$. Now, the compensation filter $H_{\mathrm{COMP}}(j\omega)$ can be calculated for any vent dimension and ear canal. Fig. 2.17 shows the compensation filter of the ITE-HM for different vent radii and Fig. 2.18 is the correspondent two-port simulation.

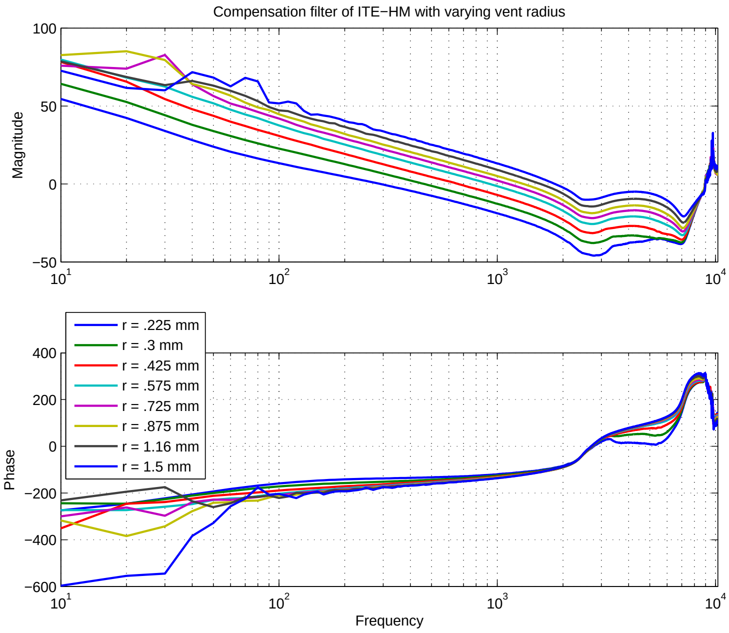

Figure 2.17: Compensation filter of the ITE-HM based on the measured REOG *and* PLANT

The achieved frequency response $H_{\mathrm{COMP}}(j\omega)$ is mostly affected by the inverted microphone and inverted receiver response. At frequencies below the cutoff frequency of the REOG, the power loss of the receiver as well as the roll-off of the microphone dominate $H_{\mathrm{COMP}}(j\omega)$. Above the cutoff frequency, where the receiver and the microphone have a nearly flat response, $H_{\mathrm{COMP}}(j\omega)$ equals the phase inverted REOG. At higher frequencies, i.e. greater than the receiver resonance, the influence of the transducers increases, again. Both edges of the transfer function $H_{\mathrm{COMP}}(j\omega)$ impede a stable filter design without constrains. The inversion of the higher-order low-pass at high frequencies caused by the chain of the microphone and the receiver causes a high gain of ∞ at the Nyquist frequency f_{Nyquist}. This extends to the low frequencies, where the higher-order high-pass induced mainly by the ventloss has to be inverted, which implies a gain of $+\infty$ at DC, which is both not feasible. Thus, the compensation filter $H_{\mathrm{COMP}}(j\omega)$ has to be limited at its edges which is discussed in the Chapters 3 and 4.

It can be stated that the compensation filter $H_{\mathrm{COMP}}(j\omega)$ is significantly dependent on the transducer responses built in the hearing aid. While the filter under ideal conditions would correspond to the phase-inverted REOG, which would be roughly a 2$^{\mathrm{nd}}$ order low-pass filter,

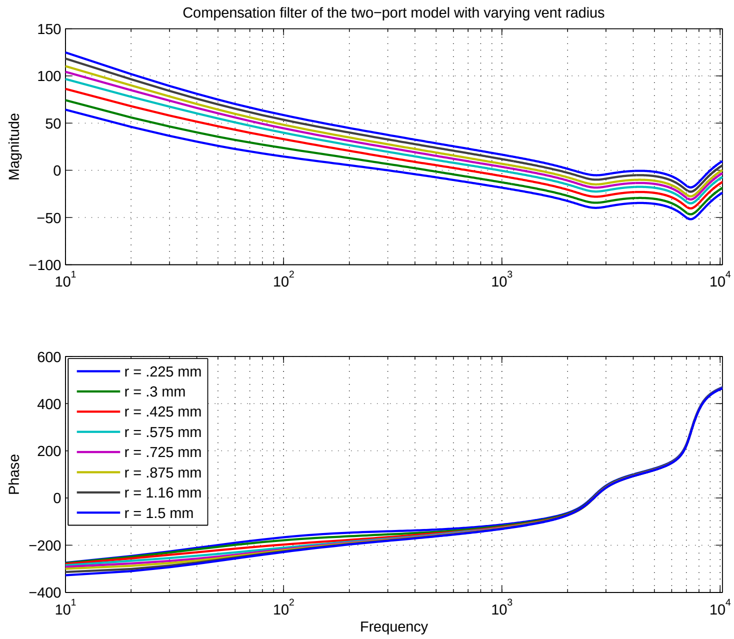

Figure 2.18: Compensation filter of the two-port model calculated from the simulations of the REOG *and the* PLANT

it must under real conditions equalize the linear and non-linear effects of the transducer. In particular the roll-off at low and high frequencies complicates the filter design and requires trade-offs in regard to the performance of the ADSC system.

2.2 Measurement of the transfer functions

Two assumptions are made for the measurement of the transfer function of the REOG and the PLANT in this thesis: Since it is impracticable to place the microphones neither at the vent entry nor at the ear drum, the sound pressure at the outer microphone M_0 and at the canal microphone M_c are good estimates of the sound pressure at the desired positions, respectively (see Section 2.2.1). Furthermore, the acoustic environment is identically for both measures. This implicates that the positions of the transducers as well as the vent dimensions and ear canal volume remain the same.

Then from the recorded microphone signals depicted in Fig. 2.15 an approximation of the REOG can be calculated by

$$\tilde{H}_{\mathrm{REOG}}(j\omega) = \frac{S_{xe_{\mathrm{el}}}(j\omega)}{|S_{xx}(j\omega)|} = \frac{\hat{H}_{\mathrm{REOG}}(j\omega) \cdot H_{\mathrm{M_c}}(j\omega)}{H_{\mathrm{M_0}}(j\omega)} \tag{2.13}$$

where $S_{xe_{\mathrm{el}}}(j\omega)$ is the cross power spectral density between the microphone signals x and e_{el} and $S_{xx}(j\omega)$ is the power spectral density of the outer microphone signal x. Thus, the measured REOG consists not only of the direct sound path but includes also the ratio between the measured transducer responses. An estimate of the PLANT is achieved by recording the output of the receiver with the canal microphone:

$$\hat{H}_{\mathrm{PLANT}}(j\omega) = \frac{S_{ye_{\mathrm{el}}}(j\omega)}{|S_{yy}(j\omega)|} = H_{\mathrm{M_c}}(j\omega) \cdot \hat{H}_{\mathrm{R}}(j\omega) \tag{2.14}$$

where $S_{ye_{\mathrm{el}}}(j\omega)$ is the cross power spectral density between the receiver and the canal microphone signals y and e_{el} and $S_{yy}(j\omega)$ is the power-spectral density of the receiver signal y.

From Eq. (2.13) and Eq. (2.14) it follows the estimated compensation filter $\hat{H}_{\mathrm{COMP}}(j\omega)$:

$$\hat{H}_{\mathrm{COMP}}(j\omega) = -\frac{\tilde{H}_{\mathrm{REOG}}(j\omega)}{\hat{H}_{\mathrm{PLANT}}(j\omega)} = -\frac{\hat{H}_{\mathrm{REOG}}(j\omega)}{H_{\mathrm{M}_0}(j\omega) \cdot \hat{H}_{\mathrm{R}}(j\omega)} \tag{2.15}$$

High requirements are imposed on the measurement of the REOG and the PLANT. To achieve a good attenuation both the magnitude and the phase of the ADSC signal have to be accurate. Therefore, any additive ambient noise or non-linearities caused by the transducers must be avoided to ensure a good estimation of the compensation filter $H_{\mathrm{COMP}}(j\omega)$. A familiar measure to detect additive noise or non-linearities of a transfer function is the coherence between the input and the output signal of the underlying system. The coherence is defined as

$$\gamma_{xy}^2(j\omega) = \frac{|\langle S_{xy}(j\omega)\rangle|^2}{\langle S_{xx}(j\omega)\rangle \cdot \langle S_{yy}(j\omega)\rangle} \tag{2.16}$$

where the operator $\langle\cdot\rangle$ denotes averaging of the spectral densities over time. The values of the coherence satisfy always $0 \leq \gamma_{xy}^2(j\omega) \leq 1$ and attain the value 1 over all frequencies for a linear time-invariant (LTI) system under ideal conditions.

2.2.1 Canal microphone position

Until now, it was said that using the canal microphone of the ITE instead of a microphone in front of the ear drum would be a valid approximation of the REOG. This is true, as long as the ear canal volume can be seen as an ideal acoustic volume with stiff walls. Recalling Fig. 2.3, this is the case up to approximately 1 kHz. Above this frequency the assumption of an ideal acoustic volume does not hold any more, thus the sound pressure varies also with the microphone position. Fig. 2.19 shows the effect of the canal microphone position on the REOG (*blue*) and on the PLANT (*green*) for the two-port model. Additionally, it shows the transfer function from the ITE to the ear drum (*red*).

The significant difference between the simulations with the canal microphone at the ITE or at the ear drum is the resonance, here at $f_{\mathrm{res}} = 6640$ Hz. This resonance arises from the $\lambda/4$-resonator caused by the shortened ear canal with the terminating ear drum for both the REOG and the PLANT measurement. Nevertheless, this effect can be neglected since the main focus of the ADSC system in this application relies on low and mid frequencies up to $f = 2f_{\mathrm{c}}$, where f_{c} is the cut-off frequency of the REOG. Furthermore, since both the REOG and the PLANT are measured under the same acoustic conditions, any position-dependent effect on the transfer functions is canceled out with an ideal compensation filter $H_{\mathrm{COMP}}(j\omega)$.

In contrast to the simulations done in Section 2.1.1, the REOG of this simulation has an additional resonance around $f_{\mathrm{res}} = 8.4$ kHz. This results from the difference of the vent length: while this simulation uses vent dimensions that correspond to real earshells, the simulations of Fig. 2.7 corresponds to the vents of the ITE-HM, which have a length of $l_{\mathrm{v}} = 5$ mm. In reality, a common vent of an earshell has a length between 15 to 20 mm and a diameter of 0.8 to 3 mm. The vent radius of this simulation amounts to $r_{\mathrm{v}} = 1$ mm, whose acoustic mass corresponds to the vent radius $r_{\mathrm{v}} = 0.575$ mm of the ITE-HM (Eq. (2.1)). The resonance arises from the $\lambda/2$-resonator that occurs, as long as both endings of the vent are equally terminated either by a high or by a low impedance. This is approximately the case in the scenario, where the impedance of the ear canal and the impedance of the ambient volume are small compared to

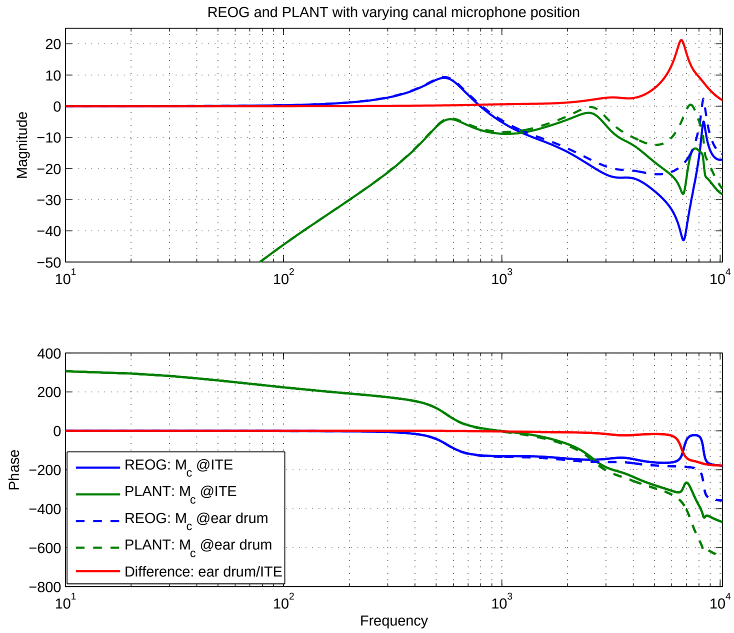

Figure 2.19: Difference of the REOG and the PLANT due to the canal microphone position: vent length $l_{\mathrm{v}} = 20$ mm, radius $r_{\mathrm{v}} = 1$ mm and ear simulator "earCanal$_{\mathrm{v2}}$"

the impedance of the vent. The boost due to the resonance is high which implies that the direct sound reaches pressure levels similar to the sound at the vent entry.

In summary, the canal microphone position does not infringe the performance of the ADSC system unless the microphone is at a node of the $\lambda/4$-resonator and the signal has a bad SNR at that distinct frequency. Then the estimation of the transfer functions may deteriorate and so the cancellation of the direct sound. The high frequency resonance induced by the $\lambda/2$-resonator is negligible, since at this region a common hearing aid user needs an amplification which masks the direct sound. Thus, it is not necessary to attenuate this resonance with the ADSC system.

2.2.2 Measurement of the REOG

The measurement of the REOG is largely resistant to distortions by ambient noise, because the signals of both microphones are used for the calculation. Any source that propagates to both microphones can be used for the measurement. Here, the excitation signal is produced by an external sound source that affords enough energy over the frequency band in order to drown the noise floor of the microphones. At high frequencies, though, the sound pressure in the ear canal decreases due to the low-pass effect of the REOG. This effect is even reinforced since the measurements are performed with pink noise to reduce the annoyance for the test subject. However, in this thesis no post-processing of the calculated $\tilde{H}_{\mathrm{REOG}}(j\omega)$ has to be performed, since the coherence decays only significantly at f_{Nyquist} (see Fig. 2.20 *blue*).

Nevertheless, in order to review the estimation, the propagation delay between the outer and the canal microphone can be estimated. Therefore, the underlying assumptions is made that the REOG is a linear time-invariant (LTI) system, which can be split into a minimum-phase system, that includes the direct path and the microphones, and an all-pass system, that describes the propagation delay between the microphones and thus has a linear phase. The minimum-phase system can be calculated by applying the Hilbert transform depicted in [22, Section 11.3] and implemented in the MATLAB® function `minphase.m`. The propagation delay can then be estimated by the phase difference between the measured REOG and its minimum-phase representation.

The estimated propagation delay of the REOG of Fig. 2.20 corresponds very precisely to the real situation. The delay of $\hat{\tau}_{\text{REOG}} = 0.074$ ms coincides with the distance of the microphones M_0 and M_c of an ITE prototype, i.e.

$$\Delta d = c \cdot \hat{\tau}_{\text{REOG}} \approx 25 \text{ mm},$$

where $c = 343 \frac{\text{m}}{\text{s}}$ is the speed of sound.

2.2.3 Measurement of the PLANT

The measurement of the PLANT is potentially more effected by additive noise because the receiver response decays both at low and high frequencies which results in a bad SNR. The consequence is depicted in Fig. 2.14, where both the magnitude and the phase at the edges of the frequency spectrum, in particular with big vents, are not usable for the filter design of $H_{\text{COMP}}(j\omega)$. Since the main focus of this work lies on the attenuation of the direct sound at low and mid frequencies, an accurate representation of that frequency region is important. Therefore, two assumptions are made to get suitable values: from the simulations of Section 2.1.2 it is known that the receiver response $H_\text{R}(j\omega)$ decays approximately with 2^{nd} order towards low frequencies, such that an extrapolation by a line, i.e. a 1^{st} order polynomial, in the logarithmic space is a reliable estimation of the measured frequency response. Additionally, the PLANT is assumed to be a linear time-invariant (LTI) system. Since the transducers are assumed to be minimum-phase as well as the ear canal volume, the all-pass system describes the propagation delay between the receiver and the microphone. This allows to recalculate the phase of the extrapolated magnitude of $H_{\text{PLANT}}(j\omega)$ by the Hilbert transform. The propagation delay can then be estimated by the phase difference between the measured PLANT and its minimum-phase representation. These processes are implemented in the MATLAB® function `extrapol.m`, which first calculates the low frequency extrapolation and then calls the function `minphase.m`, that computes the minimum-phase system out of the extrapolated magnitude spectrum and the propagation delay. The post-processed PLANT can then be written

$$\tilde{H}_{\text{PLANT}}(j\omega) = \hat{H}_{\text{PLANT}_{\min}}(j\omega) \cdot \text{e}^{-j\omega \cdot \hat{\tau}_{\text{PLANT}}} \tag{2.17}$$

where $\hat{H}_{\text{PLANT}_{\min}}(j\omega)$ is the estimated minimum-phase response of the measured $\hat{H}_{\text{PLANT}}(j\omega)$ and $\hat{\tau}_{\text{PLANT}}$ is the estimated propagation delay.

Fig. 2.20 shows the transfer function $\tilde{H}_{\text{REOG}}(j\omega)$ and $\hat{H}_{\text{PLANT}}(j\omega)$ as well as the respective coherence functions of an ITE prototype (*solid*). The dashed curve shows the post-processed transfer function $\tilde{H}_{\text{PLANT}}(j\omega)$. The coherence of both transfer functions drops once the signal in the ear canal decays below -20 dB. This is caused by the noise floor of the canal microphone M_c and the recording system as well as by the ambient noise, which is not part of the excitation signal and thus deteriorates the coherence. An increase of the SNR solves this problem but is limited by the sensitivity of the test subject and the non-linear behavior of the transducers.

Although the post-processed PLANT $\tilde{H}_{\text{PLANT}}(j\omega)$ matches with the simulated transfer function (see Fig. 2.13), the calculation of the Hilbert transform of the extrapolated PLANT yields a propagation delay of $\hat{\tau}_{\text{PLANT}} = 0.125$ ms, which corresponds to a "receiver-to-microphone" distance around $\Delta d \approx 43$ mm and thus differs from the real setup. The physical distance between the receiver R and the canal microphone M_c namely is approximately 1.5 to 2 mm, i.e. $4.373\ \mu\text{s} \leq \hat{\tau}_{\text{PLANT}} \leq 5.831\ \mu\text{s}$, thus the estimated delay arises from erroneous measurement and

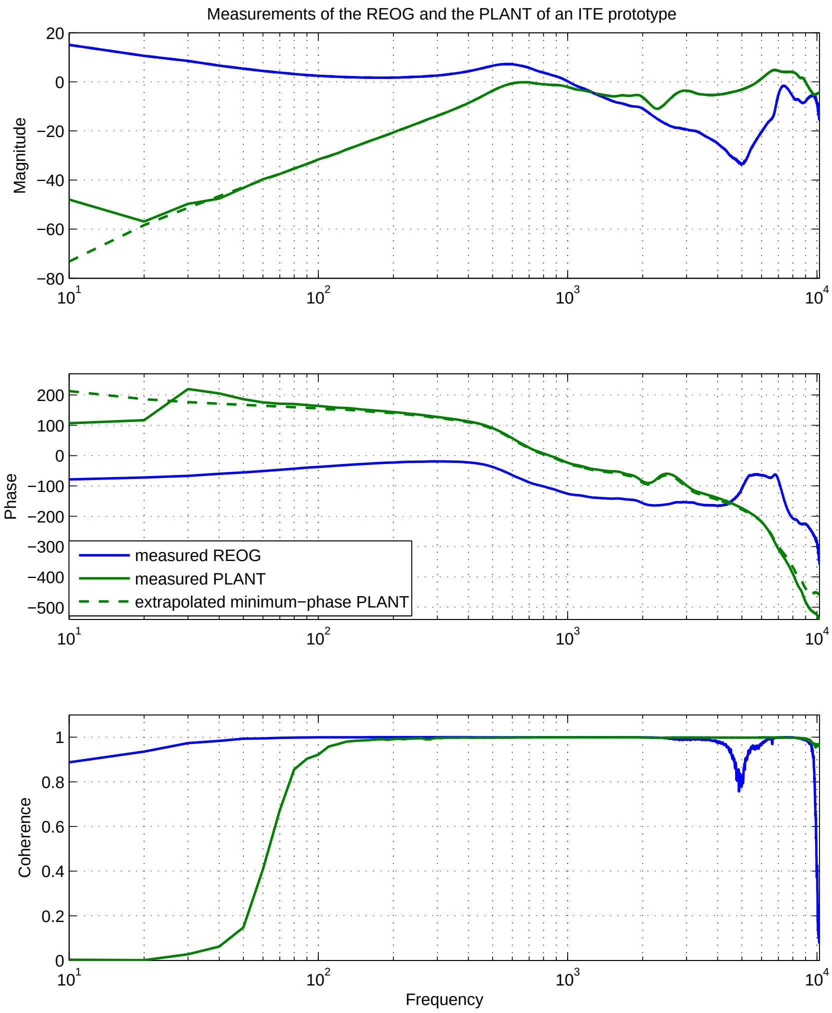

Figure 2.20: Transfer function and coherence of the REOG *and the* PLANT *of an ITE prototype: original data (solid) and enhanced data (dashed) by the MATLAB® function* `extrapol.m`

analysis.

Actually, Zurbrügg and Stirnemann showed in [23] that a balanced-armature receiver with a purely capacitive load can be modeled as a 5^{th} order minimum-phase system with a time delay of 50 μs or as a 6^{th} order minimum-phase system without any time delay by adding a pole at the upper edge of the band-limited spectrum. This means that the measurement does not capture the behavior of the receiver at high frequencies correctly, since it is assumed that it has a minimum-phase and thus no delay. This is due to the power loss of the receiver above its resonance peak, which leads to a poor SNR above 10 kHz. While a pole has only a small effect on the magnitude below its frequency location, the influence on the phase is noticeable more than a decade below. From this follows that a pole located above 10 kHz is barely detectable by analyzing the receiver magnitude response but has a significant impact in its respective phase (see Fig. 2.21). Part of the time delay occurring from the phase difference of the measured data and the supposed minimum-phase system is thus an effect arising from the band-limited measurement and the poor SNR of the receiver at high frequencies.

However, the main error on the estimated propagation delay arises from the application of the

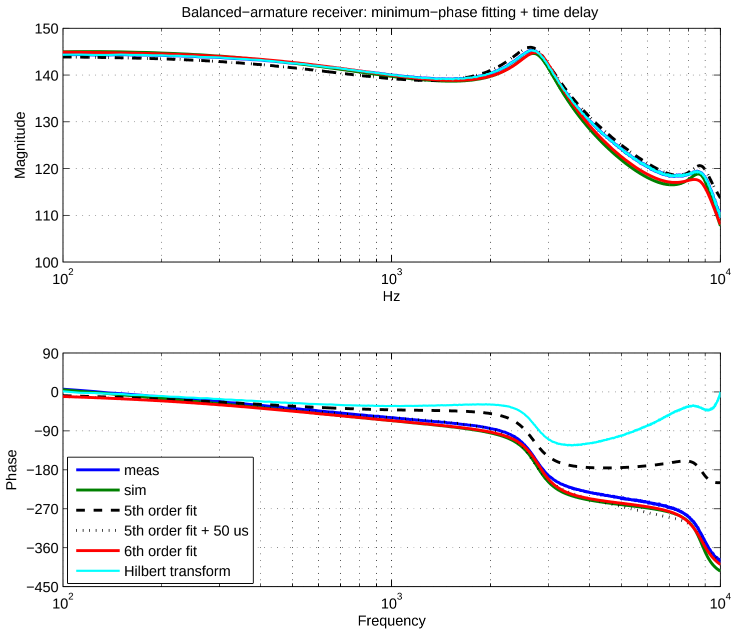

Figure 2.21: Measurement, simulation and modeling of a balanced-armature receiver: simulation with two-port model (green), 6^{th} *order minimum-phase model (red) and* 5^{th} *order minimum-phase model indicating* 50 μs *time delay (black)* [23]

Hilbert transformation itself. Analyzing the minimum-phase estimation by the Hilbert transform of an analogous and a digital filter, one can see that the estimated minimum-phase system depends on the frequency mapping from the continuous space to the discrete space. Fig. 2.22 shows two 6^{th} order minimum-phase low-pass filters with cut-off frequency $f_{\mathrm{c}} = 3$ kHz and the corresponding minimum-phase estimations by the Hilbert transform, one designed in the Laplace-domain and the other in the z-domain using the bilinear transformation [22, Section 7.1.2]. The estimation of the minimum-phase from the magnitude response of the bilinear transformation method (*red*) coincides with the original phase (*blue*), whereas the minimum-phase estimation based on the magnitude response of the Laplace filter (*cyan*) deviates considerably from the original phase (*green*). This is due to the different mapping of the frequency vector. While the frequency is mapped linearly in the Laplace-domain, the bilinear-transform maps the frequency from $-\infty \leq \omega_{\mathrm{c}} \leq \infty$ non-linearly onto the unit circle. Thus, for a correct identification of the minimum-phase the Hilbert transform requires the entire magnitude spectrum mapped to $-\pi < \omega_d < \pi$, which is not the case for the sampled measurements of the PLANT.

The effect of the Hilbert transform on the receiver is shown in Fig. 2.21 (*cyan*). Since the compensation filter $H_{\mathrm{COMP}}(j\omega)$ is approximated with IIR filters in Chapter 3 which have a non-linear frequency warping, the estimated delay can not be neglected and has to be incorporated in the filter approximation method. Moreover, according to Eq. (2.15) the PLANT has to be inverted which implicates a constant negative group delay, because $\hat{\tau}_{\mathrm{PLANT}} > \hat{\tau}_{\mathrm{REOG}}$.

In summary, it can be stated that the measurement of the REOG does not need any further processing as long as the excitation signal level is high enough over all frequencies. This does not apply to the PLANT measurement of a vented earpiece, since the sound pressure decay at low and high frequencies implicates a bad SNR. Amplifying the excitation signal will evoke annoyance for the subject as well as drive the receiver likely into non-linearities and thus it will

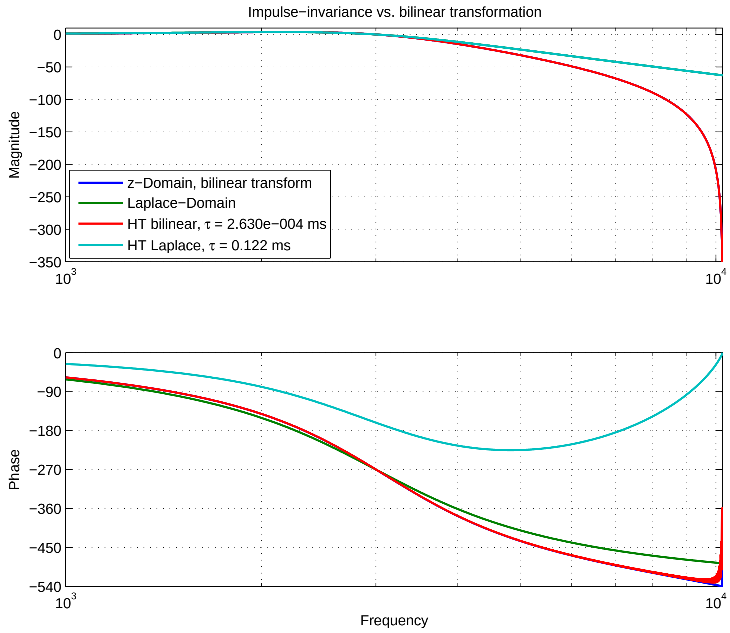

*Figure 2.22: Minimum-phase and delay estimation by the Hilbert transform of an 6^{th} order minimum-phase low-pass filter: bilinear transformation filter design (*blue*), Laplace filter design (*green*), minimum-phase estimation of the bilinear transformation (*red*), minimum-phase estimation of the Laplace filter (*cyan*)*

lead to an erroneous estimation of the transfer function for the ADSC system. An extrapolation of the low frequency range is inevitable in order to design a compensation filter, which matches the magnitude and phase of the PLANT also at low frequencies. The application of the Hilbert transform is necessary for the computation of the phase response, although its estimation deviates from the real response. The difference can be described by a constant group delay, which can be compensated by a boost filter as described in Section 3.4.3 and Section 4.3.2.

2.3 Variability of the transfer functions

In this section the variability of individual ears is analyzed (inter-individual variability) as well as the reproducibility of the measurements within them for several reinsertions of the ITE prototype (intra-individual variability). A small inter-individual variability is desired since it would enable the possibility to design an universal prototype compensation filter $H_{\mathrm{COMP}}(j\omega)$ with an acceptable attenuation for all individuals. A small intra-individual variability would at least make the use of one static filter per individual possible. A high inter- and intra-individual variability calls for an adaptive filter design as for each individual and each reinsertion the compensation filter must be adapt in order to have a good ADSC performance.

From the simple model defined in Sections 2.1.1 and 2.1.2 it is known that the cutoff frequency f_{c} and the quality factor q change linearly with the vent radius r_{v} but only with the square root of the volume V_{ear} and the length l_{v}. From this follows that the transfer functions are more sensitive to the variations of the vent radius than to its length or the ear canal volume. Also the mounted transducers of the ITE prototypes influence $H_{\mathrm{COMP}}(j\omega)$ as depicted in Eq. (2.12). Thus, their variations contribute to the variability of the ADSC compensation filter as well. Furthermore, the transducer response may drift from their initial response over time and be soiled by cerumen. This has an impact on the transducer responses and consequently deteriorates the attenuation. Fig. 2.23 shows the measurements of the REOG and the PLANT of 6 ears for a small vent, i.e. $r_\mathrm{v} = 0.4$ mm. For each ear a custom fitted ITE prototype were built with similar transducers. The transfer functions are measured for 3 reinsertions to trace the intra-individual variation of a small vent. It is plain to see that the REOG of each individual is subjected to variations, whereas the PLANT has a high reproducibility. The deviations of the REOG arise from the so called leakage effect that occurs if the earmold does not seal the ear canal completely and the ambient sound intrudes to the ear canal not exclusively through the vent but also through a parallel path. It is impossible to avoid leakage at all and, moreover, it changes significantly with each insertion of the ITE prototype. Thus, the leakage effect has to be included in the acoustic environment as an additional direct path, or simplified as an additional parallel vent. Thus, it can also be seen as an increase of the vent radius r_v denoted by:

$$\hat{r}_\mathrm{v} = \sqrt{r_\mathrm{v}^2 + r_\mathrm{leak}^2} \tag{2.18}$$

where r_leak is the radius of a tube that models the effective leakage.

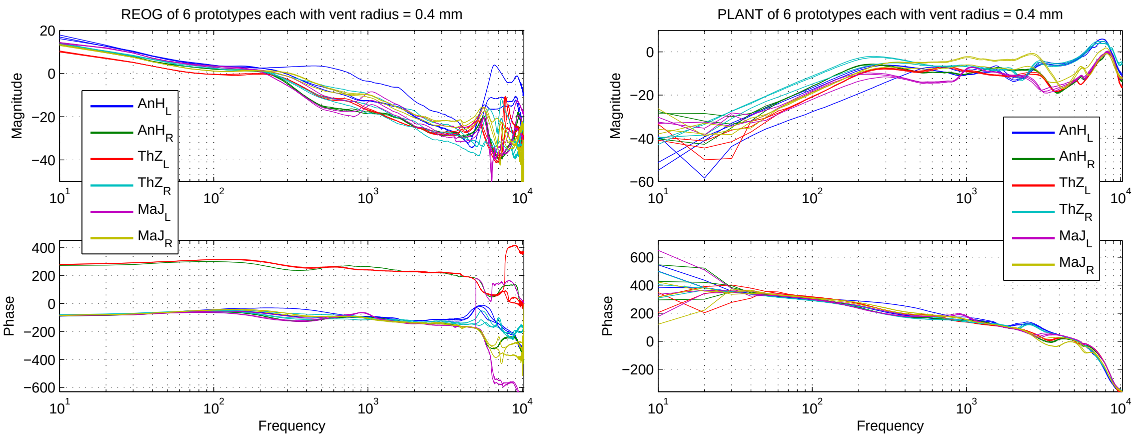

(a) REOG with 0.4 mm vent radius

(b) PLANT with 0.4 mm vent radius

Figure 2.23: Variability of the transfer function of 6 individuals

From this equation it is evident that the influence of the leakage on the REOG and the ventloss is significant if the vent radius is small. On the other side, the significance of the leakage effect vanishes with increasing radius r_v (see Fig. 2.24). The leakage in combination with a small vent radius has a less important influence on $H_\mathrm{PLANT}(j\omega)$ than on $H_\mathrm{REOG}(j\omega)$ as any change will affect the response below the resonance frequency f_c, which is at the low frequency range. In contrast, the effect on $H_\mathrm{REOG}(j\omega)$ is prominent for all frequencies above f_c and thus it has a huge impact on the compensation filter $H_\mathrm{COMP}(j\omega)$ in the frequency range of interest, i.e. low and mid frequencies. While a small vent is beneficial regarding the electro-acoustics, since the receiver looses power in a small range, its variability requires a repeated or even continuous identification of the REOG, for instance by an adaptive algorithm (Chapter 4). For big vent radii, however, the receiver response is significantly deteriorated by the ventloss but the reproducibility of the measurements for several insertions indicates that a prototype compensation filter $H_\mathrm{COMP}(j\omega)$ designed for each individual would achieve a fair attenuation. This concept is discussed in Chapter 3, where a static compensation filter is designed for each individual based on the measurements taken with its ITE prototype and a specific vent.

The inter-individual variability, though, is very pronounced independently of the vent radius.

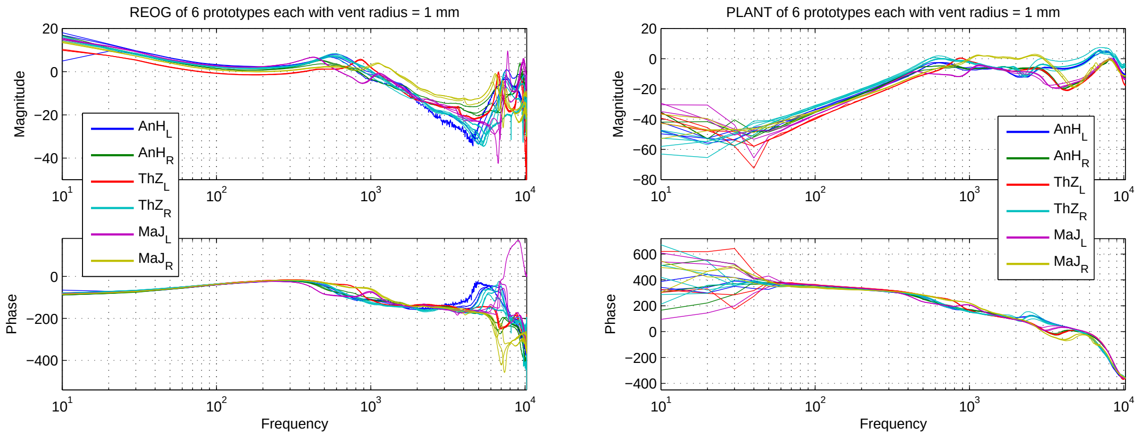

(a) REOG with 1 mm vent radius

(b) PLANT with 1 mm vent radius

Figure 2.24: Variability of the transfer function of 6 individuals

This arises not only from the variations between the mounted transducers, but also from the geometry of the prototypes and the individual ears. The shape of the ear canal defines on the one hand the dimensions of the ITE prototype and thus influences the vent size as well. On the other hand, even if the acoustic mass of the vent is well defined, it is not possible to predict the filter response $H_{\mathrm{COMP}}(j\omega)$ accurately, since the acoustic impedance of the individual ear is not known. Nevertheless, this does not imply that it is not possible to design a set of universal prototype compensation filters for standard vent sizes that would achieve an adequate attenuation for most individuals. However, the design of an individual prototype compensation filter $H_{\mathrm{COMP}}(j\omega)$ outperforms an universal solution.

100 Hz < f < 1 kHz		#1	#2	#3	#4	#5	#6	Inter-individual
Intra-individual:	Magnitude [dB]	2.64	0.89	7.32	1.37	8.48	**11.52**	18.41
0.4 mm	Phase [°]	11.35	4.04	14.62	8.59	18.74	**25.14**	39.09
Intra-individual:	Magnitude [dB]	1.28	1.10	0.80	2.12	2.17	**2.51**	6.73
1 mm	Phase [°]	9.89	4.89	4.66	**11.19**	7.42	9.21	28.12

Table 2.1: Intra- and inter-individual variability of the compensation filter for 6 ears: maximal magnitude and phase difference between 100 Hz and 1 kHz

Tab. 2.1 shows the maximal intra- and inter-individual differences between 100 Hz and 1 kHz of the compensation filter calculated from the measurements depicted in Figs. 2.23 and 2.24. A magnitude and phase deviation from the transfer functions used for the design of $\hat{H}_{\mathrm{COMP}}(j\omega)$ deteriorates the ADSC performance, as it will be explained in Section 2.4.2. The greater the deviation, the worse is the ADSC attenuation. However, it should be noticed that a broad band magnitude deviation may be compensated by an overall gain, while the phase deviation can not be equalized without redesigning the compensation filter.

Regarding the intra-individual differences they get smaller in general with an increasing vent. However, it is noticeable, that the magnitude and phase deviation vary heavily from individual to individual. Nevertheless, Chapter 5 will show the achievable attenuation with an individual static ADSC compensation filter design and compare it to the attenuation with compensation filters of other prototypes (see Section 5.1.2).

In summary, it can be stated that the intra-individual variability for vent radii starting at 1 mm is sufficiently small in order to design individual static filters. The design of an universal prototype filter, however, has to be investigated in more detail. This implies that further measurements with more individuals and different vents must be conducted to allow a more accurate conclusion about the variability.

2.4 Receiver Distortion Limits

So far, the electro-acoustic transducers were assumed to be linear time-invariant systems. This is only a valid estimation for low input levels, where all components work approximately linear. For higher amplitudes, though, the assumption must be discarded as the output of the transducers is a non-linear function of its input. Any non-linear behavior of the transducers deteriorates the ADSC attenuation. Furthermore, non-linearities appear as harmonic or non-harmonic spectral components in the output, which acoustically means a deterioration of the sound quality.

In this work it is assumed that the mounted microphones M_0 and M_c are designed for the applied sound pressure levels and thus do not introduce any distortions. This is certainly not the case for the receiver whose input signal has to compensate the low-frequency sound pressure decay caused by the vented fitting of the hearing device in order to achieve a broad band attenuation. From Section 2.1.2 it is known that the output impedance of the receiver is independent of the acoustic load. From this follows that the appearance of non-linear behavior of the receiver depends only on the input signal and is the same for closed fitted or vented receivers. As the compensation filter $H_{\mathrm{COMP}}(j\omega)$ boosts the low frequencies, the electrical and mechanical components will start to distort already for moderate sound pressure levels. The amount of the distortion depends thereby on the compensation filter as well as on the spectrum and the energy of the signal recorded by the outer microphone M_0.

Several works have already outlined the origins of non-linearities of electro-acoustic transducers [24, 25]. Jensen et al. [18] have particularly analyzed the non-linear characteristics of the balanced-armature receivers, which are used in this work. In general, non-linearities can occur in any part of an electro-acoustic device, i.e. the electro-magnetic, the mechanical or the acoustic part. The origin of the non-linearities, however, lies beyond the scope of this work. The focus is rather on the symptoms which are audible or deteriorate the ADSC performance, i.e. new spectral harmonic or non-harmonic components which are not masked, as well as amplitude and phase variations due to saturation effects.

The challenge of finding the limits of the receiver is to understand the dependencies between the signal spectrum, the compensation filter, the mounted receiver and the auditory sensation of each individual. While the linear and non-linear behavior of the receiver can be represented by a Volterra series [26,27], it is much more difficult to design an accurate model of the auditory network [28], in particular with an additional hearing impairment. Furthermore, the destructive interference of the direct sound and the receiver output may even fortify the perceivable distortions. Assuming an ideal compensation filter $H_{\mathrm{COMP}}(j\omega)$ such that the direct sound is perfectly canceled, the distortion effects remain and are prominent. Whereas, if the direct sound is not broadly attenuated, the distortion effects may be masked by the remaining signal and thus be unnoticeable. In addition, any HI-processed sound which compensates the hearing loss reinforces even more the masking effect. Hence, to get accurate results, it is necessary to analyze the remaining signal of the destructive interference rather then the receiver signal on its own.

Nevertheless, for reasons of simplification, only the receiver signals were evaluated regarding the audible distortions. Therefore, the receiver "Sonion E50DA012" (parallel circuit) is connected to a '2cc'-coupler as it is specified in the datasheet [20] and the sound pressure is recorded with the measurement microphone "Type 40AG" from G.R.A.S. [29].

The following sections present objective measures that are used to detect non-linearities of the receiver. Their relation to the audible distortions (subjective bound) as well as their influence on the performance of the ADSC system (algorithmic bound) is outlined. Furthermore, the maximum sound pressure level in front of the ear for common signals like speech and babble noise are outlined, at which the ADSC system attenuates the direct sound properly without adding audible distortions.

2.4.1 Subjective bound

The subjective bound, in general, can be defined as the threshold at which the distortions, induced by a sound device, start to annoy the listener. Certainly, this bound depends strongly on the auditory sensation of each individual. Moreover the subjectiv perception depends on the hearing loss and may vary from day to day, which makes the auditory system time-variant. The perception of the distortions is furthermore dependent on the signal which produces them. While distortions resulting from a speech signal are mostly very well detected, it is much harder to discriminate between a distorted noise signal and a clean one.

To find a threshold that covers the vast majority of people several psychoacoustic tests with a large number of individuals have to be conducted in order to achieve general accepted limits. In this thesis, though, the subjective evaluation of the receiver distortion is done by the author, since the objective is to achieve first results about the possible sound pressure levels at which the ADSC system works desirable.

2.4.1.1 Narrow band signals

Narrow band signals are signals that have their energy only in a small frequency range. A well-known representative is the sinusoidal signal, which has all its energy in one single frequency and has a defined crest factor $c_{\text{crest}} = \sqrt{2}$. While such signals do not occur in nature, they are very useful to understand some characteristics of an unknown system. It is possible to measure the linear transfer function of a system with a sine sweep, where the output is analyzed only at the frequency, which is actually excited. Any non-linear system like a receiver develops harmonics of the fundamental frequency of the sinusoidal excitation signal. The amount of harmonics and their power indicate the harmonic distortion of the system and allow to draw conclusions about the annoyance for the user.

An objective measure of the distortions caused by sine waves is the total harmonic distortion (THD). Different definitions of this measure are used. The THD is either defined as the ratio of the sum of the harmonic power to the power of the fundamental frequency or as the sum of the harmonic power to the overall signal power [30]. Furthermore, the square root of the ratio is commonly used for audio devices and specified as a percentage. In this work the THD is computed as defined by the IEEE standard 1459-2010 [31] in percentage:

$$\text{THD} = \sqrt{\left(\frac{U}{U_0}\right)^2 - 1} \cdot 100\ [\%] = \frac{\sqrt{U_1^2 + U_2^2 + U_3^2 + \cdots + U_\infty^2}}{U_0} \cdot 100\ [\%] \tag{2.19}$$

where U_n is the voltage of the n^{th} harmonic of the fundamental signal U_0.

The advantage of the THD is the simple calculation of the measure and popularly accepted thresholds for different audio devices, which are used to describe their quality. This thresholds depend highly on the application and vary from very low values below 1 percentage (hifi devices) up to few percentage points (consumer devices). The tolerated THD for hearing aids is limited to 5% which for a normal hearing individual is already considerably perceptible but allows higher sound pressure levels still within a good speech understanding. In the ANSI S3.22-2009 [32] several measurements and parameters are specified for hearing aids which are useful in determining the electro-acoustic performance, including the THD measurement. There, the tolerance of the THD is up to 3% and measured at 500, 800 and 1600 Hz. Nevertheless, at Phonak AG, the measurements on the receivers are taken on a logarithmically spaced frequencies axis from 100 Hz to 10 kHz to get the transfer function, the current consumption and the THD as a function of the input voltage. An important value is the maximal power output (MPO) which denotes the maximal sound pressure of the receiver connected to a '2cc'-coupler over frequency. Thereby, the MPO is limited either by the maximal voltage (800 mV), by the maximal current (7 mA) or by the maximal THD (5%).

In this thesis the THD is analyzed at 4 distinct frequencies, i.e. 125, 250, 500 and 1000 Hz. The harmonic distortion of high frequencies is less relevant, because the compensation filter $H_{\mathrm{COMP}}(j\omega)$ amplifies only the frequencies below the vent resonance f_{c}, which for standard vents is usually smaller than 1 kHz.

Distortion measurments

The THD is analyzed for the 4 distinct frequencies with increasing input voltage. The results are depicted in Fig. 2.25 and show that the slope of the THD is moderate up to 400 mV but increases strongly for higher input voltage. This is in particular pronounced at the 500 Hz frequency, which exceeds the subjective bound of 5% already for an input level of 0.5 volt. Nevertheless, it is still possible to achieve sound pressure levels up to 115 dB with THD values below 4%. It should be mentioned that the parallel wiring of the receiver augments the volume velocity by a factor of 4 in comparison with the reference curve denoted in the datasheet [20]. Thus, the SPL curve of the measured receiver is 12 dB above the reference at a similar input voltage level.

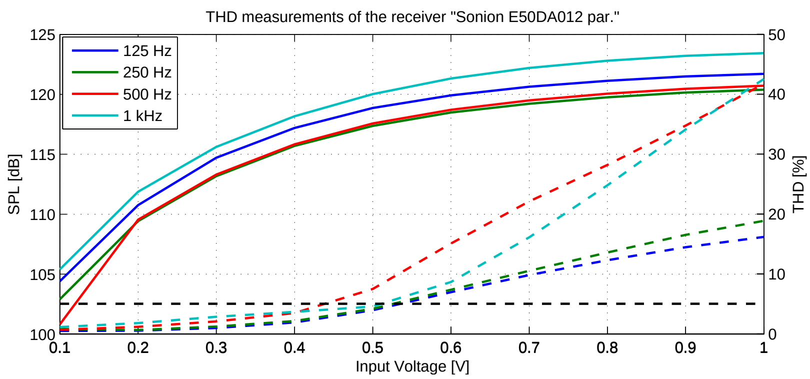

Figure 2.25: THD measurements of the receiver "Sonion E50DA012" (parallel circuit) connected to a '2cc'-coupler for 4 distinct frequencies at varying input voltages

Furthermore, the maximum input voltage (peak) at a THD of 5% of an identically constructed receiver is recorded for linearly spaced frequencies starting from 50 Hz to 1 kHz with 10 Hz resolution. Again, the receiver is connected to a '2cc'-coupler and a measurement microphone records the sound pressure inside the volume. Fig. 2.26 shows the results, which coincide with the first measurements at the distinct frequencies.

It can be noted that the maximum input voltage, which generates a THD of 5%, depends strongly on the frequency and varies between 210 mV and 540 mV for the mentioned receiver. Since the receiver response is nearly flat between 100 and 1000 Hz (see Fig. 2.9) the receiver can produce higher sound pressure levels at low frequencies than at high frequencies at the THD of 5%. This is advantageous for the ADSC system since the low frequencies are boosted by the compensation filter to cancel the power loss caused by the vent.

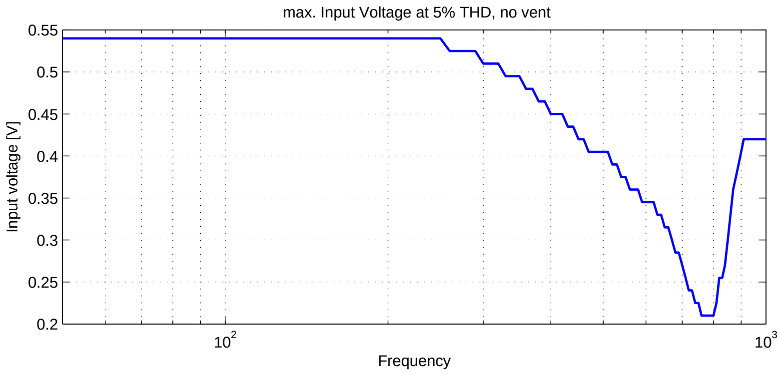

Figure 2.26: Maximum input voltage (peak) at a THD of 5% of the receiver "Sonion E50DA012" (parallel circuit) connected to a '2cc'-coupler over frequency: frequency resolution $\Delta f = 10$ Hz, input voltage resolution $\Delta u = 20$ mV

Maximum SPL in front of the ear

From the recorded SPL in the '2cc'-coupler it is possible to calculate the SPL in front of the ear, since both the REOG and the ventloss are assumed to be LTI systems, by

$$L_{\hat{p}_{\text{out}}}(j\omega) = 20\log_{10}\left(\frac{\hat{p}_{2\text{cc}}(j\omega)\left|\frac{H_{\text{Vloss}}(j\omega)}{H_{\text{REOG}}(j\omega)}\right|}{p_0}\right) \tag{2.20}$$

where $L_{\hat{p}_{\text{out}}}(j\omega)$ is the SPL in dB in front of the ear at frequency $f = \frac{\omega}{2\pi}$, $\hat{p}_{2\text{cc}}(j\omega)$ is the peak pressure measured in the '2cc'-coupler and $p_0 = 20$ μPa is the reference pressure. The ratio between the ventloss and the REOG is approximately the inverse of the compensation filter $H_{\text{COMP}}(j\omega)$ since the outer microphone and the receiver have a nearly flat frequency response in the range of 100 to 1000 Hz. Thus, the compensation filters of Fig. 2.17 are applied to the SPL levels of the 4 distinct frequencies. Tab. 2.2 shows the calculated SPL in front of the ear for varying vent sizes with THD of 5% and 10%.

Sinus	**THD**	**'2cc'**	**closed**	**0.225**	**0.3**	**0.425**	**0.575**	**0.725**	**0.875**	**1.16**	**1.5**	mm
125 HZ	5%	119.28	145.45	108.78	99.71	92.21	85.90	82.05	78.53	75.21	69.75	dB SPL
	10%	120.68	146.84	110.18	101.11	93.61	87.29	83.44	79.93	76.60	71.15	dB SPL
250 Hz	5%	117.82	164.43	115.84	108.39	102.23	96.29	92.45	89.40	85.59	80.29	dB SPL
	10%	119.17	165.78	117.19	109.74	103.58	97.64	93.80	90.75	86.94	81.64	dB SPL
500 Hz	5%	116.93	170.44	124.51	118.18	112.44	106.77	103.12	100.11	95.92	91.79	dB SPL
	10%	118.09	171.60	125.67	119.34	113.60	107.94	104.28	101.27	97.08	92.95	dB SPL
1 kHz	5%	120.50	167.44	139.29	133.21	127.54	121.88	118.30	115.41	111.45	107.31	dB SPL
	10%	121.64	168.57	140.43	134.35	128.67	123.02	119.44	116.55	112.59	108.44	dB SPL

Table 2.2: Maximum SPL [dB] in front of the ear for 4 distinct sine waves at THD 5% and 10%

From there it can be stated that the passive attenuation of the closed fitting scenario is greater than 20 dB and, moreover, increases with the frequency. Regarding the vented cases, the values at 125 and 250 Hz fall below the values in the coupler, whereas at 500 and 1000 Hz the tested receiver can even compensate sound pressure levels above the measured value assuming small vents up to $r_\mathrm{v} = 0.3$ and $r_\mathrm{v} = 0.575$ mm, respectively. Since the compensation filter boosts strongly the input voltage at low frequencies, the receiver generates harmonic distortions earlier in this frequency range than at high frequencies. Nevertheless, the results highlight that even for medium vent sizes the receiver may emit high sound pressure levels and thus makes it practicable to be used in the ADSC system.

The THD measure is a simple way to detect the harmonic distortions of a system. Moreover, a fix threshold for hearing aids is defined which denotes the tolerated distortions of impaired individuals and thus maps their subjective perception to an objective measure. Though, it is little meaningful regarding the distortions provoked by real world broad band signals such as speech, music and ambient sound. A big disadvantage is that the system under test is only excited at a single frequency each time, which cannot reveal any interaction between two or more frequencies. Effects like the summed- and difference-tones or the frequency and amplitude modulation do not arise, but contribute substantially to the audible distortion of a receiver when stimulated with more than one frequency [26]. Thus, the following sections analyzes the perceptive distortions of the receiver caused by broad band excitation.

2.4.1.4 Broad band signals

In contrast to the widely used THD measure for narrow band signals, there is no corresponding objective measure for broad band signals which evaluates in general audio equipment such as receivers. Although the ANSI developed a standard that describes the testing of hearing aids with broad-band noise signals [33], it is not commonly used since it is not required by the industry. Another reason is the fact that real world broad band signals vary substantially in spectra and provoke different hearing sensations even with similar RMS values or crest factors. In contrast to sinusoidal signals, a broad band signal does not have in general any periodicity and its energy fluctuates over time, in particular with speech and music signals [34]. However, artificial signals with an approximately constant RMS value and determinable crest factor like white, pink or babble noise are much more difficult to evaluate in regard of their distortions compared to real speech signals and thus are of limited use for subjective distortion tests. Therefore, the subjective bound for broad band signals in this thesis is examined only with different real speech signals, which allow a good detection of even slight distortions by a test person.

Several studies have examined the non-linearities of loudspeakers caused by broad band signals and the possibility to determine them with objective measures. While most of the studies were motivated by the possibility to detect any hardware defect of the loudspeaker, only a few analyzed the impact of non-linearities to the perceived sound quality [28, 34, 35]. This topic is still under research and, until today, no meaningful relation between an objective measure of non-linear distortion and their subjective perception was found. Nevertheless, Tan et al. [36] conducted psychoacoustic tests with distorted speech and music signals and came to the conclusion that it should be possible to evaluate broad band signals with objective measures. Temme et al. [28] used the ITU standard for objective measurement of perceived audio quality (PEAQ), which was mainly developed to rate encoded audio signals [37], in their study to detect any Rub & Buzz distortion with single tone excitation. The use of this standard, though, for broad band signals is less meaningful since the distortions produced by a loudspeaker add spectral components to the output whereas encoded signals withdraw signal information [34].

Distortion effects in hearing aids were also examined in several studies but with the main focus on speech intelligibility and not on perceived audio quality [38–44]. In this thesis the focus relies on the attenuation of the direct sound without adding any audible distortion rather than on the intelligibility.

The coherence $\gamma_{xy}^2(j\omega)$ between the stimulus and the response is a common measure to detect non-linear signal components of any unknown system and is defined by Eq. (2.16). The coherence of a LTI system under ideal conditions is 1 over all frequencies. Any signal component which has not a linear relation to the excitation signal deteriorates the coherence. The same occurs whenever the system variates during the averaging process of the spectral densities. Moreover, if the decay of the impulse response of a system under test is longer than the analysis window used to calculate the spectral densities of the signals, the coherence drops as well [45]. Measurements of a closed fitted receiver excited with white noise showed a coherence above 0.99 over the entire frequency range except the outermost bins. From there follows that the receiver works linearly and is time-invariant at least up to moderate excitation levels. The decline on the edges of the measured spectrum is caused by the high- respectively low-pass characteristic of the receiver, which deteriorate the SNR, and, at the lower edge, additionally by the inevitable leakage of the setup. It is assumed that any audible distortion generated by the receiver deteriorates the coherence significantly such that it can be detected by analyzing it. Therefore, 4 different measures based on the coherence function and one based on the transfer function are examined in the frequency range between 100 Hz and 1 kHz.

Mean and standard deviation of the coherence For moderate input levels the coherence is nearly 1 in the defined frequency range and so is its mean. Any non-linearity will reduce the mean and is consequently detectable. The opposite is the case for the standard deviation, which is 0 whenever the coherence has a constant value. Any deviation within the observed range of the mean increases the standard deviation.

THD coherence $\mathrm{THD}_{\mathrm{coh}}$ is inspired by the THD measure of single band signals. In [15, pp. 93] the $\mathrm{THD}_{\mathrm{coh}}$ is a frequency dependent function defined as the square root of the ratio of the non-coherence function to the coherence function at a specific frequency and given in percentage. In this thesis the N results are averaged in order to get a single value for the representation of the distortion:

$$\mathrm{THD}_{\mathrm{coh}}(j\omega) = \frac{1}{N}\sum_{\omega}\sqrt{\frac{1-\gamma_{xy}^2(j\omega)}{\gamma_{xy}^2(j\omega)}} \tag{2.21}$$

Total noncoherent distortion (TNCD) The TNCD reveals the noncoherent signal power of the system under test and is described in [27]. The idea is to get a function opposed to the coherence, the so called noncoherent distortion (NCD), which is the ratio of the noncoherent power spectral density $S_{nn}(f)$ to the total output power. The noncoherent power spectral density contains the power of the non-linear part of the system plus any additive noise. Similar to the coherence it lies in the range between 0 and 1, whereby a LTI system without additive noise has a NCD of 0.

$$\eta^2(j\omega) = \frac{\left(1-\gamma_{xy}^2(j\omega)\right)\cdot S_{yy}(j\omega)}{\sum\limits_{\omega} S_{yy}(j\omega)} = \frac{S_{nn}(j\omega)}{\sum\limits_{\omega} S_{yy}(j\omega)} \tag{2.22}$$

The total noncoherent distortion can then be written as the square root of the sum of the noncoherent distortion:

$$\lambda = \sqrt{\sum_{\omega} \eta^2(j\omega)} = \sqrt{\frac{\sum_{\omega} S_{nn}(j\omega)}{\sum_{\omega} S_{yy}(j\omega)}} \tag{2.23}$$

Mean of the transfer function $\mathrm{TF_{mean}}$ is the mean of the transfer function of the system under test related to the mean of the distortion-free transfer function of the same system. This implicates, as long as the system is linear and time-invariant the objective measure is 1. Further, it is assumed that the measure decreases once the receiver starts to distort.

Overview measurments

The objective measures were tested by the author in an overview measurement. The goal was to determine a threshold similar to the THD of the narrow band signals, which would define whether a signal has audible distortions or not. This would allow to set the maximum SPL of a broad band signal dependent on the specific spectral shape. For the overview measurement five different speech signals, which are favorable to detect audible distortions and have moreover a similar spectral shape, were selected from the Phonak AG Media DB (two female voices, two male voices, one mixed voices). Fig. 2.27 shows the power spectral densities (PSD) of the original (*solid*) and of the pre-filtered signals (*dashed*). The latter are the original speech signals filtered by a second order low-pass filter with cutoff frequency at 30 Hz. This simulates the effect of the compensation filter $H_{\mathrm{COMP}}(j\omega)$ such that not only the distortions of the receiver produced by the original clean speech signals but also the effect of the compensation filter $H_{\mathrm{COMP}}(j\omega)$ could be analyzed.

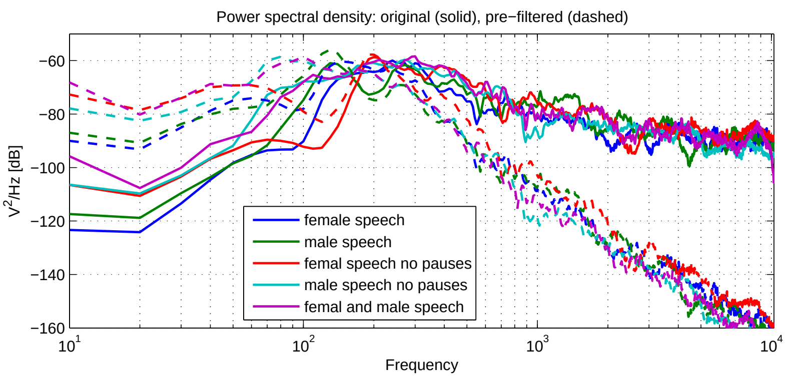

Figure 2.27: PSD of different speech samples used for the evaluation of the receiver distortion: original signals (solid), pre-filtered signals (dashed)

The approximation of the compensation filter by a 2$^{\mathrm{nd}}$ order low-pass filter is sufficiently accurate, since only frequencies between 100 Hz and 1 kHz are considered for the objective measures. In this frequency range, namely, the compensation filters differ mainly just in an overall gain (see Fig. 2.17).

Due to the closed fitting of the coupler, the receiver works as denoted in the datasheet, which makes it simpler to detect distortions at low frequencies and to compare it with other measurements conducted with a '2cc'-coupler. The drawback of this method is that some distortions may either be masked by other frequencies or, on the contrary, be very prominent due to the low frequency boost, which is not consistent with the vented environment.

Tabs. 2.3 and 2.4 list the results of the overview measurements. Each signal was evaluated for three different input levels: the lowest level defines the upper bound at which no audible distortion occurs during the playback time (subjective: *no*). In contrast, the highest level is the lower bound of the signals, which distort permanently during the playback (*severe*). The signals labeled with *slight* lie between the two bounds and have only audible distortions at their loudest parts. This three subjective classes allow to verify the progression of the objective measures in regard of increasing distortion and to withdraw meaningless parameters.

Signal	**CrestFactor**	**Input V (RMS)**	**Output dB SPL (RMS)**	$\mathbf{TF_{mean}}$	$\mathbf{Coh_{mean}}$	$\mathbf{Coh_{std}}$	$\mathbf{THD_{coh}}$	**TNCD**	**subjectiv**
female no pauses	9.7639	0.0485	97.36	1.0000	0.9953	0.0139	0.0498	0.0011	no
		0.2680	112.73	1.0780	0.9813	0.0238	0.1209	0.0054	slight
		0.5383	117.40	0.7084	0.8752	0.1183	0.3576	0.0451	severe
male no pauses	11.0855	0.0557	98.44	1.0000	0.9966	0.0039	0.0525	0.0016	no
		0.2094	110.27	1.0863	0.9427	0.0953	0.1874	0.0056	slight
		0.3244	113.42	0.9215	0.8509	0.2112	0.3912	0.0249	severe
female	6.8942	0.1115	104.91	1.0000	0.9977	0.0051	0.0415	0.0011	no
		0.2304	111.33	1.0361	0.9871	0.0178	0.0945	0.0028	slight
		0.3730	114.67	0.8508	0.9320	0.0710	0.2424	0.0217	severe
male	12.3539	0.1025	104.77	1.0000	0.9979	0.0014	0.0436	0.0014	no
		0.2143	111.36	0.9532	0.9876	0.0111	0.1012	0.0044	slight
		0.4354	116.36	0.6329	0.8878	0.1012	0.3317	0.0370	severe
female & male	13.5144	0.0735	101.07	1.0000	0.9972	0.0023	0.0506	0.0018	no
		0.2142	110.47	1.0042	0.9517	0.0943	0.1899	0.0096	slight
		0.3267	113.55	0.8378	0.8870	0.1238	0.3304	0.0302	severe

Table 2.3: Subjective analysis of different clean speech signals in regard of their distortion

Signal	**CrestFactor**	**Input V (RMS)**	**Output dB SPL (RMS)**	$\mathbf{TF_{mean}}$	$\mathbf{Coh_{mean}}$	$\mathbf{Coh_{std}}$	$\mathbf{THD_{coh}}$	**TNCD**	**subjectiv**
female no pauses	5.5045	0.0924	102.60	1.0000	0.9871	0.0192	0.0894	0.0009	no
		0.2370	111.21	1.0910	0.8659	0.1846	0.3357	0.0013	slight
		0.4829	116.47	0.7895	0.5715	0.4015	2.1879	0.0228	severe
male no pauses	7.8713	0.0910	102.11	1.0000	0.9165	0.1373	0.2317	0.0013	no
		0.1825	108.54	0.9131	0.7452	0.2926	0.6398	0.0019	slight
		0.4514	115.57	0.6290	0.4101	0.3788	2.1743	0.0334	severe
female	4.0765	0.0765	100.88	1.0000	0.9803	0.0209	0.1182	0.0010	no
		0.1723	108.42	1.1032	0.9356	0.0619	0.2198	0.0009	slight
		0.4015	115.14	2.7867	0.2395	0.3753	13.9555	0.5906	severe
male	4.5927	0.1034	103.52	1.0000	0.9817	0.0193	0.1139	0.0011	no
		0.2431	111.30	1.0134	0.8307	0.1810	0.4130	0.0015	slight
		0.4492	115.88	0.7725	0.5131	0.3316	1.2950	0.0142	severe
female & male	9.8664	0.0868	101.83	1.0000	0.9210	0.1038	0.2375	0.0020	no
		0.1783	108.33	1.0068	0.7600	0.2101	0.5433	0.0040	slight
		0.3785	114.13	0.8497	0.4539	0.3406	1.6721	0.0380	severe

Table 2.4: Subjective analysis of different speech signals in regard of their distortion, pre-filtered by the compensation filter $H_{\mathrm{COMP}}(j\omega)$ of a 2 mm vent of the ITE prototypes

It can be seen that the measure $\mathrm{TF}_{\mathrm{mean}}$ has no validity regarding the audible distortions of the receiver, neither for the original sounds nor for the pre-filtered versions. Instead of a continuous decay the value increases for the majority of the signals marked with *slight* distortion. In contrast, all the other measures increase continuously ($\mathrm{Coh}_{\mathrm{std}}$, $\mathrm{THD}_{\mathrm{coh}}$ and TNCD), respectively decrease ($\mathrm{Coh}_{\mathrm{mean}}$), within a signal with increasing input RMS level. Thus, regarding each signal apart, it would be possible to define always the objective value, where *no* distortions occurred, as threshold. An exception is the speech signal 'female' of Tab. 2.4, where the TNCD value of the *slight* case falls below the *no* distortion case.

It is difficult to find a threshold, which is valid for all tested signals within a table, although they have similar spectra. This is because of the small differences between the *no* distortion values and the *slight* distortion values. Certainly, it would be possible to choose the lowest ($\mathrm{Coh}_{\mathrm{std}}$, $\mathrm{THD}_{\mathrm{coh}}$ and TNCD) respectively the highest ($\mathrm{Coh}_{\mathrm{mean}}$) value of the five signals. Though, this would restrict the objective measure to this five signals, since it can not be guaranteed that the threshold is also valid for other broad band signals to be distortion-free. This would be possible if a correlation between the input signals and the objective measures could be stated.

A noticeable correlation between the input signals and the objective measures can only be assumed for the $\mathrm{Coh}_{\mathrm{mean}}$ measure, which increases with the input RMS for almost all signals. For all other measures no meaningful correlations are achievable. Combining both tables and comparing the objective values of the pre-filtered signals with the original ones, the dependency of the $\mathrm{Coh}_{\mathrm{mean}}$ and the RMS values of the input signal vanishes. Moreover, for each objective measure there is at least one excitation signal, whose value of the pre-filtered version for the *no* distortion scenario is worse than the value of the original version for the *slight* scenario. Thus, it seems inevitable to develop further objective measures, which consider the spectral shape of the input signal as well as the input level, in order to classify whether audible distortions occur or not.

In summary, it can be stated that from the overview measurement it is not possible to find an objective measure comparable to the THD, that guarantees distortion-free signals. This may originate from the measurement setup, where the pre-filtered signals are recorded in a closed volume instead of a vented volume and thus the audible distortions may differ from the real case. It may also arise from the speech signals used for the test, which decay fast towards high frequencies, in particular in the pre-filtered scenario, and thus deteriorate the coherence there. The input RMS of a signal has no significance about its spectral density and thus is poorly correlated with the objective measures. It should also be mentioned that the evaluation of the signals was done only by the author, whose auditory sensation must not correspond with the general hearing perception.

Nevertheless, the SPL of the signals was also recorded during the measurements which allows to set an overall subjective threshold of 100 dB SPL in a '2cc'-coupler, that guarantees an almost distortion-free receiver output for signals with a typical speech spectrum. Since the relation between the input and the output is at least linear for the *no* distortion scenario, it is also possible to limit the input RMS of the signal to approximately 0.0667 volt RMS. Since the receiver can be assumed as an ideal volume velocity source, limiting its input for distortion-free playback will avoid audible distortions independently from the acoustic network to which the receiver is connected.

Maximal SPL in front of the ear

Based on the output RMS values of the pre-filtered signals it is possible to calculate the SPLs of the different signals in front of the ear. The ADSC system shall be capable of canceling ambient noise levels of typical public spaces such as cafeterias and restaurants (approx. 70 to 80 dB SPL) without producing any annoyance for the user. Though, it is of interest to know up to which vent sizes the receiver is able to emit the desired distortion-free sound pressure. For that, the reciprocal of the compensation filters of the ITE-HM are used, similar to Eq. (2.20) of the narrow band case. This is valid since the conducted measurements were done with identically constructed receivers, that have a similar frequency response and sensitivity. Tab. 2.5 lists the

SPL of the five speech signals for the different vent sizes of the ITE-HM.

The broad band passive attenuation of the closed fitted scenario is more than 35 dB, which

Signal	'2cc'	closed	0.225	0.3	0.425	0.575	0.725	0.875	1.16	1.5	mm
female no pauses	102.60	144.28	100.28	93.05	86.95	81.11	77.35	74.34	70.02	65.86	dB SPL
male no pauses	102.11	139.21	95.88	88.41	82.18	76.29	72.51	69.48	65.21	61.09	dB SPL
female	100.88	142.26	97.08	89.58	83.35	77.44	73.65	70.62	66.36	62.20	dB SPL
male	103.52	139.37	96.61	88.85	82.46	76.51	72.76	69.67	65.58	61.54	dB SPL
female & male	101.83	138.17	94.99	87.39	81.08	75.16	71.37	68.33	64.08	59.95	dB SPL

Table 2.5: Simulation of the maximum SPL for different signals at the outer microphone $\mathrm{M_c}$ *at which no audible distortion is perceptible. Calculations based on the pre-filtered sound samples and the measured compensation filters* $H_{\mathrm{COMP}}(j\omega)$ *of the ITE-HM (see Fig. 2.17)*

allows the compensation of sound pressure level around 140 dB. For the vents, though, the maximum SPL of the direct sound at their entry is lower than the pre-filtered sound pressure in the '2cc'-coupler. Moreover, all values of the respective vents fall below the maximum SPLs of the narrow band signals listed in Tab. 2.2. Thus, broad band signals are the limiting factor of the subjective bound. Only the 125 Hz values of the narrow band measurements are in the vicinity of the RMS levels of the broad band excitation. Since the compensation filters shift the energy of the signals to the low frequencies and damp the higher frequencies, it may be possible to describe the limits of the receiver with the narrow band THD measure at a frequency below 100 Hz. This depends also on the design of the compensation filter, which must be limited at low frequencies. Nevertheless, the table shows that the ADSC system supports SPLs of more than 70 dB even with medium-size vents, i.e. $r_{\mathrm{v}} = 0.725$ mm @ $l_{\mathrm{v}} = 5$ mm, which are commonly used in ITEs. This outcome allows the application to be used in public spaces with moderate background levels and encourages the further development of the system.

While the perceived distortion caused by narrow band signals can be accurately estimated with the objective measure THD, the degradation of the perceived audio quality due to broad band distortion is still not defined and has to be further investigated. As mentioned in [34], the difficulty lies in the interaction of the different elements which are causing the distortions: the receiver is a complex system which generates non-linearities that are not only describable by harmonic distortions. Further, the response of the receiver to broad band excitation depends strongly on the signal characteristics, which vary in reality heavily regarding their spectra and temporal behavior. The complexity of the highly non-linear human auditory system makes it further complicated to find a measure which accurately states whether a signal is annoying or not. Moreover, in this thesis, the signal emitted by the receiver is used to cancel out the direct sound at the ear drum. As a consequence, distortions, which are masked by other signal components, may become prominent after the destructive interference with the direct sound.

The gained data give some indications of the possible sound pressure levels, at which the ADSC system works without introducing perceivable distortions to the listener. In Chapter 5 the attenuation of the ADSC system is presented for different compensation filters $H_{\mathrm{COMP}}(j\omega)$ and ITE prototypes. Each measurement records also the sound pressure level of the excitation signal at the outer microphone $\mathrm{M_0}$ and the resulting signal in the ear canal is further evaluated in regard of its sound quality, i.e. audible distortion, by the user.

2.4.2 Algorithmic bound

The algorithmic bound limits the maximum allowed deviation of the receiver response in magnitude and phase from its linear response in order to achieve a determined attenuation. It is a lower bound which defines the minimum attenuation that the ADSC application reaches with an ideal compensation filter. Assuming an ideal compensation filter, as defined in Eq. (2.12), the achievable attenuation D is ∞ dB as long as the transducer work linearly. Any deviation of the recorded transducer response implicates a degradation of the ADSC performance. Since the outer microphone is assumed to work ideally, only the magnitude and phase stability of the receiver is analyzed as a function of the input signal.

Despite the audible distortions, discussed in Section 2.4.1, the receiver enters also into saturation with increasing input level. The saturation arises from the electromagnetic and the mechanical part of the receiver, i.e. the coil and the armature stiffness [18]. Furthermore, the receiver has a hard upper bound which is stated by the maximal physical displacement of the diaphragm. These effects influence the receiver response progressively with increasing input level. The objective is to define the maximum input level that still ensures a predefined performance of the attenuation. Moreover, the subjective and the algorithmic bounds are compared in order to find out which bound is encountered first and thus limits the ADSC application.

The effect of the magnitude and phase deviation on the attenuation can easily be calculated. Assuming a single sine wave as direct signal

$$d(t) = A \cdot \cos(\omega t) \tag{2.24}$$

where A is the amplitude and $\omega = 2\pi f$ is the angular frequency, then the ADSC signal, which should attenuate the direct signal, has to be

$$z(t) = \hat{A} \cdot \cos(\omega t + \pi + \Delta\phi) = -A \cdot 10^{\frac{\Delta A}{20}} \cdot \cos(\omega t + \Delta\phi) \tag{2.25}$$

where, for a perfect cancellation, the amplitude deviation has to be $\Delta A = 0$ and the phase deviation $\Delta\phi = 0$, too. The attenuation in dB can then be formulated as the ratio between the direct signal and the residual signal, which results from the superposition of both signals:

$$D = 20 \log_{10}\left(\frac{\overline{d(t)}}{\overline{d(t) + z(t)}}\right) = 20 \log_{10}\left(\frac{\overline{d(t)}}{\overline{e_{ac}(t)}}\right) \tag{2.26}$$

Solving this equation (see Appendix A [46]) yields the attenuation as a function of the amplitude deviation ΔA and phase shift $\Delta\phi$:

$$D = -10 \cdot \log_{10}\left(1 - 2 \cdot 10^{\frac{\Delta A}{20}} \cdot \cos(\Delta\phi) + 10^{\frac{\Delta A}{10}}\right) \tag{2.27}$$

The attenuation D is plotted over the amplitude and the phase deviation in Fig. 2.28. It can be seen that the attenuation is symmetrical regarding the phase deviation but unsymmetrical regarding the amplitude deviation. This is due to the fact that the amplitude of the signals is defined as a positive number. Thus, if the ADSC signal vanishes, i.e. $\hat{A} = 0$, then the amplitude deviation becomes $\Delta A = -\infty$ and the attenuation results in $D = 0$. In contrast, if the amplitude of the ADSC signal is $\hat{A} = +\infty$, then the deviation is also $\Delta A = +\infty$, which yields $D = -\infty$ dB.

The following two subsections analyze the saturation effects of the receiver for narrow band and for broad band excitation signals, where the algorithmic bound is set to $D = 15$ dB, which is higher than the desired broad band attenuation of the ADSC system, i.e. $D \geq 10$ dB. From Fig. 2.28 (b) one can conclude that the phase deviation may deviate maximal $\pm 10°$ degrees and the amplitude deviation must not be greater than -1.7 respectively $+1.4$ dB to satisfy the chosen algorithmic bound

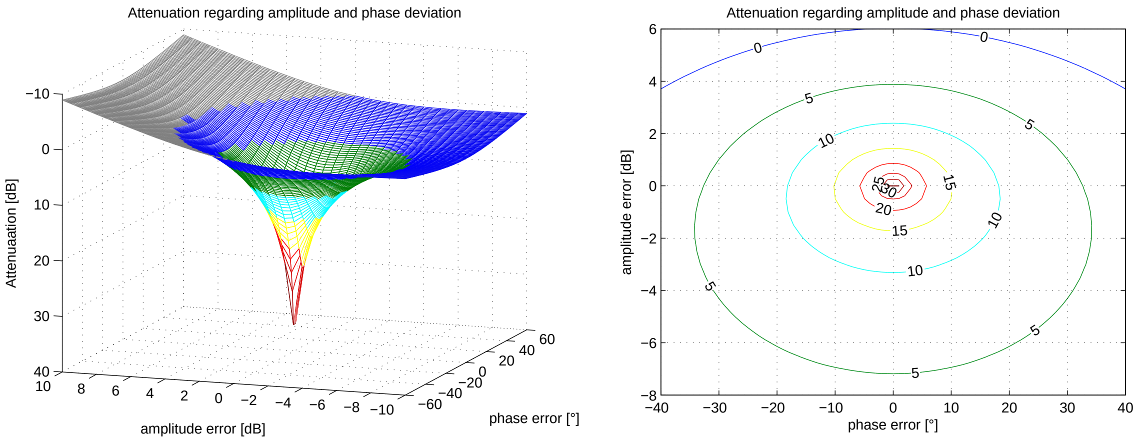

(a) (b)

Figure 2.28: Attenuation regarding amplitude and phase deviation: $D \geq 20$ dB - red, $20 > D \geq 15$ dB - yellow, $15 > D \geq 10$ dB - cyan, $10 > D \geq 5$ dB - green, $5 > D \geq 0$ dB - blue, $0 > D$ dB - gray

2.4.2.1 Narrow band signals

The saturation of the receiver is examined for narrow band signals with the same excitation signals under the same measurement conditions as used for the subjective bound which allows to compare the results of both bounds.

Based on the data of the THD measurement it is possible to achieve the amplitude and phase deviation and calculate the resulting attenuation with Eq. (2.27). For that, the receiver response measured with the lowest input level is used as the reference, since it is known that the receiver is almost completely linear at this excitation level. The frequency response of the higher input levels are then compared in magnitude and phase with the reference as depicted in Fig. 2.29. The subjective bounds are additionally plotted as circles (THD 5%) and as squares (THD 10%), respectively.

The results show that, other than expected, the sensitivity of the receiver increases first up to an input level of 0.3 volt, which, however, was not further investigated due to time limitations. Above 0.3 volt it decays continuously with higher excitation levels. This occurs with the 4 frequencies, whereby the deviation at 125 Hz exceeds the others. This is somehow contradictory to the subjective bound which allows the highest input level at the lowest frequencies (see Fig. 2.26). Nevertheless, the defined algorithmic bound of $D = 15$ dB is reached only for input voltages higher than 0.8 volt for the examined frequencies. At this input levels even the THD 10% limits are already exceeded which implicates that the limiting factor for narrow band signals is determined by the audible distortions and, particularly in this application, by the THD 5%. This extends also to the vented cases since the compensation filter $H_{\mathrm{COMP}}(j\omega)$ is linear and time-invariant and thus it does neither introduce any level dependent change in magnitude and phase nor generate any additional distortions.

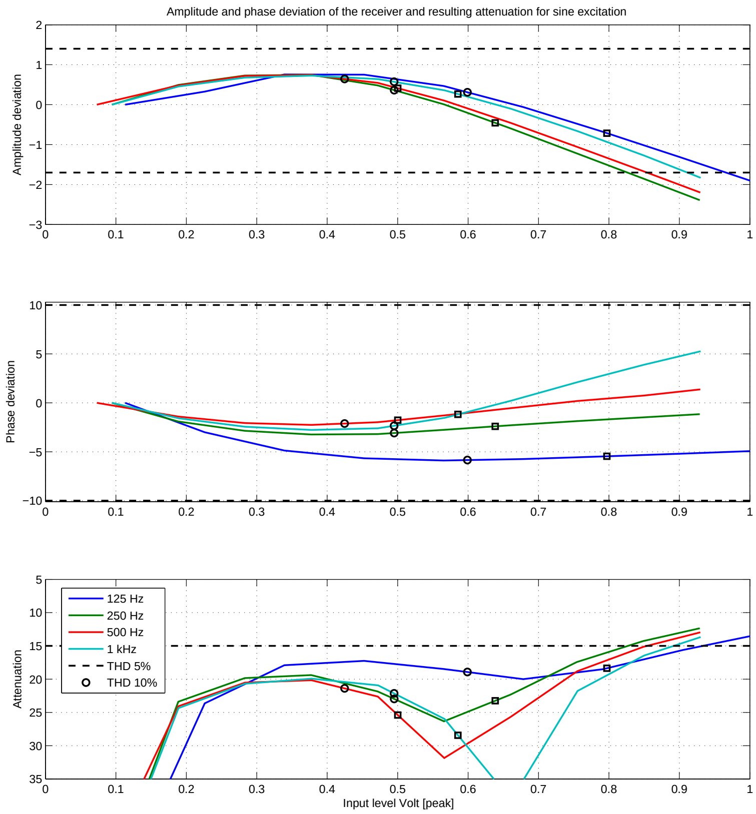

Figure 2.29: Amplitude and phase deviation of sinusoidal excitation with varying input level for the 4 distinct frequencies. The black dashed lines determine the limits for an attenuation of $D \geq 15$ dB and the circles and the squares mark the THD *thresholds,* 5 % *and* 10 % *respectively*

2.4.2.2 Broad band signals

Since sinusoidal signals are not common in a real scenario, the behavior of the receiver, regarding its amplitude and phase for different input levels, has to be determined above all for broad band signals. Contrary to the subjective bound, the evaluation of the signals is not done by the user but calculated. This enables the use of any broad band signal including the speech signals introduced before but also broad band noise.

The objective is to determine the maximum input level of the broad band signals at which the algorithmic bound is not yet infringed, similar to the subjective bound. Therefore, the signals are analyzed in 10 linearly spaced bands with bandwidth of 100 Hz between 50 and 1050 Hz. Additionally, the mean over all bands is also analyzed in regard of its deviations. The reference frequency response of the receiver is defined for input levels at which the receiver works linearly, which is verified with the coherence function.

Fig. 2.30 depicts the deviation of the receiver response for a white noise input signal and the resulting attenuation. The input level is gradually increased by 0.1 volt and starts with the level of the reference response. The outcome resembles the narrow band curves of Fig. 2.29, where the sensitivity increases first and only above 2.8 volt the receiver enters in saturation. Moreover, the low frequency bands suffer from the greatest deviations and the algorithmic bound is already infringed at 0.18 volt by the lowest band. The other bands do not fall below the bound until 0.7 volt, which is in the vicinity of the narrow band result.

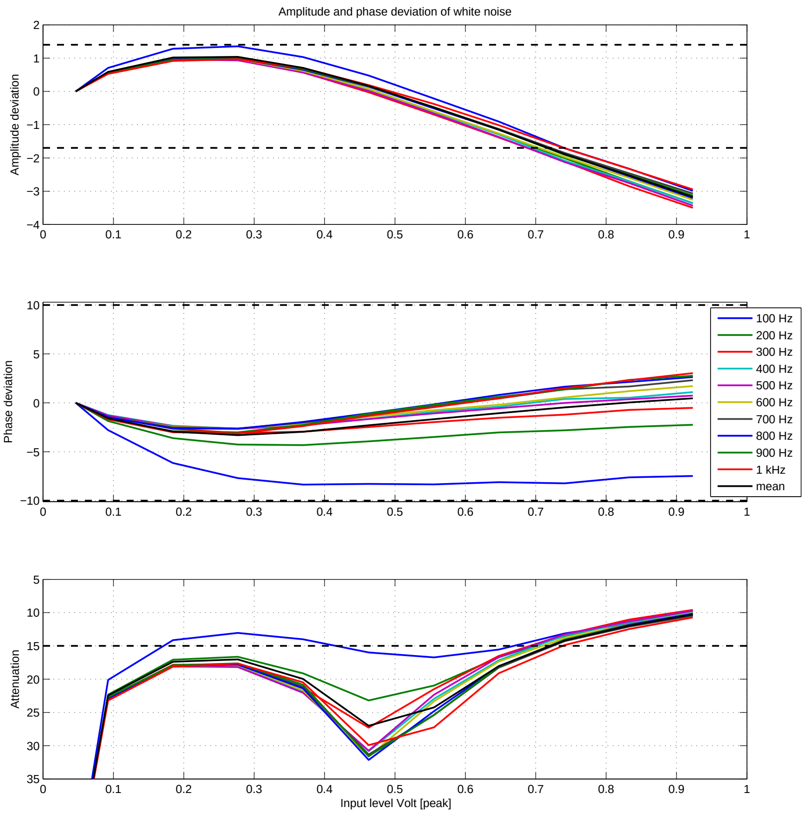

Figure 2.30: Amplitude and phase deviation of the receiver "Sonion E50DA012 (par. circuit)" measured in a '2cc'-coupler for varying input level of white noise, 10 *distinct frequency bins plotted*

Furthermore, 6 different real world signals were also examined, of which 5 (female no pause, male no pause, female & male, babble noise and cafeteria noise) have a speech-like spectrum and do not evoke audible distortions up to 100 dB (SPL) in the '2cc'-coupler. The remaining signal (traffic noise) has its main energy below 100 Hz and thus the receiver starts to distort already at lower input levels which reduces the subjective bound to approximately 80 dB. All 6 sound samples were pre-filtered with the approximation of $H_{\mathrm{COMP}}(j\omega)$ as explained in Section 2.4.1.4, since the input of the receiver in the ADSC system is the output of the compensation filter (see Fig. 2.15). The reference frequency response of the receiver is determined again by the coherence function of each signal. Fig. 2.31 shows the resulting attenuation of the different signals at a specific SPL in the '2cc'-coupler. This allows the comparison with the subjective bound measurements, which were conducted under the same measurement conditions.

It can be stated that the response of the receiver regarding its magnitude and phase deviation varies highly with the excitation signals. While the attenuation for the babble noise and the cafeteria noise decreases uniformly in all frequency bands with increasing input level, the response of the speech signals differs strongly in each band. This is because of the slightly different spectral density of the signals. While the speech signals have their main energy in a small frequency range around the fundamental frequency of the talker, the cafeteria and babble noise have a flatter spectrum mainly originated from several different voices and ambient noise.

Comparing the SPL of the speech signals with Tab. 2.4 it can be seen that the subjective bound is the limiting case for the 'female no pause' and the 'female & male' signal independently of the frequency band. Only for the 'male no pause' signal this is not true, since the 200

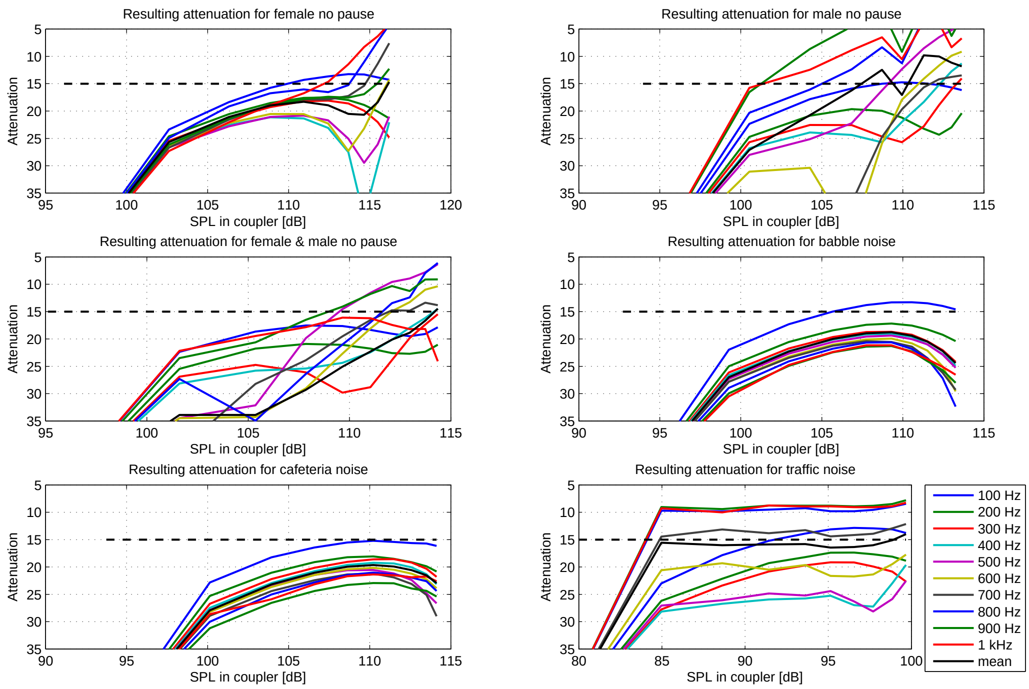

Figure 2.31: Resulting attenuation for different broad band signals over SPL in a '2cc'-coupler

Hz and the 300 Hz band infringe the algorithmic bound at values below 103.52 dB. Nevertheless, assuming a subjective bound of 100 dB and an algorithmic bound of 15 dB, the subjective bound limits the applicability of the ADSC system for all tested signals except the traffic noise. But also for the traffic noise, where the subjective bound is set to 80 dB, the subjective bound is outreached before the algorithmic bound is violated.

It can be summarized, that the algorithmic bound in general is not the limiting factor of the ADSC application system. Both for the narrow band and for the broad band signals the bound is reached at levels where audible distortions already occur. It should be noted that the introduced algorithmic bound is not only meaningful regarding the receiver distortion but is also used for the evaluation of the static and adaptive ADSC compensation filter as it shows the possible attenuation of the designed filters.

2.5 Conclusion

In this chapter the acoustic environment of the active direct sound control system was presented. The transfer function of the direct sound path and the receiver response in dependency of the vent dimensions were discussed and the resulting ideal compensation filter $H_{\mathrm{COMP}}(j\omega)$ introduced, which yields an infinite attenuation of the direct sound in front of the ear drum. Moreover, the measurement of the transfer functions and their intra- respectively inter-individual variability was analyzed, which both decrease with an increase of the vent dimensions.

In the last section the receiver distortion caused by narrow and broad band signals was analyzed. It was not possible to define an objective threshold for broad band distortion, nevertheless, it can be inferred from the simulations that the ADSC system with a mid-sized vent can be used to attenuate speech sounds up to levels found typically in public spaces like cafeterias.

3 Static ADSC Filter Design

In order to cancel the direct sound, the compensation filter $H_{\text{COMP}}(j\omega)$ has to be implemented as either a finite impulse response (FIR) or an infinite impulse response (IIR) filter. Because of delay constraints it is not feasible to perform the filtering of the recorded ambient sound in the frequency domain. The latency in this application is highly critical: the calculation of the destructive signal $z(t)$ must be made within the time, in which the direct sound propagates from the outside into the ear canal. Any additional computational delay τ_{calc} introduces a frequency dependent phase deviation $\Delta\phi(\omega) = \omega \cdot \tau_{\text{calc}}$ which deteriorates the attenuation according to Eq. (2.27).

This chapter discusses the design of static filters, which approximate the compensation filter $H_{\text{COMP}}(j\omega)$, in order to cancel the direct sound. A static compensation filter has a low complexity compared to an adaptive method, since the calculation of the coefficients is done once off-line and then saved on the DSP of the hearing instrument. This ensures also stability of the ADSC system as long as the designed compensation filter is stable. Furthermore, the static filter is signal independent and reaches for all signals the same attenuation. Though, the drawback of the static design is that it can not compensate any deviation from the measured transfer functions caused by the reinsertion of the earpiece or by an alteration of the transducers, e.g. by grime. As a sudden change of the transducer responses is not to be expected and the variability at least of medium vent sizes is small, the static filter design seems to be promising for this application. The block diagram in Fig. 3.1 shows the static ADSC system used in this application, where $\hat{H}(j\omega)$ is the designed filter. The estimated compensation filter is denoted by the cascade of $\hat{H}(j\omega)$ and $H_{\text{preEQ}}(j\omega)$, where $H_{\text{preEQ}}(j\omega)$ is a pre-equalization filter, which is discussed in Section 3.4.3.

In the following sections a manual filter design approach as well as a filter approximation framework is presented which both approximate the calculated compensation filter $H_{\text{COMP}}(j\omega)$ with IIR filters. The underlying estimation algorithm is outlined and the adjustments performed in order to achieve viable coefficients are discussed. In this thesis only the design of IIR filters is investigated, since FIR filters are not implementable on the hearing aid DSP in the near future due to its high number of coefficients for an adequate approximation of $H_{\text{COMP}}(j\omega)$ (see Chapter 4).

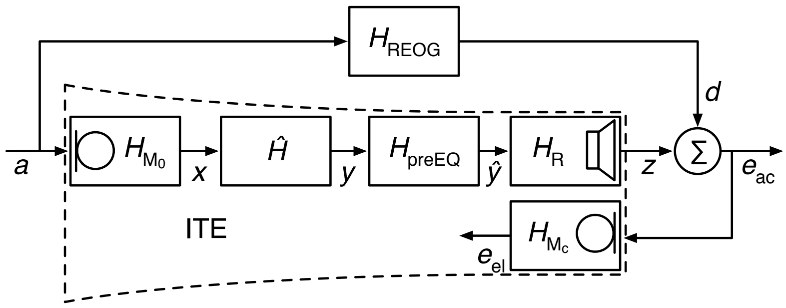

Figure 3.1: Block diagram of the implemented static ADSC system: H_{REOG} is the direct path, H_{M_0} is the frequency response of the outer microphone, $\hat{H}$ is the designed filter, H_{preEQ} is a pre-equalization filter and H_{R} is the receiver response. a is the ambient sound in front of the ear, x is the recorded signal, y is the output of the designed filter, $\hat{y}$ is the pre-equalized output and z is the sound pressure emitted by the receiver. The acoustic error signal e_{ac} vanishes if z is the phase inverted version of the direct sound d. e_{el} is the electric output of the canal microphone.

3.1 Design Requirements

In general, it is desired that the developed static filter approximates the measured compensation filter $H_{\mathrm{COMP}}(j\omega)$ over the entire frequency range very accurately in order to achieve a strong broad band attenuation. Since this is not feasible due to receiver distortions and restrictions on the IIR filter order, the design requirements, which have to be fulfilled by the compensation filters, were defined as follows

- **high attenuation between 100 Hz and 1 kHz**: the focus of this application lies on the attenuation of the frequency range, where the ambient sound propagates undamped into the ear canal. The parameter D_{avg} describes the average attenuation in this frequency band on the logarithmic scale and is used to validate the designed filter. The attenuation is always referred to the unbounded frequency response of the compensation filter denoted by Eq. (2.12) and is said to be high for $D_{\mathrm{avg}} \geq 10$ dB.

- **receiver limitation at low frequencies**: the maximal amplification gain of the compensation filter is set in order to avoid receiver distortions. The limit is chosen according to the transducer and the requirements on the application.

- **receiver limitation at high frequencies**: the residual signal $e_{\mathrm{ac}}(t)$, which results from the destructive interference, must always be inferior to the ambient sound signal $a(t)$ in front of the ear. At high frequencies, where the direct sound is passively damped by the roll-off of the REOG above the cut-off frequency, this constraint can be infringed as long as the residual signal is masked by the HI-sound, which compensates the hearing loss of the patient, and is thus not perceived.

- **stability and causality**: the impulse response of the filter must be stable and causal in order to be used for the cancellation of the direct sound.

These requirements are valid for all compensation design techniques in this work, including also the adaptive filter design of Chapter 4.

3.2 Manual Biquad Filter Design

The upcoming DSP platform "Palio 3"of Phonak AG opens up the possibility to run ADSC on it. In contrast to the actual generation, it has two fast time-domain signal paths running at the fourfold and the eightfold hearing aid sampling frequency $f_s = 20480$ Hz, respectively. These reduce the Input/Output-delay to approximately $50\,\mu$s and $25\,\mu$s, respectively, which is both faster than the propagation time through a vent length of 20 mm, i.e. $\tau_{\text{vent}} \approx 58\,\mu$s. Furthermore, 2x5 biquad filter blocks are available on this path and allow the implementation of IIR filters with maximal 20^{th} order.

In contrast to a higher order IIR filter a cascade of biquad filters with the same order has the advantage of being simpler to control in regard of their stability. A stable higher order IIR filter may become eventually unstable on a DSP because of numerical problems of the filter coefficients due to a limited bit depth. This is even aggravated if the coefficients have to be defined as fixed-point numbers and a conversion of the calculated floating-point numbers has to be realized. Using a cascade of biquad filters, the stability can be guaranteed if each biquad block is stable.

The following sections show the design of static filters based on 2^{nd} order digital filters according to [47, Chapter 2]. Since both the REOG and the PLANT are assumed to be minimum-phase systems with an additional propagation delay and their frequency responses are well-known (see Section 2.1), it seems promising to fit the desired responses manually in order to get a broad band attenuation.

3.2.1 Design of REOG Filter

From Section 2.1.1 it is known that the REOG resembles roughly a 2^{nd} order low-pass filter with a certain propagation delay τ_{REOG}. Fig. 3.2 shows the measured REOG of the ITE-HM with the vent radius $r_v = 0.575$ mm and its approximation by a cascade of a 2^{nd} order low-pass filter and a 2^{nd} order lead filter[1]. The match is accurate up to 2 kHz, where the direct sound is already passively attenuated by more than 12 dB. The amplitude and phase deviation until there is small, which allows an average attenuation of $D_{\text{avg}} = 20.43$ dB between 100 Hz and 1 kHz, assuming a perfect PLANT approximation. The deviation at the lowest frequency bins can be neglected, since it arises from the microphone mismatch between M_0 and M_c and vanishes for H_{COMP}.

[1] Lead and lag filters are the terms used in control literature for the shelving filters in audio applications

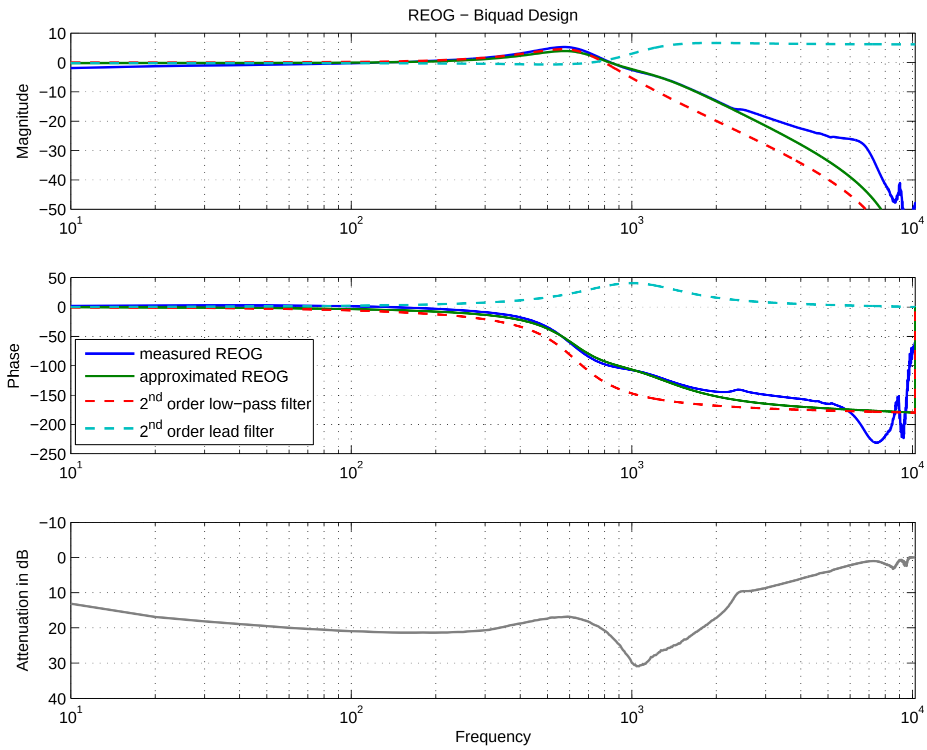

Figure 3.2: Approximation of the REOG with a cascade of 2^{nd} *order filters: low-pass filter with* $f_c = 630$ *Hz and* $q = 1.6$ *(red dashed), lead filter with* $fc = 1$ *kHz,* $q = 1$ *and* $\phi = -20°$ *degrees (cyan dashed), overall gain* $g = 3$ *dB. The filters are implemented in the MATLAB® functions* `lowpass2.m` *and* `leadlag.m`*. Assuming perfect* PLANT *approximation, the average attenuation between* 100 *Hz and* 1 *kHz is* $D_{\text{avg}} = 20.43$ *dB*

3.2.2 Design of the inverse PLANT Filter

The approximation of the inverse PLANT by a digital IIR filter is significantly more difficult than the approximation of the REOG. The reason is that an inversion of a transfer function is only causal and stable if its poles and zeros lie inside the unit circle. Any frequency response that fulfills this requirement is defined as a minimum-phase system [22, Section 5.6]. From Section 2.2 it is known that the measured transfer function $\hat{H}_{\text{PLANT}}(j\omega)$ is not a minimum-phase system but can be split into a minimum-phase part $\hat{H}_{\text{PLANT}_{\text{min}}}(j\omega)$ and an all-pass part, which is assumed to be a constant group delay $\hat{\tau}_{\text{PLANT}}$. Since it is impossible to compensate a constant group delay with a causal all-pass filter, the phase mismatch between the measured PLANT and the estimated minimum-phase system has to be equated otherwise.

This can be done by a 2^{nd} order boost filter, whose resonance frequency is near the Nyquist frequency f_{Nyquist}. The filter lifts the phase response up until the -3 dB frequency of the boost filter and acts roughly as a negative group delay in the frequency range, where the ADSC system is supposed to cancel the direct sound. The closer the resonance of the boost filter is to the Nyquist frequency f_{Nyquist}, the less influence is noticeable on the magnitude in the range of interest. This can even be improved by using a higher sampling frequency and shifting the resonance peak to higher frequencies such that it becomes inaudible. Thus, only a change in phase appears at the lower frequencies. However, in this thesis the sampling rate was chosen according to the hearing instrument such that all simulations can be executed on the RTS.

The used boost filter compensates a negative constant group delay of roughly 25 μs up to 1 kHz and improves the attenuation between 200 Hz and 1 kHz (see Fig. 3.3).

Moreover, the higher order roll-off at the edges of the PLANT impede a stable filter design. Hence, the frequency response must be constrained at its edges in order to be invertible. A simple solution for the inverted high-pass at low frequencies is the use of 2^{nd} order lag filters, which approach well the desired magnitude and phase but limit the maximal amplification. This upper limit enables not only a stable filter design but also has an impact on the receiver distortion and the broad band attenuation. The higher the limit, the better the magnitude and phase match with the inverted PLANT at low frequencies, which means a broader attenuation. In contrast, a lower limit of the maximal gain is beneficial for the receiver since the low frequencies of a signal are less amplified and the receiver supports higher signal levels without producing audible distortions. This trade-off between a broad attenuation and an undistorted system, that is capable of canceling high sound pressure levels, is independent of the filter design method and shown in Chapter 5.

The low-pass characteristic of the PLANT at high frequencies, however, must not be approximated, since it is assumed that the compensation signal of the patient's hearing loss masks the residual sound $e_{\text{ac}}(t)$ (see Section 3.1).

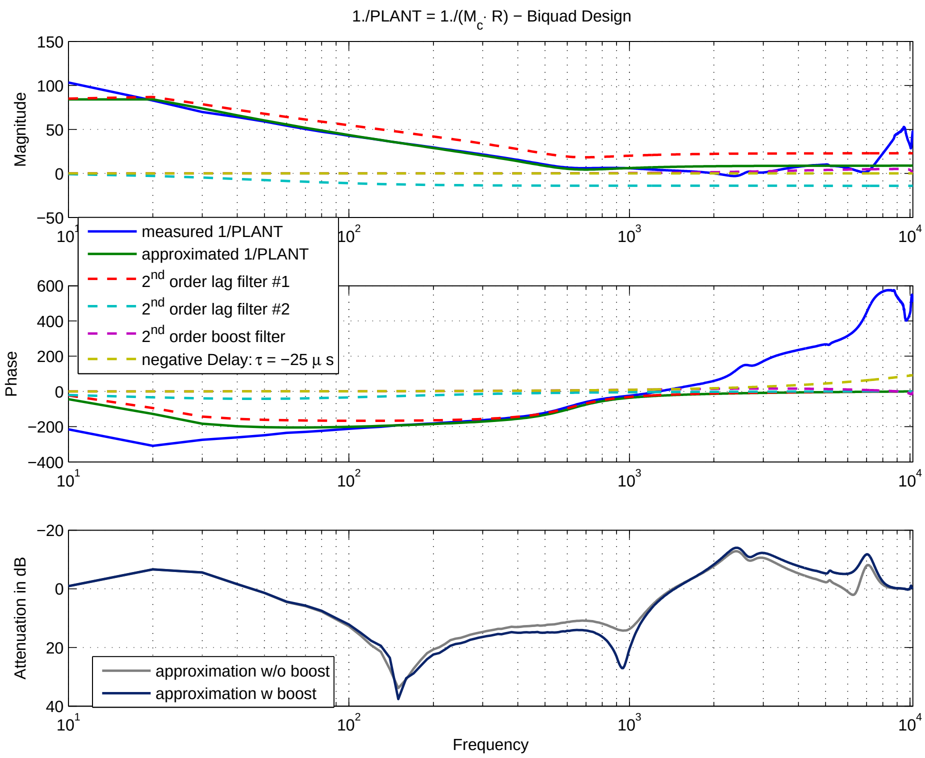

Figure 3.3: Approximation of the inverse PLANT with a cascade of 2^{nd} order filters: lag filter with $f_c = 110$ Hz, $q = 1.6$, $\phi = 83.5$ and gain $= 53$ (red dashed), lag filter with $f_c = 45$ Hz, $q = 0.46$, $\phi = 21$ and gain $= -7$ (cyan dashed), boost filter $f_c = 9$ kHz, boost $= 5$ dB and BW $= 15$ (pink dashed). The filters are implemented in the MATLAB® functions `leadlag.m` and `boostcut.m`. The average attenuation between 100 Hz and 1 kHz is $D_{\text{avg}} = 16.58$ dB (without boost filter) and $D_{\text{avg}} = 18.82$ dB (with boost filter), respectively, assuming a perfect approximation of the REOG.

Fig. 3.3 shows a rough approximation of the inverse PLANT by a cascade of 3 biquad filters. The deviation of this approximation is distinctly higher than for the REOG design, which is caused by the low frequency limitation. To achieve a higher accuracy in magnitude and phase the number of biquad sections has to be increased, which, however, makes it more complex for the manual design. The effect of the boost filter regarding the compensation of the negative delay is clearly visible in the lowest plot and enhances the average attenuation from $D_{\text{avg}} = 16.58$ dB to $D_{\text{avg}} = 18.82$ dB, assuming a perfect approximation of the REOG.

3.2.3 Design of the Compensation Filter H_{COMP}

The compensation filter can now be built as the cascade of the five 2^{nd} order filters defined to approximate the REOG and the PLANT. However, the question that arises is if it is possible to achieve better results with less or equal filter order by approximating the compensation filter directly instead each part of it separately. Since the low frequency roll-off of the PLANT, which is caused mainly by the ventloss, and the REOG are related approximately by (see Eq. (2.11))

$$H_{\text{Vloss}}(j\omega) = 1 - H_{\text{REOG}}(j\omega), \tag{3.1}$$

common characteristics such as the resonance peak are canceled out for the compensation filter. Moreover, the estimated delay $\hat{\tau}_{\text{COMP}} = \hat{\tau}_{\text{REOG}} - \hat{\tau}_{\text{PLANT}}$, which is always smaller than the negative constant group delay of the inverse PLANT $-\hat{\tau}_{\text{PLANT}}$ and thus favorable for the design, has to be compensated. This allows in this specific case to design the compensation filter with only 3 biquads, whose attenuation even outperforms the cascade of the five biquads.

Fig. 3.4 plots the desired $H_{\text{COMP}}(j\omega)$ frequency response and different approximations of $\hat{H}_{\text{COMP}}(j\omega)$, the magnitude and phase deviation as well as the resulting attenuation. Both the blue and the green curves are the results of the manual design whereas the red and the cyan curves are the output of the static framework presented in the next sections. Various conclusions can be drawn from this figure: The cascade of the biquads, which approximate the REOG and the inverse PLANT (*blue*, $D_{\text{avg}} = 13.01$ dB), achieve less attenuation than the direct design of the compensation filter $H_{\text{COMP}}(j\omega)$ by only three biquads (*green*, $D_{\text{avg}} = 19.32$ dB). Thus, instead of an individual approximation for the REOG and the inverse PLANT it is more effective to design the compensation filter directly (*red*, $D_{\text{avg}} = 14.94$ dB and *cyan*, $D_{\text{avg}} = 20.26$ dB). Furthermore, the approximation algorithm may achieve worse results than the manual design with the same order of coefficients. This is due to the static framework, which is designed to find suitable coefficients of $H_{\text{COMP}}(j\omega)$ for any ITE prototype and thus it is not optimized for the ITE-HM itself. Nevertheless, by increasing the order of the IIR filter the broad band attenuation can be increased.

It should be denoted that the algorithmic bound is obeyed only by the manual 6^{th} order design and the 11^{th} order design of the approximation algorithm in a wide range. Chapter 5 will show that the algorithmic bound of $D \geq 15$ dB is very strict and is therefore relaxed to $D \geq 10$ dB, which yields still a clearly audible attenuation.

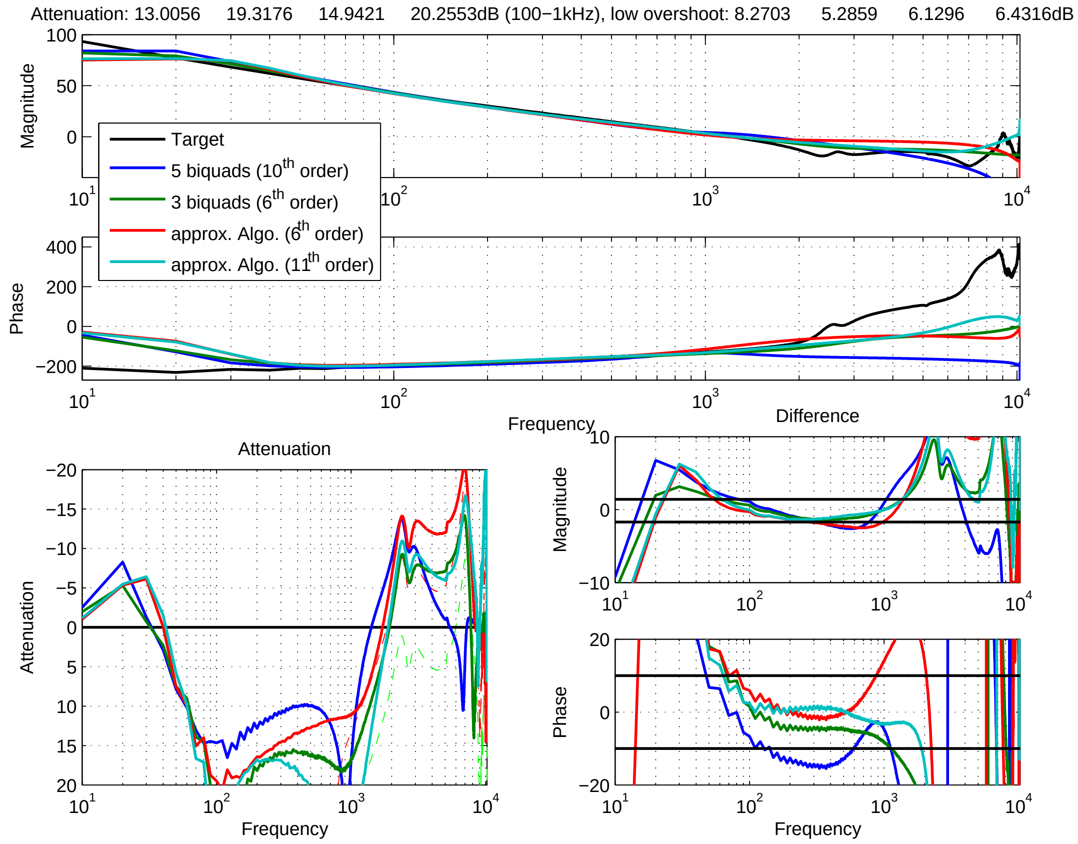

Figure 3.4: Comparison between the desired compensation filter $H_{\mathrm{COMP}}(j\omega)$ and different approximations $\hat{H}_{\mathrm{COMP}}(j\omega)$: cascade of the 5 biquads used to approximate REOG and the inverse PLANT (blue, $D_{\mathrm{avg}} = 13.01$ dB), approximation with 3 biquads: lag filter with $f_{\mathrm{c}} = 230$ Hz, $q = 1$, $\phi = 85°$ degrees and gain $= 40$ dB, lag filter with $f_{\mathrm{c}} = 45$, $q = 0.46$, $\phi = 21°$ degrees and gain $= -8$ dB, boost filter with $f_{\mathrm{c}} = 3000$ Hz, boost $b = 7.5$ dB and bandwidth $bw = 4$ (green, $D_{\mathrm{avg}} = 19.32$ dB), approximation by the static framework 6^{th} order (red, $D_{\mathrm{avg}} = 14.94$ dB), approximation by the static framework 11^{th} order (cyan, $D_{\mathrm{avg}} = 20.26$ dB).

3.3 Filter Design with Approximation Methods

3.3.1 Requirements on the Approximation Methods

The approximation of the ADSC filter by a cascade of biquad filters achieves good results regarding the attenuation but has the disadvantage of a time-consuming manual design which has to be performed for each prototype individually. This makes it impracticable for general use in hearing aids. Hence, an optimization method is used, which approximates the frequency response of a measured compensation filter with an IIR filter automatically. The requirements on the approximation methods are, beside the fulfillment of the criteria introduced in Section 3.1,

- stable filter design
- no individual preprocessing
- selectable filter order

In the following section an overview about IIR filter approximation methods is given, that fit a prescribed frequency response. Furthermore, the procedure of the approximation method used in this thesis is presented.

3.3.2 Methods overview

A common method to approximate a filter to a desired frequency response is the minimization of the sum of squared errors in the least-squares sense [48]. The error is the difference between the desired frequency response $H_{\mathrm{COMP}}(j\omega)$ and the estimated frequency response $\hat{H}_{\mathrm{COMP}}(j\omega)$ resulting from the IIR coefficients. This error is called output error E_{OE} and the minimization of its cost function for an ideally white noise input, i.e. $X(j\omega) = 1$, is defined by

$$\min \epsilon_{\mathrm{OE}} = \sum_{k=0}^{K-1} |E_{\mathrm{OE}}(j\omega_k)|^2 = \sum_{k=0}^{K-1} \left| H_{\mathrm{COMP}}(j\omega_k) - \hat{H}_{\mathrm{COMP}}(j\omega_k) \right|^2 \tag{3.2}$$

where $\hat{H}_{\mathrm{COMP}}$ is an IIR filter

$$\hat{H}_{\mathrm{COMP}}(j\omega_k) = \frac{\hat{B}(j\omega_k)}{\hat{A}(j\omega_k)} = \frac{\sum\limits_{m=0}^{M} \hat{b}_m \mathrm{e}^{-j\omega_k \cdot m}}{\sum\limits_{l=0}^{L} \hat{a}_l \mathrm{e}^{-j\omega_k \cdot l}} \tag{3.3}$$

and $\omega_k = 2\pi \frac{k}{K}$ are the discrete normalized frequency points at $k = 0, 1, \ldots, K-1$, $K > M+L+1$.

Fig. 3.5 shows the general structure of the output error with the input $x[n]$, the output $y[n]$ of the desired filter $H(j\omega)$ and the output $\hat{y}[n]$ of the approximated filter $\hat{H}(j\omega) = \frac{\hat{B}(j\omega)}{\hat{A}(j\omega)}$.

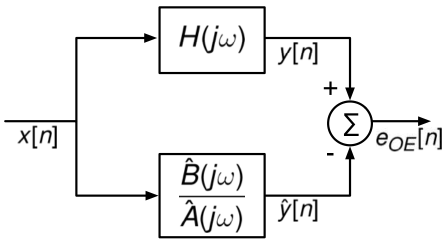

Figure 3.5: Structure of the output error [49]

The design of an IIR filter, which minimizes Eq. (3.2), can be done in the time-domain based on the impulse response $h_{\mathrm{COMP}}[n]$ as well as in the frequency-domain based on the corresponding frequency response $H_{\mathrm{COMP}}(j\omega)$.

Several studies discuss the approximation of a finite impulse response by IIR coefficients [50–55]. Since the compensation filter is calculated from the measured transfer function of the REOG and the PLANT, respectively, one has first to estimate a valid representation of the filter in the time-domain by a finite impulse response $h_{\mathrm{COMP}}[n]$, which can be done e.g. by frequency sampling [56]. The resulting FIR $h_{\mathrm{COMP}}[n]$ is then approximated by approximation algorithms such as the state-space model reduction techniques [53] or least squares approximation methods [50], in order to get an IIR filter. The resulting frequency response $\hat{H}_{\mathrm{COMP}}(j\omega)$ of the IIR filter depends both on the accuracy of the method that yields $h_{\mathrm{COMP}}[n]$ and on the approximation algorithm, which calculates the filter coefficients. Since this procedure has two approximation steps which increase the complexity and may induce errors, the time-domain methods are not further analyzed in this work.

Different methods have been developed which are aimed at calculating IIR coefficients directly from the complex frequency response H_{COMP}. Since $\hat{H}_{\mathrm{COMP}}(j\omega)$ is non-linearly related to the IIR coefficients $\hat{\underline{b}}$ and $\hat{\underline{a}}$, Eq. (3.2) is a non-linear optimization problem [57]. This can either be solved by linearizing the output error equation and then using common linear optimization methods or by applying non-linear optimization techniques.

Levy's method One of the earliest approach of frequency response fitting was developed by Levy in 1959 [58], who linearized Eq. (3.2) to

$$\min_{\hat{\underline{b}},\hat{\underline{a}}} \epsilon_{\mathrm{EE}} = \sum_{k=0}^{K-1} \left|\hat{A}(j\omega_k)E_{\mathrm{OE}}(j\omega_k)\right|^2 = \sum_{k=0}^{K-1} \left|\hat{A}(j\omega_k)H_{\mathrm{COMP}}(j\omega_k) - \hat{B}(j\omega_k)\right|^2 \tag{3.4}$$

Eq. (3.4) minimizes a weighted version of the output error, which is called equation error E_{EE} . Appendix B.1 outlines the minimization of the equation error in regard of the filter coefficients $\hat{\underline{b}}$ and $\hat{\underline{a}}$. Since the roots of $\hat{A}(j\omega_k)$ are the poles of $\hat{H}_{\mathrm{COMP}}(j\omega)$, the output error is weighted less near the poles. According to [59, Section 22.4], this deteriorates the resulting frequency response $\hat{H}_{\mathrm{COMP}}(j\omega)$ in particular near the poles of $H_{\mathrm{COMP}}(j\omega)$. Furthermore, the estimated filter coefficients may yield unstable impulse responses, since no constraints were formulated so far on the algorithm. However, the stability of the filter must be given in order to use it with the ADSC system. This can be enforced by flipping all poles which lie outside the unit circle, i.e. $p > |1|$, back into the unit circle by their reciprocals, which has no influence on the magnitude response but alters the phase response and thus reduces the attenuation.

SK method Sanathanan and Koerner [60] derived an iterative method (SK method) which weights the equation error with the denominator of the previous iteration, such that

$$\begin{aligned}\min_{\hat{\underline{b}},\hat{\underline{a}}} \epsilon_{\mathrm{SK}}^{(i)} &= \sum_{k=0}^{K-1} W_{\mathrm{SK}}^{(i)} \left|\hat{A}^{(i)}(j\omega_k)E_{\mathrm{OE}}^{(i)}(j\omega_k)\right|^2 = \\ &= \sum_{k=0}^{K-1} \frac{1}{\left|\hat{A}^{(i-1)}(j\omega_k)\right|^2} \left|\hat{A}^{(i)}(j\omega_k)H_{\mathrm{COMP}}(j\omega_k) - \hat{B}^{(i)}(j\omega_k)\right|^2\end{aligned} \tag{3.5}$$

where $\epsilon_{\mathrm{SK}}^{(i)}$ is the sum squared error of the i^{th} iteration. The influence of $\hat{A}(j\omega_k)$ on the error in Eq. (3.4) is reduced by weighting it with the denominator of the previous iteration, i.e. $W_{\mathrm{SK}}(j\omega) = \frac{1}{\left|\hat{A}^{(i-1)}(j\omega_k)\right|^2}$. Therefore, the SK method has to be initialized with an estimate of the denominator, which can be done by solving the equation error at the beginning. This method corresponds to the time domain algorithm developed by Steiglitz and McBride in [61], which is implemented by the MATLAB® function `stmcb.m`.

Vector fitting method A different iterative method which estimates the IIR coefficients in the frequency domain is called vector fitting and was originally developed to model electromagnetic transients, which occur e.g. in transmission lines [62]. The basic idea is to approximate the desired frequency response by partial fraction decomposition, such that

$$\hat{H}(j\omega) = \left(\sum_{n=1}^{N} \frac{c_n}{\mathrm{e}^{-j\omega} - p_n}\right) + d \tag{3.6}$$

where $\hat{H}(j\omega)$ is the approximated frequency response, c_n and p_n are the residues and the poles, respectively, which are either real or complex conjugate pairs, and d is a real number. By introducing a scaling function $\sigma(j\omega)$, whose zeros are the poles of the desired frequency response $H(j\omega)$, the non-linear equation Eq. (3.2) can be written as a linear equation:

$$\underbrace{H(j\omega)\cdot\left(\frac{\gamma_1^{(i)}}{\mathrm{e}^{-j\omega}-\rho_1^{(i)}}+\dots+\frac{\gamma_N^{(i)}}{\mathrm{e}^{-j\omega}-\rho_N^{(i)}}+1\right)}_{\sigma(j\omega)} \approx \underbrace{\frac{c_1^{(i)}}{\mathrm{e}^{-j\omega}-\rho_1^{(i)}}+\dots+\frac{c_N^{(i)}}{\mathrm{e}^{-j\omega}-\rho_N^{(i)}}+d^{(i)}}_{(\sigma\cdot H)(j\omega)} \quad (3.7)$$

where ρ are the poles of $\sigma(j\omega)$. Eq. (3.7) can be solved for $H(j\omega)$ according to [63]

$$H(j\omega) \approx \frac{c_1^{(i)}}{\mathrm{e}^{-j\omega}-\rho_1^{(i)}}+\dots+\frac{c_N^{(i)}}{\mathrm{e}^{-j\omega}-\rho_N^{(i)}}+d^{(i)}-\frac{\gamma_1^{(i)}\cdot H(j\omega)}{\mathrm{e}^{-j\omega}-\rho_1^{(i)}}-\dots-\frac{\gamma_N^{(i)}\cdot H(j\omega)}{\mathrm{e}^{-j\omega}-\rho_N^{(i)}} \quad (3.8)$$

and written in vector/Matrix notation yields

$$\mathbf{\Lambda}^{(i)}\underline{\hat{\zeta}}^{(i)} = \underline{H} \quad (3.9)$$

with

$$\begin{aligned}
\underline{H} &= \begin{bmatrix} H(j\omega_0) & H(j\omega_1) & \cdots & H(j\omega_{K-1}) \end{bmatrix}^\top \\
\mathbf{\Lambda}^{(i)} &= \begin{bmatrix} \underline{\Lambda}_0^{(i)} & \underline{\Lambda}_1^{(i)} & \cdots & \underline{\Lambda}_{K-1}^{(i)} \end{bmatrix}^\top \\
\underline{\Lambda}_k^{(i)} &= \begin{bmatrix} \frac{1}{\mathrm{e}^{-j\omega_k}-\rho_1^{(i)}} & \cdots & \frac{1}{\mathrm{e}^{-j\omega_k}-\rho_N^{(i)}} & 1 & \frac{-H(j\omega_k)}{\mathrm{e}^{-j\omega_k}-\rho_1^{(i)}} & \cdots & \frac{-H(j\omega_k)}{\mathrm{e}^{-j\omega}-\rho_N^{(i)}} \end{bmatrix}^\top \\
\underline{\hat{\zeta}}^{(i)} &= \begin{bmatrix} c_1^{(i)} & \cdots & c_N^{(i)} & d & \gamma_1^{(i)} & \cdots & \gamma_N^{(i)} \end{bmatrix}^\top
\end{aligned} \quad (3.10)$$

Eq. (3.9) is solved in each iteration for $\underline{\hat{\zeta}}^{(i)}$. From this the estimated zeros of $\sigma(j\omega)$ at the i^{th} iteration can be calculated, which are then used as new poles, i.e. $\rho_n^{(i+1)}$, for the next iteration as outlined in [62]. An implementation of the algorithm in MATLAB® is given by Gustavsen [64, 65]. Similar to the SK method, the vector fitting method has to be initialized with an estimate of the poles ρ_n, which has a strong influence on the outcomes. Furthermore, since the algorithm calculates constants c_n and poles p_n instead of filter coefficients $\underline{\hat{b}}$ and $\underline{\hat{a}}$, the conversion may be subjected to numerical errors and yield an unstable impulse response.

Simulations of this method with the ADSC application showed that the outcome has strong variations in regard of the attenuation performance for different prototypes. Moreover, the resulting frequency responses have often sharp resonances in particular at high frequencies, which infringe the requirements on the compensation filter. The peaks are annoying for the user and may further cause feedback under real conditions, thus the vector fitting method was discarded for this application.

Gauss-Newton method The approximation algorithm used in this thesis is called Gauss-Newton method, which fits a prescribed magnitude and phase response by iteratively minimizing the output error. The algorithm is discussed in several works [57, 66–70] and outlined in Appendix B.2. By approaching the estimated frequency response of the IIR filter $\hat{H}_{\mathrm{COMP}}(j\omega)$ with a first-order Taylor series, the algorithm performs a linearization of Eq. (3.2) and the quadratic output equation at the i^{th} iteration can be rewritten to

$$\begin{aligned}
\min_{\underline{\hat{\delta}}^{(i)}} \epsilon_{\text{OE}} &= \sum_{k=0}^{K-1} \left| E_{\text{OE}}(j\omega_k, \underline{\hat{\theta}}) \right|^2 = \sum_{k=0}^{K-1} \left| H_{\text{COMP}}(j\omega_k) - \hat{H}_{\text{COMP}}(j\omega_k, \underline{\hat{\theta}}) \right|^2 \approx \\
&\approx \sum_{k=0}^{K-1} \left| H_{\text{COMP}}(j\omega_k) - \hat{H}_{\text{COMP}}(j\omega_k, \underline{\hat{\theta}}^{(i)}) - \nabla_{\underline{\hat{\theta}}}^{\top} \hat{H}_{\text{COMP}}(j\omega_k, \underline{\hat{\theta}}^{(i)}) \cdot \underline{\hat{\delta}}^{(i)} \right|^2 = \\
&= \sum_{k=0}^{K-1} \left| E_{\text{OE}}(j\omega_k, \underline{\hat{\theta}}^{(i)}) - \nabla_{\underline{\hat{\theta}}}^{\top} \hat{H}_{\text{COMP}}(j\omega_k, \underline{\hat{\theta}}^{(i)}) \cdot \underline{\hat{\delta}}^{(i)} \right|^2
\end{aligned} \tag{3.11}$$

where $\underline{\hat{\theta}}$ is the estimated coefficient vector

$$\underline{\hat{\theta}} = \begin{bmatrix} \hat{a}_1 & \hat{a}_2 & \cdots & \hat{a}_L & \hat{b}_0 & \hat{b}_1 & \cdots & \hat{b}_M \end{bmatrix}^{\top}, \tag{3.12}$$

$E_{\text{OE}}(j\omega_k, \underline{\hat{\theta}}^{(i)})$ is the output error, $\nabla_{\underline{\hat{\theta}}}^{\top} \hat{H}_{\text{COMP}}(j\omega_k, \underline{\hat{\theta}}^{(i)})$ is the gradient of the estimated filter evaluated at $\underline{\hat{\theta}} = \underline{\hat{\theta}}^{(i)}$ and $\underline{\hat{\delta}}^{(i)} = \underline{\hat{\theta}} - \underline{\hat{\theta}}^{(i)}$ is the update vector of the i^{th} iteration [57].

Eq. (3.11) is solved at each iteration for $\underline{\hat{\delta}}^{(i)}$, from which follows the new coefficient vector

$$\underline{\hat{\theta}}^{(i+1)} = \underline{\hat{\theta}}^{(i)} + \mu \underline{\hat{\delta}}^{(i)} \tag{3.13}$$

where μ is the step size.

In order to ensure stability, the poles of $\hat{H}_{\text{COMP}}(j\omega)$ must be calculated in each iteration and for any $p > |1|$ flipped back into the unit circle.

As it is shown in Fig. 3.4 the results of the Gauss-Newton method allow a significant broad band attenuation which can be achieved for all tested prototypes (see Chapter 5).

For the sake of completeness, it should be mentioned that there are several other methods to solve the non-linear equation Eq. (3.2) such as heuristic methods to which the evolutionary algorithms belong. Teixeira and Romariz [71] discuss the use of simulated annealing, genetic algorithm and particle swarm optimization for digital filter approximation and Martinek and Tichá [72] outline the differential evolutionary algorithm. A big disadvantage of this algorithms, however, is their complexity and the computational cost, which is why they were not further investigated in this work.

In summary, several different methods are available to approximate a predefined magnitude and phase response in the frequency domain. A comprising comparison of different approximation algorithms in the frequency domain is presented in [73]. For this thesis the Gauss-Newton method is chosen, as a functional implementation of the algorithm is already available in MATLAB® (`invfreqz.m`), which achieves good results for the tested ITE prototypes. However, further research has to be done in order to find the best algorithm for this specific application.

3.3.3 Procedure of the Gauss Newton Method

The implementation of the Gauss-Newton method is realized by the MATLAB® function `invfreqz.m`, which can be divided into two sections: an initialization section and an iterative section, which incorporates two loops in order to minimize the output error.

The initialization section is necessary for the algorithm, since the Gauss-Newton method needs an initial coefficient vector $\underline{\hat{\theta}}^{(0)}$. This is obtained by solving the equation error in the least square sense for $\underline{\hat{\theta}}_{\mathrm{EE}}$ (see Appendix B.1). To ensure stability of the computed filter, the roots of the denominator polynomial are calculated and for any $p > |1|$ flipped back into the unit circle. The altered coefficient vector $\underline{\tilde{\theta}}_{\mathrm{EE}}$ is used to calculate the gradient as well as the output error of the 0^{th} iteration. By solving Eq. (3.11) one gets $\underline{\hat{\delta}}^{(0)}$.

The iterative section has an outer loop, which calculates the search direction, i.e. the update vector $\underline{\hat{\delta}}^{(i)}$. The inner loop searches along this direction until the sum squared error $\epsilon_{\mathrm{OE}}^{(i+1)}$ is smaller than the previous one, whereby the step size is reduced in each iteration j according to

$$\mu^{(j+1)} = \frac{1}{2^j}$$

where $j = 0, 1, \ldots, J$ is the counter of the inner loop. Once the sum squared error is reduced, the algorithm jumps back to the outer loop and computes the gradient and output error based on the new coefficient vector of the next iteration.

In order to get a stable filter, it is guaranteed for each new coefficient vector that the roots of the denominator polynomial lie within the unit circle. The algorithm terminates once either the inner or the outer loop reach their maximum iterations or the norm of the update vector $\underline{\hat{\delta}}^{(i)}$ falls below a defined threshold ζ.

The procedure can be summarized by the following listing:

1. Initialize the algorithm: set $i = 0$
   - i Compute initial coefficient vector $\underline{\hat{\theta}}_{\mathrm{EE}}$ by minimizing the equation error
   - ii Enforce stability $\rightarrow \underline{\tilde{\theta}}_{\mathrm{EE}}$
   - iii Set $\underline{\hat{\theta}}^{(0)} = \underline{\tilde{\theta}}_{\mathrm{EE}}$
2. Compute $\nabla_{\underline{\hat{\theta}}}^{\top} \hat{H}_{\mathrm{COMP}}(j\omega, \underline{\hat{\theta}}^{(i)})$ and $E_{\mathrm{OE}}(j\omega, \underline{\hat{\theta}}^{(i)})$
3. Solve the quadratic minimization output error for $\underline{\hat{\delta}}^{(i)}$.

   `if` $\|\underline{\hat{\delta}}^{(i)}\|_2 \leq \zeta$ or $\epsilon_{\mathrm{OE}}^{(i)} > \epsilon_{\mathrm{OE}}^{(i-1)} \rightarrow$ `end`
4. Set $j = 0$
   - I `if` $j < J \rightarrow$ set step size to $\mu = \frac{1}{2^j}$
     `otherwise` $\rightarrow$ end
   - II Compute new coefficient vector: $\underline{\hat{\theta}}^{(i+1)} = \underline{\hat{\theta}}^{(i)} + \mu \underline{\hat{\delta}}^{(i)}$
   - III Enforce stability $\rightarrow \underline{\tilde{\theta}}^{(i+1)}$
   - IV Compute new sum squared error $\epsilon_{\mathrm{OE}}^{(i+1)}$ based on $\underline{\tilde{\theta}}^{(i+1)}$
   - V `if` $\epsilon_{\mathrm{OE}}^{(i+1)} < \epsilon_{\mathrm{OE}}^{(i)} \rightarrow$ set $\underline{\hat{\theta}}^{(i+1)} = \underline{\tilde{\theta}}^{(i+1)}$ and `go to` 5.
     `otherwise` $j = j + 1 \rightarrow$ `go back to` 4.I
5. Set $i = i + 1$.
   `if` $i > i_{max} \rightarrow$ `end`
   `otherwise` $\rightarrow$ `go back to` 2.

3.4 Static Filter Approximation Framework

The static filter approximation framework calls several functions in order to determine a bounded compensation filter $\tilde{H}_{\mathrm{COMP}}(j\omega)$ from the measured transfer functions $\tilde{H}_{\mathrm{REOG}}(j\omega)$ and $\hat{H}_{\mathrm{PLANT}}(j\omega)$. The outcome of the framework is designed such that it can be used with a Simulink® Model for the static ADSC system on the RTS. As input parameters the framework requires the measurements of the REOG and the PLANT conducted with the Simulink® Model `MeasureTF.mdl`, which are loaded by the function `LoadMeasurement.m`. The framework itself is called by the function `staticFrameWork.m`.

3.4.1 Overview

The static ADSC framework can be divided in five sections. The initial section pre-processes the recorded transfer function according to Section 2.2.3, i.e. the low frequencies of the PLANT are extrapolated and its phase is reconstructed by the Hilbert transformation implemented in `extrapol.m`. The frequency range which is used for the extrapolation has to be defined by the user according to the measurement.

The second section deals with the limitation of the low frequencies in order to enable a stable filter design and to handle the distortion problems of the receiver. The alteration of the calculated compensation filter by the limitation filter $H_{\mathrm{HP}}(j\omega)$ and its influence on the ADSC performance is presented in Section 3.4.2.

In the third section two biquad filters with the overall frequency response $H_{\mathrm{preEQ}}(j\omega)$ are designed, which are used to pre-equalize the target compensation filter such that the approximation algorithm finds better results. These filters improve the performance of the static ADSC filter considerably and are outlined in detail in Section 3.4.3.

In the fourth section of the framework the actual computation of the IIR coefficients takes place. The approximation algorithm is called by the function `my_invfreqz.m`, which is an extended version of the original MATLAB® function `invfreqz.m`, that allows, if requested, also the calculation of the minimum phase IIR coefficients. Furthermore, the termination conditions were adapted such that the algorithm iterates as long as the sum squared output error gets smaller at each iteration. The pre-equalized and low frequency bounded compensation filter acts as the target filter, i.e.

$$\hat{H}(j\omega) = \frac{\hat{H}_{\mathrm{COMP}}(j\omega) \cdot H_{\mathrm{HP}}(j\omega)}{H_{\mathrm{preEQ}}(j\omega)} = \frac{\tilde{H}_{\mathrm{COMP}}(j\omega)}{H_{\mathrm{preEQ}}(j\omega)}, \tag{3.14}$$

which is approximated for $N = 2, \ldots, 20$. N is the IIR filter order where the upper limit is chosen according to the “Palio 3”platform.

In the last section the performance of 19 different estimated IIR filters is validated. The average attenuation and its centroid, the bandwidth, the maximal overshoot at low and high frequencies as well as the maximal gain are calculated. With this, the user has the possibility to compare the outcomes and to choose the best IIR filter depending on the requirements of the application, e.g. maximal attenuation bandwidth or high SPL values. The calculation of the performance parameters is explained in Section 3.4.4.

The output of the static ADSC framework is saved by calling the function `saveFilter.m`, which generates a .mat-file that can be used directly with the static ADSC Simulink® model.

3.4.2 Low Frequency Limitation

The limitation of the calculated compensation filter is essential for the applicability of the ADSC system under real conditions. On the one hand, it enables the approximation algorithm to achieve valuable coefficients and on the other hand it determines the maximum sound pressure level of the ambient sound with a given spectral shape at which the system works distortion-free regarding the perceived sound quality. The limitation of the maximum gain, thought, affects unfortunately also the phase of the compensation filter, which is why one has to trade off between the maximal allowed input SPL and the bandwidth of the attenuation.

An ideal limiter would bound the amplification of the compensation filter at low frequencies to a defined maximum gain without deteriorating the attenuation performance of the ADSC system outside the limitation. Since the attenuation at the bounded frequency range drops to 0 dB due to the negative magnitude deviation of the desired response, the phase can be aleatoric, there. This would enable the approximation algorithm to fit just the magnitude in the limitation range and generate a phase which yields the best attenuation results for all other frequencies above. The used implementation of the Gauss-Newton method, however, does not allow to fit the magnitude and phase separately. Lang presented in [57] an independent weighting of the magnitude and phase errors used to approximate low-pass filters, which was not analyzed in this work for reasons of time.

Fitting the bounded compensation filter, whose magnitude is limited to the maximum gain at low frequencies (hard limitation) without changing the original phase, yields improper results as depicted in Fig. 3.6 (*red*), since the relation between the phase and the magnitude at the limited frequencies is no longer existent.

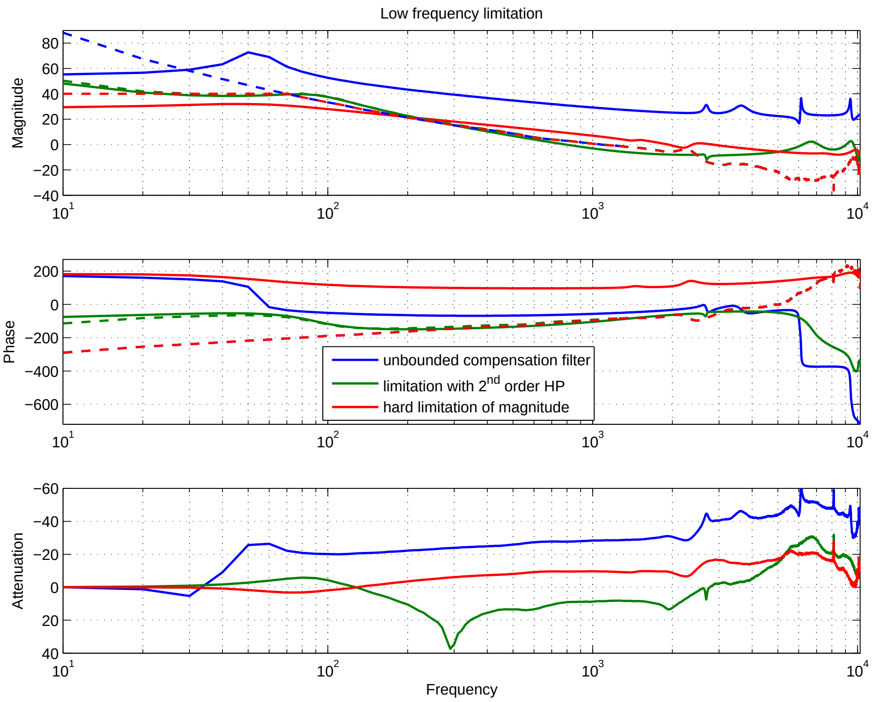

Figure 3.6: Limitation of the low frequencies: calculated compensation filter $H_{\mathrm{COMP}}(j\omega)$ (blue), approximation of the compensation filter bounded by a 2^{nd} order high-pass (green) and bounded by a hard limitation of the magnitude (red). The dashed lines denote the target responses, which are approximated by a 12^{th} order IIR-filter with the Gauss-Newton algorithm.

Therefore, a 2^{nd} order high-pass filter is used as limiter, since it bounds the approximately 2^{nd} order increase of the compensation filter towards low frequencies (see Section 2.1.3). This enables the use of the Gauss-Newton algorithm in order to get a more suitable approximation of the bounded compensation filter compared to the unbounded (see Fig. 3.6 *green* and *blue*, respectively). The high-pass filter does not only constrain the low frequencies adequately but also has the advantage that its phase influence on the original compensation filter can be controlled by changing the quality factor of the filter, which affects directly the bandwidth of the attenuation.

One of the formulated requirements on the compensation filter implies that the SPL of the residual signal $e_{\text{ac}}(t)$ at the ear drum must be lower than the SPL of the ambient signal $a(t)$ in front of the ear. This implicates that the limiting 2^{nd} order high-pass filter must be over- or critically damped, such that it has no overshoot. However, this is adverse for the attenuation of the ADSC system, since the bandwidth of the attenuation gets narrower. Increasing the quality factor q, such that the high-pass becomes underdamped, implies an infringement of the mentioned constraint, but enhances the performance of the bounded compensation filter. Since the overshoot is limited to a narrow range at low frequencies and becomes further only perceivable, if the ambient signal has enough energy there, it is worth to relax the constraint rather than discard the improvement of the attenuation bandwidth.

Fig. 3.7 shows the relationship between the overshoot and the phase of a 2^{nd} order high-pass filter as well as the influence on the attenuation. The trade-off between the overshoot and the bandwidth attenuation is clearly visible and can be formulated as: the higher the overshoot, the broader the attenuation bandwidth. This is, however, only valid, if the compensation filter increases exactly with 2^{nd} order towards low frequencies.

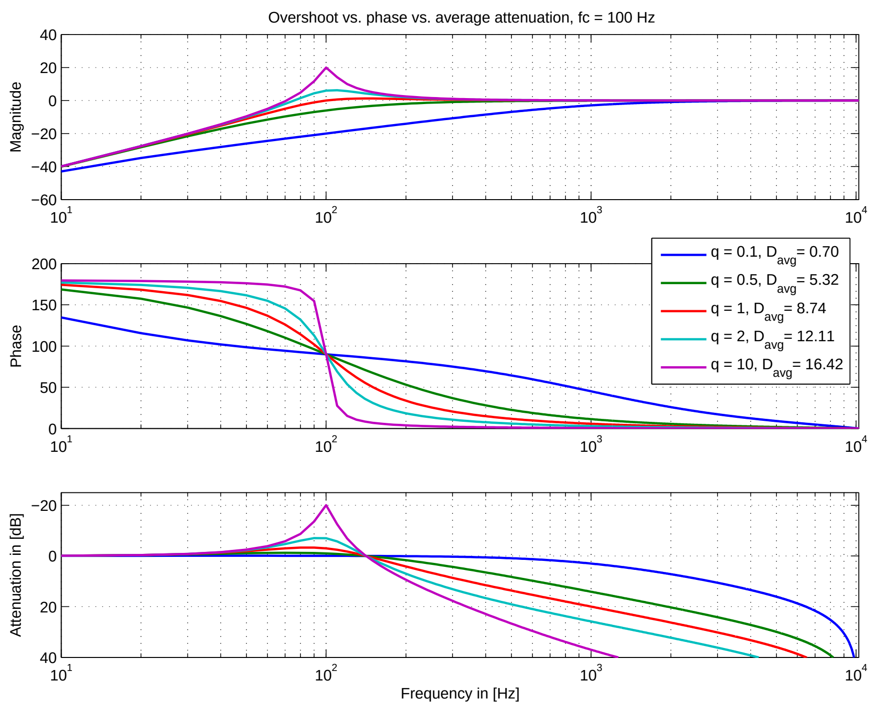

Figure 3.7: 2^{nd} order high-pass filter with cut-off frequency $f_{\text{c}} = 100$ Hz and varying quality factor q between 0.1 *and* 10

The quality factor q influences also the cut-off frequency f_c of the limiting high-pass filter. Since the maximum gain must not be surpassed by the compensation filter at all, an overshoot of the high-pass filter implies also a higher cut-off frequency. This is done numerically by the function `lowlimit1.m`. The function finds the best cut-off frequency f_c and quality factor q such that the resulting compensation filter remains within the defined limits and the attenuation bandwidth is maximal. The resulting compensation filter for a maximal gain of 40 dB and varying maximal overshoot is shown in Fig. 3.8.

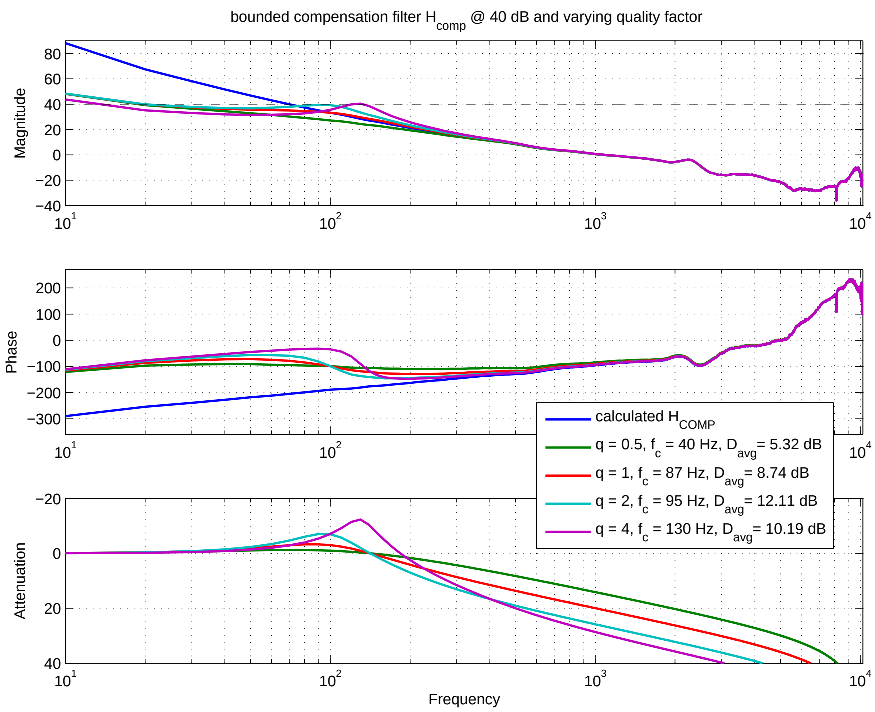

Figure 3.8: Bounded compensation filter $H_{\mathrm{COMP}}(j\omega)$ with maximum amplification gain of 40 dB and varying quality factor q between 0.5 and 4

It can be seen in Fig. 3.8, that the requested limits are satisfied but the magnitude of the frequency response still increases at the lowest frequencies. This is due to the fact that the combination of the receiver response, the ventloss and the microphone response has not exactly a 2^{nd} order roll-off but vary with the used transducer and the vent (see Fig. 2.13). Using a 3^{rd} order high-pass filter would ensure the limit at low frequencies but also deteriorate even more the attenuation, since the phase deviation increases with each order. Nevertheless, the results with the RTS for the different prototypes showed that the 2^{nd} order filters bound the compensation filter sufficiently in order to use the ADSC system in noisy environments with a broad attenuation (see Chapter 5).

It should be mentioned that the attenuation depicted in the lowest plot of Fig. 3.8 is the maximal achievable attenuation, if the bounded compensation filter is exactly approximated. The outcomes of the Gauss Newton method, however, showed that the algorithm does not find an accurate approximation and the attenuation varies heavily depending on the ITE prototype and vent size. Hence, the bounded compensation filter must be pre-processed such that the algorithm outputs usable results for the direct sound attenuation for all prototypes and vent sizes.

3.4.3 Pre-equalization of H_{COMP}

The pre-processing of the bounded compensation by an approximation of the inverse PLANT originates from the idea that the algorithm identifies accurately the REOG in contrast to the inverse PLANT. Hence, modeling the main characteristics of the latter, which is the low frequency roll-off and the negative constant group delay, with a fix pre-equalization filter improves the results of the approximation algorithm and reduces the variations on the attenuation between different prototypes and vent sizes.

In Section 3.2 the low frequency slope of the compensation filter was approximated with a cascade of two second order lag filters. By pre-equalizing the bounded compensation filter with the inverse of the approximated low frequency slope, the filter dynamic caused mainly by the inverse ventloss is reduced. Since the general shape of the compensation filter remains similar even between different prototypes and vent sizes, one can design an universal 2$^{\mathrm{nd}}$ order lag filter, whose inverse reshapes the bounded compensation filter favorably with respect to the approximation algorithm.

Adding a boost filter with a resonance frequency near f_{Nyquist} and a broad peak bandwidth to the pre-equalization lag filter, compensates in a limited range the negative constant group delay of the inverse PLANT and improves even more the output of the approximation algorithm. The altered compensation filter, which has to be approximated by the algorithm, computes to

$$\hat{H}(j\omega) = \frac{\hat{H}_{\mathrm{COMP}}(j\omega)}{H_{\mathrm{preEQ}}(j\omega)} = \frac{\hat{H}_{\mathrm{COMP}}(j\omega)}{H_{\mathrm{lag}}(j\omega) \cdot H_{\mathrm{boost}}(j\omega)} \tag{3.15}$$

Since the negative constant group delay arises from erroneous interpretation of the PLANT measurements, it may vary between different transducer models, which would implicate an adjustment of the boost filter. In this thesis, however, the boost filter is kept constant, because the built in transducer of the prototypes are similar.

Fig. 3.9 shows the influence of the pre-equalization filter H_{preEQ} (*black, dashed*), which is used for the calculations of the IIR coefficients in this work. The bounded version of two different ITE prototype compensation filters with different vent sizes (*blue* and *green*) are approximated by the algorithm with and without pre-equalization. It can be seen that the approximation without pre-equalizer yields a high deviation of the predicted attenuation (*blue, dashed* and *green, dashed*): while the filter of the bigger vent (*red*) is still suitable for direct sound cancellation, the filter of the smaller vent (*cyan*) is unusable.

On the contrary, the approximation of the pre-equalized compensation filters yields good results for both cases (*magenta* and *yellow*). The algorithm approximates the prescribed frequency response for the pre-equalized case much more accurately, such that the achieved attenuation is closed to the theoretical one, which is defined, according to Section 3.4.2, by the limiting high-pass filter H_{HP} and depicted in the lowest plot (*dashed* lines). The pre-equalization is therefore necessary in order to achieve consistently valuable IIR coefficients for different ITE prototypes and vent sizes.

Further analysis and measurements have to be made to develop a pre-equalization filter, which is optimal for the use with different vent sizes and ITE prototypes and fulfills the requirements of Section 3.1.

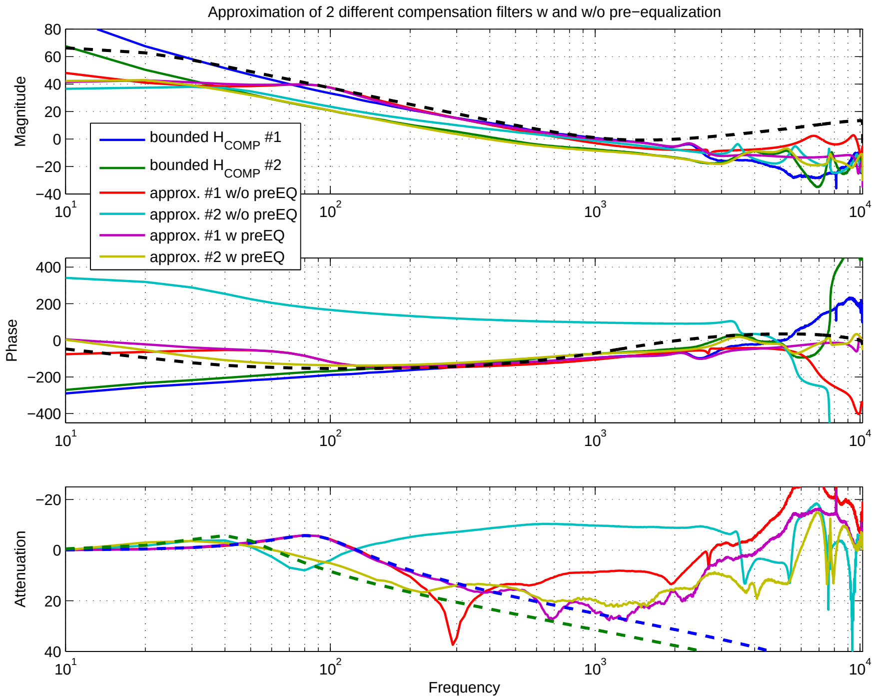

Figure 3.9: Approximation of 2 different compensation filters (blue and green): 12^{th} order IIR filter without pre-equalization (red and cyan), 12^{th} order IIR filter with pre-equalization (magenta and yellow). The pre-equalization filter is depicted as black, dashed line.

3.4.4 Filter Validation

The validation of the computed IIR filters is done by the function `FilterVal.m`. Six different measures are calculated for each filter and used to rate it according to its performance. Above all, the function verifies if the requirements on the compensation filter are satisfied. These are the maximum gain and overshoot at low frequencies and the maximum overshoot at high frequencies.

Additionally, parameters which describe the attenuation of the filters are computed: the average attenuation, the centroid and the bandwidth. In order to consider the human auditory perception, the average attenuation and its centroid are calculated on a logarithmic instead of a linear spaced frequency axis.

Maximum gain and overshoot at low frequencies The maximum gain of the filter is determined between 0 Hz and f_{low}, where f_{low} is the frequency at which the attenuation starts to be greater than 0 dB. This ensures, that a possible overshoot of the limitation filter is also considered in the calculations. The maximum overshoot is then computed by determining the maximum level of the attenuation resulting from the approximated filter in the same frequency range.

Maximum overshoot at high frequencies The maximum overshoot at high frequencies is calculated relatively to the measured REOG and a definable REAG which compensates the hearing loss of the patient. The overshoot is the difference between the sound pressure in front of the ear drum with and without the ADSC system enabled in dB. As long as the ADSC signal falls below the signal, which compensates the hearing loss, the overshoot is negative and the filter applicable.

Average attenuation The average attenuation D_{avg} is defined as the mean of the attenuation in dB, spaced on a logarithmic frequency axis. Therefore, the linearly space frequency bins are interpolated and the attenuation is calculated at the new frequencies. The lower and upper frequencies are fixed to 100 Hz and 1 kHz in order to compare the results between different prototypes and vent sizes.

Centroid This parameter denotes the frequency location of the centroid of the area, which is enclosed between the attenuation curve and the 0 dB axis between 100 Hz and 1 kHz. Therefore, the cumulative sum of the attenuation at the logarithmic spaced frequencies is calculated. The frequency, where the cumulative sum surpasses 50% is set as the centroid location. A low centroid frequency location implies a good attenuation at low frequencies, which is favorable in this application.

Bandwidth The frequency range, in which the attenuation is consistently greater than 10 dB, is defined as the attenuation bandwidth. The function searches the edges of this range and outputs the lowest and highest frequency.

The outcomes of the approximation algorithm show that the limits regarding the overshoot at low and high frequencies are in most cases satisfied, whereby the maximum gain is usually exceeded. The reason is that the 2^{nd} order high-pass filter does not limit the compensation filter adequately, thus its approximation is also most probably erroneous. This could be solve by increasing the order of the limitation filter $H_{\text{HP}}(j\omega)$, which in contrast would deteriorate the broad band attenuation.

The ideal IIR filter based on the introduced validation parameters must, on the one hand, fulfill the limiting requirements and, on the other hand, have a broad attenuation bandwidth together with a centroid located at low frequencies and a high average attenuation. This depends above all on the maximal allowed gain and overshoot at low frequencies, which has to be choose according to the built-in receiver.

4
Adaptive ADSC Filter Design

In many applications of active noise control, it is not feasible to use static filters for the attenuation of a specific signal at a desired location. The reason is that the acoustic environment can usually not be assumed as time-invariant, which implies that the primary and/or the secondary path change during the attenuation process. It is necessary to implement an algorithm in the system which tracks the changes and adapts the filter coefficients accordingly. This becomes more important the greater the changes are.

A major result of this work is the finding that with HIs the acoustic environment is not subject to strong variations, in particular for medium and big vent sizes as outlined in Section 2.3. Moreover, the major variations do not occur in general during the adaptation process but at the insertion of the earpiece into the ear canal. This signifies that a remeasurement of the transfer functions and the recalculation of static filter coefficients is sufficient to compensate the changes at each insertion.

Nevertheless, two adaptive methods were analyzed and implemented in this work in order to determine a possible improvement of the attenuation compared to the static approach. Identically to the static method, the computation of the destructive signal $z(t)$ must be done within the propagation time of the direct sound. This implies a time-domain realization of the filtering, independently of the applied adaptation algorithm. Therefore, either an adaptive FIR or an adaptive IIR filter must be used. Since adaptive IIR filters suffer from bad convergence, local minimum solutions and stability problems [69], only adaptive FIR structures were studied. Although it will not be feasible to implement them on the "Palio 3"embedded HI platform, since the required number of coefficients for an adequate attenuation is not available on it, a fundamental potential analysis of adaptive ADSC algorithms can be most easily done with FIR structures.

The requirements on the adaptive ADSC filter are equal to the static case, which were described in Section 3.1. A general adaptive block diagram for FF-ANC in hearing aids is depicted in Fig. 4.1.

In the following sections an overview of the adaptive filter structure used in this work is given and the two implemented approaches are outlined. The modifications made on the general adaptive structure in order to achieve feasible FIR coefficients for the attenuation of the direct sound in hearing aids are presented.

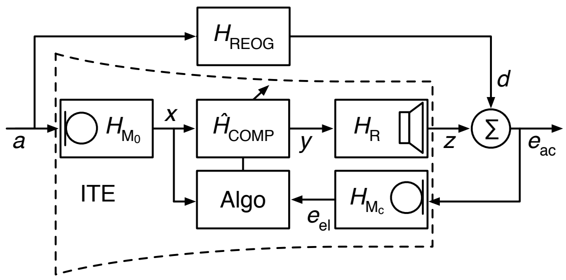

Figure 4.1: Block diagram of the adaptive ADSC system: $H_{\mathrm{REOG}}(j\omega)$ is the direct path, $H_{\mathrm{M}_0}(j\omega)$ is the frequency response of the outer microphone, $\hat{H}_{\mathrm{COMP}}(j\omega)$ is the adaptive compensation filter and H_{R} is the receiver response. a is the ambient sound in front of the ear, x is the recorded sound, y is the output of the filter and z is the sound pressure emitted by the receiver. The acoustic error signal e_{ac} vanishes if z is the phase inverted version of the direct sound d. e_{el} is the electric output of the canal microphone with frequency response $H_{\mathrm{M_c}}$, which is used for the adaptation process. The adaptation process in this work is performed by the LMS algorithm.

4.1 LMS algorithm for ADSC

The adaptive filter structure depicted in Fig. 4.1 differs mainly in one point from the general system identification structure (see [74, Section 1.2]): The adaptive filter must not only identify the unknown frequency response $H_{\mathrm{REOG}}(j\omega)$, but also compensate the frequency responses of the transducer $H_{\mathrm{M}_0}(j\omega)$, $H_{\mathrm{M_c}}(j\omega)$ and $H_{\mathrm{R}}(j\omega)$ in order to cancel the direct sound. While the frequency response of the outer microphone is detected and compensated by the algorithm using $x[n]$ as reference signal, the receiver and the canal microphone, i.e. the PLANT, are not “seen” by it and thus not compensated. Both change the output of the adaptive filter in magnitude and phase and bias the error signal which is used to estimate the filter coefficients. In consequence the algorithm does not find the desired frequency response. Hence, the adaptive structure has to be modified such that the algorithm “sees” the frequency response of the PLANT and converges to the desired filter

$$H_{\mathrm{COMP}}(j\omega) = -\frac{H_{\mathrm{REOG}}(j\omega)}{H_{\mathrm{M}_0}(j\omega) \cdot H_{\mathrm{R}}(j\omega)}$$

.

4.1.1 Inclusion of the PLANT - the FxLMS algorithm

In this work a specific form of the least mean squared (LMS) algorithm is used for the adaptation process. The general update equation of the LMS is, according to [74, Section 3.1.3], denoted by

$$\underline{\hat{h}}[n+1] = \underline{\hat{h}}[n] + \mu \underline{x}[n] e[n] \tag{4.1}$$

where $\underline{\hat{h}}[n]$ is the coefficient vector of the adaptive FIR filter at the sample time n and

$$e[n] = d[n] - \underline{\hat{h}}^T[n]\underline{x}[n] \tag{4.2}$$

is the error signal. $x[n]$ is the reference signal of the algorithm and also the input signal of the adaptive filter and μ is a weighting parameter called step size.
The update term of Eq. (4.1) is the instantaneous estimate of the gradient of the mean squared

error $\mathrm{E}\{e[n]^2\}$, i.e.

$$\nabla_{\underline{\hat{h}}[n]} J = \frac{\partial e^2[n]}{\partial \underline{\hat{h}}[n]} = -2\underline{x}[n]e[n] \tag{4.3}$$

The error signal of the adaptive ADSC system, however, differs from Eq. (4.2), since it is the acoustic superposition of the direct signal $d[n]$ and the receiver output $z[n]$ recorded by the canal microphone $\mathrm{M_c}$. Furthermore, the emitted signal $z[n]$ is an altered version of the adaptive filter output $y[n]$ due to the frequency response of the receiver. Thus, the error has to be rewritten as

$$\begin{aligned} e_{\mathrm{el}}[n] &= h_{\mathrm{M_c}} * e_{\mathrm{ac}}[n] = h_{\mathrm{M_c}} * (d[n] + z[n]) = h_{\mathrm{M_c}} * \Big(d[n] + h_{\mathrm{R}} * \Big(\hat{h}_{\mathrm{COMP}}[n] * x[n]\Big)\Big) = \\ &= \tilde{d}[n] + h_{\mathrm{PLANT}} * \Big(\hat{h}_{\mathrm{COMP}}[n] * x[n]\Big) \end{aligned} \tag{4.4}$$

The operator $(*)$ denotes the convolution of the signals and the respective IRs. $h_{\mathrm{M_c}}$, h_{R} and h_{PLANT} are the IRs of the canal microphone, the receiver with the secondary acoustic path included and the PLANT, respectively, and assumed to be linear and time-invariant. The time-varying IR of the adaptive filter is described by $\hat{h}_{\mathrm{COMP}}[n]$ at the time step n. The desired signal $\tilde{d}[n]$ filtered by the IR of the canal microphone is the recorded direct sound signal in the ear canal. The input signal $x[n]$ of the adaptive filter is the ambient signal $a[n]$ recorded by the outer microphone $\mathrm{M_0}$.

Using the error $e_{\mathrm{el}}[n]$ of the adaptive ADSC system for the computation of the instantaneous gradient according to Eq. (4.3) results in a biased version of the gradient and deteriorates or even inhibits the identification process of the desired filter response. This can be solved by using a reference signal, which is pre-filtered by the IR of the PLANT, i.e.

$$r[n] = \underline{h}_{\mathrm{PLANT}}^T \underline{x}[n] \tag{4.5}$$

This is valid if one assumes a nearly time-invariant adaptive filter $\hat{h}_{\mathrm{COMP}}[n]$, whose coefficients change slower than the impulse response decay time of the PLANT [75], which is given in this application. Then the sequence of the filters $\hat{h}_{\mathrm{COMP}}[n]$ and h_{PLANT} of Eq. (4.4) can be commuted which yields, according to [76, Section 3.4], approximately

$$\begin{aligned} e_{\mathrm{el}}[n] &\approx \tilde{d}[n] + \hat{h}_{\mathrm{COMP}}[n] * (h_{\mathrm{PLANT}} * x[n]) = \\ &= \tilde{d}[n] + \underline{\hat{h}}_{\mathrm{COMP}}^T[n]\underline{r}[n] \end{aligned} \tag{4.6}$$

Since the input signal $x[n]$ of the adaptive filter has to be filtered such that the algorithm identifies the coefficients correctly, this approach is called *filtered-x LMS* (FxLMS). The update equation in this specific application can now be formulated to

$$\underline{\hat{h}}_{\mathrm{COMP}}[n+1] = \underline{\hat{h}}_{\mathrm{COMP}}[n] - \mu \underline{r}[n] e_{\mathrm{el}}[n] \tag{4.7}$$

Fig. 4.2 shows the general ADSC structure used in this work. The recorded signal $x[n]$ is the input signal of the adaptive filter but has to be filtered by an estimate of the IR of the PLANT in order to be used as the reference signal of the LMS algorithm.

Different structures were developed, which compensate the effect of the PLANT on the adaptation process, such as a modified version of the depicted model [77], a lattice structure [78] or a filtered-error structure [76, Section 3.4.6]. Furthermore, different adaptation algorithms were

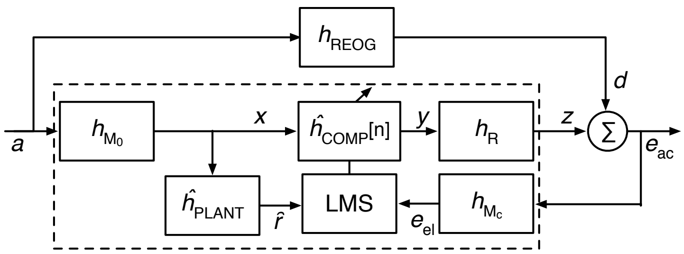

Figure 4.2: Block diagram of the FxLMS algorithm used in this thesis: h_{REOG} *is the IR of the primary path,* $h_{\mathrm{M_0}}$, h_{R} *and* $h_{\mathrm{M_c}}$ *are the IRs of the respective transducer.* $\hat{h}_{\mathrm{COMP}}[n]$ *is the time-variant adaptive filter and* $\hat{h}_{\mathrm{PLANT}}$ *is the estimated* PLANT

adapted to the ADSC application, including block processing techniques [79], averaging-based algorithms [80], recursive least square (RLS)-based algorithms (FxRLS) and Fast-Transversal-Filter algorithms (FxFTF) [77].

The adaptation process can be implemented both in the time- and in the frequency-domain, whereby the filtering itself must always be realized in real time with low delay for the application in hearing aids.

For the sake of completeness, it should be mentioned that for the adaptive IIR filter approach in ADSC applications the reference signal has also to be pre-filtered by the PLANT as outlined in [81]. A general overview of different IIR algorithms and their performance in system identification applications is given by Netto et al. in [69].

4.1.2 PLANT estimation

The pre-filtering of the reference signal by an estimate of the PLANT in order to identify the compensation filter $H_{\mathrm{COMP}}(j\omega)$ influences the stability and convergence characteristics of the adaptation algorithm. Estimation errors degrade the performance of the adaptation process and should therefore be avoided. The closer the estimation of the IR is to the real IR, the better is the performance of the algorithm and of the converged adaptive filter $\underline{\hat{h}}_{\mathrm{COMP}}^{(\infty)}$ regarding the attenuation of the direct sound $d[n]$.

The PLANT estimation can be done either off-line or on-line. The choice of the method depends on the application and the variations to which the PLANT is subjected.

In the off-line method the PLANT is estimated only when the adaptation process is paused. The estimation can be done either by an adaptive algorithm or by taking measurements as described in Section 2.2. In both cases any excitation signal can be used, which gives the possibility to achieve a high SNR and thus a high coherence over the entire frequency range. Furthermore, potential errors of the estimation can be fixed by post-processing the data. However, it is not possible to track any changes of the PLANT during the adaptation process, which in the worst case can yield an unstable adaptation process.

The on-line method estimates the PLANT during the adaptation process of the compensation filter. This is done by extending the ADSC structure of Fig. 4.2 with an additional adaptation process. This modified structure is known as *Eriksson's method* and was proposed first by Eriksson and Allie in [82]. The on-line methods can be divided into approaches which need an additional excitation signal and those which use only the residual signal [76, Section 3.6.2]. The former approaches have the advantage that the entire frequency range can be explicitly excited which is favorable for the PLANT estimation. However, if the additional excitation signal is not masked by the residual signal, it becomes audible and thus unfeasible for the application in hearing aids.

In this application the receiver emits not only the ADSC signal but also the HI-processed sound, which compensates a patient's hearing loss and can be used as excitation signal. Its drawback is the spectral shape which is adverse for an accurate estimation in particular at low frequencies, where the sound pressure in the ear canal decays due to the vented earpiece. In order to get a valid estimation over the entire frequency range it is inevitable to use an additional signal which excites explicitly the lower frequencies.

In this thesis the estimated PLANT is obtained from the measurements also used for the static ADSC filter design (see Section 2.2.3), since the variations in phase at each insertion are assumed to be considerably smaller than ±90°.

4.1.3 Step size and Stability of the FxLMS

According to [74, Section 3.2.3], the stability of the standard LMS algorithm is given by

$$0 < \mu < \frac{2}{\lambda_{\max}} = \mu_{\max} \tag{4.8}$$

where μ is the step size of the update equation (4.1) and $\lambda_{\max}$ is the greatest eigenvalue of the auto-correlation matrix of the reference signal, i.e. $\mathrm{E}\{\underline{x}[n]\underline{x}^T[n]\}$, which is positive definite assuming a broad band reference signal $x[n]$.
Assuming again slowly changing filter coefficients, the update equation (4.7) can be expanded to

$$\hat{\underline{h}}_{\mathrm{COMP}}[n+1] = \hat{\underline{h}}_{\mathrm{COMP}}[n] - \mu\left(\hat{\underline{r}}[n]\tilde{d}[n] + \hat{\underline{r}}[n]\underline{r}^T[n]\hat{\underline{h}}_{\mathrm{COMP}}[n]\right) \tag{4.9}$$

where $\hat{r}[n]$ is the input signal $x[n]$ filtered by an estimate of PLANT $\hat{h}_{\mathrm{PLANT}}$ and $r[n]$ is the reference signal filtered by the true PLANT h_{PLANT}.
For the converged adaptive filter $\hat{\underline{h}}^{(\infty)}_{\mathrm{COMP}}$ the update term of Eq. (4.9) vanishes and the coefficient vector is defined according to [76, Section 3.4] by

$$\hat{\underline{h}}^{(\infty)}_{\mathrm{COMP}} = -\mathrm{E}\{\hat{\underline{r}}[n]\underline{r}^T[n]\}^{-1}\,\mathrm{E}\left\{\hat{\underline{r}}[n]\tilde{d}[n]\right\} \tag{4.10}$$

where $\mathrm{E}\{\cdot\}$ denotes the expectation operator. Assuming a correct PLANT estimation, Eq. (4.10) gives the Wiener solution. The converged coefficient vector reaches only the optimal solution if the estimated PLANT is the true PLANT, i.e. $\hat{r}[n] = r[n]$. For that case the stability of the adaptation process is ensured as long as Eq. (4.8) is fulfilled, whereby $\lambda_{\max}$ is the maximal eigenvalue of the filtered auto-correlation matrix $\mathrm{E}\{\underline{r}[n]\underline{r}^T[n]\}$.

Morgan formulated in [83] a more general formula, which defines the stability limits of the FxLMS algorithm by

$$0 < \mu < \left(\frac{2\mathrm{Re}\{\lambda_i\}}{|\lambda_i|^2}\right)_{\min} = \mu_{\max} \tag{4.11}$$

where λ_i denotes the i^{th} eigenvalue of the cross-correlation matrix $\mathrm{E}\{\hat{\underline{r}}[n]\underline{r}^T[n]\}$. Eq. (4.11) requires positive real parts of all eigenvalues in order to guarantee stability. It was shown in [84] that a step size μ, which ensures a stable adaptation process of the FxLMS algorithm, can always be found as long as the ratio between the estimated and the true PLANT is strictly positive real for all frequencies, which implies that

$$\mathrm{Re}\left\{\frac{\hat{H}_{\mathrm{PLANT}}(j\omega)}{H_{\mathrm{PLANT}}(j\omega)}\right\} > 0 \Longrightarrow \cos\left(\Delta\phi\left(j\omega\right)\right) > 0 \tag{4.12}$$

where $\Delta\phi(j\omega)$ is the phase difference between the estimated and the true PLANT. Hence, stability is ensured if the phase difference is within ±90°, whereby any amplitude difference has no influence.

It should be mentioned that the condition on the phase difference may be infringed at some frequencies and still allow a stable adaptation process. This, however, is dependent on the input signal spectrum, which is usually not predictable. Thus, to guarantee stability independently of the signal spectrum, it is necessary that the phase deviation between the estimated and true PLANT is always smaller than 90°.

A stricter upper bound of the step size, which depends on the number of filter coefficients and the reference signal power, is usually used in standard LMS applications and was adapted to the FxLMS by Elliot in [76, Section 3.4.4]:

$$\mu_{\mathrm{max2}} \approx \frac{2}{(N+\tau_{ac})\cdot\overline{r^2}} \tag{4.13}$$

where N is the number of filter coefficients, τ_{ac} is the acoustic propagation delay of the secondary path between receiver R and canal microphone $\mathrm{M_c}$ and $\overline{r^2}$ is the average power of the reference signal. This signifies that a small distance between the receiver and the secondary sensor allows a bigger step size value which is advantageous for the convergence time.

4.1.4 Convergence time of the FxLMS

The maximal convergence time τ of the standard LMS algorithm is denoted according to [74, Section 3.2.4] by

$$\tau = \max_i \tau_i = \frac{-1}{\ln\left(1-\mu\min_i \lambda_i\right)} \tag{4.14}$$

and can be approximated for $\mu \ll \mu_{\mathrm{max}}$ by

$$\tau \approx \frac{1}{\mu\lambda_{\mathrm{min}}} \tag{4.15}$$

Hence, the maximal convergence time depends just as the stability on the eigenvalues of the correlation matrix and is for the FxLMS case subjected to the filtering of the estimated and the true PLANT. Combining Eq. (4.8) and Eq. (4.14) one can formulate the equation

$$\tau \approx \frac{\lambda_{\mathrm{max}}}{2\alpha\lambda_{\mathrm{min}}}\ , \quad 0<\alpha\ll 1 \tag{4.16}$$

which can be reformulated according to [83] for the general cross-correlation matrix $\mathrm{E}\{\underline{\hat{r}}[n]\underline{r}^T[n]\}$ to

$$\tau_{\max} \approx \frac{1}{2\alpha \mathrm{Re}\{\lambda_{\min}\}} \left(\frac{|\lambda_i|^2}{\mathrm{Re}\{\lambda_i\}} \right)_{\max} , \quad 0 < \alpha \ll 1 \tag{4.17}$$

where λ_i is the i^{th} eigenvalue of the cross-correlation matrix.

Boucher et al. [85] analyzed the minimum convergence time of the FxLMS with a sinusoidal reference signal in regard to a propagation delay Δ of the PLANT and to phase errors between the estimated and the real PLANT. It turned out that the convergence time increases with increasing delay, whereby it seems to be little sensitive to phase errors up to ±40°.

In summary, it can be stated that the smaller the propagation delay τ_{ac} and the phase errors $\Delta\phi(j\omega)$ are, the faster the algorithm converges to $\underline{\hat{h}}^{(\infty)}_{\mathrm{COMP}}$.

4.1.5 Performance of the FxLMS

The performance of the FxLMS in regard of the attenuation of the direct sound $d[n]$ is hardly studied in ADSC literature. From Section 4.1.3 it is known that the stable algorithm converges to Eq. (4.10), which is the optimum solution if the PLANT is exactly estimated. Any estimation errors increase the residual mean squared error signal which signifies a degradation of the direct sound attenuation.

Saito and Sone analyzed in [86] the influence of PLANT modeling errors on the achievable attenuation. Thereby, they inserted errors to the estimated PLANT by reducing the number of non-zero coefficients of a measured PLANT IR with 128 coefficients gradually and calculated the resulting attenuation. Their simulations showed that the performance of the attenuation decreases only for major model errors, where less than 20 coefficients of the estimated PLANT had non-zero values. The conclusion of the study is that the performance is not influenced by PLANT estimation errors as long as the cross-correlation matrix $\mathrm{E}\{\underline{\hat{r}}[n]\underline{r}^T[n]\}$ is positive definite and the primary path, i.e. the REOG, is described by the cascade of the true PLANT and the optimum filter, to which the algorithm would converge ideally, i.e. for $\hat{r}[n] = r[n]$. While the former condition is essential to ensure also stability of the algorithm, the latter is often not fulfilled. This is also the case in this work, where the roll-off of the transducers impede an exact match.

Nevertheless, the FxLMS algorithm is very robust against PLANT estimation errors, which allows to use a rough approximation of the true PLANT and still achieve a good performance regarding the direct sound attenuation.

4.2 Time and Frequency Implementation of FxLMS

The implementation of the FxLMS algorithm can be performed either in the time- or in the frequency-domain but must in both cases filter the input signal $x[n]$ with $\hat{h}_{\mathrm{COMP}}[n]$ in the time-domain.

The time-domain implementation of the FxLMS has the advantage that it is simple to implement and fulfills implicitly the first requirement. Though, its convergence time, which depends mainly on the spectrum of the reference signal, its computational cost per iteration and the lack of frequency dependent control of the adaptation process makes it less favorable for an implementation in real time systems [74, Section 3.1.3].

In contrast, the implementation in the frequency-domain improves the convergence speed, since each frequency bin is adapted almost independently due to the discrete Fourier transformation. Furthermore, it is possible to weight the frequency bins and to control their adaptation process, which is favorable also to avoid instabilities in particular in regions with poor excitation. Although the filtering is performed in the time-domain, the computational cost of the frequency based FxLMS per sample is still smaller than the time-domain FxLMS in this application in particular with increasing number N of filter coefficients.

4.2.1 Time-Domain FxLMS

The implemented time-domain FxLMS is based on a leaky and power normalized version of the FxLMS algorithm, denoted as *FxNLMS*. Both the normalization and the leakage improve the robustness of the algorithm, in particular if the power of the reference signals is subjected to high variations and the estimated PLANT differs from the real PLANT. The general structure of the time-domain FxLMS is depicted in Fig. 4.2.

The normalization of the algorithm is done by calculating the power of the reference signal according to the recursive equation

$$p_{\hat{r}}[n] = \lambda p_{\hat{r}}[n-1] + (1-\lambda)\underline{\hat{r}}^T[n]\underline{\hat{r}}[n]\ , \quad 0 < \lambda < 1 \tag{4.18}$$

which corresponds to the filtering of the reference power by an exponentially weighted moving average window. The normalized step size can then be written as

$$\mu_{\mathrm{FxNLMS}}[n] = \frac{\alpha_{\mathrm{T}}}{\gamma + p_{\hat{r}}[n]}\ , \quad 0 < \alpha_{\mathrm{T}} < 2 \tag{4.19}$$

where γ is a small value which limits the maximal value of the step size. It can easily be seen that the normalized step size compensates the variations of the reference signal, which on the one hand enables a stable adaptation and on the other hand improves the convergence speed. The exponential averaging smooths the power estimation and thus impedes sudden changes of the step size caused by peaks in the signal, which is also favorable for the stability. It should be mentioned that with increasing delay τ_{ac} of the secondary path the parameter α_{T} has to be reduced according to Eq. (4.13) in order to ensure stability of the adaptation process.

The cost function of the leaky FxLMS is defined, according to [76, Section 3.4.7], by

$$J_{\mathrm{FxNLMS}} = e_{\mathrm{el}}^2[n] + \beta_{\mathrm{T}}\underline{\hat{h}}_{\mathrm{COMP}}^T[n]\underline{\hat{h}}_{\mathrm{COMP}}[n] \tag{4.20}$$

where β_{T} is a small positive leakage factor. The instantaneous gradient with respect to the adaptive filter $\underline{\hat{h}}_{\mathrm{COMP}}[n]$ yields

$$\nabla_{\underline{\hat{h}}_{\mathrm{COMP}}[n]} J_{\mathrm{FxnLMS}} = 2\underline{\hat{r}}[n]e_{\mathrm{el}}[n] + 2\beta_{\mathrm{T}}\underline{\hat{h}}_{\mathrm{COMP}}[n] \tag{4.21}$$

Combining Eq. (4.19) and Eq. (4.21) leads to the leaky normalized FxLMS update equation denoted by

$$\underline{\hat{h}}_{\mathrm{COMP}}[n+1] = (1-\mu_{\mathrm{FxNLMS}}[n]\beta_{\mathrm{T}})\underline{\hat{h}}_{\mathrm{COMP}}[n] - \mu_{\mathrm{FxNLMS}}[n]\underline{\hat{r}}[n]e_{\mathrm{el}}[n] \tag{4.22}$$

In Section 4.1.3 the FxLMS was denoted as stable if the real parts of the eigenvalues of the cross-correlation matrix $\mathrm{E}\{\underline{\hat{r}}[n]\underline{\hat{r}}^T[n]\}$ are positive. The cross-correlation matrix of the leaky FxNLMS is expanded by the leakage factor β_{T} to $\mathrm{E}\{\underline{\hat{r}}[n]\underline{\hat{r}}^T[n] + \beta_{\mathrm{T}}\mathbf{I}\}$, which allows to turn the real parts of all eigenvalues into positive values. On the other side, β_T deteriorates the achievable attenuation as it introduces a bias to the converged adaptive filter of Eq. (4.10). Thus, the choice of β_T is a trade off between stability and performance.

Furthermore, the allowable phase errors between the estimation and the real PLANT depend on the leakage factor and the magnitude of the PLANT. Instead of the maximal phase error of ±90° (see Eq. (4.12)), the phase deviation must fulfill the inequality according to [76, Section 3.4.7]

$$\mathrm{Re}\Big\{\hat{H}_\mathrm{PLANT}(j\omega)H^*_\mathrm{PLANT}(j\omega)\Big\} + \beta_\mathrm{T} > 0 \Longrightarrow \cos\left(\Delta\phi\left(j\omega\right)\right) > \frac{-\beta_\mathrm{T}}{\left|H_\mathrm{PLANT}(j\omega)\right|^2} \tag{4.23}$$

assuming a perfect magnitude estimation. Eq. (4.23) shows that the phase error $\Delta\phi(j\omega)$ can be greater than ±90° to ensure stability for any $\beta_\mathrm{T} > 0$. Moreover, at the frequencies where the magnitude of the PLANT is smaller than β_T, the fraction becomes smaller than -1 and the stability of the adaptation process is ensured for any phase error.

In summary, it can be stated that the normalization of the algorithm speeds up the convergence time and smooths strong variations of the power of the reference signal in order to stabilize the adaptation process. The leakage factor deteriorates the optimal achievable attenuation but allows greater robustness against phase errors between the estimated and the true PLANT. Furthermore, the leakage factor prevents the drift of the filter coefficients, which may occur due to underexcitation, finite word length of the coefficients or disturbances like measurement noise and estimation errors of the PLANT [87, 88].

4.2.2 Frequency-Domain FxLMS

The frequency-domain FxLMS algorithm (*FxFLMS*) is based on the FLMS implementation described in [74, Section 5.1] and is implemented with the so called *overlap&save* [22, Section 8.7.3] method to avoid circular correlation. This demands a specific arrangement of the signals as shown below. Other than the general FLMS algorithm, the implemented method performs the filtering process of the input signal $x[n]$ in the time-domain because of the delay constraints of the ADSC. Fig. 4.3 shows the structure of the FxFLMS, where the single arrows denote the sample based processing in the time-domain and the double arrows denote block processing in the frequency-domain.

The adaptation process of the FxFLMS is performed in the frequency-domain. Therefore, the time signals are buffered into blocks of K samples and transformed to the frequency-domain by the DFT of the same size. The block shift is set to L samples, which implies that the update of the adaptive filter occurs only every L samples, i.e. $n = m \cdot L$, where m is the block index. This restricts the usability of the frequency-domain algorithm to applications where the system to be identified changes slower than the update rate L of the adaptation filter. This is the case for ADSC in hearing aids, where the acoustic environment is assumed to be slowly time varying. In order to meet the *overlap&save* constraint [74, Appendix B], the number of FIR coefficients is set to be $N = K - L$.

The update equation of the implemented FxFLMS algorithm is formulated by

$$\underline{\hat{H}}_\mathrm{COMP}[m+1] = \underline{\beta}_\mathrm{F} \odot \underline{\hat{H}}_\mathrm{COMP}[m] + \underline{\mu}[m] \odot \underline{\hat{R}}^*[m] \odot \underline{E}_\mathrm{el}[m] \tag{4.24}$$

where $\odot$ is the element wise multiplication operator. $\underline{\beta}_\mathrm{F}$ and $\underline{\mu}[m]$ are the frequency dependent

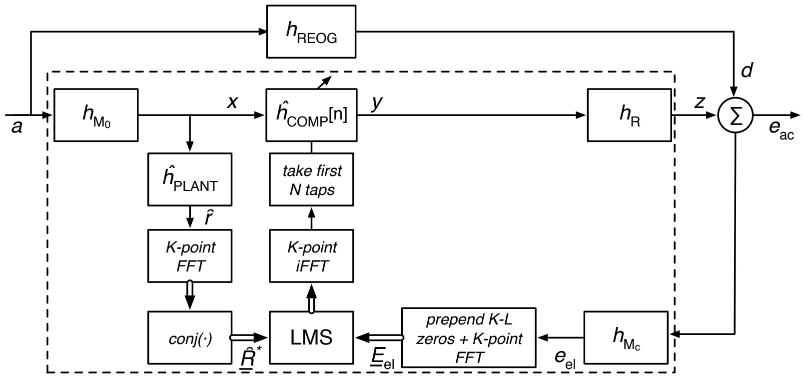

Figure 4.3: Block diagram of the FxFLMS algorithm: h_{REOG} is the IR of the primary path, h_{M_0}, h_{R} and h_{M_c} are the IRs of the respective transducer. $\hat{h}_{\text{COMP}}[n]$ is the time-variant adaptive filter and $\hat{h}_{\text{PLANT}}$ is the estimated PLANT. *K is the number of FFT-bins, L is the block shift and N is the number of filter taps. The single arrows denote the sample based processing in the time-domain and the double arrows denote the block processing in the frequency-domain.*

forgetting factor and step size, respectively, and $\underline{\hat{H}}_{\text{COMP}}[m]$ is the adaptive filter at block m. The update term of Eq. (4.24) is the cross-correlation between the reference and the error signal vector at the m^{th} block in the frequency-domain. In order to avoid a circular correlation, N zeros must be append to the error signal vector $\underline{e}_{\text{el}}[m]$, such that the DFT of the reference and the error signal yields

$$\begin{aligned} \underline{\hat{R}}^*[m] &= \mathcal{F}\{\underline{\hat{r}}[m]\}^*\,, & \underline{\hat{r}}[m] &= \begin{bmatrix}\hat{r}[mL-N] & \cdots & \hat{r}[mL+L-1]\end{bmatrix}^T \\ \underline{E}[m] &= \mathcal{F}\left\{\begin{bmatrix}\underline{0}^T & \underline{e}_{\text{el}}[m]^T\end{bmatrix}^T\right\}, & \underline{e}_{\text{el}}[m] &= \begin{bmatrix}e_{\text{el}}[mL] & \cdots & e_{\text{el}}[mL+L-1]\end{bmatrix}^T \end{aligned} \tag{4.25}$$

where $\mathcal{F}\{\cdot\}$ is the discrete Fourier transform operator.

An important characteristic of the FxFLMS algorithm is that each frequency bin is adapted almost independently, which means that it can be seen as K independent LMS algorithms which adapt only one coefficient. Hence the step size can be chosen for each bin separately, which improves the convergence speed. Thus, the normalization of the step size is performed in each frequency bin, which implies a bin-wise calculation of the reference signal power $P_{\hat{R}_k}[m]$. To prevent fast modifications of the step size the power is exponentially smoothed over time, i.e. for the k^{th} bin

$$P_{\hat{R}_k}[m] = \lambda P_{\hat{R}_k}[m-1] + (1-\lambda)\left|\hat{R}_k[m]\right|^2\,,\quad 0<\lambda<1\,,\quad \text{for } k=0,\dots,K-1 \tag{4.26}$$

According to the strict upper bound of Eq. (4.13) the step size at the k^{th} bin can then be written as

$$\mu_{\text{FxFLMS}_k}[m] = \frac{\alpha_{\text{F}_k}}{\gamma + P_{\hat{R}_k}[m]}\,,\quad 0<\alpha_{\text{F}_k}<2\,,\quad \text{for } k=0,\dots,K-1 \tag{4.27}$$

where α_{F_k} is a frequency dependent weighting factor, which allows to control further the adaptation process in each bin, and γ is a small value which limits the maximal value of the step size. Similar to the step size of the FxNLMS of Eq. (4.19), α_{F_k} has to be reduced with increasing delay τ_{ac} of the PLANT.

The frequency dependent forgetting factor $0 \leq \beta_{\mathrm{F}_k} \leq 1$ of Eq. (4.24) introduces the leakage effect to the FxFLMS algorithm. Similar to the leaky LMS in the time-domain, it improves the stability of the algorithm. Furthermore, by weighting frequency regions differently it is possible to shape also the magnitude response of the resulting adaptive filter according to the requirements imposed by the specific application.

It should be mentioned that both the frequency dependent step size and forgetting factor correspond to a filtering process with the correlation term between the reference and the error signal and with the current adaptive filter coefficients, respectively (see Eq. (4.24)). In order to reduce the effects of a circular convolution in the frequency-domain, the IRs of the step size and the forgetting factor must be short, which implies small changes between adjacent bins. In order to ensure this the IR of the step size in each block m is weighted by a hann window of length $\frac{K}{4}$. On the contrary, the frequency dependent forgetting factor is once defined and ensured to have a compact IR. Hence, it must not be smoothed during the adaptation process.

The frequency-domain FxLMS gives the possibility to control each frequency bin almost independently. This allows a weighting of the error similar to the static approximation algorithm and gives the possibility to define, where the adaptive filter has to be accurate and where a greater deviations from the optimum solution is tolerate. Further, the stability can be ensured by choosing a small β_{F_k} in those frequencies, where the adaptive filter tends to become unstable because of a poor SNR of the excitation signal. Compared to the time-domain FxLMS, the advantage in convergence speed, lower computational complexity and the control of the particular frequencies make the frequency-domain approach favorable.

4.3 Algorithm Modification for ADSC in HI framework

The presented adaptation algorithms for ADSC application have to be modified in order to fulfill the requirements and constraints on the compensation filter formulated in Section 3.1. With the presented structures the adaptive filters would ideally converge to the unconstrained frequency response $H_{\mathrm{COMP}}(\mathrm{e}^{j\Omega})$, where Ω is the discrete radian frequency. This, however, would demand an unbounded linearly working receiver as well as an infinitely high number of filter coefficients. Both is not given in a real world scenario which is why a limitation at low frequencies has to be applied and the target filter has to be reshaped. While the former requires a modification of the error signal and is outlined in Section 4.3.1, the latter is obtained by a pre-equalization filter block equal to the static filter design and discussed in Section 4.3.2.

4.3.1 Low frequency limitation

The adaptive filter has to converge to the bounded compensation filter

$$\tilde{H}_{\mathrm{COMP}}(\mathrm{e}^{j\Omega}) = H_{\mathrm{COMP}}(\mathrm{e}^{j\Omega}) \cdot H_{\mathrm{HP}}(\mathrm{e}^{j\Omega}) \ ,$$

where $H_{\mathrm{HP}}(\mathrm{e}^{j\Omega})$ is a limiting high-pass filter. In Section 3.4.2 it was shown that a 2^{nd} order high-pass filter is adequate for the limitation of the compensation filter response. In order that the adaptive algorithm converges to the bounded compensation filter $\tilde{H}_{\mathrm{COMP}}(\mathrm{e}^{j\Omega})$, the direct signal $d[n]$ has to be filtered by the high-pass filter. Since the acoustic direct signal can not be modified, it is necessary to manipulate the recorded residual signal $e_{\mathrm{el}}[n]$ such that the minimization of a new error signal yields the desired solution.

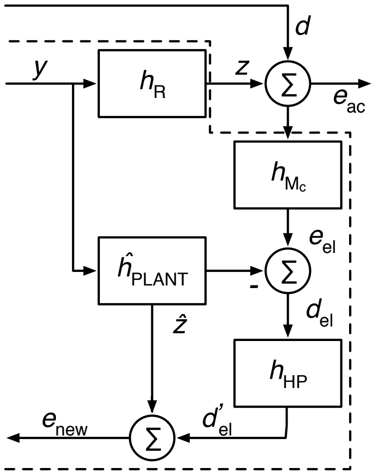

Figure 4.4: Low frequency limitation of the adaptive ADSC structure: $y[n]$ is the adaptive filter output, $e_{ac}[n]$ is the acoustic residual signal. $d_{el}[n]$ is the direct signal recomposed from the electrical residual signal $e_{el}[n]$ and the estimated ADSC signal $\hat{z}[n]$. d'_{el} is the bounded direct signal and $e_{new}[n]$ is the resulting error signal, which should be minimized. h_R and h_{M_c} are the IRs of the transducer, $\hat{h}_{PLANT}[n]$ is the IR of the estimated PLANT *and $h_{HP}[n]$ is the limiting high-pass*

Fig. 4.4 shows the new error calculation used for both the FxNLMS and FxFLMS algorithm in this work. In order to achieve the new error signal, the direct signal $d[n]$ has to be recomposed electrically. Thus, the estimate of the destructive ADSC signal $\hat{z}[n]$ is subtracted from the recorded residual signal $e_{el}[n]$ which results in the electrical representation of the direct signal, i.e. $d_{el}[n]$. By filtering this signal with the 2nd order high-pass filter $H_{HP}(e^{j\Omega})$ the desired low frequency bounded signal $d'_{el}[n]$ is generated. The destructive interference is then conducted electrically which yields the new error signal $e_{new}[n]$. This error signal can be formulated in the frequency-domain by

$$E_{new}(e^{j\Omega}) = H_{HP}(e^{j\Omega})H_{M_c}(e^{j\Omega})D(e^{j\Omega}) + \underbrace{\tilde{H}_{COMP}(e^{j\Omega})R(e^{j\Omega})}_{Z(e^{j\Omega})} - (1 - H_{HP}(e^{j\Omega}))\tilde{H}_{COMP}(e^{j\Omega})\Delta R(e^{j\Omega}) \tag{4.28}$$

where $\tilde{H}_{COMP}(e^{j\Omega})$ is the bounded compensation filter. The last term arises from the differences between the estimated and the true PLANT denoted by

$$\Delta R(e^{j\Omega}) = H_{PLANT}(e^{j\Omega})X(e^{j\Omega}) - \hat{H}_{PLANT}(e^{j\Omega})X(e^{j\Omega}) ,$$

where $X(e^{j\Omega})$ is the input signal of the adaptive filter. It can be seen that this influence of the PLANT errors on the adaptation process is frequency dependent and decays towards high frequencies according to $(1 - H_{HP}(e^{j\Omega}))$. The increase of the mean squared error vanishes either if the estimated PLANT corresponds to the true PLANT or the limitation of the low frequencies is abolished, i.e. $H_{HP}(e^{j\Omega}) = 1,\ \forall\Omega$.

Nevertheless, it is possible to bound the desired frequency response such that it meets the requested criteria. Again, the adaptive filter reaches only the optimum solution, if the estimated PLANT is the real PLANT, i.e $\Delta R(e^{j\Omega}) = 0,\ \forall\Omega$.

4.3.2 Pre-equalization of the adaptive Filter

The characteristic of the bounded compensation filter $\tilde{H}_{\text{COMP}}(\mathrm{e}^{j\Omega})$ is its arise towards low frequencies and the resonances at high frequencies caused by the inversion of the receiver and the outer microphone (see Fig. 3.8). Both properties are unfavorable for an FIR filter since it requires a high number of coefficients to model the decay of the low frequencies as well as to model the pronounced resonances [76, Section 2.2]. Furthermore, the bounded compensation filter has a negative constant group delay $\hat{\tau}_{\text{COMP}}$ which arises from the erroneous interpretation of the measurement of the PLANT and requests noncausal filter taps. Since the requirements on the adaptive FIR filter imply causality, it is not possible to approximate the desired filter response in magnitude and phase perfectly.

Using the pre-equalization filter introduced in Section 3.4.3, i.e.

$$H_{\text{preEQ}}(\mathrm{e}^{j\Omega}) = H_{\text{lag}}(\mathrm{e}^{j\Omega}) \cdot H_{\text{boost}}(\mathrm{e}^{j\Omega}),$$

the number of filter coefficients can be reduced while increasing the attenuation.

Due to the compensation of the 2^{nd} order roll-off of the PLANT towards low frequencies by the lag filter, the resulting magnitude response becomes flatter. Adding a sufficient delay τ to the REOG such that the filter becomes causal yields an accurate approximation of the bounded compensation filter. Fig. 4.5 shows the FIRs of the delayed bounded compensation filter with and without pre-equalization by the lag filter. They are calculated by the frequency sampling method [56], which is used as reference for the adaptive algorithms, with $N = 2048$ and $N = 8192$ filter coefficients, respectively. It can be seen that only the FIRs of the pre-equalized frequency response meet the requirement of causality, whereas filtering by the FIRs of the unaltered frequency response yield an inapplicable ADSC signal.

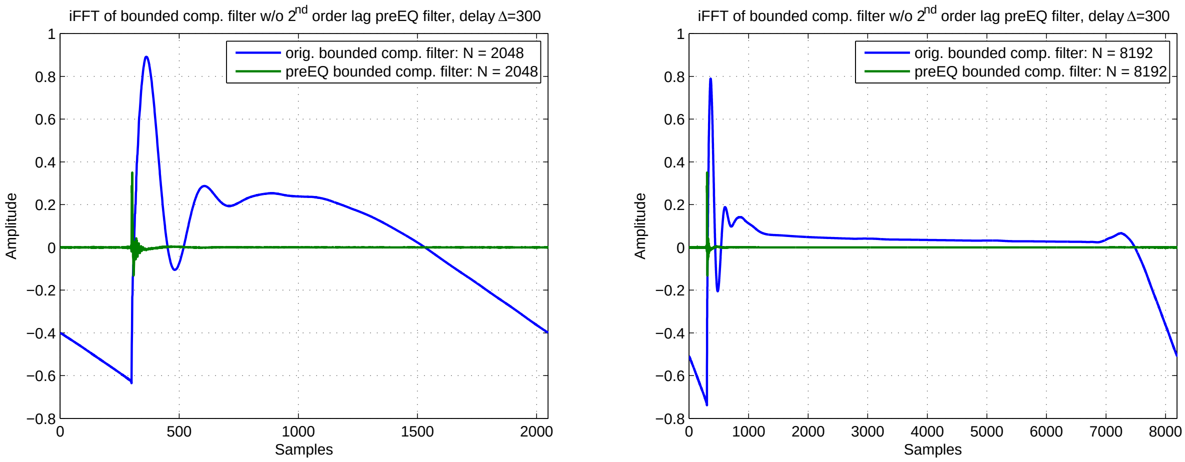

(a) FIR filter with $N = 2048$ filter coefficients

(b) FIR filter with $N = 8192$ filter coefficients

Figure 4.5: FIR of a bounded compensation filter with an additional delay of $\Delta = 300$ samples: iDFT of the unaltered filter response (blue) and iDFT of the filter response pre-equalized with a 2^{nd} order lag filter (green). The FIRs of the unaltered filter response have noncausal filter taps, which arise at the end of the FIR due to the circularity of the DFT.

Since it is impossible to delay the real direct sound path, i.e. the REOG, as done above it is necessary to compensate the negative constant group delay by pre-processing of the adaptive filter. From Section 3.4.3 it is known that a boost filter with its peak close to the Nyquist frequency f_{Nyquist} can be used as compensation of the negative group delay in a bounded frequency range and improves the attenuation in the desired frequency region. The influence of the pre-equalization on the achievable attenuation using FIR filters is depicted in Fig. 4.6. Again, the FIRs are computed by the frequency sampling method, whereby the results are weighted with the negative slope of a raised cosine, i.e. $w = 0.5\left(1 + \cos\left(\frac{\pi n}{N-1}\right)\right)$ with $n = 0, \ldots, N-1$, in order to eliminate all noncausal taps.

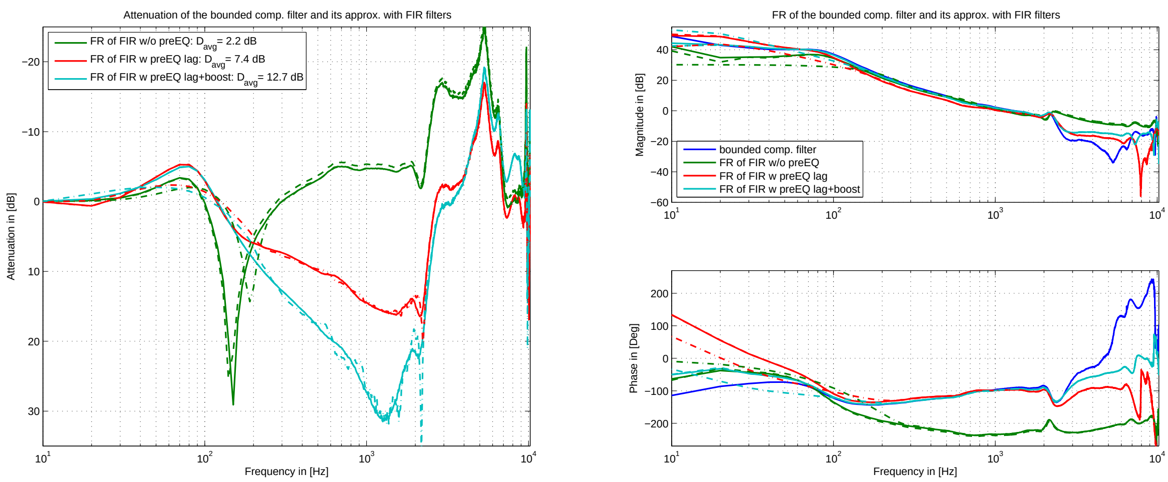

(a) Attenuation of approximated FIR filters

(b) FR of approximated FIR filter

Figure 4.6: Attenuation and frequency response of FIR filters with and without pre-equalization: approximation of the bounded compensation filter (blue) without pre-equalization (green), with lag filter pre-equalization (red) and with lag+boost pre-equalization (cyan). The results are shown for $N = 128$ (dash-dotted), $N = 2048$ (solid) and $N = 8192$ (dashed) filter coefficients.

It can be seen that the average attenuation D_{avg} improves by 5.3dB by adding the 2$^{\text{nd}}$ order boost filter to the pre-equalization filter (*cyan solid*). Above 2 kHz the deviation from the target frequency response (*blue*) increases but still meets the requirements imposed on the compensation filter. Furthermore, Fig. 4.6(a) shows the influence of the filter length regarding the attenuation. While an increase from 2048 (*solid*) to 8192 (*dashed*) filter coefficients has no improvement for the pre-equalized cases, which signifies that the IR decays within 2048 samples, a reduction to 128 (*dash-dotted*) filter coefficients infringes the maximal amplification threshold at low frequencies, in this case set to 40dB, and thus is impracticable for the ADSC application in hearing aids.

Adding a pre-equalization filter to the adaptive ADSC structure has the positive side effect that the reference signal $\hat{r}[n]$ has also to be pre-equalized. Since this filter is an approximation of the inverse PLANT frequency response, it reshapes the reference signal such that it resembles the recorded input signal $x[n]$. In particular for the FxNLMS algorithm, where the spectral shape of the reference signal influences the convergence speed, the reshape of the reference signal shortens the convergence time of the algorithm. Fig. 4.7 shows the overall frequency response of the estimated PLANT and the pre-equalization filter.

In summary, adding a pre-equalization filter to the adaptive ADSC system is crucial for the application of ADSC in hearing aids, since only with this it is possible to get causal, fast decaying FIR filters for the attenuation of the direct sound. Furthermore, the reshape of the reference signal is favorable for the convergence speed of the algorithms. As it will be shown in Chapter 5 the adaptive algorithms converge to the finite impulse responses computed by the frequency

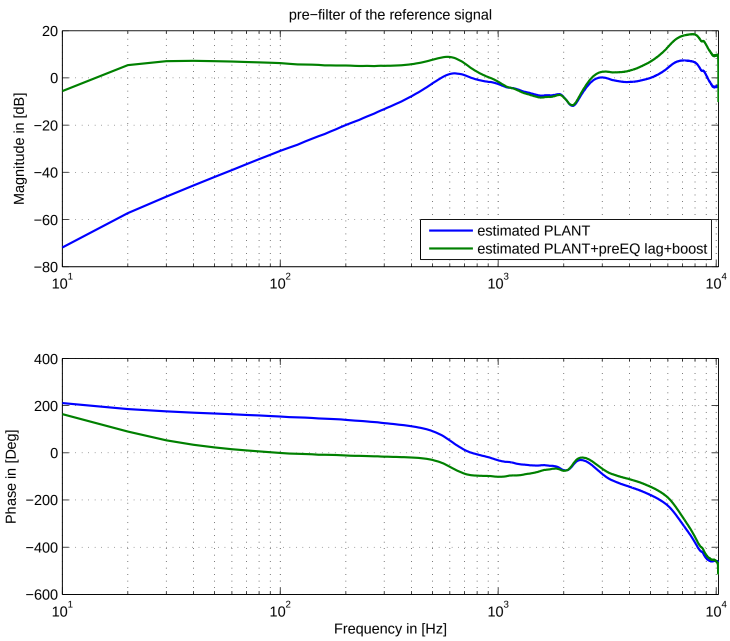

Figure 4.7: Pre-filtering of the recorded input signal $x[n]$ with the estimated PLANT *(blue) and the pre-equalized estimated* PLANT *(green). The pre-equalization filter consists of a 2^{nd} order lag and boost filter, which approximate the inverse* PLANT.

sampling method.

Fig. 4.8 shows the complete structure of the FxNLMS (a) and the FxFLMS (b) including the pre-equalization filter and the low frequency limitation used in this work and implemented in Simulink® on the RTS.

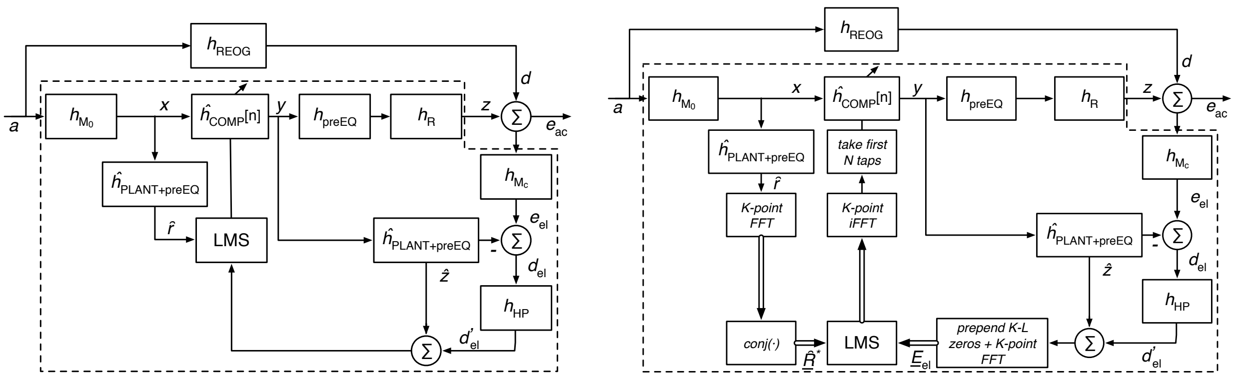

(a) FxNLMS structure (b) FxFLMS structure

Figure 4.8: Structure of the adaptive ADSC system for the attenuation of the direct sound with pre-equalization filter and enhanced error calculation network for low frequency limitation

5 Results

In this chapter the performance of the static and adaptive active direct sound control (ADSC) system implemented on the RTS is outlined and discussed. Therefore, several simulations and measurements were conducted and evaluated by the five objective parameters introduced in Section 3.4.4. In order to calculate the objective parameters the REOG was measured for each trial with and without the ADSC system activated, from which the attenuation curve can be calculated.

The performance is measured with pink noise and cafeteria noise as excitation signals for a big and a small vent size, which are typically used in hearing aids. The hardware used for the performance measurements as well as the measurement setup are listed in Appendix D. The complete results are depicted in Appendix C.

5.1 Static Design

The measurements of the static ADSC system were done with the author's left (AnH_L) and right (AnH_R) ITE prototypes with the excitation signals played via an equalized headphone [89]. The diameter of the vents were 2 mm respectively 0.8 mm with a length of 15 mm. It should be noted that the smaller vent diameter is achieved by inserting a tube into the 2 mm vent, which can not be perfectly reproduced and is a potential source of error regarding deviations of a reference transfer function.

The static filters $\hat{H}(j\omega)$ were calculated as described in Section 3.4 based on transfer functions measured in August 2012. Unless otherwise noted, the maximum gain was limited to 40 dB and the low frequency overshoot to 6 dB. At each insertion of the prototype an overall gain G of the filter $\hat{H}(j\omega)$ was adjusted in 0.5 dB steps such that the defined maximum low frequency overshoot was reached. Since one is interested in the upper bound of a distortion-free ADSC system, the excitation signal is set to the maximum level, where still no audible receiver distortions are perceptible by the test subject. For lack of an objective measure for broad band noise distortions (see Section 2.4.1), the audible distortions are evaluated by the author and the volume of the excitation signal adjusted correspondingly.

In the following sections the performance of the static filter design is outlined in regard of the variability of insertions, the application of different compensation filters, the excitation with different signals and the variation of the low frequency limitation and the overshoot.

5.1.1 Difference between Calculations and Measurements

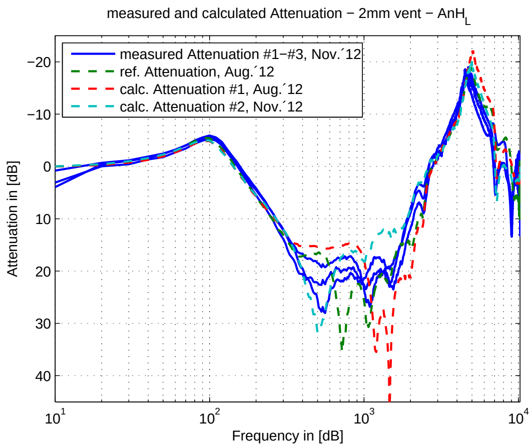

(a) AnH_L prototype

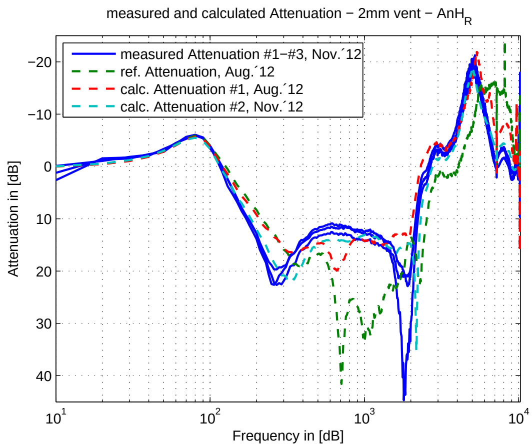

(b) AnH_R prototype

Figure 5.1: Attenuation of two prototypes: three measured attenuations (blue, solid) and three calculated attenuation with an individually designed static compensation filter for each prototype. Each compensation filter is based on a measured REOG *and* PLANT *which yields the reference attenuation curve (green, dashed), respectively*

Fig. 5.1 shows the measured (*solid*) and the calculated (*dashed*) attenuation of the left and the right ITE prototype with the 2 mm vent. For each side, an individual static filter $\hat{H}(j\omega)$ is computed, which under ideal conditions yields the reference attenuation curve (*green, dashed*). As one can see, neither the calculated nor the measured attenuation curves of both prototypes match exactly the reference, which arises from the variability of the transfer functions with each insertion of the prototype.

The measurements and calculations of the AnH_L prototype deviate only significantly in that region, where the attenuation is already high, i.e. $D > 12$ dB. From Section 2.4.2 it is known that even a small deviation in magnitude and phase influences considerably the achievable attenuation. Since the transfer functions vary with each insertion (see Section 2.3), the resulting attenuation deviates from the reference, which may yield narrow notches but also a lower average attenuation. Beyond the frequency region of high attenuation the calculated and the measured curves correlate well, which is also visible in Tab. C.1.

However, the variability of the transfer functions at each insertion does not explain the differences of the AnH_R prototype between the measured and the reference attenuation. Other than the AnH_L prototype the measured attenuations between 100 and 300 Hz differs significantly from the reference. This points to the fact that the receiver response must have permanently changed since the calculation of the static compensation filter. This assumption is enforced by comparing the calculated attenuation based on transfer functions from August 2012 (*red, dashed*) and from November 2012 (*cyan, dashed*). While the former resembles the reference curve, the latter resembles the measurement curves, which were taken over the same period.

A possible explanation of the transfer function drift is that the AnH_R prototype was used more frequently over the last months and the receiver often exposed to high input voltages, which can result in an irreversible alteration of the receiver response. Nevertheless, in this case the receiver response changed beneficially in regard of the bandwidth of the attenuation, but yields an inferior average attenuation (see Tab. C.1).

5.1.2 Variability of the attenuation

In Section 2.3 the deviation of the REOG and the PLANT between different subjects and within a subject were outlined. It was concluded that with decreasing vent size the intra- and inter-individual variability of the transfer functions increases, which makes at least for small vent dimension an individual filter design necessary. In this section the effect of the intra- and inter-individual variability on the attenuation is analyzed based on measured data of the two ITE prototypes with two different vent diameters.

Intra-individual variability

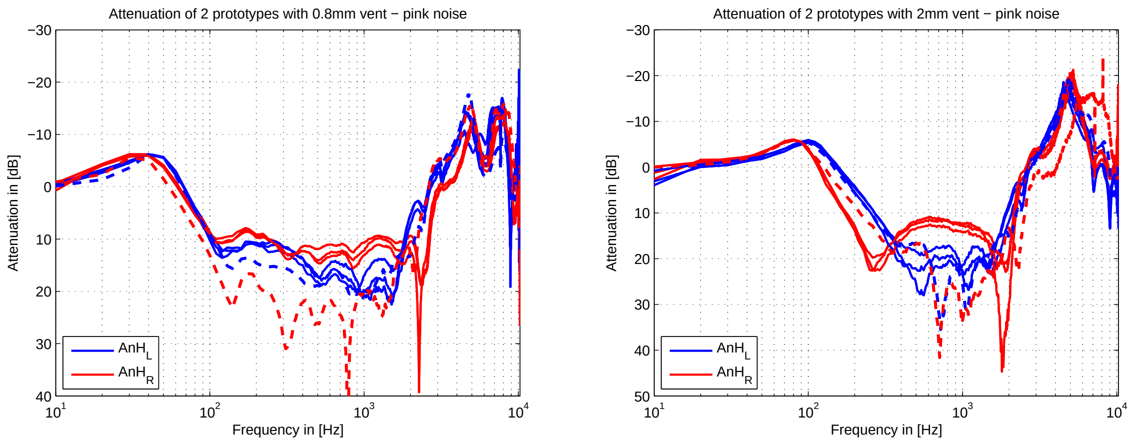

(a) 0.8 mm vent diameter

(b) 2 mm vent diameter

Figure 5.2: Variability of the two ITE prototypes with two different vent diameters: for each configuration the attenuation of three insertions was measured (different colors, solid). The dashed curves show the calculated reference attenuation, respectively.

Fig. 5.2 shows the measured and reference attenuation of the ITE prototypes for two different vent diameters. With these prototypes, the intra-individual variability of the attenuation is low even for the 0.8 mm vent, which results in an approximately constant bandwidth, average attenuation and SPL within each of the three insertions (see Tabs. C.2 and C.3). The deviation from the reference attenuation (*dashed*) increases with lower vent diameter and is in particular high for the AnH_R prototype due to the altered receiver response. In order to fulfill the 6 dB overshoot at low frequencies the overall gain G variates between -0.5 and 1 dB (2 mm vent) and -5 and -2.5 dB (0.8 mm vent), respectively.

In summary, it can be stated that an individual static filter $\hat{H}(j\omega)$ yields a similar attenuation for each insertion, which correlates well with the calculated reference curve. Contrary to the conclusion of Section 2.3, the variability of the attenuation does not increase with diminishing the vent diameter as long as the overall gain G can be controlled.

Inter-individual variability

In order to find out the inter-individual variability 6 different static filter, each based on the transfer functions of a different prototype (AnH_R, AnH_L, MaJ_L, MaJ_R, ThZ_L and ThZ_R), were used with the two ITE prototypes AnH_L and AnH_R with a 2 mm and a 0.8 mm vent diameter,

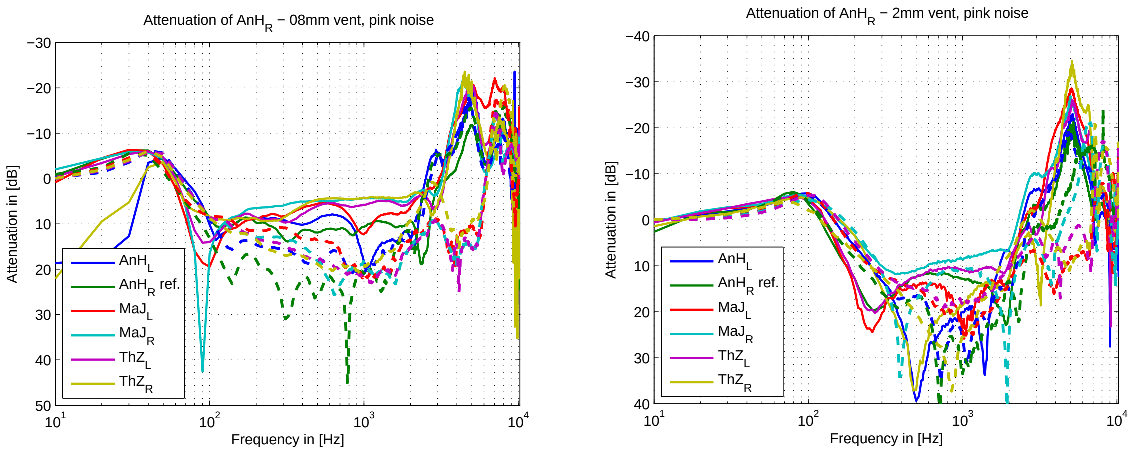

(a) AnH_R prototype, 0.8 mm vent diameter (b) AnH_R prototype, 2 mm vent diameter

Figure 5.3: Attenuation of the AnH_R prototype for two different vent diameters with varying static filters based on 6 different prototypes: measured attenuation (different colors, solid) and reference attenuation achieved by the static filters based on the particular prototype (different colors, dashed)

respectively. The resulting attenuation for both vent diameters of the AnH_R prototype are depicted in Fig. 5.3.

For the bigger vent it can be stated that a broad attenuation can be achieved without an individual design, which even may outperform the attenuation of the individual filter (*blue* and *yellow*). Only the attenuation based on the transfer functions of the MaJ_R prototype (*cyan*) is significantly worse, which is due to its distinct REOG depicted in Fig. 2.24 (*magenta*). While the average attenuation and the SPL stays in the expected range, the changes in bandwidth are substantial compared to the intra-individual variability. Moreover, the overall gain G has to be adjusted within a larger range of -4 to 2.5 dB (see Tab. C.4).

The impact on the attenuation for the smaller vent with non-individually designed compensation filters is much higher. The average attenuation decreases down to half of the reference and has only a small bandwidth with $D \geq 10$ dB (see Tab. C.5). An exception is the use of the AnH_L filter on the AnH_R prototype and vice versa, which yields a similar attenuation as the respective individual filter. In order to satisfy the low frequency overshoot, the overall gain G has to be regulated strongly between -10 and 4 dB.

The intra-individual variability in regard of the maximum allowed SPL is low for both prototypes and vent diameters, since for all compensation filters the maximal gain level is satisfied.

Furthermore, the application of static filters, which were designed for a 0.8 mm vents, on prototypes with 2 mm vent and vice versa was analyzed. As expected for both vent diameters, the resulting average attenuation as well as the bandwidth is small and hence not useful for ADSC in hearing aids. The attenuation curves for the AnH_L and AnH_R prototype are depicted in Fig. C.2 and their respective objective parameters in Tabs. C.4 and C.5.

From the measured results it can be concluded that the applicability of non-individual compensation filters depends on the vent diameter. The greater it is, the more feasible is the design of a generic filter, which achieves a broad attenuation at the desired frequency range. This is because the inter-individual differences of the REOG and the PLANT decrease, assuming similar transducers built-in in the prototypes. For the 0.8 mm vent the outcomes show that an individual compensation filter has to be designed such that an adequate attenuation of the direct sound can be achieved. These results are also valid for the AnH_L ITE prototype (see

Fig. C.1, Tabs. C.4 and C.5). However, further measurements with more prototypes and varying vent diameters have to be conducted in order to find out the usability of generic filters and their limits.

5.1.3 Maximal SPL

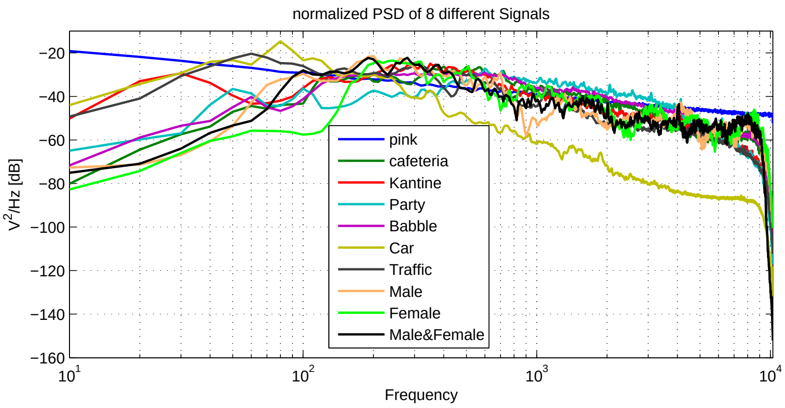

Figure 5.4: Power spectral density of 10 *different excitation signals*

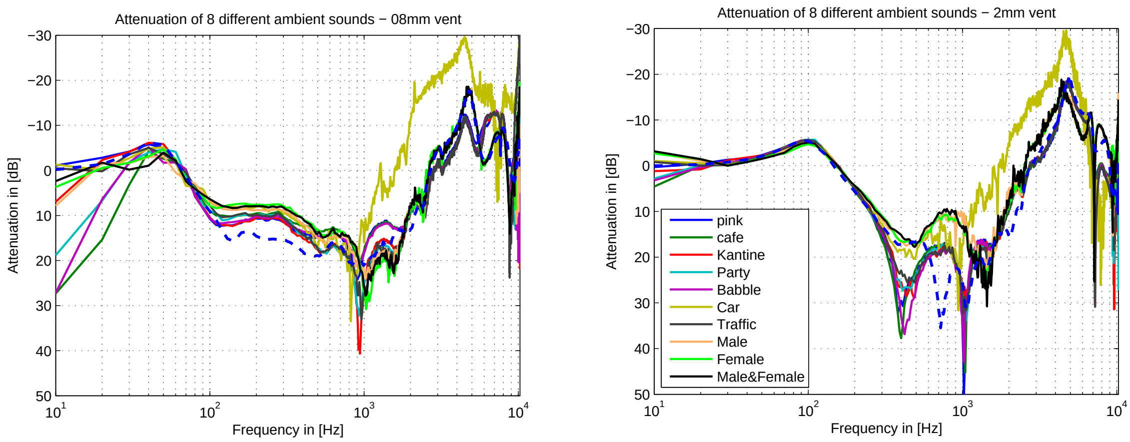

(a) AnH_L prototype with 0.8 mm vent (b) AnH_L prototype with 2 mm vent

Figure 5.5: Attenuation of 10 *different excitation signals measured with the AnH_L prototype with two different vent diameters*

For a potential usability of the developed ADSC system in hearing aids it is crucial to determine its limits regarding audible distortions generated by the receiver. From Section 2.4 it is concluded that the maximum SPL threshold of broad band noise has to be found out subjectively, since no meaningful objective measures are available. Hence, the perceived sound quality regarding receiver distortions is evaluated by the test subject, in this case the author. The upper limit of the ADSC system is determined by increasing the volume of the playback device, i.e. the headphones, up to the maximum level at which the receiver still works without audible distortion.

Since this bound depends not only on the static filter or the transducers but also on the signal spectrum, the ADSC performance was tested with 10 different signals on the AnH_L prototype with a 0.8 mm and a 2 mm vent diameter and its individual designed filter, respectively. The overall gain G was adjusted with pink noise, such that the low frequency overshoot reaches the 6 dB. The spectra of the used excitation signals and the resulting attenuations are depicted in Fig. 5.4 and Fig. 5.5, respectively. Tab. C.8 shows the objective parameters and the correspondent SPL in front of the ear.

Although most of the excitation signals have a similar spectrum above 200 Hz, the maximal achievable SPL differs highly between the signals. While the noise signals with speech-like spectra, i.e. *cafeteria*, *Kantine*, *Party* and *Babble*, may reach SPLs between 83 and 91 dB (2 mm vent) and 97 and 103 dB (0.8 mm vent), the signals with high energy below 100 Hz (*Car* and *Traffic*) are limited to levels up to 75 dB and 80 dB, respectively. This results fulfill the expectations, since the compensation filters boost mainly low frequencies, which yields audible distortions in that frequency region already at lower SPLs.

From the Tab. C.8 it can be seen that the SPLs of the voice signals (*Male*, *Female* and *Male&Female*) are similar or even lower as the signals with energy predominantly at lower frequencies, although their spectral shape resembles the speech-like noise signals. This is due to the RTS which produces artifacts that become only audible using voice signals as source and are usually masked by broader excitation signals. Since it is hard to distinguish them from the receiver distortions, the headphones volume was lowered until no artifacts at all were perceivable. Hence, these results are not comparable with the outcomes of the other excitation signals. However, since the spectra of the voice signals correspond to the speech-like noise signals, one can assume that similar high SPLs can be achieved without audible receiver distortions.

In order to produce a more realistic scene, a cafeteria environment was reproduced in a laboratory with sound samples recorded in the cafeteria of the Phonak AG. The excitation signals were played over 6 loudspeakers, which where placed equidistantly on a circle with 1.5 m radius around the subject with the inserted ITE prototype. The sound samples were equalized such that their spectra corresponded with the real scene. In addition to the created diffuse sound field a single speaker was played over the loudspeaker in front of the subject with an SNR of 0 dB. The maximal achievable SPL, at which no receiver distortions were perceived, was found at 84 dB, which coincides with the measured SPLs of the speech-like noise signals.

In summary, it can be stated that the tested system can manage SPLs which occur typically in a cafeteria. Furthermore, the measured SPLs of the speech-like noise signals even surpass the values found in Tab. 2.5, where the 0.575 mm vent radius of the ITE hardware model (ITE-HM) corresponds approximately to the 2 mm vent diameter and the 0.225 mm to the 0.8 mm vent of the used ITE prototypes, respectively. On the other side, the results show that signals with high energy at low frequencies produce audible distortions already at low SPLs, which means that the ambient signal has to be monitored continuously in order to down-regulate or switch off the ADSC system if necessary. Furthermore, comparing the achievable SPLs of the two ITE prototypes using pink noise as excitation signal (e.g. Tab. C.1) it is clearly visible that each prototype has its own limits depending on the built-in transducers and the static filter design. This implicates that not only the signal spectrum has to be known but also the receiver characteristics and the used ADSC filter such that perceivable distortions can be prevented.

5.1.4 Low frequency Limitation

From Section 3.4.2 it is known that the ideal compensation filter has to be limited towards low frequencies in order to enable a stable filter design as well as to avoid audible distortions. In this work, this is achieved by adding a second order high-pass filter to the compensation filter.

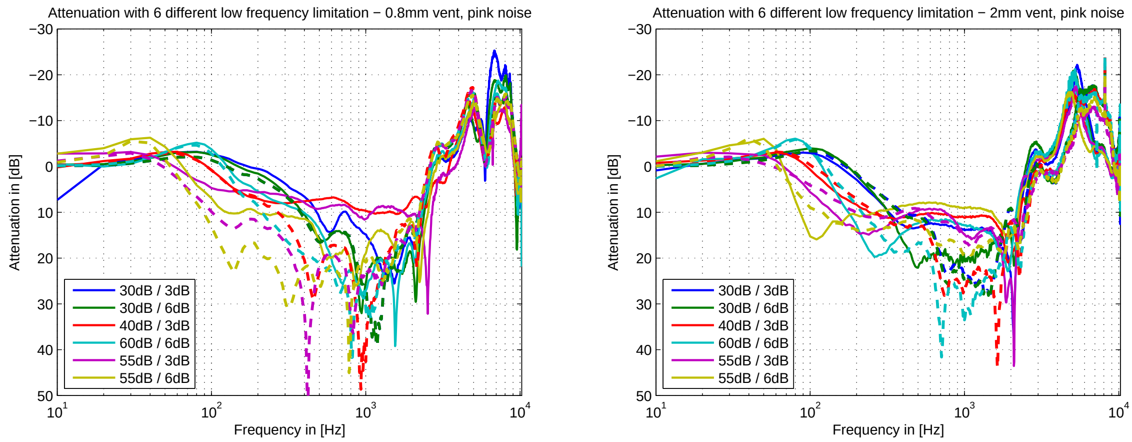

(a) AnH_R prototype with 0.8 mm vent

(b) AnH_R prototype with 2 mm vent

Figure 5.6: Attenuation of 6 different compensation filters with varying maximal gain (first value) and low frequency overshoot (second value)

Fig. 5.6 shows the attenuation of 6 different compensation filters, whose maximal gain and low frequency overshoot is varied using the AnH_R prototype with a 0.8 mm and 2 mm vent diameter. The cut-off frequency of the second order high-passes was set to 120, 95 and 40 Hz, which corresponds to 30, 40 and 55 dB (2 mm vent) and 15, 23 and 40 dB (0.8 mm vent) maximal gain, respectively. For each cut-off frequency the compensation filter was designed with an allowed low frequency overshoot of 3 and 6 dB.

From the results with pink noise excitation depicted in Tab. C.9 it can be stated that a higher maximal gain increases in general the bandwidth but lowers also the tolerable SPL in front of the ear. This is not valid for the cafeteria noise, whose main energy lies above all cut-off frequencies of the second order high-pass filters. Since the speech spectrum decays fast towards DC, changing the high-pass cut-off frequency has no significant influence on the SPL. For signals with high energy at low frequencies an increase of the cut-off frequency yields a higher SPL without audible distortions, though, at the expense of a reduced average attenuation and a narrower bandwidth.

Since the developed static filter framework selects the high-pass filter such that the limits are fulfilled and the average attenuation is maximized, the overshoot of the calculated compensation filters may be lower than stated (see Tab. C.9). Moreover, only for the 2 mm vent the measured objective parameters coincide well with the calculated ones. The high deviations for the smaller vent are mainly caused by the alteration of the receiver response, which is also visible on the spread of the overall gain G.

The results of the different low frequency limitations show that the maximal SPL in front of the ear can be controlled by changing the cut-off frequency of the high-pass filter, which defines the maximum gain of the compensation filter. However, this influences the average attenuation and the bandwidth. By lowering the overshoot, the average attenuation and the bandwidth decrease, whereby no significant increase of the SPL could be measured. The low frequency limitation allows to trade between a high SPL and a broad attenuation and may be adjusted according to the acoustic situation to which the subject is exposed.

5.2 Adaptive Design

The adaptive ADSC system was tested only with the ITE hardware model (ITE-HM) in order to avoid any hearing damage due to potential instabilities of the algorithms. The used vents of the ITE-HM have a radius of 0.575 and 0.225 mm and both a length of 5 mm, which corresponds approximately to the 2 mm and 0.8 mm vents of the ITE prototypes. In this work the focus of the adaptive system lies on its achievable attenuation and differences to the static filter design. Thus, the parameters of the algorithms, i.e. the leakage factor β_{T} of the FxNLMS algorithm and β_{F} of the FxFLMS algorithm as well as the forgetting factor λ used for the signal power estimation, were not optimized but kept constant for all trials. As long as a stable identification process was guaranteed, the step size parameter α_{T} respectively α_{F} was set to 0.5, otherwise appropriately reduced. Each adaptation process was measured for a time period of 25 seconds, which showed to be sufficient for convergence in this ADSC application.

All adaptation processes were simulated off-line in Simulink® and measured with the RTS on-line each for pink and cafeteria noise excitation. In order to evaluate the results achieved with the adaptive filters, also the performance of a FIR-filter with the same length and computed with the frequency sampling method [56] was calculated. Furthermore, for each vent size a static compensation filter was computed by the framework outlined in Section 3.4 and its performance calculated and measured with the RTS, which allows to compare between the both design methods.

Since the adaptive ADSC system was not tested with the author's ITE prototypes and the built-in receiver of the ITE-HM differs from the ones in the prototypes, no maximum SPL was recorded. Nevertheless, assuming a stable adaptation process which converges to the frequency response of the static compensation filter, the same maximum SPLs measured with the static filter approach are valid for the adaptive filter approach.

5.2.1 Simulation with ideal transfer functions

As a first step, the stability and the convergence of the two algorithms was examined off-line with simple REOG and PLANT transfer functions, which were chosen according to the simple acoustic model introduced in Section 2.1, i.e. the REOG as a 2^{nd} order butterworth low-pass filter with an additional delay of 9 samples at $f_{\mathrm{s}} = 20480$ Hz and the PLANT as a 2^{nd} order butterworth high-pass filter with 3 samples delay. The additional delays ensure that the resulting ideal compensation filters are causal.

Fig. 5.7 shows 4 different learning curves of the FxNLMS and the FxFLMS algorithm with $N = 2048$ filter coefficients and a white noise excitation signal. In the first case (*blue*), where only the REOG has to be identified, i.e. the PLANT is 1, the mean squared error (MSE) decreases by a factor of nearly 10^{-30}, which is close to the floating-point relative accuracy of MATLAB® , i.e. eps $= 2^{-52}$. Adding a low frequency limiting 2^{nd} order high-pass in cascade to the REOG transfer function (*green*) yields still a reduction of the MSE by a factor of approximately 10^{-12}, which still signifies a high attenuation.

Expanding the configuration with the simple model of the PLANT results only in usable filter coefficients, if the equalization filter introduced in Section 4.3.2 is part of the system (*cyan*). Otherwise, the filter length is too short in order to represent the impulse response of the compensation filter accurately (*red*).

From Fig. 5.7 one can see that the convergence time differs between the two algorithms which results from the different step sizes μ_{FxNLMS} and μ_{FxFLMS}. However, this was not further ana-

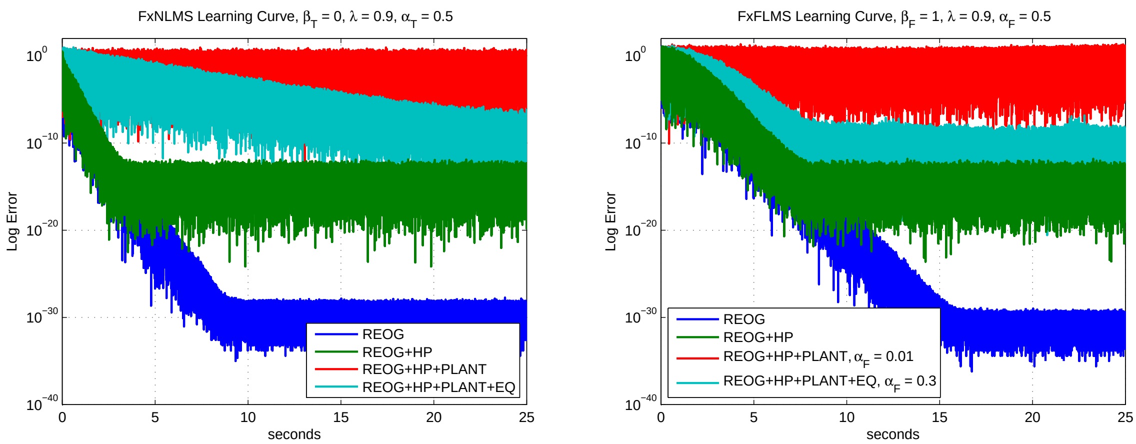

(a) FxNLMS algorithm, $\beta_{\mathrm{T}} = 0$, $\lambda = 0.9$

(b) FxFLMS algorithm, $\beta_{\mathrm{F}} = 1$, $\lambda = 0.9$

Figure 5.7: Learning curve of 4 *simple* REOG *and* PLANT *transfer functions*

lyzed since the convergence speed is not relevant in this work.

The impulse response, the corresponding frequency response and the resulting attenuation of the 4 adaptive filters are plotted in Section C.2.1.

5.2.2 Measurements with real transfer functions

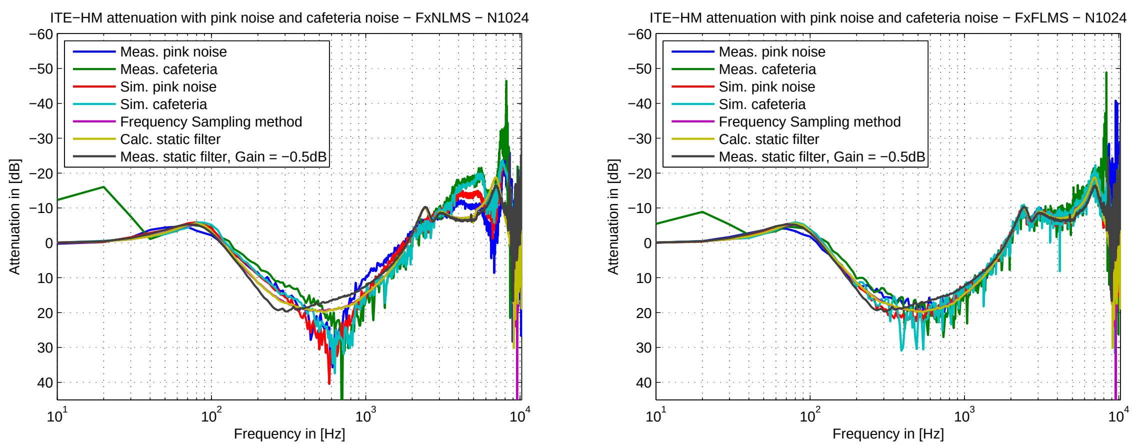

(a) FxNLMS algorithm, $\beta_{\mathrm{T}} = 0$, $\lambda = 0.9$

(b) FxFLMS algorithm, $\beta_{\mathrm{F}} = 1$, $\lambda = 0.9$

Figure 5.8: Attenuation of the ITE-HM with 0.575 *mm vent radius and* $N = 1024$ *filter coefficients*

Fig. 5.8 depicts the attenuations of the ITE-HM with a vent radius of 0.575 mm and $N = 1024$ filter coefficients. One can see that the calculated static filter (*yellow*) and the calculated FIR-filter (*magenta*) correspond closely to each other, which means that the number of coefficients is chosen sufficiently high. The differences between the measured and the calculated attenuation of the static filter is assumed to arise from a deviation of the transfer functions over time similar to the differences of the AnH_R ITE prototype discussed in Section 5.1.1, since the static filter are also based on transfer function measured in August 2012.

Comparing the different algorithms one can see that the resulting attenuation curves of the converged FxFLMS agree well with the outcome of the static filter design. The FxNLMS algorithm produces a high attenuation around 600 Hz, which is where the REOG of the 0.575 mm vent has its cut-off frequency (see Fig. 2.4, *magenta*). This is at the cost of a deviation in particular between 3 and 7 kHz, which, however, is still tolerable for this application.

Contrary to the simulated attenuation, the measured attenuation of both algorithms (*blue* and *green*) deviates strongly from the static filter attenuation (*yellow*) around 8 kHz, because of a poor excitation of this frequency region. This may be caused by either low energy of the excitation signal in this frequency region or by the $\lambda/4$ resonance of the residual ear canal, which provokes a decay of the sound pressure in front of the canal microphone M_c (see Fig. 2.4). A huge deviation also occurs at low frequencies using the cafeteria noise as excitation (*green*) due to a poor SNR, which results in a high overshoot at 20 Hz of -16 and -8.9 dB. In order to avoid such erroneous adaptations, which may lead to an unstable adaptation process, one has to modify the leakage factor β_T and β_F, respectively, which, however, was not further investigated in this work.

Tab. C.11 lists the objective parameters of the ITE-HM with a 0.575 mm vent radius for $N = 1024$ filter coefficients. From there one can see that the on-line measurements correlate very well with the off-line simulated values and both algorithms adapt as expected.

Decreasing the number of filter coefficients to $N = 128$ yields a greater difference between the static and the adaptive case (see Fig. C.9). In contrast to the case with $N = 1024$, the attenuation achieved with the calculated FIR-filter (*magenta*) does not fit anymore accurately the attenuation achieved with the static filter design (*yellow*). Nevertheless, the smaller number of filter coefficients does not deteriorate the performance (see Tab. C.12). However, instead of a smooth curve the resulting attenuation curve has several peaks and valleys, which may influence the sound quality of the ADSC system.

The achievable attenuation of the ITE-HM with the smaller vent, i.e. 0.225 mm vent radius, are depicted in Fig. C.12 ($N = 1024$) and Fig. C.15 ($N = 128$). Contrary to the 0.575 mm vent, neither the calculated nor the measured attenuation of the static filter design fit with the calculated FIR-filter. Furthermore, the differences between the simulated and measured attenuation of the adaptive system are clearly visible. This is mainly caused by the poor SNR of the excitation signal at the canal microphone, which deteriorates the adaptation process.

The average attenuation D_{avg} achieved by the simulated adaptive system outperforms the static filter case considerably but at the expense of either violating the low frequency overshoot limit or the maximal gain limit or reducing the bandwidth. Since exceeding the low frequency limits yields most probably audible distortions, it is not feasible to use the developed adaptive ADSC system for small vents without adjusting the algorithm parameters.

Reducing the number of filter coefficients from $N = 1024$ to $N = 128$ results in this case even in better objective parameters (see Tabs. C.13 and C.14). This occurs because for the higher number of filter coefficients both algorithms have difficulties to converge to a causal adaptive filter in particular with pink noise excitation. It is assumed that by optimizing the algorithm parameters, i.e. the step size, the leakage factor and the forgetting factor, the filter with more coefficients achieves also a better performance.

In summary, it can be stated that the adaptive ADSC system identifies the desired frequency response, i.e. the bounded compensation filter $\tilde{H}_{\text{COMP}}(j\omega)$, as long as all frequencies are sufficiently excited by a signal. This is valid for both algorithms, though the results achieved by the FxFLMS algorithm, $\beta_F = 1$, $\lambda = 0.9$ are closer to the static IIR filter design. Although the adaptive method may surpass the static method regarding some objective parameters, the computational costs and the complexity in order to ensure an absolute stable adaptation process makes the adaptive ADSC system less attractive for the application in hearing aids. Furthermore, the upcoming platform has only 10 biquads, which would restrict an adaptive FIR-filter to 20 coefficients.

6 Conclusion and Further Work

6.1 Conclusion

In this thesis, ADSC was developed for vented hearing aids using a feed-forward structure with a static and an adaptive filter design. Therefore, the acoustic environment and its effect on the direct sound as well as on the receiver response were outlined. Furthermore, the variability of the acoustic environment was analyzed for 6 ITE prototypes.

Different objective measures for the characterization of audible distortions generated by the receiver were examined and presented in the context of ADSC. So far, no significant mapping could be found between the measures and the perceived distortion.

Furthermore, a framework for the static filter design was developed in MATLAB® and its performance measured in Simulink® with a real time system (RTS) on ITE prototypes (see Appendix D). For the adaptive filter the calculation of the error signal had to be adjusted to the requirements of this application and the time- and frequency-domain algorithms were implemented on Simulink® and tested with the RTS on an ITE hardware model.

In general, it can be concluded from the results that ADSC achieves a broadband direct sound attenuation of 10 to 20 dB between 200 Hz and 2 kHz with SPLs in front of the ear up to 90 dB with a 2 mm vent diameter. This outcome signifies that ADSC yields certainly an improvement of the HI-algorithm performance as well as of the sound quality for the hearing aid user.

The low variability of the transfer functions for vents with 2 mm diameter requires only a small adaptation of the overall gain in order to achieve a similar attenuation of the direct sound for each insertion of the ITE prototype. Even more, it is possible to applicate non-individual static filters and still obtain a comparable good attenuation.

This is not the case for the smaller vent dimensions, where the variability increases due to the no more negligible leakage effect, which deteriorates the performance of the static filter approach. However, the individual designed filters extend the bandwidth down to 100 Hz and performs distortion-free up to 100 dB SPLs with speech-like ambient sounds.

The comparison of the static filter approach and the adaptive filter approach shows that for medium vents both designs achieve a similar attenuation and the adaptive system has no additional advantage. For the smaller vent diameters the attenuation performance of the adaptive

ADSC system outperforms the static approach at the costs of a high overshoot at low frequencies and a high maximal gain, which exceed the imposed requirements. This occurs because the adaptive system has difficulties to identify the desired impulse response, since the SNR in the ear canal decreases with diminishing vent diameter. It is assumed that by optimizing the parameters of the adaptive algorithms the identification process can be improved, which was not further investigated in this work.

Since the improvement of an adaptive solution is little in comparison with the static one concerning the attenuation performance and fulfillment of the imposed limits is not ensured, the additional computational costs and the requirements on the hardware are high and the adaptive process may suffer from stability issues, it is worth to focus on the static filter design.

The results show also that the usability of the ADSC system depends highly on the spectra of the ambient sounds and the vent dimension. While the developed system performs distortion-free up to SPLs of 90 dB (2 mm vent diameter) for signals with speech-like spectra, the maximal SPLs decay below 50 dB for signals with high energy at the low frequencies such as traffic noise. This signifies that either the low frequency limitation has to be done more restrictive at the cost of the attenuation bandwidth or the overall gain of the ADSC system has to be reduced dependent on the signal such that audible distortions are avoided.

6.2 Further Work

So far, the feasibility of a static ADSC system for hearing instruments was only shown on a real time system with low latency input/output cards running a Simulink® model. This allowed to develop the ADSC system without any constraints concerning the hardware. Implementing the static ADSC system on modern HI platform implies a modification of the filter design, since the sampling frequency is on a higher rate and the filter coefficients have to be defined as fix-point numbers instead of floating-point. Furthermore, the input/output delay may exceed the one of the RTS and also the SNR could be reduced. Finally, by now the power consumption of the receiver was not considered but may surpass the available power, which signifies a reduction of the maximal gain.

The mentioned issues on the one hand demand for an adaptation of the developed static filter design framework and on the other hand may limit the achievable attenuation.

All measurements in this thesis were conducted with ITE prototypes or models. Since nowadays RICs and BTEs are the most commonly used hearing aids, it is worth to adapt the static ADSC system to work with those models. However, this implicates a huge modification of the developed system, since the microphones are not placed anymore in the vicinity of the vent entry but behind the ear. Thus, the performance will be highly direction-dependent and may even amplify the direct sound for certain incident angles. A solution is to place an additional microphone at the entry of the vent, which would allow the application of the developed ADSC system.

The ADSC with static filter design showed satisfying results on the ITE prototype for two vent dimensions. However, especially for a small vent it is necessary to adjust an overall gain in order to achieve the pre-calculated attenuation. This is done manually by the user, which is not feasible for the implementation in hearing aids. This could be solved with an adaptive overall gain control, which maximizes the broadband attenuation on the condition that the low frequency thresholds concerning the overshoot and the maximal gain are always fulfilled.

Furthermore, in order to avoid audible distortions the spectrum of the ambient sound has to be monitored and the direct sound attenuation accordingly adapted. Further research has to be done regarding the detection of audible receiver distortion and their coherence to the driving receiver signal has to be investigated in more detail. The distortions can be avoided by either changing the compensation filter coefficients in real time or by adjusting the overall gain. Both needs an adaptive solution without delay to ensure a distortion-free ADSC system.

The focus of this thesis relied on the maximization of the broadband direct sound attenuation without analyzing the potential improvement for the hearing impaired people. Thus, further measurements have to be conducted where the ADSC system is used in combination with the hearing instrument and the superposition of both the HI-processed signal and the ADSC signal is emitted by the receiver. This allows to quantify the achieved improvement in SNR an its effect for hearing impaired people, which can be used as a base for further enhancement regarding HI performance.

Furthermore, the impact of the developed ADSC system on the sound quality has to be studied. It may be necessary to modify the ADSC system due to sound quality reasons and aim at the reduction of the comb filter effect instead of maximizing the direct sound attenuation.

A

Calculation of the Algorithmic Bound

The computation of the algorithmic bound is derived according to the internal Phonak AG report written by Zurbrügg [46].
The direct sound signal $d(t)$, which is to be attenuated, is given by

$$d(t) = A \cdot \cos(\omega t) \tag{A.1}$$

where $\omega = 2\pi f$ is the angular frequency of the single sine wave and A is its peak value.
The ADSC signal $z(t)$ is denoted by

$$z(t) = \hat{A} \cdot \cos(\omega t + \pi + \Delta\phi) = -A \cdot 10^{\frac{\Delta A}{20}} \cdot \cos(\omega t + \Delta\phi) \tag{A.2}$$

where $\Delta\phi$ is the phase deviation and ΔA is the amplitude deviation in dB. The attenuation is then the ratio of the RMS of the direct signal to the RMS of the superposition of the direct and ADSC signal, i.e.

$$D = 20\log_{10}\left(\frac{\overline{d(t)}}{\overline{d(t)+z(t)}}\right) = -20\log_{10}\left(\frac{\overline{d(t)+z(t)}}{\overline{d(t)}}\right) \tag{A.3}$$

which can be reformulated to

$$D = -20\log_{10}\left(\frac{\sqrt{\frac{\omega}{2\pi}\int_t^{t+\frac{2\pi}{\omega}}(d(t)+z(t))^2dt}}{\sqrt{\frac{\omega}{2\pi}\int_t^{t+\frac{2\pi}{\omega}}d^2(t)dt}}\right) \tag{A.4}$$

Since the RMS value of a single sine wave is $A_{\mathrm{RMS}} = \frac{A}{\sqrt{2}}, Eq.\ (A.4)$ can be simplified

$$\begin{aligned} D &= -20\log_{10}\left(\sqrt{\frac{\omega}{A^2\cdot\pi}\int_t^{t+\frac{2\pi}{\omega}}(d(t)+z(t))^2dt}\right) \\ &= -10\log_{10}\left(\frac{\omega}{A^2\cdot\pi}\int_t^{t+\frac{2\pi}{\omega}}(d(t)+z(t))^2dt\right) \end{aligned} \tag{A.5}$$

Combining Eqs. (A.1) and A.2 with Eq. (A.5) yields

$$D = -10\log_{10}\left(\frac{\omega}{A^2\cdot\pi}\int_t^{t+\frac{2\pi}{\omega}}\Big(A\cdot cos(\omega t) - \hat{A}\cdot cos(\omega t + \Delta\phi)\Big)^2 dt\right) \tag{A.6}$$

Expanding the quadratic equation in Eq. (A.6) results in

$$\begin{aligned} D &= -10\log_{10}\left(\frac{\omega}{A^2\pi}\int_t^{t+\frac{2\pi}{\omega}}\Big(A^2\cdot cos^2(\omega t) - 2A\hat{A}\cdot cos(\omega t)\cdot cos(\omega t+\Delta\phi) + \hat{A}^2\cdot cos^2(\omega t+\Delta\phi)\Big)\,dt\right) = \\ &= -10\log_{10}\left(\frac{\omega}{\pi}\int_t^{t+\frac{2\pi}{\omega}}\Big(cos^2(\omega t) - 2\cdot 10^{\frac{\Delta A}{20}}cos(\omega t)\cdot cos(\omega t+\Delta\phi) + 10^{\frac{\Delta A}{10}}cos^2(\omega t+\Delta\phi)\Big)\,dt\right) \end{aligned} \tag{A.7}$$

Since

$$\frac{\omega}{\pi}\int_t^{t+\frac{2\pi}{\omega}} cos^2(\omega t+\Delta\phi)dt = \frac{\omega}{\pi}\int_t^{t+\frac{2\pi}{\omega}} cos^2(\omega t)dt = 1 \tag{A.8}$$

and

$$\frac{\omega}{\pi}\int_t^{t+\frac{2\pi}{\omega}} cos(\omega t)\cdot cos(\omega t+\Delta\phi)dt = cos(\Delta\phi) \tag{A.9}$$

one can formulate the attenuation D in relation to the amplitude and phase deviation:

$$D = -10\log_{10}\Big(1 - 2\cdot 10^{\frac{\Delta A}{20}}\cdot cos(\Delta\phi) + 10^{\frac{\Delta A}{10}}\Big) \tag{A.10}$$

B

Approximation Algorithm

B.1 Equation error minimization

The equation error minimizes the sum squared error in the least squares sense denoted by

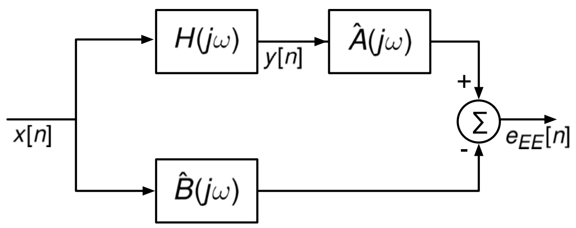

Figure B.1: Structure of the equation error [49]

Fig. B.1 shows the structure of the equation error, whose difference equation can be written as

$$\begin{aligned} e_{\mathrm{EE}}[n] &= y[n] - \widetilde{y}[n] = \\ &= y[n] + \hat{a}_1 \cdot y[n-1] + \cdots + \hat{a}_L \cdot y[n-L] - \hat{b}_0 \cdot x[n] - \cdots - \hat{b}_M \cdot x[n-M] \end{aligned} \tag{B.1}$$

where $x[n]$ is the input signal and $y[n]$ is the output signal of the desired filter $H(j\omega)$. $\hat{b}_m$ and $\hat{a}_l$ are the coefficients of the nominator and denominator polynomial of the estimated filter, respectively. Transforming Eq. (B.1) to the frequency domain and assuming an ideal dirac delta function as input, i.e.

$$\begin{aligned} x[n] &= \delta[n] & \Longleftrightarrow X(j\omega) &= \mathcal{F}\{\delta[n]\} &&= 1,\ \forall\omega \\ y[n] &= h[n] * \delta[n] & \Longleftrightarrow Y(j\omega) &= \mathcal{F}\{h[n] * \delta[n]\} &&= H(j\omega) \end{aligned} \tag{B.2}$$

where $h[n]$ is the impulse response of the desired frequency response $H(j\omega)$, yields

$$\begin{aligned} E_{\mathrm{EE}}(j\omega) &= H(j\omega) + \hat{a}_1 \cdot \mathrm{e}^{-j\omega} H(j\omega) + \cdots + \hat{a}_L \cdot \mathrm{e}^{-j\omega\cdot L} H(j\omega) - \hat{b}_0 \cdot \mathrm{e}^{-j\omega\cdot 0} - \cdots - \hat{b}_M \cdot \mathrm{e}^{-j\omega\cdot M} \\ &= \hat{A}(j\omega) H(j\omega) - \hat{B}(j\omega) \end{aligned}$$

(B.3)

Evaluating Eq. (B.3) at the discrete normalized frequency points $\omega_k = 2\pi\frac{k}{K}$, where $k = 0, \ldots, K-1$, and applying the vector/matrix notation, results in

$$\underline{E}_{\mathrm{EE}} = \underline{H} - \mathbf{\Phi}\underline{\hat{\theta}} \tag{B.4}$$

with

$$\begin{aligned}
\underline{H} &= \begin{bmatrix} H(j\omega_0) & H(j\omega_1) & \cdots & H(j\omega_{K-1}) \end{bmatrix}^T \\
\mathbf{\Phi} &= \begin{bmatrix} \underline{\Phi}_0 & \underline{\Phi}_1 & \cdots & \underline{\Phi}_{K-1} \end{bmatrix}^T \\
\underline{\Phi}_k &= \begin{bmatrix} -\mathrm{e}^{-j\omega_k} H(j\omega_k) & -\mathrm{e}^{-j\omega_k \cdot 2} H(j\omega_k) & \cdots & -\mathrm{e}^{-j\omega_k \cdot L} H(j\omega_k) & 1 & \mathrm{e}^{-j\omega_k} & \cdots & \mathrm{e}^{-j\omega_k \cdot M} \end{bmatrix}^T \\
\underline{\hat{\theta}} &= \begin{bmatrix} \hat{a}_1 & \hat{a}_2 & \cdots & \hat{a}_L & \hat{b}_0 & \hat{b}_1 & \cdots & \hat{b}_M \end{bmatrix}^T
\end{aligned} \tag{B.5}$$

A solution of the coefficient vector $\underline{\hat{\theta}}$ in the least square sense can be derived by minimizing the sum of the square of the equation error

$$\min_{\underline{\hat{b}},\underline{\hat{a}}} \epsilon_{\mathrm{EE}} = \sum_{k=0}^{K-1} |E_{\mathrm{EE}}(j\omega_k)|^2 = \underline{E}_{\mathrm{EE}}^H \underline{E}_{\mathrm{EE}} \tag{B.6}$$

Combining Eq. (B.6) and Eq. (B.4) yields

$$\min_{\underline{\hat{\theta}}} \epsilon_{\mathrm{EE}} = \left(\underline{H} - \mathbf{\Phi}\underline{\hat{\theta}}\right)^H \mathbf{W} \left(\underline{H} - \mathbf{\Phi}\underline{\hat{\theta}}\right) \;\; = \underline{H}^H \mathbf{W} \underline{H} - 2\underline{\hat{\theta}}^H \mathbf{\Phi}^H \mathbf{W} \underline{H} + \underline{\hat{\theta}}^H \mathbf{\Phi}^H \mathbf{W} \mathbf{\Phi} \underline{\hat{\theta}} \tag{B.7}$$

where ^{H} denotes the transposed conjugate complex of a matrix and $\mathbf{W}$ is a diagonal weighting matrix. The minimization of Eq. (B.7) with respect to $\underline{\hat{\theta}}$ is derived by calculating the gradient and setting it to zero, i.e. $\nabla_{\underline{\hat{\theta}}} \epsilon_{\mathrm{EE}} = \underline{0}$, and solving it for $\underline{\hat{\theta}}$:

$$\underline{\hat{\theta}} = \left(\mathbf{\Phi}^H \mathbf{W} \mathbf{\Phi}\right)^{-1} \mathrm{Re}\left\{\left(\mathbf{\Phi}^H \mathbf{W} \underline{H}\right)\right\} \tag{B.8}$$

It should be denoted that the estimated filter coefficients may yield to a non-minimum and unstable impulse response, since no constraints were formulated so far. Particularly the stability of the filter must be given in order to use it with the ANC system. This is achieved by flipping all poles $p > |1|$ into the unit circle, which has no influence on the magnitude response but alters the phase response.

B.2 Gauss-Newton method

Fig. B.2 shows the structure of the output error, whose difference equation can be written as

$$\begin{aligned}
e_{\mathrm{EE}}[n] &= y[n] - \hat{y}[n] = \\
&= y[n] + \hat{a}_1 \cdot \hat{y}[n-1] + \cdots + \hat{a}_L \cdot \hat{y}[n-L] - \hat{b}_0 \cdot x[n] - \cdots - \hat{b}_M \cdot x[n-M]
\end{aligned} \tag{B.9}$$

where $x[n]$ is the input signal, $y[n]$ is the output of the desired filter $H(j\omega)$ and $\hat{y}[n]$ is the output of the estimated filter $\hat{H}(j\omega) = \frac{\hat{B}(j\omega)}{\hat{A}(j\omega)}$.

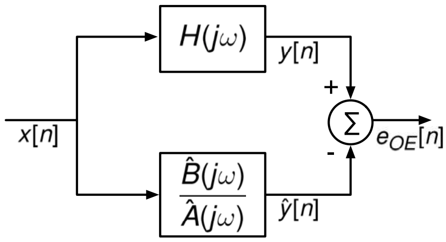

Figure B.2: Structure of the output error [49]

The Gauss-Newton method minimizes the sum of the square of the output error in the least squares sense, i.e.

$$\min \epsilon_{\mathrm{OE}} = \sum_{k=0}^{K-1} |E_{\mathrm{OE}}(j\omega_k)|^2 = \sum_{k=0}^{K-1} \left| H(j\omega_k) - \hat{H}(j\omega_k) \right|^2 \tag{B.10}$$

Therefore, it linearizes Eq. (B.10) by approximating the estimated filter $\hat{H}(j\omega)$ by the first-order Taylor series [57], i.e.

$$\begin{aligned} \hat{H}(j\omega, \underline{\hat{\theta}}) &\approx \hat{H}(j\omega, \underline{\hat{\theta}}^{(i)}) + \nabla^T_{\underline{\hat{\theta}}} \hat{H}(j\omega, \underline{\hat{\theta}}^{(i)}) \cdot \underline{\hat{\delta}}^{(i)} \\ \underline{\hat{\delta}}^{(i)} &= \underline{\hat{\theta}} - \underline{\hat{\theta}}^{(i)} \end{aligned} \tag{B.11}$$

where $\underline{\hat{\theta}}^{(i)}$ is the coefficient vector of the i^{th} iteration and $\nabla_{\underline{\hat{\theta}}} \hat{H}(j\omega, \underline{\hat{\theta}}^{(i)})$ is the gradient vector of $\hat{H}(j\omega, \underline{\hat{\theta}}^{(i)})$. According to [67] the calculation of the gradient is denoted by

$$\begin{aligned} \nabla_{\underline{\hat{\theta}}} \hat{H}(j\omega, \underline{\hat{\theta}}^{(i)}) = \frac{1}{\hat{A}(j\omega, \underline{\hat{\theta}}^{(i)})} \Big[-\mathrm{e}^{-j\omega} \hat{H}(j\omega, \underline{\hat{\theta}}^{(i)}) \quad \cdots \quad -\mathrm{e}^{-j\omega \cdot L} \hat{H}(j\omega, \underline{\hat{\theta}}^{(i)}) \\ \mathrm{e}^{-j\omega \cdot 0} \quad \cdots \quad \mathrm{e}^{j\omega \cdot M} \Big]^T \end{aligned} \tag{B.12}$$

From Eq. (B.11) the output error can then be rewritten to

$$\begin{aligned} E_{\mathrm{OE}}(j\omega, \underline{\hat{\theta}}) &\approx H(j\omega) - \hat{H}(j\omega, \underline{\hat{\theta}}^{(i)}) - \nabla^T_{\underline{\hat{\theta}}} \hat{H}(j\omega, \underline{\hat{\theta}}^{(i)}) \cdot \underline{\hat{\delta}}^{(i)} \\ &= E_{\mathrm{OE}}(j\omega, \underline{\hat{\theta}}^{(i)}) - \nabla^T_{\underline{\hat{\theta}}} \hat{H}(j\omega, \underline{\hat{\theta}}^{(i)}) \cdot \underline{\hat{\delta}}^{(i)} \end{aligned} \tag{B.13}$$

Using the vector/matrix notation and evaluating Eq. (B.13) at the discrete normalized frequency points $\omega_k = 2\pi\frac{k}{K}$, the weighted quadratic output error follows as

$$\min_{\underline{\hat{\delta}}^{(i)}} \epsilon_{\mathrm{OE}} = \left(\underline{E}^{(i)}_{\mathrm{OE}} - \mathbf{\Psi}^{(i)} \underline{\hat{\delta}}^{(i)} \right)^H \mathbf{W} \left(\underline{E}^{(i)}_{\mathrm{OE}} - \mathbf{\Psi}^{(i)} \underline{\hat{\delta}}^{(i)} \right) \tag{B.14}$$

with

$$\begin{aligned} \underline{E}^{(i)}_{\mathrm{OE}} &= \left[E_{\mathrm{OE}}(j\omega_0, \underline{\hat{\theta}}^{(i)}) \quad E_{\mathrm{OE}}(j\omega_1, \underline{\hat{\theta}}^{(i)}) \quad \cdots \quad E_{\mathrm{OE}}(j\omega_{K-1}, \underline{\hat{\theta}}^{(i)}) \right]^T \\ \mathbf{\Psi}^{(i)} &= \left[\nabla_{\underline{\hat{\theta}}} \hat{H}(j\omega_0, \underline{\hat{\theta}}^{(i)}) \quad \nabla_{\underline{\hat{\theta}}} \hat{H}(j\omega_1, \underline{\hat{\theta}}^{(i)}) \quad \cdots \quad \nabla_{\underline{\hat{\theta}}} \hat{H}(j\omega_{K-1}, \underline{\hat{\theta}}^{(i)}) \right]^T \end{aligned} \tag{B.15}$$

Eq. (B.14) is similar to Eq. (B.7) of the equation error and is solved identically, i.e.

$$\underline{\hat{\delta}}^{(i)} = \left(\boldsymbol{\Psi}^{(i)H}\mathbf{W}\boldsymbol{\Psi}^{(i)}\right)^{-1}\mathrm{Re}\Big\{\left(\boldsymbol{\Psi}^{(i)H}\mathbf{W}\underline{E}_{\mathrm{OE}}^{(i)}\right)\Big\} \tag{B.16}$$

Now it is possible to calculate the new IIR coefficient vector with the update vector $\underline{\hat{\delta}}^{(i)}$ by

$$\underline{\hat{\theta}}^{(i+1)} = \underline{\hat{\theta}}^{(i)} + \mu\underline{\hat{\delta}}^{(i)} \tag{B.17}$$

where μ is the step size.

C
Additional Results

C.1 Static results

C.1.1 Differences between Calculations and Measurements

Vent	Prototype	Signal	D_avg [dB]	Over_low [dB]	Over_high [dB]	Centroid [Hz]	dB_max [dB]	f1_10dB [Hz]	f2_10dB [Hz]	Gain [dB]	SPL [dB]	dB(A) [dB]
2mm	AnH_L	pink #1	10.2	5.3	5.7	527.5	49.5	271	2081	1.0	72.4	69.8
		pink #2	12.0	5.9	2.3	541.2	49.0	269	1929	0.5	77.1	75.3
		pink #3	11.9	5.6	0.8	514.2	49.0	254	1889	0.5	74.8	70.3
		ref.	*12.2*	*5.5*	*1.4*	*584.3*	*48.5*	*260*	*2220*			
		calc. #1	*9.4*	*4.9*	*2.5*	*501.2*	*48.5*	*270*	*2430*			
		calc. #2	*12.1*	*5.0*	*2.5*	*501.2*	*48.5*	*270*	*1900*			
	AnH_R	pink #1	11.4	6.1	0.1	359.4	45.9	178	2169	-0.5	81.4	79.7
		pink #2	11.7	5.9	1.4	341.5	45.9	171	2215	-0.5	82.6	80.9
		pink #3	12.4	6.0	0.3	359.4	46.4	176	2140	0.0	80.6	78.6
		ref.	*14.5*	*5.9*	*-5.7*	*541.2*	*46.4*	*220*	*2530*			
		calc. #1	*11.4*	*5.7*	*-0.3*	*441.0*	*46.4*	*210*	*2040*			
		calc. #2	*12.6*	*5.5*	*-1.1*	*378.2*	*46.4*	*190*	*2310*			

Table C.1: Differences between calculated and measured performance of the AnH_L and AnH_R ITE prototype with 2 mm vent diameter

C.1.2 Variability of the attenuation

Intra-individual variability

Vent	Prototype	Signal	D_avg	Over_low	Over_high	Centroid	dB_max	f1_10dB	f2_10dB	Gain	SPL	dB(A)
			[dB]	[dB]	[dB]	[Hz]	[dB]	[Hz]	[Hz]	[dB]	[dB]	[dB]
2mm	AnH_L	pink	10.2	5.3	5.7	527.5	49.5	271	2081	1.0	74.9	72.3
		pink	12.0	5.9	2.3	541.2	49.0	269	1929	0.5	79.6	77.8
		pink	11.9	5.6	0.8	514.2	49.0	254	1889	0.5	77.3	72.8
		ref.	*12.2*	*5.5*	*1.4*	*584.3*	*48.5*	*260*	*2220*			
	AnH_R	pink	11.4	6.1	0.1	359.4	45.9	178	2169	-0.5	83.4	81.7
		pink	11.7	5.9	1.4	341.5	45.9	171	2215	-0.5	84.5	82.9
		pink	12.4	6.0	0.3	359.4	46.4	176	2140	0.0	82.6	80.6
		ref.	*14.5*	*5.9*	*-5.7*	*541.2*	*46.4*	*220*	*2530*			
08mm	AnH_L	pink	14.4	6.2	-10.5	398.1	41.1	107	1812	-2.5	87.2	84.4
		pink	14.0	6.2	-10.9	388.1	40.1	99	1876	-3.5	91.1	87.5
		pink	13.3	6.1	-10.6	388.1	40.1	102	1812	-3.5	90.4	87.5
		ref.	*16.2*	*6.2*	*-3.2*	*368.7*	*43.6*	*110*	*2120*			
	AnH_R	pink	11.0	6.2	-15.5	341.5	35.1	234	1072	-5.0	94.5	92.8
		pink	11.5	6.2	-16.2	359.4	35.1	241	1181	-5.0	96.3	94.9
		pink	11.6	5.9	-16.4	378.2	35.1	239	2597	-5.0	95.8	94.3
		ref.	*22.4*	*5.5*	*-12.4*	*350.3*	*40.1*	*90*	*2230*			

Table C.2: Intra-individual variability of the attenuation of the AnH_L and AnH_R ITE prototype with 2 and 0.8 mm vent diameter measured with pink noise

Vent	Prototype	Signal	D_avg	Over_low	Over_high	Centroid	dB_max	f1_10dB	f2_10dB	Gain	SPL	dB(A)
			[dB]	[dB]	[dB]	[Hz]	[dB]	[Hz]	[Hz]	[dB]	[dB]	[dB]
2mm	AnH_L	cafeteria	10.6	5.7	6.0	555.2	49.5	280	2010	1.0	89.6	87.4
		cafeteria	10.8	5.9	2.7	541.2	49.0	274	1956	0.5	90.4	88.5
		cafeteria	11.0	5.7	1.0	541.2	49.0	271	1916	0.5	85.9	83.6
		ref.	*12.2*	*5.5*	*1.4*	*584.3*	*48.5*	*260*	*2220*			
	AnH_R	cafeteria	10.8	5.4	0.3	378.2	45.9	185	2154	-0.5	94.3	92.3
		cafeteria	11.0	5.1	1.4	359.4	45.9	182	2215	-0.5	95.7	93.5
		cafeteria	11.6	5.6	0.6	378.2	46.4	185	2140	0.0	94.8	92.7
		ref.	*14.5*	*5.9*	*-5.7*	*541.2*	*46.4*	*220*	*2530*			
08mm	AnH_L	cafeteria	12.0	4.4	-10.6	398.1	41.1	246	1763	-2.5	100.3	97.7
		cafeteria	10.7	3.7	-11.2	398.1	40.1	393	1838	-3.5	100.6	98.0
		cafeteria	11.2	3.7	-10.7	398.1	40.1	335	1825	-3.5	101.0	98.4
		ref.	*16.2*	*6.2*	*-3.2*	*368.7*	*43.6*	*110*	*2120*			
	AnH_R	cafeteria	10.3	12.3	-15.4	359.4	35.1	267	1140	-5.0	106.5	104.3
		cafeteria	10.3	14.0	-16.2	388.1	35.1	288	1231	-5.0	104.8	102.8
		cafeteria	10.4	14.0	-16.1	398.1	35.1	276	2579	-5.0	104.7	102.5
		ref.	*22.4*	*5.5*	*-12.4*	*350.3*	*40.1*	*90*	*2230*			

Table C.3: Intra-individual variability of the attenuation of the AnH_L and AnH_R ITE prototype with 2 and 0.8 mm vent diameter measured with cafeteria noise

Inter-individual variability

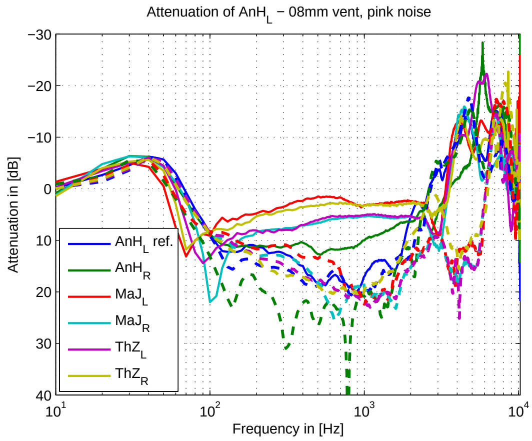

(a) AnH_L prototype, 0.8 mm vent diameter

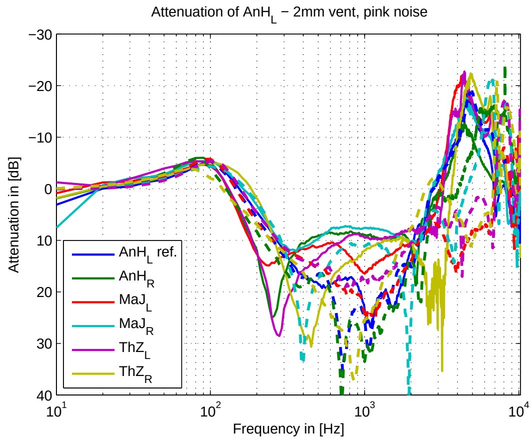

(b) AnH_L prototype, 2 mm vent diameter

Figure C.1: Attenuation of the AnH_L prototype for two different vent diameters with varying static filters based on 6 different prototypes: measured attenuation (different colors, solid) and reference attenuation achieved by the static filters based on the particular prototype

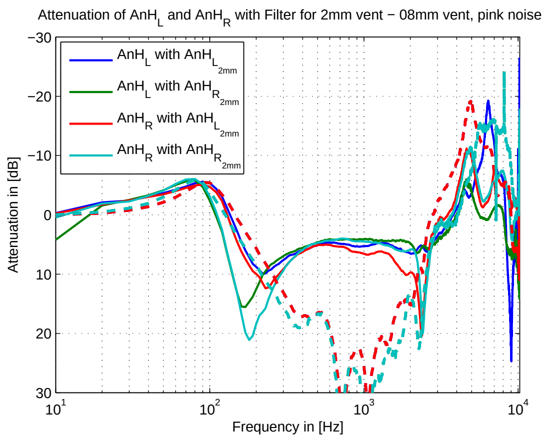

(a) 0.8 mm vent diameter

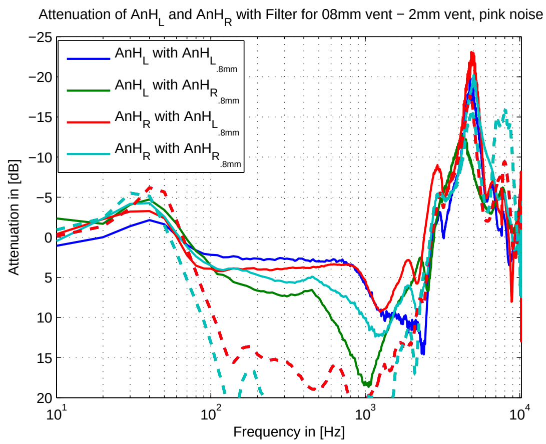

(b) 2 mm vent diameter

Figure C.2: Attenuation of the AnH_L and AnH_R prototype with two different vent diameters: application of the static filter of the 2 mm vent on the 0.8 mm vent prototype (a) and vice versa (b) (different colors, solid) and their respective reference attenuation (dashed)

Filter	Prototype	Signal	D_avg	Over_low	Over_high	Centroid	dB_max	f1_10dB	f2_10dB	Gain	SPL	dB(A)
			[dB]	[dB]	[dB]	[Hz]	[dB]	[Hz]	[Hz]	[dB]	[dB]	[dB]
AnH_L	AnH_L	pink	10.2	5.3	5.7	527	49.5	271	2081	1.0	74.9	72.3
	AnH_R	pink	14.4	5.8	-1.0	527	46.5	254	1739	-2.0	83.5	82.0
		ref.	*12.2*	*5.5*	*1.4*	*584*	*48.5*	*260*	*2220*			
AnH_R	AnH_L	pink	9.4	6.0	6.3	324	48.9	188	433	2.5	77.4	74.4
	AnH_R	pink	11.4	6.1	0.1	359	45.9	178	2169	-0.5	83.4	81.7
		ref.	*14.5*	*5.9*	*-5.7*	*541*	*46.4*	*220*	*2530*			
MaJ_L	AnH_L	pink	9.8	4.7	7.0	398	49.3	181	2200	-1.0	75.5	72.3
	AnH_R	pink	13.2	5.1	5.1	378	47.3	176	2067	-3.0	78.6	77.2
		ref.	*10.2*	*5.7*	*-1.0*	*555*	*50.3*	*260*	*2290*			
MaJ_R	AnH_L	pink	5.6	5.4	6.5	452	47.7	278	477	-1.0	74.1	71.1
	AnH_R	pink	6.1	5.4	3.7	476	44.7	298	587	-4.0	78.6	76.7
		ref.	*9.1*	*4.3*	*2.9*	*464*	*48.7*	*290*	*2320*			
ThZ_L	AnH_L	pink	11.4	5.3	11.9	341	52.2	188	723	0.0	69.4	66.0
	AnH_R	pink	10.6	5.0	7.9	359	48.7	184	1956	-3.5	79.2	77.5
		ref.	*9.1*	*5.3*	*-0.3*	*555*	*52.2*	*280*	*2050*			
ThZ_R	AnH_L	pink	10.8	4.9	14.3	476	44.4	261	1319	1.0	75.4	72.8
	AnH_R	pink	13.6	4.9	11.0	514	41.4	254	2081	-2.0	78.9	77.1
		ref.	*14.3*	*3.9*	*-2.6*	*570*	*43.4*	*250*	*1760*			
AnH_L_08mm	AnH_L	pink	2.9	2.1	3.0	359	49.6	1850	2474	6.0	86.4	82.0
	AnH_R	pink	3.9	3.3	1.3	308	48.1	NaN	NaN	4.5	87.3	86.3
		ref.	*16.2*	*6.2*	*-3.2*	*369*	*43.6*	*110*	*2120*			
AnH_R_08mm	AnH_L	pink	8.2	4.7	13.5	464	44.1	599	1483	4.0	84.9	82.6
	AnH_R	pink	5.6	4.3	2.2	398	38.6	986	1504	-1.5	94.6	93.2
		ref.	*22.4*	*5.5*	*-12.4*	*350*	*40.1*	*90*	*2230*			

Table C.4: Inter-individual variability of the attenuation of the AnH_L and AnH_R ITE prototype with 2 *mm vent diameter measured with pink noise*

Filter	Prototype	Signal	D_avg	Over_low	Over_high	Centroid	dB_max	f1_10dB	f2_10dB	Gain	SPL	dB(A)
			[dB]	[dB]	[dB]	[Hz]	[dB]	[Hz]	[Hz]	[dB]	[dB]	[dB]
AnH_L	AnH_L	pink	14.4	6.2	-10.5	398	41.1	107	1812	-2.5	87.2	84.4
	AnH_R	pink	9.9	4.6	-14.6	316	35.6	824	2246	-8.0	94.3	92.2
		ref.	*16.2*	*6.2*	*-3.2*	*369*	*43.6*	*110*	*2120*			
AnH_R	AnH_L	pink	11.2	6.3	-11.1	324	30.1	111	1000	-10.0	104.1	101.8
	AnH_R	pink	11.0	6.2	-15.5	341	35.1	234	1072	-5.0	94.5	92.8
		ref.	*22.4*	*5.5*	*-12.4*	*350*	*40.1*	*90*	*2230*			
MaJ_L	AnH_L	pink	3.7	5.0	0.2	205	45.4	64	80	4.0	84.1	81.2
	AnH_R	pink	8.9	6.4	-7.9	251	38.4	72	159	-3.0	96.9	95.5
		ref.	*12.8*	*5.6*	*-16.4*	*398*	*41.4*	*3210*	*5810*			
MaJ_R	AnH_L	pink	8.8	6.3	-2.0	221	43.7	86	155	2.0	87.0	84.4
	AnH_R	pink	6.5	5.8	-4.1	233	39.7	75	121	-2.0	92.3	90.5
		ref.	*15.3*	*5.9*	*-20.7*	*419*	*41.7*	*3050*	*5640*			
ThZ_L	AnH_L	pink	7.6	6.0	-10.3	251	40.2	76	129	-1.5	96.1	93.9
	AnH_R	pink	8.1	6.0	-11.7	264	34.2	78	127	-7.5	96.8	95.3
		ref.	*15.3*	*5.9*	*-21.1*	*408*	*41.7*	*140*	*2730*			
ThZ_R	AnH_L	pink	4.8	5.6	2.1	215	44.3	69	80	2.5	90.4	86.1
	AnH_R	pink	7.0	3.6	-5.6	245	34.8	9397	19	-7.0	92.6	90.2
		ref.	*16.0*	*6.1*	*-14.6*	*388*	*41.8*	*120*	*1910*			
AnH_L_2mm	AnH_L	pink	4.8	5.6	-12.9	350	35.5	8589	9204	-13.0	95.5	92.8
	AnH_R	pink	5.8	5.1	-14.1	324	28.5	201	280	-20.0	95.9	93.9
		ref.	*12.2*	*5.5*	*1.4*	*584*	*48.5*	*260*	*2220*			
AnH_R_2mm	AnH_L	pink	6.7	5.8	-11.9	239	35.4	140	221	-11.0	87.6	85.0
	AnH_R	pink	8.1	6.0	-15.4	233	28.9	141	288	-17.5	95.4	94.0
		ref.	*14.5*	*5.9*	*-5.7*	*541*	*46.4*	*220*	*2530*			

Table C.5: Inter-individual variability of the attenuation of the AnH_L and AnH_R ITE prototype with 0.8 *mm vent diameter measured with pink noise*

Filter	Prototype	Signal	D_avg [dB]	Over_low [dB]	Over_high [dB]	Centroid [Hz]	dB_max [dB]	f1_10dB [Hz]	f2_10dB [Hz]	Gain [dB]	SPL [dB]	dB(A) [dB]
AnH_L	AnH_L	cafeteria	10.6	5.7	6.0	555	49.5	280	2010	1.0	89.6	87.4
	AnH_R	cafeteria	13.3	5.9	-0.9	514	46.5	260	1727	-2.0	91.9	89.9
		ref.	*12.2*	*5.5*	*1.4*	*584*	*48.5*	*260*	*2220*			
AnH_R	AnH_L	cafeteria	8.4	6.4	6.2	341	48.9	200	410	2.5	84.9	82.6
	AnH_R	cafeteria	10.8	5.4	0.3	378	45.9	185	14	-0.5	94.3	92.3
		ref.	*14.5*	*5.9*	*-5.7*	*541*	*46.4*	*220*	*2530*			
MaJ_L	AnH_L	cafeteria	9.1	5.1	6.9	419	49.3	189	2277	-1.0	85.3	83.0
	AnH_R	cafeteria	11.1	5.1	4.9	398	47.3	180	2053	-3.0	87.7	85.8
		ref.	*10.2*	*5.7*	*-1.0*	*555*	*50.3*	*260*	*2290*			
MaJ_R	AnH_L	cafeteria	6.5	5.4	6.0	441	47.7	269	559	-1.0	84.9	82.5
	AnH_R	cafeteria	6.8	6.0	3.5	476	44.7	280	684	-4.0	87.0	84.9
		ref.	*9.1*	*4.3*	*2.9*	*464*	*48.7*	*290*	*2320*			
ThZ_L	AnH_L	cafeteria	11.2	5.7	11.8	350	52.2	188	758	0.0	81.2	78.8
	AnH_R	cafeteria	11.5	4.8	7.7	333	48.7	180	1443	-3.5	89.6	87.5
		ref.	*9.1*	*5.3*	*-0.3*	*555*	*52.2*	*280*	*2050*			
ThZ_R	AnH_L	cafeteria	11.6	5.5	14.2	489	44.4	256	1337	1.0	82.1	79.8
	AnH_R	cafeteria	13.3	5.1	11.0	527	41.4	258	2081	-2.0	85.6	83.6
		ref.	*14.3*	*3.9*	*-2.6*	*570*	*43.4*	*250*	*1760*			
AnH_L_08mm	AnH_L	cafeteria	2.5	2.2	3.2	378	49.6	1863	2474	6.0	87.6	84.6
	AnH_R	cafeteria	3.5	3.3	1.6	316	48.1	NaN	NaN	4.5	95.0	92.9
		ref.	*16.2*	*6.2*	*-3.2*	*369*	*43.6*	*110*	*2120*			
AnH_R_08mm	AnH_L	cafeteria	7.6	4.4	13.7	514	44.1	621	1600	4.0	103.6	101.3
	AnH_R	cafeteria	5.0	4.5	1.9	419	35.1	1007	1483	-5.0	103.7	101.6
		ref.	*22.4*	*5.5*	*-12.4*	*350*	*40.1*	*90*	*2230*			

Table C.6: Inter-individual variability of the attenuation of the AnH_L and AnH_R ITE prototype with 2 mm vent diameter measured with cafeteria noise

Filter	Prototype	Signal	D_avg [dB]	Over_low [dB]	Over_high [dB]	Centroid [Hz]	dB_max [dB]	f1_10dB [Hz]	f2_10dB [Hz]	Gain [dB]	SPL [dB]	dB(A) [dB]
AnH_L	AnH_L	cafeteria	12.0	4.4	-10.6	398	41.1	246	1763	-2.5	100.3	97.7
	AnH_R	cafeteria	9.9	4.6	-14.6	316	35.6	824	2246	-8.0	104.9	102.8
		ref.	*16.2*	*6.2*	*-3.2*	*369*	*43.6*	*110*	*2120*			
AnH_R	AnH_L	cafeteria	10.2	7.7	-11.3	350	30.1	418	986	-10.0	112.8	110.4
	AnH_R	cafeteria	10.3	12.3	-15.4	359	35.1	267	1140	-5.0	106.5	104.3
		ref.	*22.4*	*5.5*	*-12.4*	*350*	*40.1*	*90*	*2230*			
MaJ_L	AnH_L	cafeteria	3.9	1.8	0.4	251	45.4	NaN	NaN	4.0	93.1	90.5
	AnH_R	cafeteria	8.4	2.9	-7.7	278	38.4	85	135	-3.0	103.7	101.7
		ref.	*12.8*	*5.6*	*-16.4*	*398*	*41.4*	*3210*	*5810*			
MaJ_R	AnH_L	cafeteria	9.0	4.5	-2.2	215	43.7	98	194	2.0	92.8	90.5
	AnH_R	cafeteria	6.4	4.3	-4.3	227	39.7	77	122	-2.0	101.9	99.8
		ref.	*15.3*	*5.9*	*-20.7*	*419*	*41.7*	*3050*	*5640*			
ThZ_L	AnH_L	cafeteria	6.9	6.3	-8.1	251	40.2	9268	9268	-1.5	104.9	102.7
	AnH_R	cafeteria	7.3	7.4	-11.6	271	34.2	91	108	-7.5	104.0	101.9
		ref.	*15.3*	*5.9*	*-21.1*	*408*	*41.7*	*140*	*2730*			
ThZ_R	AnH_L	cafeteria	5.0	-0.5	3.9	185	44.3	2802	109	2.5	99.4	95.6
	AnH_R	cafeteria	7.0	3.6	-5.6	245	34.8	9397	19	-7.0	103.1	100.8
		ref.	*16.0*	*6.1*	*-14.6*	*388*	*41.8*	*120*	*1910*			
AnH_L_2mm	AnH_L	cafeteria	6.1	5.7	-12.7	350	35.5	202	307	-13.0	103.2	101.0
	AnH_R	cafeteria	5.8	5.1	-14.1	324	28.5	146	246	-20.0	106.5	104.4
		ref.	*12.2*	*5.5*	*1.4*	*584*	*48.5*	*260*	*2220*			
AnH_R_2mm	AnH_L	cafeteria	7.6	5.1	-11.9	210	35.4	201	280	-11.0	94.6	92.2
	AnH_R	cafeteria	8.6	6.7	-15.3	227	28.9	142	300	-17.5	103.3	101.2
		ref.	*14.5*	*5.9*	*-5.7*	*541*	*46.4*	*220*	*2530*			

Table C.7: Inter-individual variability of the attenuation of the AnH_L and AnH_R ITE prototype with 0.8 mm vent diameter measured with cafeteria noise

C.1.3 Maximal SPL

Vent	Prototype	Signal	D_avg [dB]	Over_low [dB]	Over_high [dB]	Centroid [Hz]	dB_max [dB]	f1_10dB [Hz]	f2_10dB [Hz]	Gain [dB]	SPL [dB]	dB(A) [dB]
2mm	AnH_L	pink	12.99	5.7	5.6	489	50.5	249	1956	2.0	77.3	75.3
		cafeteria	13.10	5.7	5.6	476	50.5	251	1942	2.0	89.6	87.5
		Kantine	12.51	5.5	4.2	501	50.5	258	1983	2.0	83.8	80.4
		Party	12.37	5.7	4.3	489	50.5	253	1983	2.0	91.4	91.1
		Babble	13.64	5.6	4.4	489	50.5	256	1956	2.0	90.6	89.1
		Car	10.18	5.3	4.5	501	50.5	261	1125	2.0	61.1	45.2
		Traffic	12.24	5.6	3.7	501	50.5	256	1969	2.0	75.0	69.7
		Male	8.39	5.2	2.5	489	49.5	276	1850	1.0	63.9	59.7
		Female	8.30	4.7	2.8	489	49.5	284	1929	1.0	70.9	67.8
		M&F	7.96	5.1	2.7	476	49.5	276	743	1.0	62.4	57.5
		ref.	*12.20*	*5.5*	*1.4*	*584*	*48.5*	*260*	*2220*			
0.8mm	AnH_L	pink	13.52	5.8	-8.6	378	40.6	97	1929	-3.0	88.7	86.1
		cafeteria	11.88	4.2	-8.4	388	40.6	296	1942	-3.0	100.6	98.4
		Kantine	15.00	6.1	-8.9	430	40.6	99	1969	-3.0	97.0	93.5
		Party	14.18	4.7	-9.0	452	40.6	286	1969	-3.0	99.1	98.8
		Babble	13.03	5.2	-8.4	388	40.6	97	1916	-3.0	103.5	101.8
		Car	12.01	5.1	-0.7	452	40.6	326	1072	-3.0	72.8	55.4
		Traffic	13.83	5.0	-4.7	441	40.6	288	1916	-3.0	80.7	74.6
		Male	11.66	3.2	-9.2	441	40.6	340	1889	-3.0	84.8	79.8
		Female	10.73	4.6	-9.0	452	40.6	369	1902	-3.0	76.3	72.8
		M&F	10.97	3.9	-9.1	441	40.6	364	1902	-3.0	75.9	70.7
		ref.	*16.18*	*6.2*	*-3.2*	*369*	*43.6*	*110*	*2120*			

Table C.8: Objective parameters and SPL of the AnH_L ITE prototype with 2 and 0.8 mm vent diameter measured for 10 different excitation signals

C.1.4 Low frequency Limitation

vent	dB_max	Over_low	Signal	D_avg [dB]	Over_low [dB]	Over_high [dB]	Centroid [Hz]	dB_max [dB]	f1_10dB [Hz]	f2_10dB [Hz]	Gain [dB]	SPL [dB]	dB(A) [dB]
2mm	30	3	pink	7.4	3.0	-1.4	527	39.0	324	2293	-0.5	88.2	86.6
			ref.	*7.9*	*3.0*	*-5.7*	*664*	*39.5*	*410*	*1910*			
		6	pink	9.8	3.9	-0.2	570	39.4	320	2246	0.5	88.0	86.3
			ref.	*8.1*	*3.4*	*-5.7*	*681*	*38.9*	*380*	*1900*			
	40	3	pink	8.8	3.0	-0.5	388	46.7	242	2293	-1.0	85.5	84.0
			ref.	*11.9*	*3.2*	*-5.6*	*555*	*47.7*	*270*	*2600*			
		6	pink	11.4	6.1	0.1	359	45.9	178	2169	-0.5	83.4	81.7
			ref.	*14.5*	*5.9*	*-5.7*	*541*	*46.4*	*220*	*2530*			
	55	3	pink	11.2	3.0	-2.4	308	60.1	140	467	1.0	78.4	76.9
			ref.	*9.9*	*2.1*	*-9.5*	*369*	*59.1*	*560*	*2430*			
		6	pink	10.2	6.0	-1.4	258	56.6	87	269	-1.0	77.6	75.9
			ref.	*13.5*	*6.1*	*-7.5*	*341*	*57.6*	*130*	*2570*			
08mm	15	3	pink	5.3	3.2	-14.7	615	16.3	748	2325	-2.0	100.9	98.2
			ref.	*8.7*	*2.1*	*-12.6*	*570*	*18.3*	*380*	*2210*			
		6	pink	8.3	3.2	-12.9	615	17.8	393	2390	-0.5	98.2	93.7
			ref.	*8.7*	*2.1*	*-12.6*	*570*	*18.3*	*380*	*2210*			
	23	3	pink	6.8	3.2	-10.7	369	25.2	1094	1374	0.0	99.1	96.0
			ref.	*14.7*	*2.8*	*-12.5*	*501*	*25.2*	*270*	*2280*			
		6	pink	10.7	5.2	-15.1	615	20.0	396	2309	-2.5	91.3	88.5
			ref.	*15.4*	*4.6*	*-12.0*	*527*	*22.5*	*220*	*2210*			
	40	3	pink	7.2	3.2	-18.5	408	32.7	1763	2688	-6.5	93.5	91.3
			ref.	*19.2*	*2.9*	*-12.6*	*419*	*39.2*	*110*	*2220*			
		6	pink	13.5	6.3	-16.7	452	36.1	198	2526	-4.0	89.5	87.3
			ref.	*22.4*	*5.5*	*-12.4*	*350*	*40.1*	*90*	*2230*			

Table C.9: Objective parameters and SPL of the AnH_R ITE prototype with 2 and 0.8 mm vent diameter measured with 6 different compensation filters and pink noise excitation signal

vent	dB_max	Over_low	Signal	D_avg [dB]	Over_low [dB]	Over_high [dB]	Centroid [Hz]	dB_max [dB]	f1_10dB [Hz]	f2_10dB [Hz]	Gain [dB]	SPL [dB]	dB(A) [dB]
2mm	30	3	cafeteria	7.0	2.9	-1.4	541	39.0	340	2293	-0.5	94.3	92.4
			ref.	*7.9*	*3.0*	*-5.7*	*664*	*39.5*	*410*	*1910*			
		6	cafeteria	8.9	3.4	0.1	584	39.4	328	2261	0.5	94.9	93.0
			ref.	*8.1*	*3.4*	*-5.7*	*681*	*38.9*	*380*	*1900*			
	40	3	cafeteria	8.0	2.6	-0.5	408	46.7	634	2293	-1.0	93.5	91.6
			ref.	*11.9*	*3.2*	*-5.6*	*555*	*47.7*	*270*	*2600*			
		6	cafeteria	10.8	5.4	0.3	378	45.9	185	2154	-0.5	94.3	92.3
			ref.	*14.5*	*5.9*	*-5.7*	*541*	*46.4*	*220*	*2530*			
	55	3	cafeteria	10.5	1.5	-3.3	324	60.1	708	2246	1.0	93.8	91.9
			ref.	*9.9*	*2.1*	*-9.5*	*369*	*59.1*	*560*	*2430*			
		6	cafeteria	9.8	4.3	-1.2	271	56.6	97	241	-1.0	96.0	93.9
			ref.	*13.5*	*6.1*	*-7.5*	*341*	*57.6*	*130*	*2570*			
08mm	15	3	cafeteria	4.5	9.9	-14.8	615	16.3	824	2230	-2.0	104.7	102.3
			ref.	*8.7*	*2.1*	*-12.6*	*570*	*18.3*	*380*	*2210*			
		6	cafeteria	7.5	3.2	-12.7	631	17.8	413	2341	-0.5	100.5	97.9
			ref.	*8.7*	*2.1*	*-12.6*	*570*	*18.3*	*380*	*2210*			
	23	3	cafeteria	0.0	1.2	-10.9	103	25.2	9332	9332	0.0	105.7	103.5
			ref.	*14.7*	*2.8*	*-12.5*	*501*	*25.2*	*270*	*2280*			
		6	cafeteria	10.6	5.9	-14.9	615	20.0	390	2293	-2.5	105.0	102.3
			ref.	*15.4*	*4.6*	*-12.0*	*527*	*22.5*	*220*	*2210*			
	40	3	cafeteria	6.3	26.2	-18.6	452	32.7	859	1148	-6.5	100.6	97.9
			ref.	*19.2*	*2.9*	*-12.6*	*419*	*39.2*	*110*	*2220*			
		6	cafeteria	12.3	2.0	-16.6	489	36.1	430	2491	-4.0	96.2	94.0
			ref.	*22.4*	*5.5*	*-12.4*	*350*	*40.1*	*90*	*2230*			

Table C.10: Objective parameters and SPL of the AnH$_R$ ITE prototype with 2 and 0.8 mm vent diameter measured with 6 different compensation filters and cafeteria noise excitation signal

C.2 Adaptive results

C.2.1 Simulation with ideal transfer functions

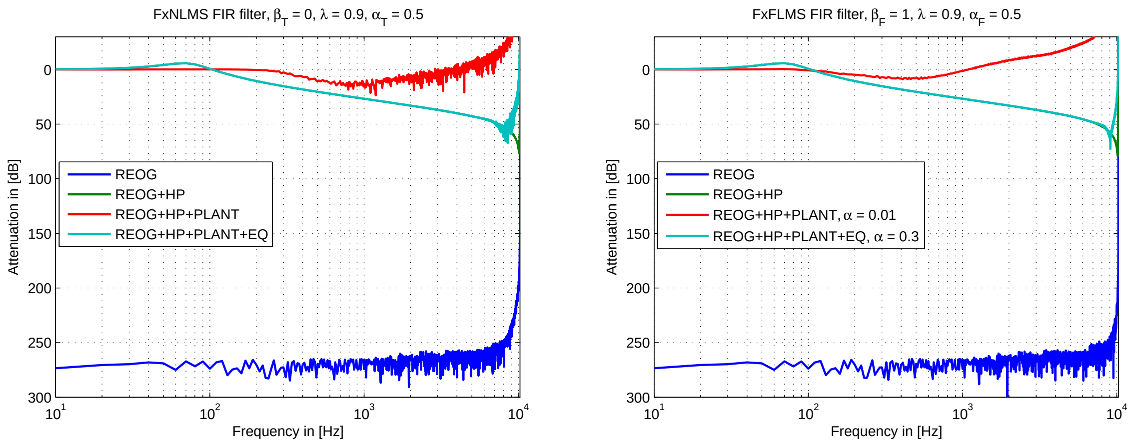

(a) FxNLMS algorithm, $\beta_{\mathrm{T}} = 0$, $\lambda = 0.9$ (b) FxFLMS algorithm, $\beta_{\mathrm{F}} = 1$, $\lambda = 0.9$

Figure C.3: Attenuation of the adaptive ADSC system with $N = 2048$ filter coefficients relative to the ideal compensation filter $H_{\mathrm{COMP}}(j\omega) = \frac{H_{\mathrm{REOG}}(j\omega)}{H_{\mathrm{PLANT}}(j\omega)}$. The REOG is a 2^{nd} order butterworth low-pass filter with $f_c = 1$ kHz and 9 samples delay and the PLANT is either 1 (blue and green) or a 2^{nd} order high-pass filter with $f_c = 1$ kHz and 3 samples delay (red and cyan).

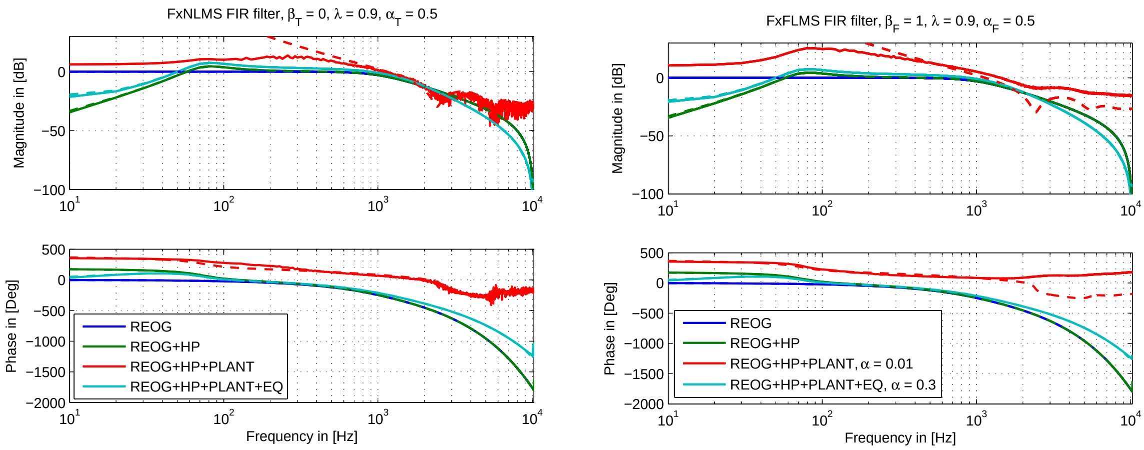

(a) FxNLMS algorithm, $\beta_{\mathrm{T}} = 0$, $\lambda = 0.9$ (b) FxFLMS algorithm, $\beta_{\mathrm{F}} = 1$, $\lambda = 0.9$

Figure C.4: Bode plot of the adaptive filters after 25 seconds (solid) and the desired frequency responses (dashed).

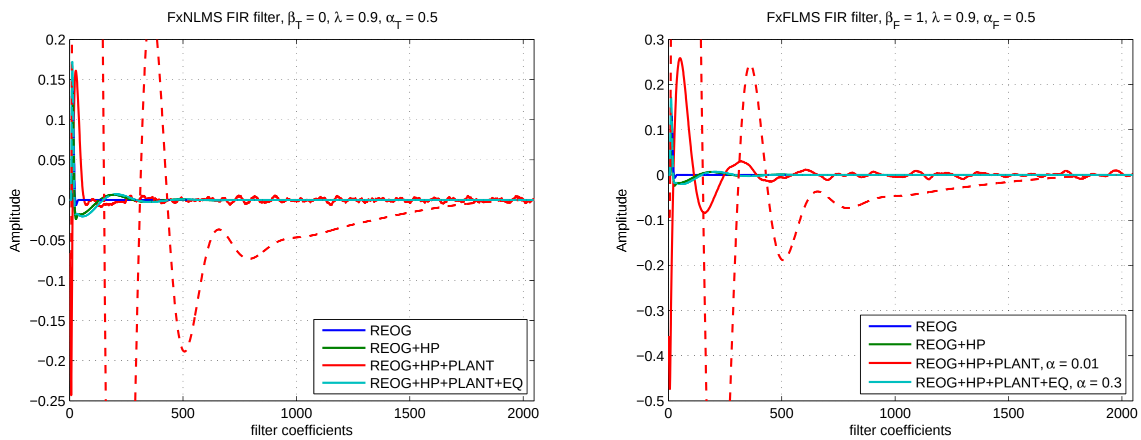

(a) FxNLMS algorithm, $\beta_{\mathrm{T}} = 0$, $\lambda = 0.9$ (b) FxFLMS algorithm, $\beta_{\mathrm{F}} = 1$, $\lambda = 0.9$

Figure C.5: Impulse response of the adaptive filters after 25 seconds (solid) and the desired IRs (dashed).

C.2.2 Measurements with real transfer functions

ITE-HM with 0.575 mm vent radius and $N = 1024$ filter coefficients

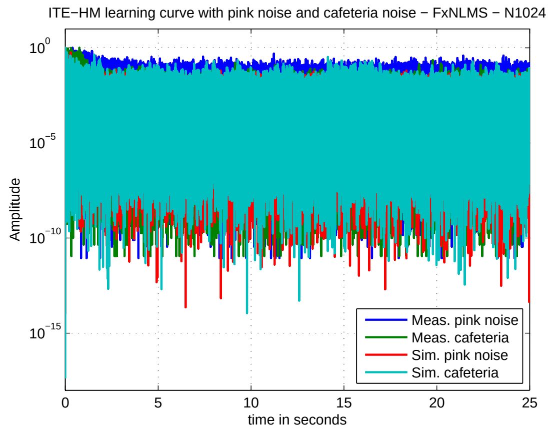

(a) FxNLMS algorithm, $\beta_{\mathrm{T}} = 0$, $\lambda = 0.9$

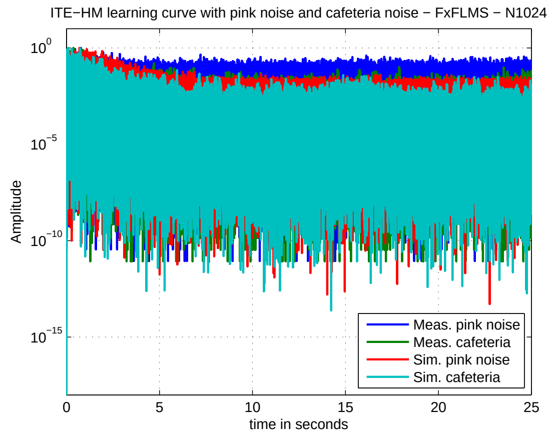

(b) FxFLMS algorithm, $\beta_{\mathrm{F}} = 1$, $\lambda = 0.9$

Figure C.6: Learning curve of the ITE-HM with 0.575 *mm vent radius and* $N = 1024$ *filter coefficients*

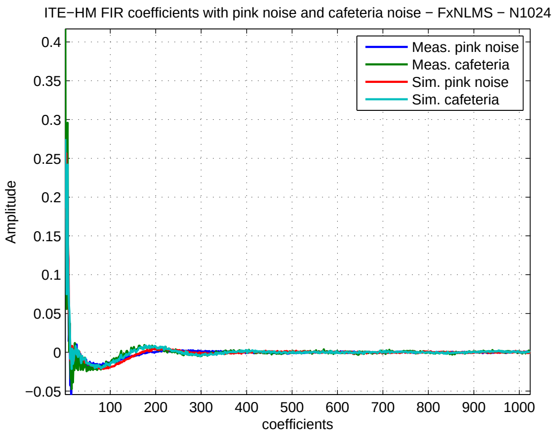

(a) FxNLMS algorithm, $\beta_{\mathrm{T}} = 0$, $\lambda = 0.9$

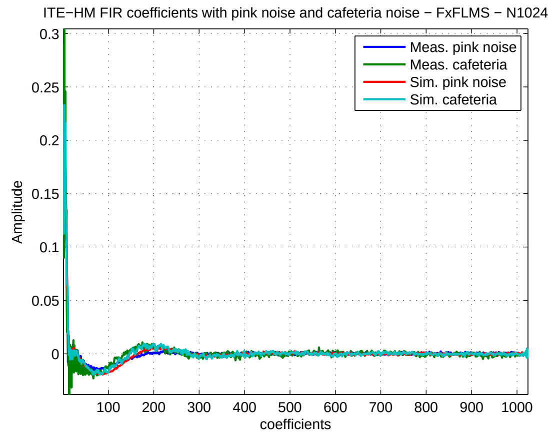

(b) FxFLMS algorithm, $\beta_{\mathrm{F}} = 1$, $\lambda = 0.9$

Figure C.7: Impulse response of the ITE-HM with 0.575 *mm vent radius and* $N = 1024$ *filter coefficients*

Method		**Signal**	**D_avg** [dB]	**Over_low** [dB]	**Over_high** [dB]	**Centroid** [Hz]	**dB_max** [dB]	**f1_10dB** [Hz]	**f2_10dB** [Hz]
FxFLMS	measured	pink	12.7	4.2	-5.5	441	59.5	190	1270
		cafe	12.5	8.9	-4.9	476	62.8	200	1160
	simulated	pink	13.9	5.7	-5.4	419	57.1	190	1150
		cafe	14.0	5.9	-4.9	441	62.0	190	1150
FxNLMS	measured	pink	13.5	0.2	3.8	476	45.0	240	990
		cafe	12.5	16.0	-4.4	555	56.2	250	1150
	simulated	pink	15.0	5.9	-7.6	501	59.5	220	1150
		cafe	14.2	5.9	-5.2	514	61.1	220	1240
frequency sampling	calculated	-	13.3	5.2	-5.7	430	59.0	190	1300
Static Design	calculated	-	13.3	5.6	-5.8	430	58.1	190	1300
	measured	pink	13.2	5.3	-5.7	388	55.8	180	1180

Table C.11: 0.575 *mm vent radius,* $N = 1024$

ITE-HM with 0.575 mm vent radius and $N = 128$ filter coefficients

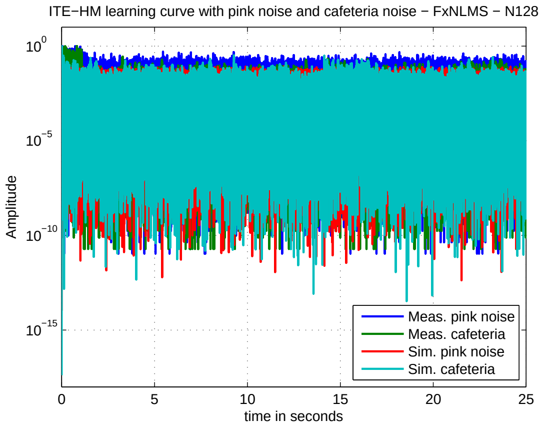

(a) FxNLMS algorithm, $\beta_{\mathrm{T}} = 0$, $\lambda = 0.9$

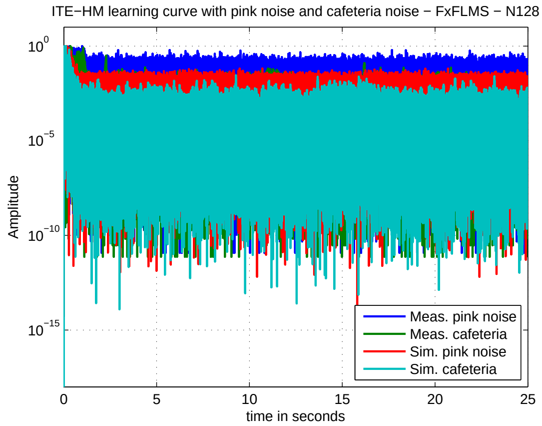

(b) FxFLMS algorithm, $\beta_{\mathrm{F}} = 1$, $\lambda = 0.9$

Figure C.8: Learning curve of the ITE-HM with 0.575 mm vent radius and $N = 128$ filter coefficients

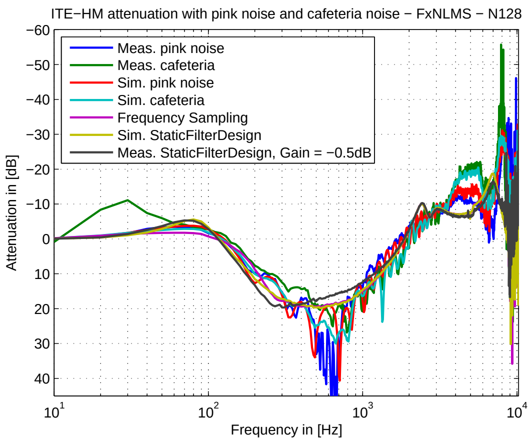

(a) FxNLMS algorithm, $\beta_{\mathrm{T}} = 0$, $\lambda = 0.9$

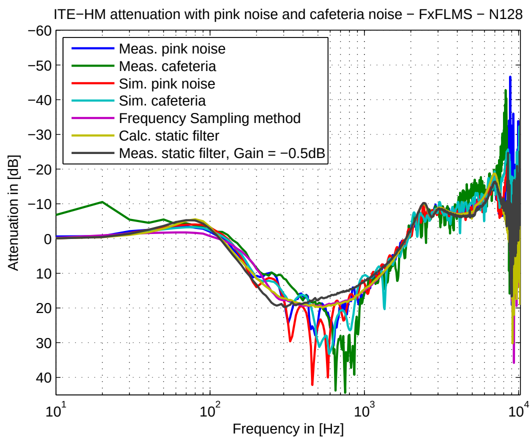

(b) FxFLMS algorithm, $\beta_{\mathrm{F}} = 1$, $\lambda = 0.9$

Figure C.9: Attenuation of the ITE-HM with 0.575 mm vent radius and $N = 128$ filter coefficients

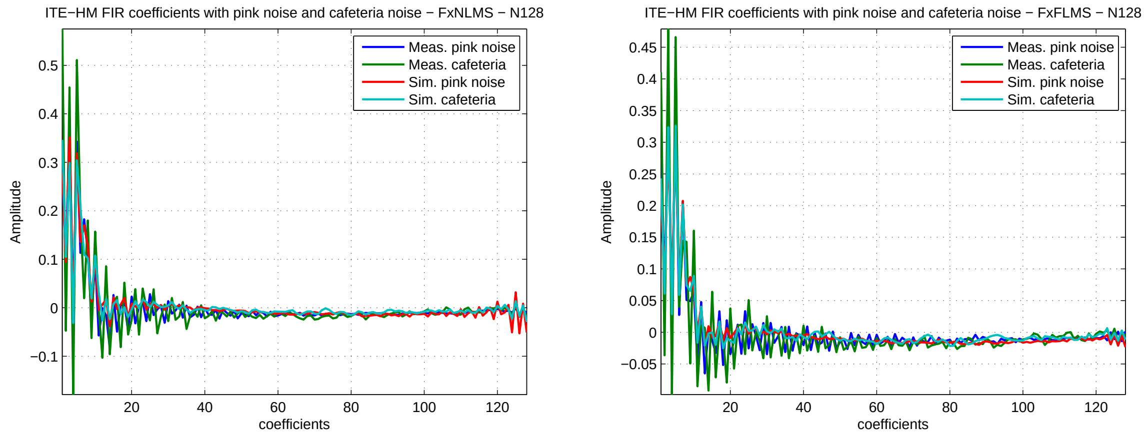

(a) FxNLMS algorithm, $\beta_{\mathrm{T}} = 0$, $\lambda = 0.9$

(b) FxFLMS algorithm, $\beta_{\mathrm{F}} = 1$, $\lambda = 0.9$

Figure C.10: Impulse response of the ITE-HM with 0.575 *mm vent radius and* $N = 128$ *filter coefficients*

Method		**Signal**	**D_avg** [dB]	**Over_low** [dB]	**Over_high** [dB]	**Centroid** [Hz]	**dB_max** [dB]	**f1_10dB** [Hz]	**f2_10dB** [Hz]
FxFLMS	measured	pink	13.7	3.5	-8.0	464	57.8	260	1250
		cafe	13.9	10.5	-6.2	584	58.0	260	1240
	simulated	pink	15.0	4.1	-6.3	464	59.8	180	1120
		cafe	14.2	3.3	-5.9	501	61.7	200	1160
FxNLMS	measured	pink	15.4	3.5	-8.6	514	58.4	240	1060
		cafe	11.5	8.4	3.0	528	56.7	250	1230
	simulated	pink	14.5	3.8	-7.0	476	63.3	180	1220
		cafe	14.5	2.9	-3.6	501	66.2	200	1390
frequency sampling	calculated	-	12.8	1.8	-5.7	441	66.6	220	1310
Static Design	calculated	-	13.3	5.6	-5.8	430	58.1	190	1300
	measured	pink	13.2	5.3	-5.7	388	55.8	180	1180

Table C.12: 0.575 *mm vent radius,* $N = 128$

ITE-HM with 0.225 mm vent radius and $N = 1024$ filter coefficients

Method		**Signal**	**D_avg** [dB]	**Over_low** [dB]	**Over_high** [dB]	**Centroid** [Hz]	**dB_max** [dB]	**f1_10dB** [Hz]	**f2_10dB** [Hz]
FxFLMS	measured	pink	9.3	8.7	17.2	398	51.5	570	660
		cafe	12.9	5.6	5.3	324	22.7	220	1150
	simulated	pink	15.3	7.9	-23.4	324	48.0	90	1070
		cafe	14.6	7.8	-22.3	324	44.1	120	890
FxNLMS	measured	pink	11.4	15.7	-21.4	264	75.6	160	430
		cafe	21.0	14.5	-5.1	342	46.4	110	730
	simulated	pink	18.8	6.6	-21.9	286	50.5	90	650
		cafe	22.4	7.2	-23.2	324	41.5	100	870
frequency sampling	calculated	-	11.2	5.6	-22.5	369	39.2	200	1120
Static Design	calculated	-	11.5	3.8	-22.1	350	40.0	140	1080
	measured	pink	12.6	4.4	-21.9	441	40.4	180	1170

Table C.13: 0.225 *mm vent radius,* $N = 1024$

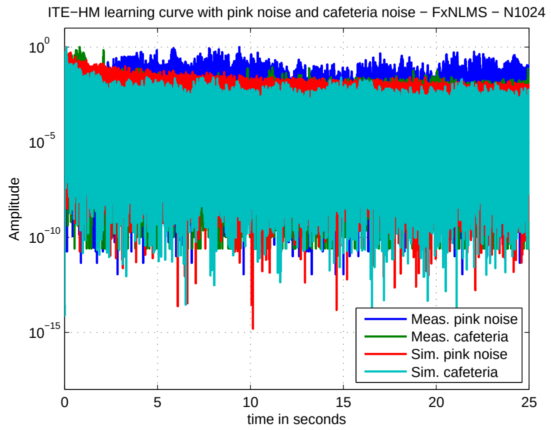

(a) FxNLMS algorithm, $\beta_{\mathrm{T}} = 0$, $\lambda = 0.9$

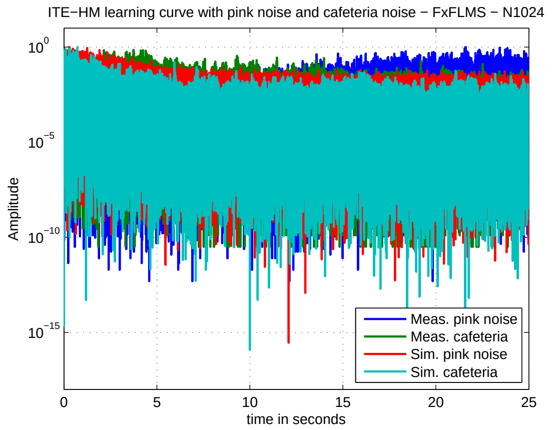

(b) FxFLMS algorithm, $\beta_{\mathrm{F}} = 1$, $\lambda = 0.9$

Figure C.11: Learning curve of the ITE-HM with 0.224 mm vent radius and $N = 1024$ filter coefficients

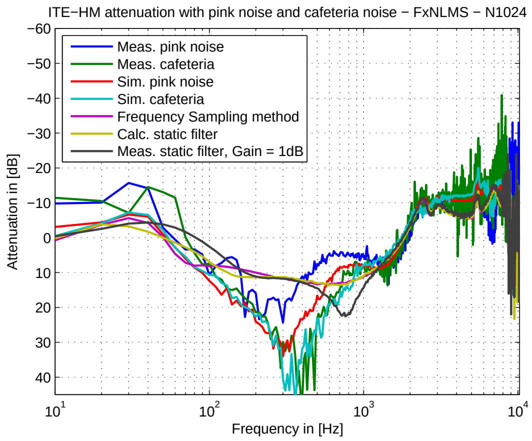

(a) FxNLMS algorithm, $\beta_{\mathrm{T}} = 0$, $\lambda = 0.9$

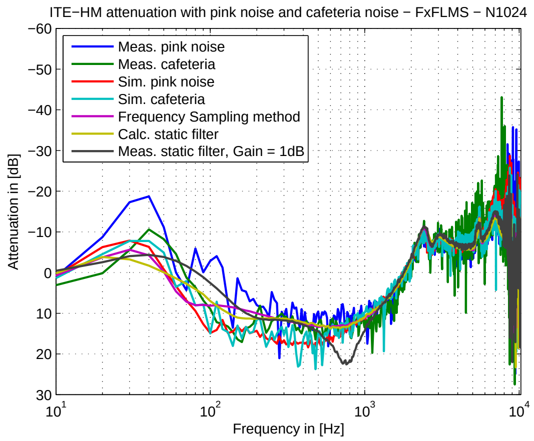

(b) FxFLMS algorithm, $\beta_{\mathrm{F}} = 1$, $\lambda = 0.9$

Figure C.12: Attenuation of the ITE-HM with 0.225 mm vent radius and $N = 1024$ filter coefficients

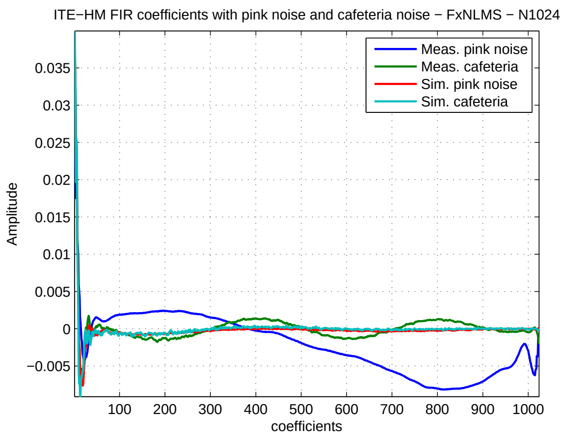

(a) FxNLMS algorithm, $\beta_{\mathrm{T}} = 0$, $\lambda = 0.9$

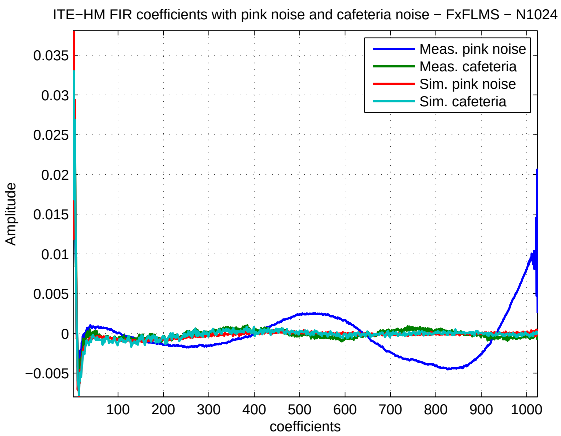

(b) FxFLMS algorithm, $\beta_{\mathrm{F}} = 1$, $\lambda = 0.9$

Figure C.13: Impulse response of the ITE-HM with 0.225 mm vent radius and $N = 1024$ filter coefficients

ITE-HM with 0.225 mm vent radius and $N = 128$ filter coefficients

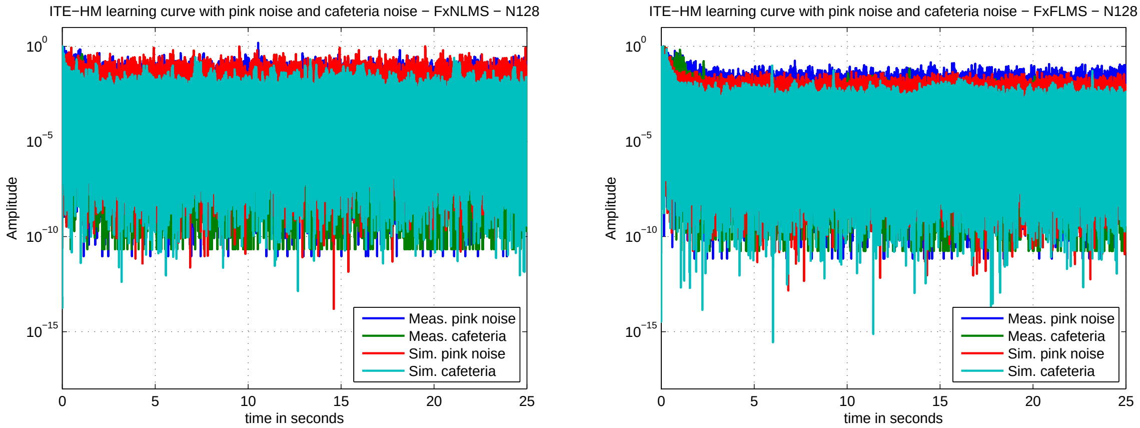

(a) FxNLMS algorithm, $\beta_{\mathrm{T}} = 0$, $\lambda = 0.9$ (b) FxFLMS algorithm, $\beta_{\mathrm{F}} = 1$, $\lambda = 0.9$

Figure C.14: Learning curve of the ITE-HM with 0.225 mm vent radius and $N = 128$ filter coefficients

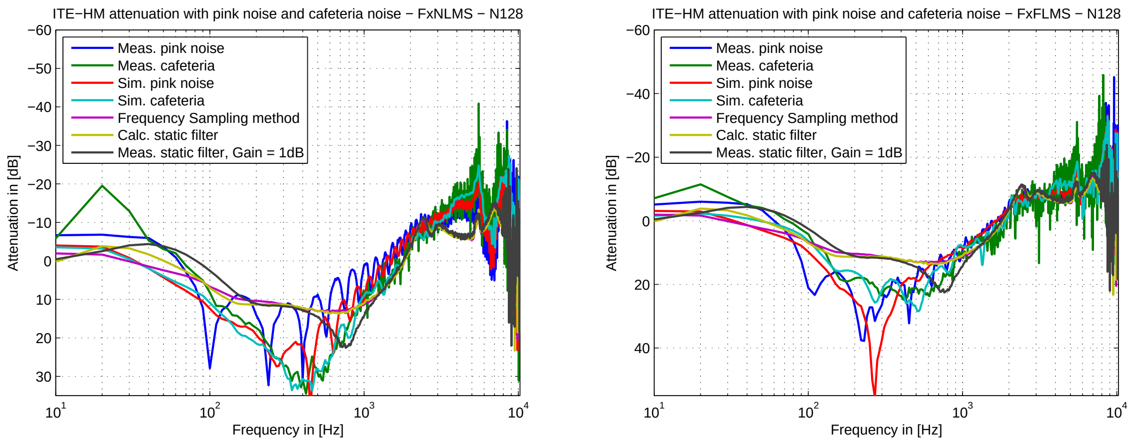

(a) FxNLMS algorithm, $\beta_{\mathrm{T}} = 0$, $\lambda = 0.9$ (b) FxFLMS algorithm, $\beta_{\mathrm{F}} = 1$, $\lambda = 0.9$

Figure C.15: Attenuation of the ITE-HM with 0.225 mm vent radius and $N = 128$ filter coefficients

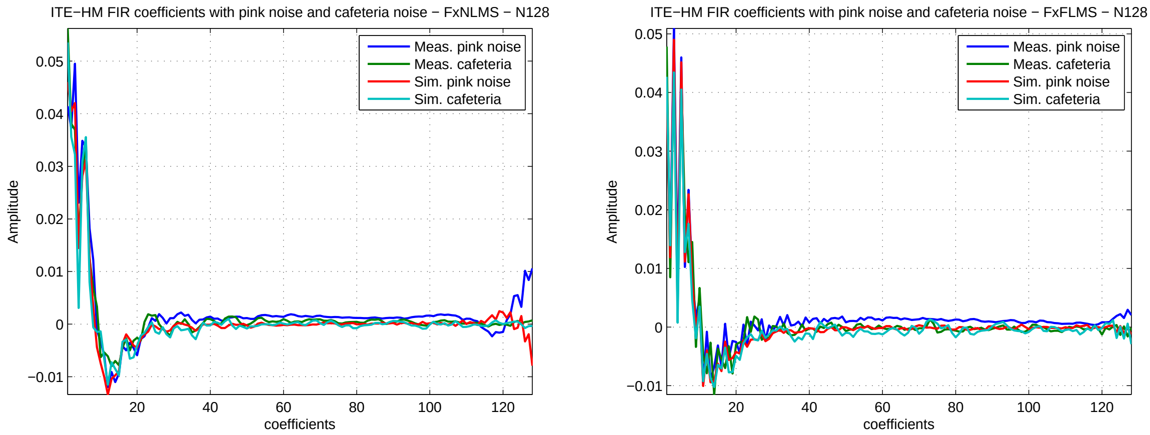

(a) FxNLMS algorithm, $\beta_T = 0$, $\lambda = 0.9$ (b) FxFLMS algorithm, $\beta_F = 1$, $\lambda = 0.9$

Figure C.16: Impulse response of the ITE-HM with 0.225 *mm vent radius and* $N = 128$ *filter coefficients*

Method		**Signal**	**D_avg** [dB]	**Over_low** [dB]	**Over_high** [dB]	**Centroid** [Hz]	**dB_max** [dB]	**f1_10dB** [Hz]	**f2_10dB** [Hz]
FxFLMS	measured	pink	20.5	6.0	-23.8	271	55.2	90	850
		cafe	17.9	11.5	-4.1	359	47.5	130	940
	simulated	pink	20.9	3.1	-25.0	278	45.5	110	870
		cafe	17.4	2.3	-23.7	342	38.6	120	890
FxNLMS	measured	pink	12.8	6.8	-20.8	258	56.9	190	460
		cafe	20.6	19.5	-5.7	359	53.2	110	960
	simulated	pink	18.6	4.0	-22.5	308	48.4	90	850
		cafe	22.0	3.5	-22.2	342	47.0	100	960
frequency sampling	calculated	-	11.1	1.9	-22.5	359	40.9	170	1120
Static Design	calculated	-	11.5	3.8	-22.1	350	40.0	140	1080
	measured	pink	12.6	4.4	-21.9	441	40.4	180	1170

Table C.14: 0.225 *mm vent radius,* $N = 128$

D
Measurement Equipement

D.1 Hardware

Real time system

The real time system used to run the two developed ADSC systems is the “basic real-time target machine” by Speedgoat GmbH with the low latency Input/Output-module “IO104”. The system has 8 input channels and 4 output channels and allows sample rates up to 100 kHz. It is optimized for Simulink® and xPC Target which gives the possibility to run Simulink® models in real time. The models are compiled on a Host PC running Windows 7 and MATLAB® 2009a and downloaded via Ethernet to the target machine. It is possible to fetch data during operation from the real time target machine with the Host PC and use it in MATLAB® for further processing.

Measurements of the Input/Output delay of the used system were conducted by Zurbrügg and are depicted in [90].

Transducers

All hearing instrument transducers used in this thesis are developed by Sonion A/S. For the distortion measurements the “E50DA012” receiver is used [20], whereby the wiring is not in series but in parallel in order to achieve higher SPLs with the same input voltage. This receiver is also built in the ITE hardware model (ITE-HM).
For the ITE prototypes the “26UA01” receiver is used as it requires considerably less space and can be mounted in a shell also for individuals with a small ear canal diameter.

The hearing instrument microphones of the ITE prototypes and the ITE-HM are based on the 5000 Omni series, which have in general an electric 1$^{\mathrm{st}}$ oder high-pass with the cut-off frequency at $f_{\mathrm{c}} = 200$ Hz additional to the mechanical high-pass arisen by the hole in the membrane, that compensates changes of the static pressure [21]. The canal microphone of the ITE prototypes has no additional electric high-pass, which is beneficial for the measurements in the ear canal concerning the SNR at low frequencies.

For the conducted distortion measurements the sound pressure is recorded with the 1/2" pressure microphone "Type 40AG" from G.R.A.S. Sound & Vibration [29]. This microphone ensures a magnitude deviation less than ±2 dB up to 20 kHz. In this thesis, it is used also to calculate the absolute SPL in the ear simulators and to determine the sensitivity of the hearing aid microphones for the estimation of the SPL at the vent entry.

ITE prototypes and hardware model

The ITE hardware model is depicted in Fig. D.1. The model is designed in such a way that it can be plugged on an ear simulator perfectly. The receiver and the canal microphone are acoustically connected to the ear simulator volume, while the outer microphone senses the sound outside of the ear simulator. The vent of the model has a length of 5 mm and a maximal diameter of 3 mm, which can be reduced to 0.45 mm by inserting smaller tubes. The power supply of the microphones is done by a hearing aid battery.

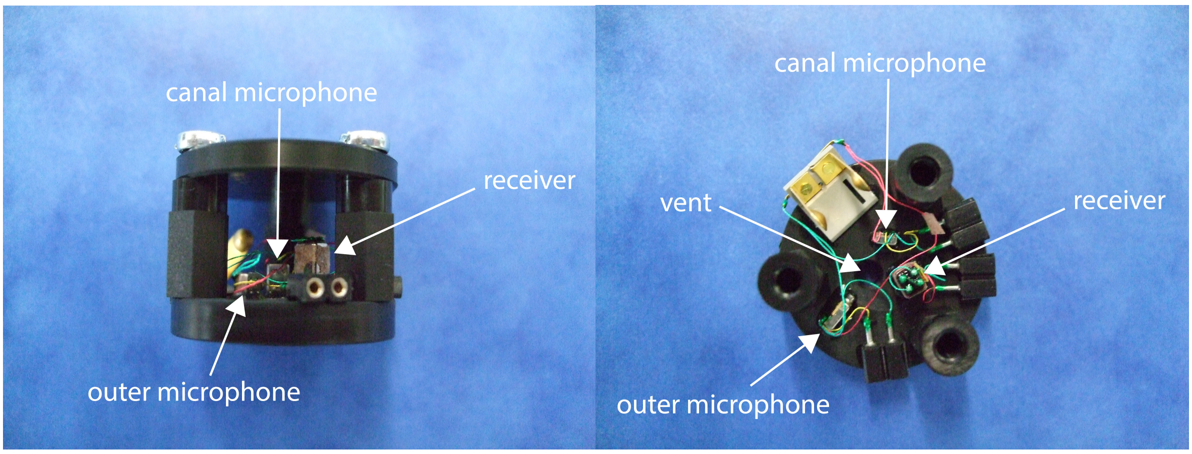

(a) Front view (b) Top view

Figure D.1: ITE hardware model with the transducers and the vent

Fig. D.2 shows two ITE prototypes with their microphone, their receiver and their vent locations. The vent diameter is maximal 2 mm and can be reduced by inserting tubes with smaller vent diameter or can be even sealed. The shell contains solely the three transducers, since the power supply for the microphones is afforded by the preamplifier.

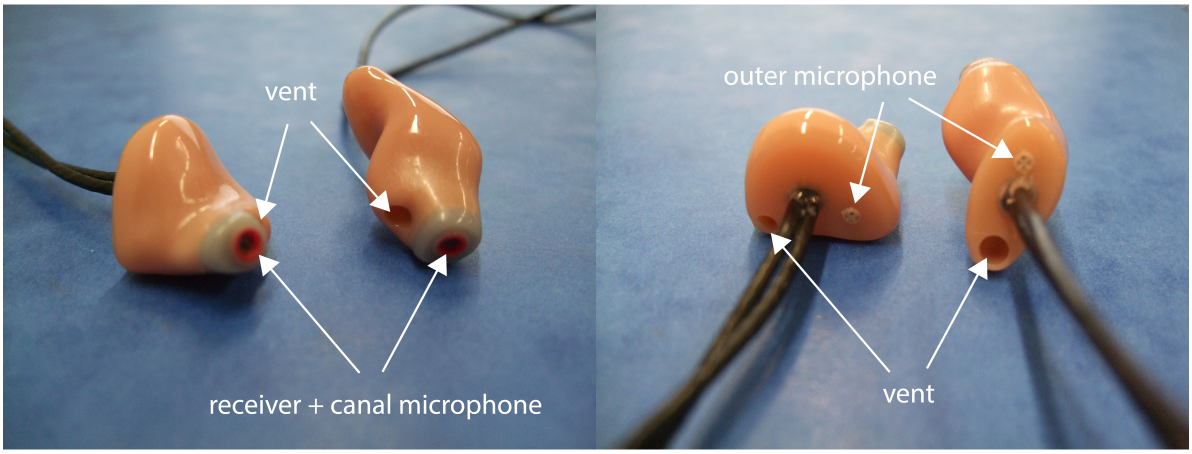

(a) View from the ear drum (b) View from outside the ear

Figure D.2: Two ITE prototypes with the transducers and the vent

Coupler and Ear Simulator

The distortion measurements of the receivers are done with a '2cc' coupler of G.R.A.S. Sound & Vibration, which allows to compare the results with the datasheets of the manufactures. For the ITE-HM measurements a "IEC711" ear simulator of G.R.A.S. Sound & Vibration is used, which approximates the real ear.

Preamplifier and amplifier

The microphones of the ITE prototypes are connected to a custom-made preamplifier for the Phonak AG, which affords the necessary voltage supply for the microphones. The microphones of the ITE-HM are connected to the "Nexus Conditioning Amplifier" by Brüel &Kjær Sound & Vibration Measurement A/S. The 1/2" pressure microphone from G.R.A.S. Sound & Vibration uses the company own preamplifier "Power Module - Type 12AA".

The receivers of the ITE prototypes and of the ITE-HM are directly connected to the output module of the RTS and need no additional amplifier. For the distortion measurements the "SA 106" from BST is used as amplifier, which offers more power than the RTS.

Playback devices

As playback device for the transfer function measurements and the performance measurements of the ITE prototypes the "HD 280-13" headphones from Sennheiser electronic GmbH & Co. KG are used. In order to have a flat frequency response the headphones are equalized according to [89].

The measurements of the ITE-HM are done in an acoustically sealed box from Interacoustics A/S which includes a loudspeaker. The loudspeaker is driven by the "DAD-M100 dc$^+$ BI" amplifier by Flying Mole CORP.

Both playback devices are connected to the output channel of the sound card of the Host PC, from where the signals are played back.

Recording device

The output signals of the outer microphone and the canal microphone of the ITE prototypes and the ITE-HM are sent to the “828 mkII USB2.0” audio interface by MOTU, Inc., and recorded with MATLAB® .

D.3 Measurement Setup

Static ADSC System

Measurement of the transfer functions

The REOG of the ITE prototype is measured with the Simulink® model `MeasureTF.mdl` on the RTS and the excitation signal played back over the headphones. Both ITE microphones are connected via their preamplifier to the RTS on which the cross power spectral density between both signals, the power-spectral density of each, their coherence and the estimated transfer function is calculated. For the measurement of the PLANT the same model is used but the excitation signal is now fed to the receiver, which is connected to the RTS, while the headphones are muted.

A similar configuration is used for the performance measurements of the static ADSC system. The used Simulink® model `ANC_RTS_staticFrameWork_Prototype.mdl` runs on the RTS and the sound, which should be attenuated, is played back over the headphones. In addition to the transfer function measurement, the sensed microphone signals are fed to the audio interface and recorded in MATLAB® . In order to measure the direct sound attenuation, the REOG is measured once without and once with the ADSC system switched on. The ratio between both measurements yields the achieved direct sound attenuation.

Adaptive ADSC System

The performance of the adaptive ADSC system is only measured with the ITE-HM in the acoustically sealed box. The microphones are connected to the RTS via the Nexus preamplifier and the RTS runs the Simulink® model `ANC_RTS_FxFLMS_adaptiveFrameWork.mdl` and `ANC_RTS_FxnLMS_adaptiveFrameWork.mdl`, respectively. The sound, which should be attenuated, is played back by the loudspeaker inside of the box. Again, the signals recorded by the microphones of the ITE-HM are also sent to the audio interface and recorded with MATLAB® . The achievable attenuation is measured just as for the static case. In addition, it is possible to listen to the sound recorded by the 1/2” pressure microphone in the ear simulator, which corresponds approximately to the sound at the ear drum.

Bibliography

[1] S. Kuo and D. R. Morgan, "Active Noise Control: A Tutorial Review," *Proceedings of the IEEE*, vol. 87, no. 6, pp. 943–973.

[2] P. Lueg, "Process of silencing sound oscillations," U.S. Patent 2 043 416, June 9, 1936.

[3] E. Langberg and G. Caruso, "Active Noise Reduction System," U.S. Patent 4 985 925, Jan. 15, 1991.

[4] J. Chalupper, W. Lipski, and U. Rass, "Active Noise Suppression for a Hearing Aid Device which can be worn in the Ear or a Hearing Aid Device with Otoplastic which can be worn in the Ear," U.S. Patent 6 920 227, Jul. 19, 2005.

[5] J. Olsen, "Hearing aid with active noise canceling," U.S. Patent 7 590 254, Sep. 15, 2009.

[6] I. Jorgensen, K. B. Rasmussen, and S. O. Petersen, "Active Noise Cancellation in Hearing Devices," U.S. Patent 8 229 127, Jul. 24, 2012.

[7] R. Serizel, "Integrated active noise control and noise reduction in hearing aids," Ph.D. dissertation, Katholieke Universiteit Leuven, 2011.

[8] H. F. Olson and E. G. May, "Electronic Sound Absorber," *The Journal of the Acoustical Society of America*, vol. 25, no. 6, pp. 1130–1136, 1953.

[9] S. Elliott and P. Nelson, "Active Noise Control," *IEEE Signal Processing Magazine*, vol. 10, no. 4, pp. 12–35, 1993.

[10] J. Mejia, H. Dillon, and M. Fisher, "Active cancellation of occlusion: an electronic vent for hearing aids and hearing protectors," *The Journal of the Acoustical Society of America*, vol. 124, no. 1, pp. 235–40, 2008.

[11] T. Zurbrügg, M. Joho, and A. Stirnemann, "Feed-forward active noise control," Phonak AG, Stäfa, Research Rep., 2011.

[12] S. Kochkin, "MarkeTrak VIII: Consumer satisfaction with hearing aids is slowly increasing," *The Hearing Journal*, vol. 63, no. 1, pp. 19–32, 2010.

[13] J. Blauert and N. Xiang, *Acoustics for Engineers*, 2nd ed. Berlin Heidelberg: Springer-Verlag, 2009.

[14] D. H. Keefe, "Transmission line parameter approximations for isothermal and nonisothermal boundary conditions," *The Journal of the Acoustical Society of America*, vol. 75, no. 1, pp. 58–62, 1984.

[15] H. Dillion, *Hearing Aids*, 2nd ed. Turramurra, Australia: Boomerang Press, 2012.

[16] A. Stirnemann, "Impedanzmessungen und Netwerkmodeel zur Ermittlung der Übertragungseigentschaften des Mittelohrs," Ph.D. dissertation, ETH Zürich, 1980.

[17] R. W. Carlisle, "History and Current Status of Miniature Variable-Reluctance Balanced-Armature Transducers," *J. Audio Eng. Soc*, vol. 13, no. 1, pp. 45–49, 1965.

[18] J. O. E. Jensen, F. T. Agerkvist, and J. M. Harte, "Nonlinear Time-Domain Modeling of Balanced- Armature Receivers," *J. Audio Eng. Soc*, vol. 59, no. 3, pp. 91–101, 2011.

[19] A. Stirnemann, "Ventloss from REOG," Phonak AG, Stäfa, Research Rep., 2011.

[20] Sonion, "Receiver E50DA012," 2012. [Online]. Available: http://www.sonion.com/Products/Transducers/Receivers/~/media/Files/Products/DataSheets/Transducers/Receivers/ReceiversE50D/E50DA012_v2.ashx

[21] ——, "Microphone 50GC31," 2012. [Online]. Available: http://www.sonion.com/Products/Transducers/Microphones/~/media/Files/Products/DataSheets/Transducers/Microphones/OmniDirectionalMicrophones/5000/50GC31_v2.ashx

[22] A. Oppenheim, R. Schafer, J. Buck, and Others, *Discrete-time signal processing*, 2nd ed. New Jersey: Prentice-Hall, 1999.

[23] T. Zurbrügg and A. Stirnemann, "Electro-acoustic transducers in active feedback control for hearing aids," in *Fortschritte der Akustik - DAGA 2011*, Düsseldorf, 2011, pp. 121–122.

[24] H. Schurer, "Linearization of Electroacoustic Transducers," Ph.D. dissertation, University of Twente, 1997.

[25] W. Klippel, "Tutorial: Loudspeaker Nonlinearities - Causes, Parameters, Symptoms," *J. Audio Eng. Soc*, vol. 54, no. 10, pp. 907–939, 2006.

[26] A. Voishvillo, A. Terekhov, E. Czerwinski, and S. Alexandrov, "Graphing, interpretation, and comparison of results of loudspeaker nonlinear distortion measurements," *J. Audio Eng. Soc*, vol. 52, no. 4, pp. 332–357, 2004.

[27] S. Temme and P. Brunet, "A New Method for Measuring Distortion Using a Multitone Stimulus and Noncoherence," *J. Audio Eng. Soc*, vol. 56, no. 3, pp. 176–188, 2008.

[28] S. Temme, P. Brunet, and d. D. J. Keele, "Practical Measurement of Loudspeaker Distortion Using a Simplified Auditory Preceptual Model," in *Audio Engineering Society Convention 127*, New York, 2009.

[29] G.R.A.S, "1/2-inch Wide-frequency, Pressure Microphone Type 40AG," 2007. [Online]. Available: http://www.grasinfo.dk/documents/pd_40AG_ver_16_01_07.PDF

[30] D. Shmilovitz, "On the Definition of Total Harmonic Distortion and Its Effect on Measurement Interpretation," *IEEE Transactions on Power Delivery*, vol. 20, no. 1, pp. 526–528, Jan. 2005.

[31] "IEEE Standard Definitions for the Measurement of Electric Power Quantities Under Sinusoidal, Nonsinusoidal, Balanced, or Unbalanced Conditions," IEEE Standard 1459, 2010.

[32] "Specification of Hearing Aid Characteristics," ANSI/ASA Standard S3.22-2009.

[33] "American National Standard Testing Hearing Aids with a Broad-Band Noise Signal," ANSI/ASA Standard S3.42-1992 (R2012).

[34] A. Voishvillo, "Measurements and Perception of Nonlinear Distortion—Comparing Numbers and Sound Quality," in *Audio Engineering Society Convention 123*, New York, 2007.

[35] ——, "Assessment of Nonlinearity in Transducers and Sound Systems – From THD to Perceptual Models," in *Audio Engineering Society Convention 121*, San Francisco, 2006.

[36] C.-t. Tan, B. C. J. Moore, and N. Zacharov, "The Effect of Nonlinear Distortion on the Perceived Quality of Music and Speech Signals," *J. Audio Eng. Soc*, vol. 51, no. 11, pp. 1012–1031, 2003.

[37] "Method for objective measurements of perceived audio quality," ITU Recommendation BS.1387-1, 2001.

[38] J. M. Kates, "A test suite for hearing aid evaluation," *The Journal of Rehabilitation Research and Development*, vol. 27, no. 3, pp. 255–278, 1990.

[39] ——, "On using coherence to measure distortion in hearing aids," *The Journal of the Acoustical Society of America*, vol. 91, no. 4 Pt 1, pp. 2236–44, Apr. 1992.

[40] ——, "Cross-correlation procedures for measuring noise and distortion in AGC hearing aids." *The Journal of the Acoustical Society of America*, vol. 107, no. 6, pp. 3407–14, Jun. 2000.

[41] J. M. Kates and K. H. Arehart, "Coherence and the speech intelligibility index," *The Journal of the Acoustical Society of America*, vol. 117, no. 4, pp. 2224–2237, 2005.

[42] W. Dreschler, H. Verschuure, C. Ludvigsen, and S. Westermann, "ICRA noises: artificial noise signals with speech-like spectral and temporal properties for hearing instrument assessment," *Journal of Auditory Communication*, vol. 40, no. 3, pp. 148–157, 2001.

[43] T. Schneider and D. G. Jamieson, "Using maximum length sequence coherence for broadband distortion measurements on hearing aids," *The Journal of the Acoustical Society of America*, vol. 97, no. 4, pp. 2282–2292, 1995.

[44] K. H. Arehart, J. M. Kates, M. C. Anderson, and L. O. Harvey, "Effects of noise and distortion on speech quality judgments in normal-hearing and hearing-impaired listeners," *The Journal of the Acoustical Society of America*, vol. 122, no. 2, pp. 1150–64, Aug. 2007.

[45] M. Hofbauer, "Optimal linear separation and deconvolution of acoustical convolutive mixtures," Ph.D. dissertation, ETH Zürich, Konstanz, 2005.

[46] T. Zurbrügg, "ANC-Dämpfung in Abhängigkeit des Phasen und Amplitudenfehlers," Phonak AG, Stäfa, Tech. Rep., 2006.

[47] U. Zölzer, *DAFX: Digital Audio Effects*, 2nd ed. Chichester, UK: John Wiley & Sons, Ltd, Mar. 2011.

[48] A. Tarczynski, G. D. Cain, E. Hermanowicz, and M. Rojewski, "A WISE method for designing IIR filters," *IEEE Transactions on Signal Processing*, vol. 49, no. 7, pp. 1421–1432, Jul. 2001.

[49] E. Tohme, "Initialization of Output Error Identification Algorithms," Ph.D. dissertation, L'Universite de Poitiers, 2008.

[50] H. Brandenstein and R. Unbehauen, "Least-Squares Approximation of FIR by IIR Digital Filters," *IEEE Transactions on Signal Processing*, vol. 46, no. 1, pp. 21–30, 1998.

[51] H. K. Kwan and A. Jiang, "Recent Advances in FIR Approximation by IIR Digital Filters," in *International Conference on Communications, Circuits and Systems Proceedings*, vol. 1, 2006, pp. 185–190.

[52] J. Bednar, “On the approximation of FIR by IIR digital filters,” *IEEE Transactions on Acoustics, Speech, and Signal Processing*, vol. 31, no. 1, pp. 28–34, Feb. 1983.

[53] B. Beliczynski, I. Kale, and G. D. Cain, “Approximation of FIR by IIR Digital Filters : An Algorithm Based on Balanced Model Reduction,” *IEEE Transactions on Signal Processing*, vol. 40, no. 3, pp. 532–542, 1992.

[54] R. Vargas, “3.3 Least squares design of IIR filters,” pp. 1–21, 2010. [Online]. Available: http://cnx.org/content/m41681/1.1/

[55] C. S. Burrus, “Direct Frequency Domain IIR Filter Design Methods,” pp. 1–10, 2008. [Online]. Available: http://cnx.org/content/m16902/1.1/

[56] L. R. Rabiner and R. W. Schafer, “Recursive and Nonrecursive Realizations of Digital Filters Designed by Frequency Sampling Techniques,” *IEEE Transactions on Audio and Electroacoustics*, vol. 19, no. 3, pp. 200–207, 1971.

[57] M. Lang, “Least-squares design of IIR filters with prescribed magnitude and phase responses and a pole radius constraint,” *IEEE Transactions on Signal Processing*, vol. 48, no. 11, pp. 3109–3121, 2000.

[58] E. C. Levy, “Complex curve fitting,” *IRE Transactions on Automatic Control*, vol. 4, pp. 37–43, 1959.

[59] J. O. Smith, “Introduction to Digital Filters with Audio Applications,” 2007. [Online]. Available: http://ccrma.stanford.edu/~jos/filters/

[60] C. K. Sanathanan and J. Koerner, “Transfer Function Synthesis as a Ratio of Two Complex Polynomials,” *IEEE Transactions on Automatic Control*, vol. 8, no. 1, pp. 56–58, 1963.

[61] K. Steiglitz and L. E. McBride, “A Technique for the Identification of Linear Systems,” *IEEE Transactions on Automatic Control*, vol. 10, no. 4, pp. 461–464, 1965.

[62] B. Gustavsen and A. Semlyen, “Rational approximation of frequency domain responses by vector fitting,” *IEEE Transactions on Power Delivery*, vol. 14, no. 3, pp. 1052–1061, 1999.

[63] N. Wong and C.-U. Lei, “FIR Filter Approximation by IIR Filters Based on Discrete-Time Vector Fitting,” in *IEEE International Symposium on Circuits and Systems (ISCAS)*, New Orleans, May 2007, pp. 2343–2346.

[64] B. Gustavsen, “The Vector Fitting Web Site,” 2009. [Online]. Available: http://www.energy.sintef.no/Produkt/VECTFIT/

[65] ——, “Computer Code for Rational Approximation of Frequency Dependent Admittance Matrices,” *IEEE Transactions on Power Delivery*, vol. 17, no. 4, pp. 1093–1098, 2002.

[66] M. Lang, “Algorithms for the Constrained Design of Digital Filters with Arbitrary Magnitude and Phase Responses,” Ph.D. dissertation, TU Wien, 1999.

[67] J. Cadzow, “Recursive digital filter synthesis via gradient based algorithms,” *IEEE Transactions on Acoustics, Speech, and Signal Processing*, vol. 24, no. 5, pp. 349–355, Oct. 1976.

[68] D. Bayard, “High-order multivariable transfer function curve fitting: Algorithms, sparse matrix methods and experimental results,” *Automatica*, vol. 30, pp. 1439—-1444, 1994.

[69] S. L. Netto, P. S. R. Diniz, and P. Agathoklis, “Adaptive IIR Filtering Algorithms for System Identification : A General Framework,” *IEEE Transactions on Education*, vol. 38, no. 1, pp. 54–66, 1995.

[70] E. Tohme, R. Ouvrard, A. Abche, J.-c. Trigeassou, T. Poinot, and G. Mercère, "A Methodology to Enhance the Convergence of Output Error Identification Algorithms," in *Proceedings of the European Control Conference*, 2007, pp. 5721–5728.

[71] F. Teixeira and A. Romariz, "Digital Filter Arbitrary Magnitude and Phase Approximations - Statistical Analysis applied to a Stochastic-Based Optimization Approach," in *IEEE Congress on Evolutionary Computation*, 2008, pp. 4088–4095.

[72] P. Martinek, P. Boreš, and D. Tichá, "Filter Approximation Problem Using DE Algorithms," in *European Conference on Circuit Theory and Design (ECCTD)*, Antalya, 2009, pp. 687–690.

[73] R. Pintelon, P. Guillaume, Y. Rolain, J. Schoukens, and H. Van, "Parametric Identification of Transfer Functions in the Frequency Domain-A Survey," *IEEE Transactions on Automatic Control*, vol. 39, no. 11, pp. 2245–2260, 1994.

[74] G. Moschytz and M. Hofbauer, *Adaptive Filter.* Berlin Heidelberg: Springer-Verlag, 2000.

[75] L. Hakansson, "The Filtered-x LMS Algorithm," University of Karlskrona/Ronneby, Tech. Rep., 2004.

[76] S. Elliot, *Signal Processing for Active Control.* London: Academic Press, 2001.

[77] M. Bouchard and S. Quednau, "Multichannel Recursive-Least-Squares Algorithms and Fast-Transversal-Filter Algorithms for Active Noise Control and Sound Reproduction Systems," *IEEE Transactions on Speech and Audio Processing*, vol. 8, no. 5, pp. 606–618, 2000.

[78] Y. C. Park and S. D. Sommerfeldt, "A fast adaptive noise control algorithm based on the lattice structure," *Applied Acoustics*, vol. 47, no. 1, pp. 1–25, Jan. 1996.

[79] D. P. Das, G. Panda, and S. Kuo, "New block filtered-X LMS algorithms for active noise control systems," *IET Signal Process.*, vol. 1, no. 2, pp. 73–81, 2007.

[80] M. T. Akhtar and M. Abe, "Adaptive Filtering With Averaging-Based Algorithm for Feedforward Active Noise Control Systems," *Signal Processing*, vol. 11, no. 6, pp. 557–560, 2004.

[81] S. Chen, C. Lu, and F. Liao, "A FURLS active noise control algorithm based on least squares method," in *Second International Conference on Communication Systems, Networks and Applications (ICCSNA).* IEEE, 2010, pp. 397–400.

[82] L. J. Eriksson and M. C. Allie, "Use of random noise for on-line transducer modeling in an adpative active attenuation system," *The Journal of the Acoustical Society of America*, vol. 85, no. 2, pp. 797–802, 1989.

[83] D. R. Morgan, "An Analysis of Multiple Correlation Cancellation Loops with a Filter in the Auxiliary Path," *IEEE Transactions on Acoustics, Speech, and Signal Processing*, vol. 28, no. 4, pp. 454–467, 1980.

[84] A. K. Wang and W. Ren, "Convergence analysis of the multi-variable filtered-X LMS algorithm with application to active noise control," *IEEE Transactions on Signal Processing*, vol. 47, no. 4, pp. 1166–1169, Apr. 1999.

[85] C. Boucher, S. Elliott, and P. Nelson, "Effect of errors in the plant model on the performance of algorithms for adaptive feedforward control," *IEE Proceedings F: Radar and Signal Processing*, vol. 138, no. 4, pp. 313–319, 1991.

[86] N. Saito and T. Sone, “Influence of modeling error on noise reduction performance of active using filtered-X noise control algorithm systems,” *J. Acoust. Soc. Jpn.*, vol. 17, no. 4, pp. 195–202, 1996.

[87] W. Sethares, D. Lawrence, C. Johnson, and R. Bitmead, “Parameter drift in LMS adaptive filters,” *IEEE Transactions on Acoustics, Speech, and Signal Processing*, vol. 34, no. 4, pp. 868–879, Aug. 1986.

[88] P. List, P. Ioannou, and J. Sun, *Robust Adaptive Control.* Prentice Hall, Inc, 1996.

[89] H. Wuethrich, “Technology Assessment Headphone Presentation,” Phonak AG, Stäfa, Research Rep., 2012.

[90] T. Zurbrügg, “Notes Occlusion Control,” Phonak AG, Stäfa, Notes 107, 2011.